Thin Films of Non-Peripherally Substituted Liquid Crystalline Phthalocyanines

A thesis submitted for the degree of Doctor of Philosophy

by

Chandana Pal

Wolfson Centre for Materials Processing

Brunel University

Uxbridge, UK

April 2014

This thesis is dedicated to

Kaushik

Acknowledgements

First of all, I would like to thank my supervisor Professor A. K. Ray for his guidance, encouragement and inspiration, without whom this thesis would not have been possible. I am also grateful to my second supervisor Dr. J. Ojeda for his guidance throughout the project. A special thanks to Professor Wordsworth Price for his invaluable tips which helped me to shape this thesis.

I acknowledge with gratitude the contributions from my collaborators in East Anglia University, Professor Mike Cook and Professor Andrew Cammidge, for providing me the materials and required information, and Dr. Ashwini Sharma, USAF, Research Laboratory, Space Vehicles Directorate, United States for sponsoring the project.

I am grateful to Professor John Fyson for his help in providing the CATSIM programming software designed for electrochemical study and Dr. George Fern in assisting with TOPAS software. I convey my sincere gratitude to late Professor Robert Withnall who trained me to use the Raman spectrophotometer.

Also, thanks are due to Dr. Isabelle Fernandes, Dr. Lydia Sosa-Vargas East Anglia University for supplying the Differencial scanning calorimetric data, Dr. David Hughes, East Anglia University for single crystal X-ray crystallographic data, Dr. Carlo Ferri, Brunel University for assisting measuring the thickness using Zygo interferometer, Mr. Max Evans, Brunel University for technical support

Other big thanks to to all of my friends, colleagues and well-wishers especially Ms. Tsegie Faris, Dr. Malcom Jayamurti and Dr. Sayed Raza.

Last but not the least, I convey my respect to family for constant support and inspiration during these years of study.

Abstract

Three non-peripherally substituted liquid crystalline bisphthalocyanine (Pc) compounds have been studied to examine the role of central metal ions lutetium (Lu), and gadolinium (Gd) and substituent chain lengths, i.e. octyl (C_8H_{17}) and hexyl (C_6H_{13}), in determining the physical properties. For the octyl substituted Pc molecules, the head-to-tail or J-aggregates within the as-deposited spun films produced a redshift of the optical absorption Q bands in relation to their 0.01 mgml^{-1} solutions. Annealing at 80°C produced a well-ordered discotic liquid crystalline (LC) mesophase causing additional redshifts irrespective of the metal ion in case of C_8LuPc_2 and C_8GdPc_2. Formation of face-to-face or H-aggregated monomers led to blueshifts of the Q bands with respect to solution spectra for C_6GdPc_2, both as-deposited and annealed films. Stretching and bending vibrations of pyrrole, isoindole, and metal-nitrogen bonds in Pc rings showed Raman bands at higher energy for smaller metal ion. However, no change was observed for the difference in chain lengths. As-deposited C_8LuPc_2 and C_6GdPc_2 produced comparable Ohmic conductivity, of the value 67.55 μScm^{-1} and 42.31 μScm^{-1}, respectively. C_8GdPc_2 exhibited two orders of magnitude less conductivity than the other two due to the size effect of the central ion and side chain length. On annealing, an increase of Ohmic conductivity was noticed in the isostructural octyl substituted phthalocyanines on contrary to a reduced conductivity in hexyl substituted one. An optical band shift of the C_8LuPc_2 and C_8GdPc_2 thin films occurred on oxidation by bromine vapour. Oxidations of Pc-coated ITO were also achieved by applying potential at 0.88 V and 0.96 V electrochemically for the C_8LuPc_2 and C_8GdPc_2 compounds, respectively. To explore the applications of these compounds in biosensing, *in situ* interaction studies between bromine oxidised compounds and biological cofactors nicotinamide adenine dinucleotide (NADH) and L-ascorbic acid (vitamin C) were carried out using optical absorption spectroscopy. Thin films of a non-peripherally octyl substituted LC lead phthalocyanine was exposed to 99.9 % pure hydrogen sulfide gas to produce hybrid nanocomposites consisting of lead sulphide quantum dots embedded in the analogous metal free phthalocyanine matrix. Trapping of charge carriers caused hysteresis in the current-voltage characteristics of the film on interdigitated gold electrodes. The charge hopping distance was found to be 9.05 nm, more than the percolation limit and responsible for forming two well-defined conducting states with potential application as a memristor.

Contents

List of figures

List of tables

List of Acronyms

Amp.	Ampere
Br_2	Bromine
C_6GdPc_2	Hexyl substituted gadolinium bisphthalocyanine
C_8GdPc_2	Octyl substituted gadolinium bisphthalocyanine
C_8H_2Pc	Octyl substituted metal free phthalocyanine (compound 2)
C_8PbPc	Octyl substituted lead phthalocyanine (compound 1)
C_8LuPc_2	Octyl substituted lutetium bisphthalocyanine
Col_h	Hexagonal columnar mesophase
Col_r	Rectangular columnar mesophase
CV	Cyclic voltammetry
DC	Direct Current
Def.	Deformation
DSC	Differential scanning calorimmetry
ESR	Electron spin resonance
FWHM	Full-Width at Half Maximum
H_2S	Hydrogen sulfide
HOMO	Highest occupied molecular orbital
ITO	Indium tin oxide
LC	Liquid crystalline
$LiClO_4$	Lithium perchlorate
LUMO	Lowest unoccupied molecular orbital
NADH	Nicotinamide adenine dinucleotide hydrogen
Pc	Phthalocyanine
QDs	Quantum dots
rpm	Revolutions Per Minute
SAED	Selected-Area electron Diffraction
SCLC	Space charge limited conduction
Str.	Stretching
TEM	Transmission Electron Microscopy
UV-Vis	UltraViolet –Visible
XPS	X-ray photoelectron spectroscopy
XRD	X-Ray diffraction

List of Symbols

A	Area of the interdigitated electrodes
A_0	Absorbance of the oxidised film
A_p	Area of the ITO electrode in cm^2
A_∞	Absorbance of the completely reduced film
A_t	Absorbance at time t
a	Lattice parameter
$a*$	Exciton Bohr radius
α_a	Absorption coefficient of the substance
α_0	Inverse of the site localisation parameter
B_PF	Poole-Frenkel coefficient in eVV$^{-1/2}$
β	Half width of Bragg peak
β_PF	Poole-Frenkel coefficient in eVV$^{-1/2}$ cm$^{1/2}$
C	Capacitance
C_0	Concentration of reactant at initial time
$C(t)$	Concentration of the analyte at time t
c_a	Concentration of the absorbing species
c_j^0	Initial concentration of the analyte j in mol/cm^3,
Φ_m	Vacuum work function of the metal
D	Size of the crystals
D_0	Overall thickness of the active layer in memristor device
D_j	Diffusion coefficient for species j in cm^2/s.
d	Thickness of the film
d_a	Path length
ΔD	Van der waal interaction
ΔE	Band gap energy
ΔE_0	Optical transitional energy
$\mathbf{E}$	Electric field
$E_{1/2}$	Formal potential of oxidation or reduction
E_F	Fermi energy level
E_pa	Anodic peak potential
E_pc	Cathodic peak potential
$\in$	Extinction coefficient of the absorber

ε_o	Permittivity of vacuum
ε_r	Relative permittivity of dielectric constant of the substance
F	Faraday constant, 96,485 C/mol
g	Mass fraction of lead sulphide quantum dots in organic matrix
h	Planck's constant
I	Net current
I_0	Intensity of incident light
I_e	Current through electrolytic solution in Ampere
I_R	Intensity of Raman bands
I_{sc}	Short circuit current
I_t	Intensity of the transmitted light
I_{VRH}	variable range hopping model current
i_{pa}	Current at anodic peak potential
i_{pc}	Current at cathodic peak potential
Φ_m	Metal work function
Φ_s	Semiconductor work function
Φ_t	Coulombic potential barrier at zero field
ϕs	Liquid evaporation rate
k_B	Boltzmann constant
k_{obs}	Rate of reaction
L	Channel Length of the interdigitated electrodes
λ	Emitted wavelength of light
λ_P	Peak positions in UV-Vis spectra
λo	Photoluminescence exciting light wavelength
λ_x	Wavelength of X-ray
M	Molecular weight
$M(t)$	Charge flux
m	Mass of an oscillating particle
m^*	Reduced mass
m_e	Mass of electron
μ	Mobility of the carrier through the band gap
N	Number of fingers in the interdigitated electrodes
N_0	Density of localized states at the Fermi level
n_o	The free charge carrier density

n_e	Number of electrons to reduce/oxidize one molecule of analyte.
η_L	Viscosity of the solvent
η_s	Viscosity of the material
ν	frequency of the incident beam
ν_{Ph}	Debye frequency
q	Unit charge
θ	Angle of diffraction
R	Resistance
R_t	The first order rate of reaction
R_v	Vector direction of a specific Raman scattering mode
R_{on}	Resistance when the active region when it is completely doped
R_{off}	Resistance of active region when it is mostly undoped
S_0	Width of the potential barrier
R	Radius of SAED pattern
ρ_Q	Density of lead sulfide
ρ_o	Density of metal-free phthalocyanine
S_H	Optimum VRH hopping distance
σ	Net conductivity
σ_0	Conductivity at 0K
σ_x	In- plane conductivity
σ_z	Perpendicular-to-the-plane conductivity
T	Temperature
T_0	Characteristic temperature
t	Time
$t_{1/2}$	Half-life of the reaction ($t_{1/2}$)
τ	Time constrant
U	Activation energy for site displacement
V_a	Applied voltage
V_{oc}	Open circuit voltage
W	Width of the interdigitated electrodes
x	Volume fraction of lead sulphide quatum dots
ω	Frequency of the barrier oscillation
ω_s	Speed of rotation of the material

Chapter 1 Introduction

Phthalocyanines (Pcs) show a remarkable range of semiconducting, electrochromic and photoconducting properties due to the presence of 18π macrocyclic rings with extended conjugation. Recent research has shown that developing advanced molecular electronics is possible by custom designing the molecules, structural reorganization or generating a nanocomposite material in a phthalocyanine matrix. The molecular structures are important in determining the properties of the material. Our current research is about characterisation of novel liquid crystalline (LC) bisphthalocyanines, investigation of the *in situ* interaction between electrochromic phthalocyanines and two selected biological cofactors, and current-voltage characteristics of an inorganic quantum dots /organic phthalocyanine-based nanocomposite compound.

For that purpose, the basic structures of the phthalocyanine molecules used in the study have been introduced here. The equivalent single crystal structures reported by other authors have been explored in this context. Furthermore, the motivation and aims of the research have been discussed.

1.1 Molecular structure

Phthalocyanines are macrocyclic compounds consisting of isoindole rings linked together by nitrogen atoms. Extended conjugation of 18π electrons gives these molecules aromaticity following the Hückel rule of $(4n+2)$ where $n = 4$. The molecules exhibit intense colour and charge transport abilities owing to the extended conjugation. Phthalocyanine structures are identical to naturally occurring porphyrin rings like chlorophyll or haemoglobin. If the pyrrole rings of porphyrin are exchanged with isoindole compounds and the carbon atoms between two isoindole rings are replaced by nitrogen, phthalocyanine (Pc) (Figure 1.1a and 1.1b) will be obtained.

The advantages of using phthalocyanines over porphyrins add better stability and more effectiveness in energy harvesting and electron transfer in the organic devices (Gregory, 2000; Walter et al. 2010). Recently, synthesis of phthalocyanines with about 70 different' central metal ions including rare earth and transition metals has been achieved. The solubility problem has been overcome by replacing the H in the benzene ring by a number of moieties such as alkyls, halogens, alkoxys, thioalkyls, or phenyl, and amino groups (Cook, 1994; Nemykin and Lukyanets, 2010). Pcs with long-chain linear or branched alkyl, alkoxymethyl or alkoxy chains have been found to form a major class of discotic LC materials (Li and Zhou, 2006). Figure 2.1c is an example of a substituted metallated monophthalocyanine molecule. The 1,4,8,11,15,18,22,25 positions are called α or non-peripheral positions; the rest of the positions are called β or peripheral.

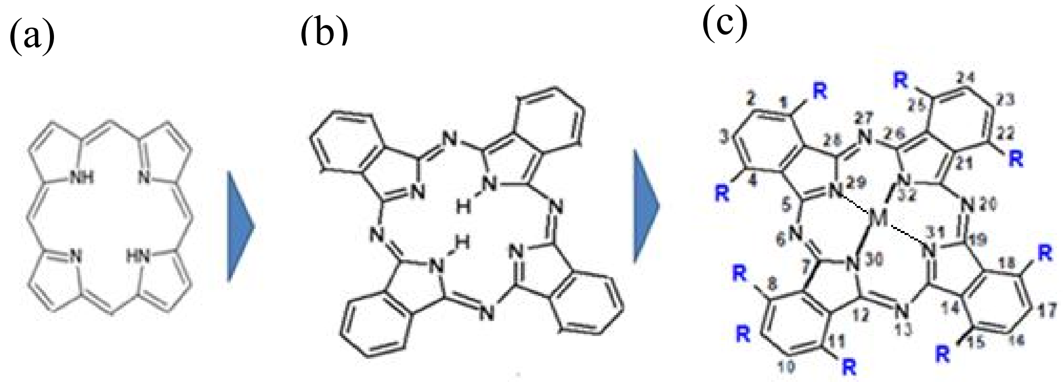

Figure 1.1: **Diagrammatic view of porphyrin-phthalocyanine relationship. (a) Porphyrin ring, (b) simplest metal-free phthalocyanine (c) Metallated mono phthalocyanine, M= Metal and R= substituent**

Recently double-decker bisphthalocyanines are of great interest as the intramolecular π-π interaction between the Pc rings adds interesting complexity over and above that of the simpler monophthalocyanine compounds. In bisphthalocyanines the central metal ion is sandwiched between two Pc rings as PcMPc (Where M is the metal), linked by coordination bonds. The newly synthesised non-peripheral bisphthalocyanine molecules used in the present study are:

Bis[1,4,8,11,15,18,22,25-octakis(octyl)phthalocyaninato]lutetium(III),C_8LuPc_2,
Bis[1,4,8,11,15,18,22,25-octakis(octyl)phthalocyaninato]gadolinium(III),C_8GdPc_2,
Bis[1,4,8,11,15,18,22,25-octakis(hexyl)phthalocyaninato]gadolinium(III),C_6GdPc_2(figure 1.2)

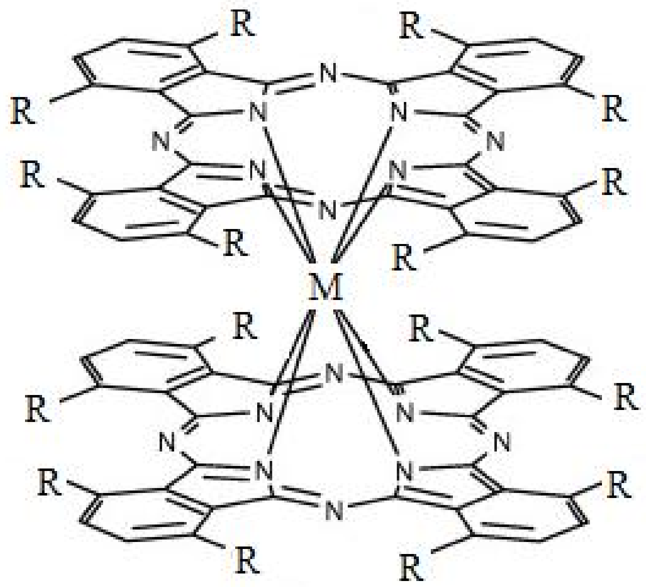

Figure1.2: Chemical structure of C_8LuPc_2, C_8GdPc_2, and C_6GdPc_2 M=Lu(III)/Gd(III) and R= C_8H_{17} for octyl and C_6H_{13} for hexyl

The structures of the rare-earth bisphthalocyanine single crystals have been established using X-ray crystallography by Gürek et al., 2006; Nekelson et al., 2007. It has been observed that the two phthalocyanine rings are not eclipsed to each other. Rather the rings make a staggered angle of 38˚ to 45˚ depending upon the substitutions, resulting in D_4 or D_{4d} symmetry (Lu et al., 2003). Figure 1.3 is a sandwich gadolinium bisphthalocyanine with hexylthio functional groups synthesised by Gürek et al., 2006. The staggering angle was 42.39° in this case. The average bond length between Gd(III) and isoindole nitrogen (N_{iso}) was noted as 2.42 Å. As the structure was distorted from planarity the angle N_{iso}-Gd-N_{iso} varied between 69° and 141°.

Most of the rare-earth bisphthalocyanines have a similar structure and the oxidation state of the metal ion is generally +3. However, the bond distance and the bond angles are sensitive to the central metal atom and the functional groups. The substituent chains may lie in or out of the plane depending on their steric hindrance.

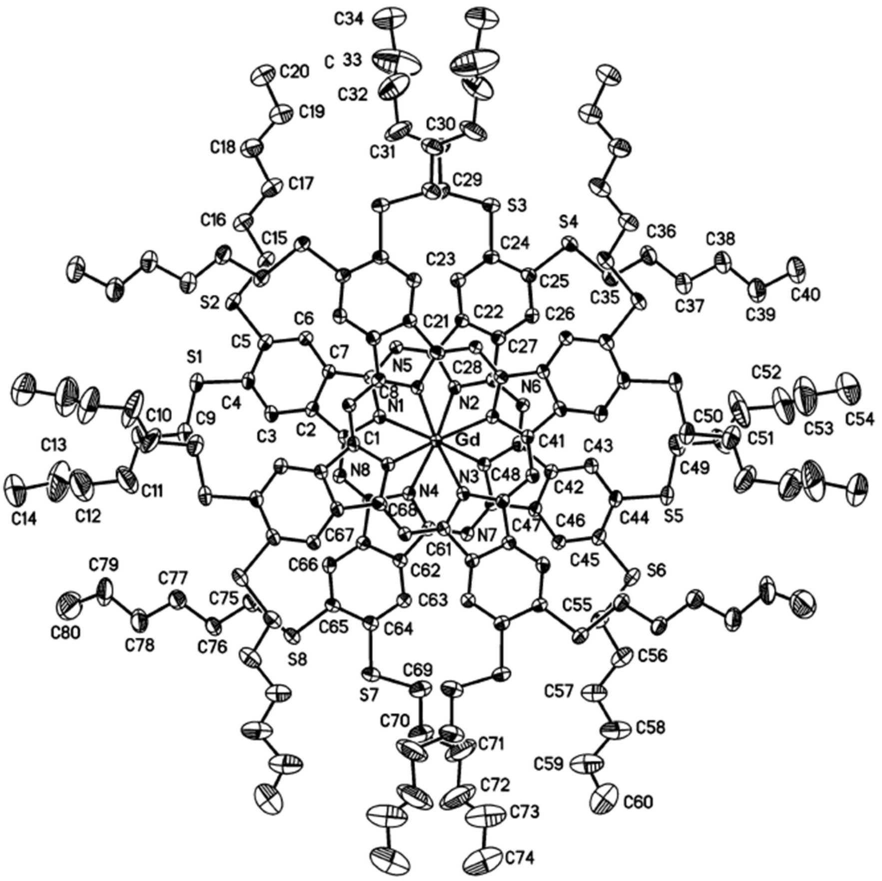

Figure 1.3: Single crystal structure of long-chain peripherally hexylthio-substituted LC gadolinium (III) bisphthalocyanine (Gürek et al., 2006)

The structure of monophthalocyanine molecules is generally planar. In the metallated monophthalocyanines, the central metal ion is coordinated to the four isoindole nitrogen atoms. These compounds generally hold the symmetrical D_{4h} point group. In metal-free phthalocyanine derivatives, two of the isoindole nitrogens are bonded to hydrogen atoms whereas the other two are iminic type functions having double bond attachments to carbon atoms in the isoindole structure (Figure 1.1b in this chapter). This type of compound holds lower degree symmetry of D_{2h}.

The presence of large central metal ions or bulky substitutions in metallated monophthalocyanines results in a non-planar structure. For instance, lead phthalocyanine molecules have been reported to have a 'shuttle-cock' like structure with C_{4v} symmetry (Baran and Larsson et al., 2010). In this case, the large lead atom (ionic radius 1.33 Å) cannot fit in the phthalocyanine cavity and distorts away from the plane. The Pb-N bonds have been found to be longer than those in other mono phthalocyanines. Atilla et al. 2011 calculated the Pb-N bond length as 2.21-2.41 Å for octakis and tetrakis (alkylthio)-

substituted lead phthalocyanines whereas the bond length in planar phthalocyanine is approximately 1.90 Å as reported by Liao and Sceiner, 2001. The out-of-plane Pb atom makes the Pb-N bond weaker and can be easily removed by a reducing agent like hydrogen sulphide gas (Nabok et al., 2004). Using X-ray crystallography, cyclomethyl-substituted metal-free phthalocyanine was found to have a twisted core due to steric hindrance of the substituent group, as reported by Cammidge et al., 2009.

In this research work, the non-planar non-peripherally octyl-substituted lead compound, 1, 4, 8, 11, 15, 18, 22, 25-octaoctyl lead phthalocyanine (C_8PbPc) was exploited for the formation of nanocomposite PbS quantum dots in a metal-free phthalocyanine (C_8H_2Pc) analogue matrix. A single solid state route developed by Nabok and coworkers has been used in this preparation (Nabok et al., 2004). The main reaction can be presented as

$$C_8PbPc + H_2S \rightarrow PbS + C_8H_2Pc \qquad (1.1)$$

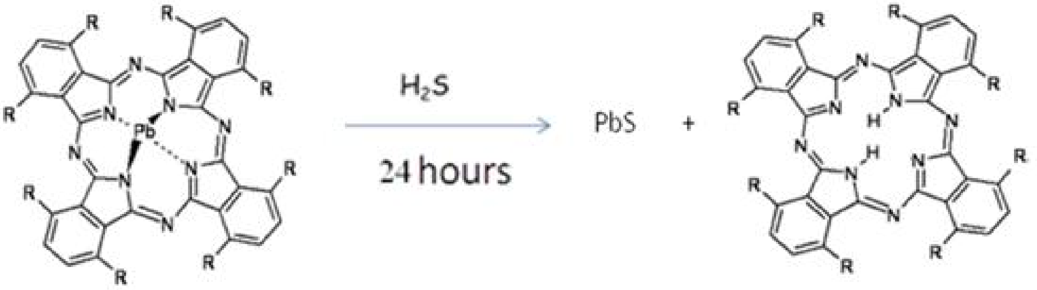

Figure 1.4: Formation of C_8H_2Pc and PbS quantum dots from C_8PbPc. Here, $R=C_8H_{17}$

1.2 Motivation and aims of this research

Our inspiration for the work is the present wide application of phthalocyanine materials for developing organic field-effect transistors (Chaure et al., 2010), memory storage devices (Mukherjee et al., 2008) sensors (Paul et al., 2009), optical switches (Huang et al., 2008) and the treatment of cancer (Ke et al., 2012) to name a few. The reasons for the progress of phthalocyanines research in order to replace conventional inorganic semconductors are as follows:

(i) Phthalocyanines are small molecules, easier to produce than large polymers, and boast higher purity and reproducibility.

(ii) These compounds are non-toxic and are chemically and thermally stable. Conventional phthalocyanines are stable in acidic or basic media with the exception of very strong acids or bases (Guillaud, Simon, and Germain, 1998).

(iii) Devices made from the solution-processible phthalocyanines are easy to fabricate with simple cost effective techniques like spin coating, dip coating or screen printing and can be deposited on any conductive or non-conductive substrates including flexible plastic sheets. Derivatives of non-peripherally substituted phthalocyanines show better solubility than that of their peripherally substituted counterparts (Cook et al., 2002).

(iv) The long-chain phthalocyanines have a tendency to aggregate showing coplanar association into oligomers. The mechanical and electrical properties of materials, like strength, hardness, conductivity, mobility of the charge carriers have been reported to be modified to suit various applications in hi-tech devices by molecular reorganisation (Gonidec et al., 2010, Msayib, Makhseed, and McKeown, 2001, Basova et al., 2008).

The only shortcoming of using the phthalocyanines is their low intrinsic electrical mobility owing to the lower density of charge carrier concentration and structural defects. For example, the carrier mobility of high purity single-crystal silicon is 450-1500 $cm^2 V^{-1}s^{-1}$ (Tao, 2008). In the same condition, most of the phthalocyanine-based devices show mobilities ranging from 10^{-5}-10 $cm^2V^{-1}s^{-1}$ in vacuum depending on structure and the deposition techniques (Li et al., 2008). More than 90% of organic devices with titanyl-phthalocyanine (TiOPc) as active layer exhibited hole mobility over 1.0 $cm^2V^{-1}s^{-1}$ because of the ultra-close interactions among the TiOPc molecules (Li et. al., 2007). Also, the self-assembling ability of the phthalocyanines arising from π-π stacking interactions in the LC mesophases shows an advance charge transport property. High field-effect mobility of 0.7 $cm^2V^{-1}s^{-1}$ for the discotic mesophase of a non-peripherally substituted copper phthalocyanine derivative has been reported by Chaure et al., 2010. Values of the electrical conductivity of undoped phthalocyanineshave been reported to be within the wide range of 10^{-5} to 10^{-15} Scm^{-1}depending upon the polymorphic form of the material (Turek et al., 1987; Hanack and Dini 2003). Organic photovoltaic cells (OPV) with very low series resistances (0.1 $Ohmcm^{-2}$) have been fabricated by Xue et al., 2004 with 4.2% conversion efficiency. Further doping by alkali metals like potassium and sodium was found to improve the OPV characteristics (Shih et al., 2011; Chen et al., 2013).Therefore, altering the structure by synthesising different custom-designed phthalocyanines or by appropriate external doping makes advanced applications of phthalocyanines in organic electronics possible.

Our current research is a ‘‘bottom-up’’ approach to fabricate more economical and efficient devices by altering the central metal ion or substituents in the molecules, heat treatment, and incorporation of quantum dots in the crystal structure.

For these purposes a review of the relationship between LC phthalocyanines structure and property and their use has been presented in Chapter 2. The cyclic voltammetry techniques used for the exploration of the electrochromism properties of phthalocyanines have also been included.

Another aspect of the current research work is to improve the conduction mechanism of a phthalocyanine thin film by generating a nanocomposite material consisting of PbS nanoparticles embedded in a Pc matrix. The advantage of the lead sulphide over other chalcogenides in forming a nanocomposite compound has been reviewed in Chapter 3 including recent developments of phthalocyanine-based nanocomposite devices.

In Chapter 4 the molecular orbital theory and the electronic charge transport models have been presented to interpret the experimental data for the optical transitions and conduction mechanism.

Chapter 5 presents the fabrication process of thin film and nanocomposite material along with the experimental techniques for their analysis. A detailed description of the thermal annealing method for the formation of C_8LuPc_2 and C_8GdPc_2 liquid crystalline phase has been described in this chapter. Different spectroscopic and thermogravimetric, electrochemical methods have been overviewed in order to study the physicochemical properties of the materials. Details of the set-up for a current-voltage measurement system at different temperatures are presented.

In Chapter 6 an optical and electrical study of the LC thin films of the materials in figure 1.2 has been explored using some of the techniques mentioned in Chapter 5. It has been shown that the optical and electrical properties of the as-deposited and annealed material are dependent on the central metal ion, substitutions and molecular orientations.

In Chapter 7 spin-coated films of octaoctyl substituted lutetium and gadolinium bisphthalocyanines exhibit pronounced chemichromic behaviour. Optical absorption spectroscopic measurements show optical shifting upon oxidation chemically or electrochemically. Recovery to the original state was achieved by the treatment of the oxidized films with NADH and vitamin C. This chapter focuses on the use of the two phthalocyanines for detection of NADH and Vitamin C *in situ* biosensing. The oxidation method, stability of the film and the kinetics study of the reduction of oxidised film by NADH along with the aging effect have been discussed.

Chapter 8 contains the topic of 'Hybrid nanocomposites of lead sulphide quantum dots/metal-free phthalocyanine'. First, the formation of the PbS quantum dots was verified by X-ray diffraction, transmission electron microscopy and thermogravimetric analysis. The band gap and the size of PbS quantum dots and interfacial interactions between the components were investigated. The current hysteresis with voltage and its variation with temperature have been studied with a view to the use of these nanocomposites as memory storage devices.

In Chapter 9, the supplementary data, main conclusions and proposals for future work are included.

Chapter 2 Liquid crystalline phthalocyanines

Some polymers have long-chain molecules which show a tendency to organize in layers by π-π stacking in the solid phase. The properties of these organic layers not only depend upon the single crystal structure but also on the arrangement of the molecules in the film. This long-range orientation order produces what is known as a ‘liquid crystal’ or the ‘mesogenic phase’.

Lehmann and Vorländer in 1888 found the ‘liquid crystal’ properties while experimenting with the soft crystals of fluid/floating crystalline cholesteryl benzoate. The name was proposed as ‘liquid crystal’ because this phase strongly resembles the liquid phase (fluidity), but maintains a high degree of orientation order (anisotropy).

Phthalocyanine (Pc) was discovered in 1928, by four chemists: Dandridge, Drescher, Dunworth and Thomas at Scottish Dyes company (Gregory, 2000). The name ‘phthalocyanine’ (phthalo or naphtha, meaning oil and cyanine meaning blue) was given by Linstead in 1934 due to its sharp blue colour. The structure was first established by Robertson, 1935 by X-Ray diffraction technique. These unsubstituted 1:1 complexes of ligand and a metal ion are insoluble and their most common commercial use was in the dye industry (Gregory, 2000). Recently, custom-designed compounds with different substituents, metal ions or multinuclear Pc rings, have been synthesized for advanced electronics. The mesogeneity of long chain phthalocyanines has been widely investigated since it was first studied by Piechocki et al., 1982. The studies have revealed that with the orientational control of conventional liquid-crystal systems can be used in different fields of molecular electronics.

This Chapter focuses on the fundamental properties like optical absorption, dc conductivity, and electrochromism in the liquid crystalline (LC) phase of phthalocyanines and their applications.

2.1 Classification of the mesophases

Two types of mesogeneity have been found in phthalocyanines. In some cases the monomers form long-ranged orientation order induced by the addition of a solvent. The main driving force behind the formation of these mesophases is minimisation of the electrostatic interactions. This is called lyotropic liquid crystallinity. The viscosity of the solvent plays an important role in the formation of the shape and size of the liquid crystal. Zharnikova et al., 2009 have investigated lyotropic liquid crystallinity with tetra triphenylmethyl phenylazophenoxy substituted zinc phthalocyanines. The column-shaped arrangements of the lyomesophases take place on evaporating the concentrated solution of the complexes in dimethyl formamide (DMF) or toluene solvents. Kudrik et al., 2006, noticed mosaic-shaped or small globule-shaped phases in copper phthalocyanine derivatives substituted with large size cyclic carboxyphenoxy groups.

Thermotropic liquid crystals are the mesophases which originate from the change in temperature of the deposited material. These phase transitions are always accompanied by a change in enthalpy (ΔH). Therefore, a ΔH versus temperature plot shows peaks at the transition points. On heating up to the melting point the orientations are broken down and isotropic behaviour is exhibited. Differential Scanning Calorimetry (DSC) is one of the most widely used methods to detect the phase transitions of phthalocyanines. Figure 2.1 shows the DSC plot of thiodecyl substituted cerium phthalocyanine reported by Nekelson et al. 2007. The three peaks corresponding to 4°C, 56°C and 217°C were identified as transitions between the solid and the mesophase, between two mesophases and between the mesophase and the isotropic liquid.

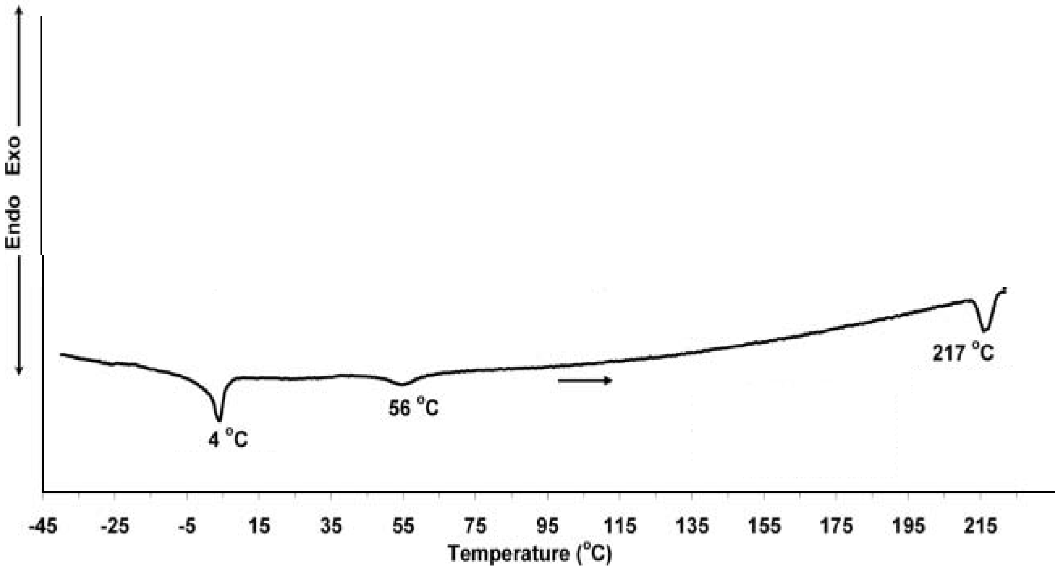

Figure2.1: DSC thermogram of thiodecyl double-decker cerium phthalocyanine (redrawn from Neckelson et al., 2007)

2.2 Liquid crystal arrangements

Thermotropic liquid crystals are mainly classified into four types according to the arrangement of the constituting groups. These are nematic-discotic, nematic-columnar, columnar heaxagonal, and columnar rectangular. Figure 2.2 displays the arrangements of the four phases, assuming each phthalocyanine monomer as being disc-like in shape.

In the nematic phase there is no positional order but the discs tend to point in the same direction. In the nematic-discotic phase shown in Figure 2.2a, the molecules point vertically but are arranged with no particular order. Figure 2.2b shows the nematic-columnar phase in which the monomers are organised in the shape of a column but do not grow in any specific direction. In the hexagonal and rectangular columnar phases the discs are densely packed as cylinders and form a one-dimensional array. The hexagonal columnar mesophase is built up by columns that arrange themselves in a hexagonal fashion, Figure 2.2(c), and is abbreviated as Col$_h$. The molecules of the rectangular columnar mesophase (Col$_r$) are packed in a rectangular lattice in Figure 2.2(d) (Kumar, 2010).

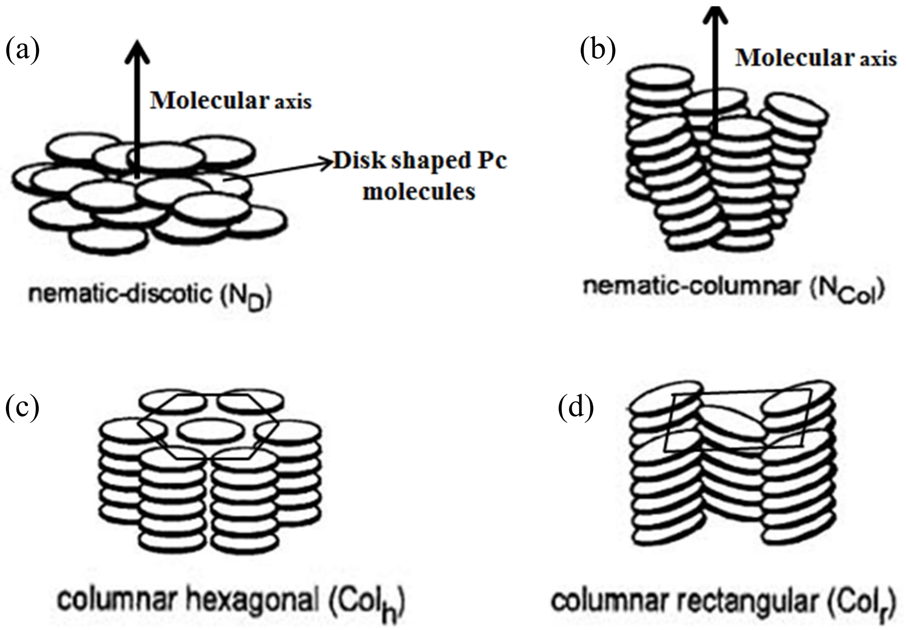

Figure 2.2: Common mesophases exhibited by phthalocyanines (redrawn from Discotic liquid crystals, 2014)

Since the charge flow of the Pcs is based on π-π interactions, the one dimensional array hexagonal and rectangular columnar phase liquid crystals are favourable for large area electronic devices. Time-of-flight and direct current conductivity studies by different authors show charge migration is facilitated along the rod axis more than in a direction perpendicular to the axis (Tans et al., 2003; Donley et al., 2004; Basova et al., 2006). Misalignment or any distortion in the columnar aggregates strongly influences the physical properties (Chwang and Frisbie, 2001; Kelly and Frisbie, 2001). This kind of long-range homeotropic alignment is difficult to achieve for other organic single crystal or polymer-based large area devices as they tend to form polycrystalline multi-domains.

For characterisation of the LC phases UV-Vis spectroscopy, atomic force microscopy (AFM), polarised optical microscopy, polarised Raman spectroscopy and X-ray diffraction (XRD) are used.

2.3 Optical absorption

The UV-Vis spectroscopy is the most common method used to characterise the discotic liquid crystal phthalocyanines. Generally all the Pc chromophores show a sharp electronic absorption band in the range of 650-800 nm (Q band) which is the origin of intense blue/green colour. The molar extinction coefficients of the π-π^* transitions have been reported as having values as great as 10^5 $dm^3mol^{-1}cm^{-1}$ (Ortiz et al., 2013). The major factors influencing the evolution of the optical transitions are the molecular orbital energy levels and the geometric structure in the film and crystals.

In solution phase the liquid crystal Pcs are present as monomers. The metallated monophthalocyanines show a single Q-band in the visible range. On the other hand, the splitted outermost molecular orbitals of the bisphthalocyanines show two Q bands in the visible region. The origin of the molecular orbitals in the Pcs will be diagrammatically explained in Chapter 4. An additional shoulder band in the range 450-480 nm for the rare-earth bisphthalocyanines correlates to their radical nature. An electron spin resonance (ESR) signal with a neutral unsubstituted LuP_{C2} supports the existence of unpaired electrons (Ishikawa, 2001). In addition to this, typical optical absorption spectra of all the Pc molecules contain a B or Soret band in the Ultra-Violet region. Figure 2.3 displays the UV-Visible spectra of a group of long-chain hexadecylthio rare-earth bisphthalocyanines having Eu, Tb and Lu central atoms in solution phase (Yoshino et al., 2000). The electronic transition patterns are similar, as three of these sandwich double-deckers bisphthalocyanine monomers have equivalent structures. The blue shift trend of the Q band in the 650-800 nm range has a direct relationship with the size of the central atom as it decreases in the order Eu>Tb> Lu.

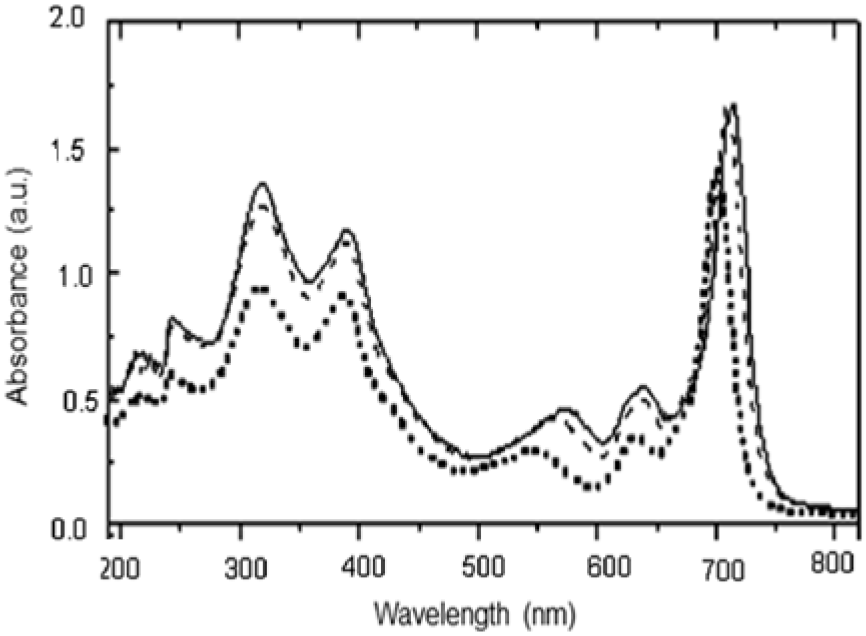

Figure 2.3: The size effect of central metal ions (M = Eu, Tb, Lu) on the UV-Vis spectra is shown. Eu[($C_{16}S_8$)$_2$]Pc_2 (solid line), Tb[($C_{16}S_8$)$_2$]Pc_2 (dashed line), and Lu[($C_{16}S_8$)$_2$]Pc_2 (dotted line) in $CHCl_3$ (Yosino et al., 2000)

The optical band gap of these compounds can be estimated from the energy required for the optical transition from the lowest unoccupied molecular orbital (LUMO) to the highest occupied molecular orbital (HOMO). Generally, the absorbed energy for electronic transition corresponding to the band gap lies in the near infra-red region in the range of 1.5-2.0 eV (Djurovich et al., 2009).

The aggregated species of the liquid crystal cause electronic coupling between the neighboring molecular orbitals. As a result, a strong spectral shift or splitting of the absorption band in the composite material can be expected with respect to the monomer spectra. Depending upon the assembling pattern of the monomers, both blue and red shifting is possible. In 1965, Kasha, Rawls, and El-Bayoumi established the molecular exciton theory to predict the spectral shifting based on the strong interaction between localized transition dipole moments of dimers. Van der Waal's interactions, hydrogen bonding, or π-π stacking were found to be the main driving forces for aggregation but no chemical bonding between the aggregates was found to form. Hence, the dimers are known as physical dimers. This model can be extended to include interactions of molecules in boundless stacks. From the spectral changes various aggregation patterns were proposed like J-type aggregates, H-type aggregates or herringbone pattern. The J-type aggregates where the monomers are layered in head-to-tail arrangements or staggered slip stacking cause bathochromic or redshifted Q bands. The patterns of the one-dimensional assemblies for J-type aggregates are displayed in Figure 2.4 (a), (b) and (c) as ladder, staircase and brickwall types, respectively. On the other hand, H-type aggregates are believed to cause the blue-shifted spectra. In this case the monomers are perpendicular to the plane and arranged in a sandwiched type array (Figure 2.4 d).

(a)Ladder-type **(b)Staircase-type** **(c)Brickwall-type** **(d)Sandwich-type**

Figure 2.4: Schematic representation of different kinds of arrangements of the chromophores (adapted from DST Unit of Nanoscience, 2014)

When there is exciton coupling between two neighbouring metallated phthalocyanine molecules the energy splitting in the dimers depends upon the orientations of the monomers. This is illustrated in Figure 2.5. In the Figure the oval represents the molecule and the transition dipole moment, denoted by an arrow, is considered parallel to the molecular profile. The energy of the composite molecule ($\Delta E_{\text{composite}}$) can be expresed as the combination of the energy band gapwithout intermolecular interaction (ΔE_{unit}), the Van der Waal interaction (ΔD), and the exciton splitting energy (ΔE_S).

$$\Delta E_{\text{composite}} = \Delta E_{\text{unit}} + \Delta D + \Delta E_s \qquad (2.1)$$

The head-to-tail orientation of the transition dipoles in the energy diagram (a) gives rise to the splitted energy levels E' and E''. Here, E' denotes the in-phase interaction resulting in a lower energy state. On the other hand E'' arises due to the out-of-phase interactions. As the transition to the higher energy level is forbidden in a parallel coplanar situation, the energy-favourable transition from the monomer level G to E' gains in intensity and causes the red shift of the J-aggregated species. In the case of H-aggregates the in-phase interactions reinforce each other and give rise to the higher energy state E'' whilst the out-of-phase dipole arrangement corresponds electrostatically to a lowering of energy E'. Following the energy-favourable transition from G→E'', the aggregated dipole gives a blue shift of the electronic spectrum in comparison to the monomer.

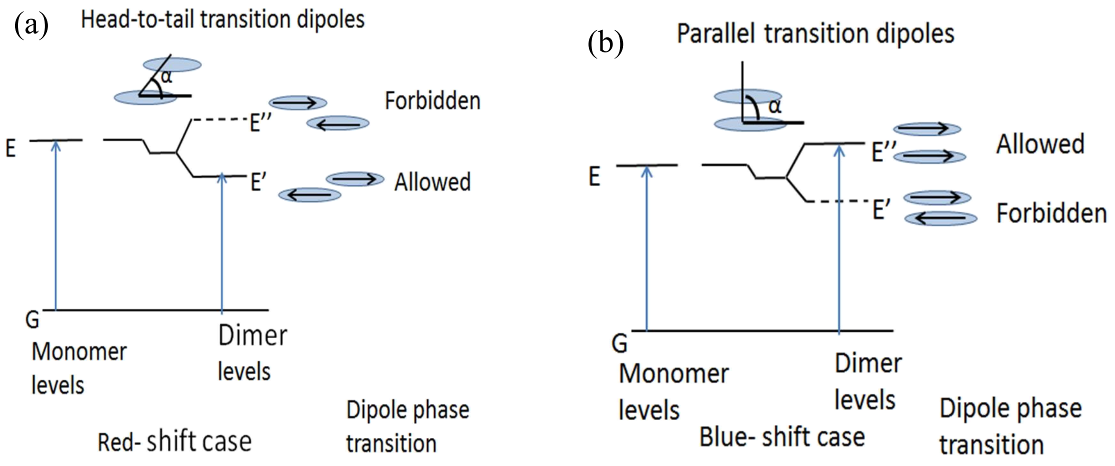

Figure 2.5: **Exciton band energy diagram for a molecular dimer, or a double molecule, with (a) J-type and (b) H-type aggregation (Kasha, Rawls, El-Bayoumi, 1965)**

The type of noncovalent interactions, the solvent polarity, or the presence of linking groups in the phthalocyanines are the switching factors from H to J aggregates. Adachi, Chayama and Watara, 2006 have investigated the formation of the aggregation between non-peripherally benzhydrylthio substituated magnesium phthalocyanine (MgPc(SBh)$_8$) and binaphthyl substituted paladium phthalocyanines (Pd(II)BINAP). It was found that the aggregates were preferentially J type in toluene-water mixture solution as the repulsive interaction between BINAP and benzhydryl group reduces the stability of the expected H-aggregate. In toluene the MgPc(SR)$_8$-Pd(II)BINAP complex was found to form an H-type aggregate (face-to-face type).

The long-chain substituted metal-free monophthalocyanines show a unique splitted Q band of equivalent intensity in the visible region, known as Davidov splitting (Claessens, Hahn and Torres, 2008). Kasha's exciton model is also useful to describe the Davydov splitting of these compounds. In 1998, Ray et al. reported that octa-substituted metal-free phthalocyanine molecules most preferably stack in a herringbone style as shown in Figure 2.6a with the tilted angle as α between the units. Figure 2.7b displays the exciton model with the transition dipoles tilted angle as α. The electrostatic interactions between the two transition dipole moment vectors lead to the higher energy state E'' and lower energy state E'. The optical transitions from ground state to two different energy states in the dimers result in band splitting in the UV-Vis spectra.

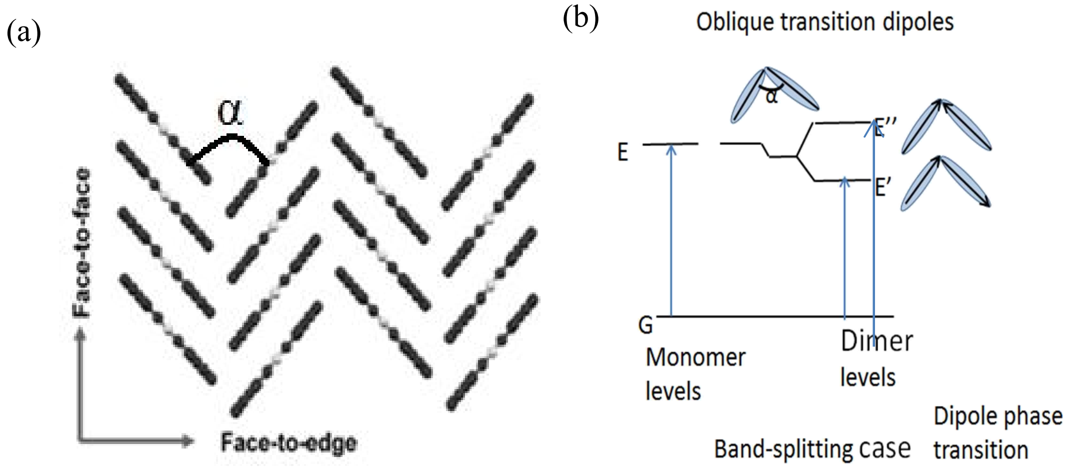

Figure 2.6: (a) Molecular arrangements of Herringbone structure (b) Optical transitions by Kasha's model (adapted From Kasha, Rawls, El-Bayoumi, 1965)

2.4 Characterisation Techniques

Surface topology is found to be a useful method to examine the quality of a liquid crystalline material. The rough surface traps the charge and consequently reduces the speed of electrical conduction. Annealing helps to eliminate the impurities or defects in the crystals. Also, removal of trapped water molecules makes the crystals collapse and decreases the grain boundary resistance in the film.

Gürek et al., 2005; Basova et al., 2007 and Chaure et al., 2012 have investigated the as-deposited and LC phases of hexyl substituted phthalocyanines. Figure 2.7 illustrates the formation of a well-connected rod-like crystallite structure from granular as-deposited film in a hexyl substituted copper phthalocyanine on annealing at 100°C. The columnar aggregates were found to enhance the transistor parameters in the LC phase of this compound (Chaure et al., 2012).

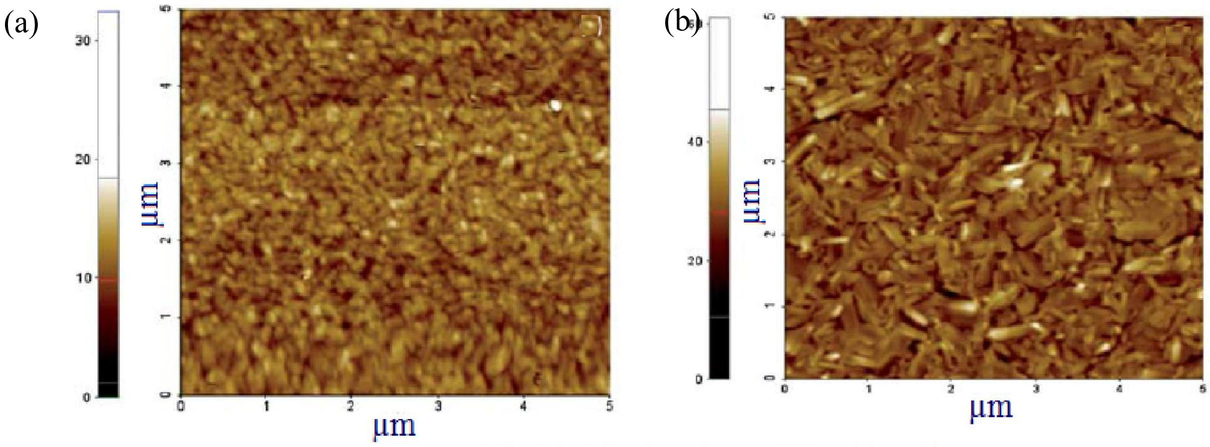

Figure 2.7: **AFM images of LC hexyl substituted copper phthalocyanine films before (a) and after (b) heating at 100°C (Chaure et al., 2012)**

The anisotropic behaviour of the liquid crystals leads to the property of polarisation of light which is also known as 'birefringence'. This property is very commonly employed to characterise the planes of orientation of the mesophases using Polarised optical microscopy (POM). In these microscopes the liquid crystal material is placed between the polarizer and analyser along the transmission axis.

Figure 2.8 illustrates the POM images of a LC tetra-substituted nickel phthalocyanine derivative with a perfect columnar mesophase array arranged perpendicular to the plane. An image of the illuminated surface was obtained on placing the analyser parallel to the polariser (Figure 2.8a). On placing the polariser and analyser in the cross-polarised position the image became completely dark (Figure 2.8b) (Basova et al., 2009).

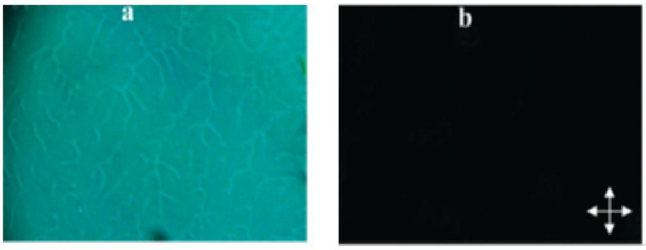

Figure 2.8: **POM images of a tetra substituted LC nickel phthalocyanine on placing polarizers in (a) parallel (b) cross position (Basova et al., 2009)**

However, in most of the cases the entire sample may not be in the same phase. Therefore, a characteristic texture for a certain type of mesophase is used for identification instead of total light or darkness. For example, a typical fan shaped texture for discotic hexagonal-columnar phase of different phthalocyanines has been published by Gürek et al. 2006; Basova et al., 2007; Nekelson et al. 2007.

Polarised Raman spectroscopy technique is used to get detailed information about the tilt angle of the monomers and the angle with the substrate. The intensity (I_R) of the Raman band is dependent on the polarisation vectors of the electric field for the incident ($\boldsymbol{E_i}$) and the scattered laser beam ($\boldsymbol{E_s}$), respectively (Basova et al., 2009).

$$I_R \propto [\mathbf{E}_i . \mathrm{R}_v . \mathbf{E}_s]^2 \qquad (2.2)$$

in which R is the Raman scattering transition moment given by

$$R = < \boldsymbol{\Psi}_i \mid a_r \mid \boldsymbol{\Psi}_j >$$

Where, $\boldsymbol{\Psi}_i$ and $\boldsymbol{\Psi}_j$ are the initial and final states, respectively, and a_r is the polarizability of the molecule.

Therefore, to use this method it is necessary to know the I_{VV}/I_{VH} (Intensity ratio of Raman modes for parallel (VV) and crossed (VH) polarizations for Raman active bands) of each symmetry type of vibration. The principles of using this technique have been described by Basova and Kolesov, 1998; Basova et al., 2001; Basova et al., 2002 for LC copper and nickel derivatives.

In X-ray Diffraction (XRD) the incident beam is reflected from different planes of the crystals. This technique can be used to determine lattice d-spacings, lattice dimensions and crystallite size as the phase change may affect both the peak intensity and position. Two complementary experimental setups are usually used: one for the long spacings, corresponding to the low-angle region (SAXS) and another designed for wide angle (WAXS), corresponding to crystal spacing of around 4.5 Å. Hatsusaka et al., 2000, and Sun et al., 2012, have used this method to determine internal structure details like the intra and intermolecular distances between the monomers and the crystallite size of the self-assembled phthalocyanines. As the optical and electrical properties are very much dependent on the π-π interaction of the Pc units, arrangement of the rings is a vital factor, whilst film deposition is important for applications in anisotropic conductors.

2.5 Role of mesophases as a charge carrier units

In general only the long-chain substituted phthalocyanines show the LC properties. This is because long flexible side chains allow the molecule to self-assemble in columnar shape. From a positional point of view, peripheral substitution leads to comparatively more ordered columnar mesophases than those obtained by non-peripheral substitution, as the linking groups in the latter cause more steric hindrance between the aromatic macrocycle and the linking group (Eichhorn, 2000; Hunter and Sanders, 1990). Furthermore, the best result of electrical conduction is expected when the Pc units are aligned to the direction of charge flow. The electrical conduction of peripheral thiohexyl substituted lutetium bisphthalocyanine and nickel phthalocyanine mesophases have been compared by Basova et al., 2006, on the basis of the anisotropic properties. The conductivity parameters reported by them regarding the annealed effect on in-plane and perpendicular-to-the-plane conductivity of the film are given in Table 2.1.

Table2.1: Electrical and Optical parameters of as-deposited and annealed film ofNiPcR$_8$ and Lu(PcR$_8$)$_2$ (R= SC$_6$H$_{13}$)

Material	**Electrical conductivity**			
	In- plane conductivity σ_x**(Scm^{-1})**		**Perpendicular-to-the-plane conductivity** σ_z **(Scm^{-1})**	
	As-deposited	**Annealed**	**As-deposited**	**Annealed**
Lu(PcR$_8$)$_2$	1.4×10^{-7}	1.2×10^{-7}	1.9×10^{-10}	6.1×10^{-14}
NiPcR$_8$	5.7×10^{-7}	2.8×10^{-7}	4.0×10^{-10}	6.1×10^{-8}

Table 2.1 shows that the perpendicular-to-the-plane conductivity (σ_z) of lutetium phthalocyanine between tin-doped indium oxide (ITO) and gold electrodes is decreased by four orders of magnitude on annealing while the in-plane conductivity (σ_x) remains unchanged. This observation suggests that the transition dipoles in the LC state were aligned in a parallel direction to the substrate (Figure 2.8a). In the case of nickel phthalocyanine the σ_z of annealed film is increased by two orders of magnitude, contrary to the decreasing value of σ_x. Comparing the values, the stacking structure of the NiPcR$_8$ monomers was proposed as being perpendicular to the substrate surface (Figure 2.8b).

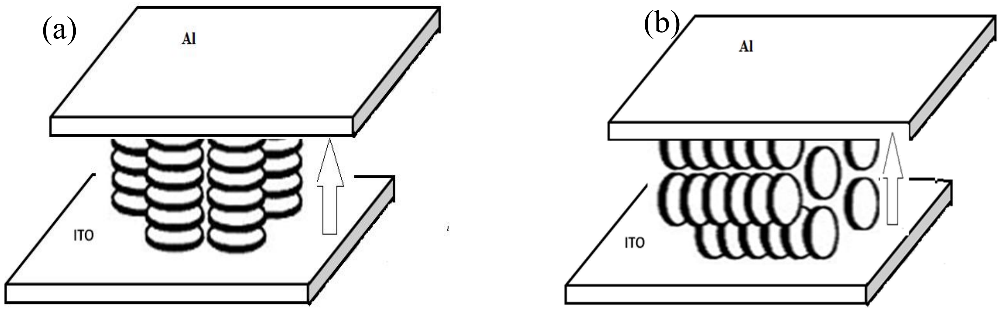

Figure 2.9: **(a) Stacking of $NiPcR_8$ monomers perpendicular to the substrate surface, (b) Stacking of $Lu(PcR_8)_2$monomers parallel to the substrate**

In addition to this, large rod-like crystals of a peripherally benzyl-oxy-ethoxy substituted copper phthalocyanine show up to three orders of magnitude higher parallel-to-the-plane conductivity with respect to the perpendicular-to-the-plane conductivity (Donley et al., 2004).

2.6 Effect of structural modification on charge migration

Liquid crystal (LC) properties have been found to change considerably on substituting with large groups or enlarging the central conjugated core. The discotic liquid crystals of a triphenylene derivative substituted with sterically bulky alkylthio groups were found to exhibit considerably higher charge carrier mobility than when substituted with alkoxy groups (Ban et al., 2000; Ban et al., 2001). Branching of the chains does not affect conduction in the LC state. The mobilities of both octa-docyloxy-substituted and octa-3,7,11-trymethyl-docyloxy-substituated phthalocyanines were reported in the range 0.063 - 0.042 $cm^2V^{-1}s^{-1}$ (Eichhorn,2000).

Increasing the chain length in the substituents of Pc molecules raises the hopping distance of charge particles. The conductivity of a series of non-peripheral alkylthio substituted lutetium phthalocyanines in the range C_6 to C_{16} was found to decrease by a three order of magnitude from 10^{-5} Scm^{-1} to 10^{-8} Scm^{-1} (Atilla et al., 2011). The central metal ions have no direct role, as the macrocyclic Pc rings take the leading role in the charge transfer mechanism, although the size of the Pc core matters for the closer overlap of the rings and the electrical conduction (Hanack and Dini, 2003)

2.7 Role of deposition techniques in arrangements of the Pc units

The application of the Pc films depends on the ability to prepare them in thin films. In the beginning, vacuum deposition was the only method for the fabrication of thin films of insoluble unsubstituted phthalocyanines. After the discovery of soluble derivatives, a number of deposition techniques have been used which are comparatively easier, faster and cheaper than vacuum deposition. Spin coating, inkjet printing, laser printing, spray coating and the Langmuir-Blodgett (LB) method are the most common among them.

The LB method has been proved to be a useful method for fabricating long-range order in phthalocyanines. Also, these films are reproducible and adhere persistently to substrates and to each other. Studies with mono-crown ether-substituted phthalocyanines have shown that the number of hydrophobic or hydrophilic groups in the substituent chain is important for the arrangement of the molecules (Chen et al., 2005). In some cases the peripherally substituted Pcs have a specific organization of the film which enhances the conducting properties by providing a pathway to charge flow (Jones, Krier and Davidson, 1997, Silerova et al., 1998).

Recently, Kilinc et al., 2012, have used a jet-spray to coat gold electrodes on glass substrates with metallated and metal-free hexyl-substituted phthaloyanines dissolved in chloroform and acetone. Roughness of the films was found to be around 90-125 nm by scanning electron microscopy (SEM) techniques, also droplets were seen on the surface. One of the most advanced techniques is Inkjet printing in which a computerised printing system creates digital images by propelling droplets of ink onto paper. Kim et al., 2009, have used this technique for water soluble phthalocyanines to be used for color filters in Liquid crystalline displays.

In this research work a simple, low-cost spin coating method has been undertaken. Very thin films with a better degree of smoothness can be obtained with this method. In Spin coating deposition the solvent is allowed to evaporate while rotating the dispersed solution at high speed. The advantage of this technique is that it is a very simple and cheap method for the deposition of films and it can be used on various substrates irrespective of whether they are conductive or non-conductive, including flexible plastic sheets. Liquid crystalline phthalocyanines are more suitable for this deposition technique because of their low molecular weight and intermolecular stacking tendency.

Investigations on non-peripherally butyl-substituted magnesium and zinc phthalocyanines spun film on gold substrates showed the shorter side chain helps to form more ordered films, indicating the influence of size and intermolecular distances (Peisert et al., in 2005).

Chaure et al., 2010, have reported spin coating of octyl-substituted lutetium bisphthalocyanine on octadecyltrichlorosolane (OTS) coated silicon dioxide substrate in chloroform solution (5 mg ml^{-1}concentration) at a speed of 2000 rpm for 30 seconds. The film thickness, ca. 100 nm, and also 30 nm roughness have been estimated by surface imaging studies. The spinning speed of the depositor is important to keep the film morphology the same for every film.

2.8 Electrochromism and the cyclic voltammetry

The self-assembling of longer chain phthalocyanines has been identified as having potential interest in solid state electrochemistry. Most of the phthalocyanines show electrochromism, which is a property of changing the colour of a compound induced by electrochemical potential.

The electrochromic property of the phthalocyanines comes from the flexible HOMO-LUMO gap of the Pc rings. As the intra and intermolecular interactions between the adjacent molecules of phthalocyanines are altered on oxidation or reduction processes, the width of the band gap changes. The subsequent shifts in the Q band of the UV-Vis spectra have been used to monitor the redox processes in the phthalocyanines. In many cases, the sharp contrast of the colour changes is visible even to the naked eye. For example, on redox potential changes, unsubstituted lutetium phthalocyanine can show five different oxidation states with a broad range of colours as shown in Figure 2.10 (Kadish et al., 2001).

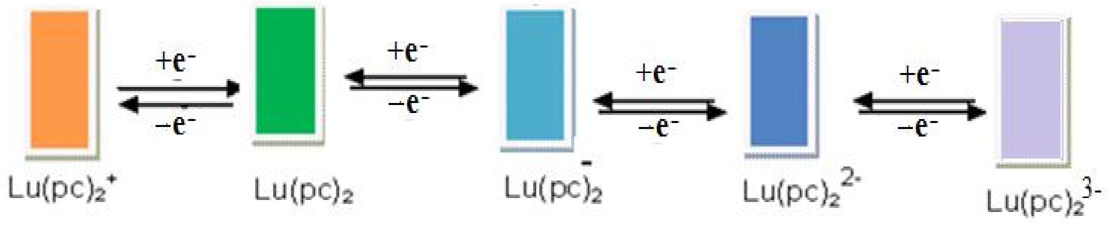

Figure 2.10: Schematic diagram of the unsubstituted Lutetium phthalocyanine electrochromism

In an electrochemical process, a potential is applied between the electrodes immersed in an electrolytic solution (water or organic solvents). The redox changes take place via electron transfer between the electrode and the electrolyte in solution. To find out the required potential, cyclic voltammetry is carried out where the current passing through the electrode is measured against the linear potential sweep. On sweeping the potential, at a certain point the current starts increasing and passes through a maximum due to the oxidation or reduction of the material. The cyclic voltammograms in Figure 2.11 display the presence of an anodic potential peak (E_{pa}) and a cathodic potential peak (E_{pc}) of a spin-coated liquid crystalline peripherally substituted $[(C_6H_{13}S)_8Pc]_2Dy$ film deposited on an ITO electrode in the voltage sweep between ±1.5 V (Basova et al., 2008). The formal potential of oxidation or reduction, $E_{1/2,}$ can be estimated from the average of an anodic and cathodic peak as $E_{1/2} = (E_{\mathrm{pa}} + E_{\mathrm{pc}})/2$ and was estimated as 0.78 V. The difference between the peak differences is designated as $\Delta E = (E_{\mathrm{pa}} - E_{\mathrm{pc}})$ which is equivalent to the band gap energy of the material.

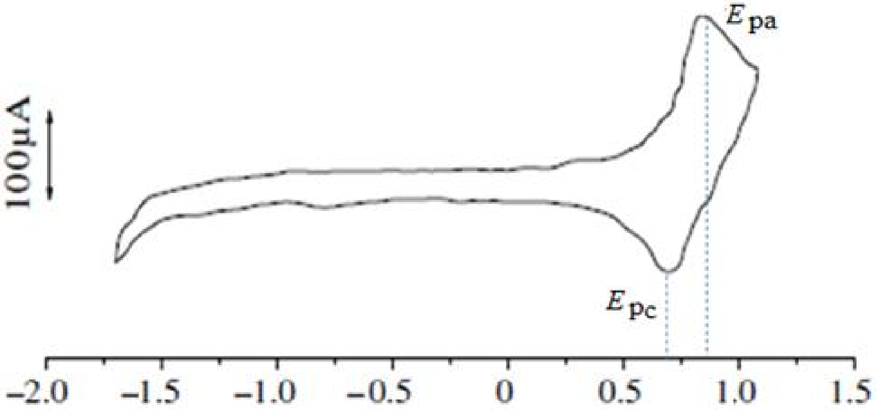

Figure 2.11: Cyclic voltammograms of a spin-coated $[(C_6H_{13}S)_8Pc]_2Dy$ film on an ITO electrode in a phosphate buffer. Scan rate, 0.1 V V/sec (redrawn from Basova et al., 2008)

A reversible CV is obtained where the redox states are stable in the total voltage sweep time scale. The ratio of current at cathodic peak potential (i_{pc}) and anodic peak potential (i_{pa}) gives a value of one in that case. The value of $i_{\mathrm{pc}}/i_{\mathrm{pa}} \neq 1$ indicates that other physical or chemical processes, like diffusion of material or formation of active redox species, are involved.

In general the redox processes in rare-earth bisphthalocyanines take place in the Pc ring. However, some of the transition metal monophthalocyanines such as Mn, Fe, and Co show metal-centered redox processes in the presence of suitable solvents and substituents (Koca et al., 2006). In this case, the electron donor solvents help in the metal-centered oxidation by thermodynamically stabilizing the oxidized species. Also, cerium derivatives show a metal-centered redox process in the lanthanide bisphthalocyanine series (Buchler and Ng, 2000).

The electrochemical study of LC zinc phthalocyanine with variable chain length from C_{10} to C_{14} was performed by Swarts et al., 2000. As the long chain assembly of the LC materials inhibits the charge migration inside the film, the rate of electron transfer between the electrode and phthalocyanines was progressively reduced with increasing chain length. This fact is revealed by the difference between first oxidation and reduction potential of the C_{14}-derivative being greater than it is for the C_{12} derivative.

2.9 Applications of phthalocyanines in technology

Photovoltaic (PV) cell: Phthalocyanines have been proved to be an effective material as charge transporters in organic PV cells. These photoconductors have been shown to produce more economical, large area, flexible devices compared with conventional silicon-based cells. The other advantages of phthalocyanines are their low-energy region absorption, high molar absorptivity, and good thermal stability. The performance of Pc-based devices has improved over the years by designing different types of PV cells such as dye-sensitized solar cells, inorganic/organic hybrid and multijunction cells. Recently, up to 5.9% of power conversion efficiency has been reported using a 2,6-diisopropylphenol-substituted zinc phthalocyanine derivative as a sensitizer in a TiO_2 dye-sensitized solar cell (Ragoussi, Ince, and Torres, 2013). The long range ultra-close alignment of carboxylic ester substituted zinc pthalocyanine of nimrods yields a quantum efficiency of 2.44% with potential application as a hole transport layer in solar cells (Lu et al., 2012). The discotic LC bis[octakis(alkylthio)phthalocyaninato] lutetium(III) with carrier mobility of 0.71 $cm^2\ V^{-1}\ s^{-1}$ has potential applications in solar batteries (Ohta et al., 2003).

Organic field effect transistor (OTFT): OTFTs are becoming an attractive alternative to inorganic FETs in some specific circuit applications such as active matrix flat panel displays, electronic paper, sensors, and switching devices (Li et al., 2008). The long-chain substituted phthalocyanines have been investigated as charge carriers in the development of light-weight, low cost, flexible OFET by many authors (Ozer et al., 2013; Trogler, Bohrer, and Kummel et al., 2012). One disadvantage of the phthalocyanine based OFET over traditional inorganic FET is the trapping of charge due to structural disorder causing lower mobility. Research has been going on to improve the parameter values like low threshold voltage and contact resistance or high on/off ratio, and mobility of these transistors. The columnar conductivity of the LC phthalocyanines has been proved to be effective in enhancing the transistor parameters. Chaure et al., 2010 gave an account of the effect of annealing on a copper phthalocyanine-based transistor. Formation of rod-like crystals at 100°C increases the on/off ratio and saturation mobility to the values 8.4×10^{7} and $0.70\ cm^{2}V^{-1}s^{-1}$ respectively compared to the as-deposited values of 1.2×10^{-6} and $0.08\ cm^{2}V^{-1}s^{-1}$.

Sensor: Taking advantage of the unique colour change behaviour of the phthalocyanines, a number of sensors have been developed for environmental monitoring, quality control and biosensing purposes. Nanowires of three lanthanoid bisphthalocyaninates have been used successfully in the food industry in the detection of caffeic, gallic, vanillic and ferulic acids in voltammetric methods (Martin et. al., 2012). Dependng on the number of phenolic groups attached to the structure (monophenol, diphenol or triphenol), the sensitivity of the electrochemical sesnsor varies. This has made possible the development of voltammetric and chronoamperometric sensors which are able to produce particular signals when immersed in different liquids.

Sharp changes in colour can also be achieved in the presence of redox gases such as SO_2, Cl_2, Br_2, NO_2 due to the formation of a charge transfer complex between oxidant and Pc molecule (Kilinc et al., 2012; Passard, Blanc and Maleysson, 1995; Clavijo et al., 1992). A series of mesogenic hexa-substituted phthalocyanines have been used for sensing benzene and chloroform vapour by Basova et al., 2005 exploiting π–π interaction between the assembled phthalocyanine ring with the organic compounds.

The detection of bovine serum albumin (BSA) using a LC hexylthio- substituted copper phthalocyanine derivative has been reported by Paul et al., 2009. In this case the hydrophobic surface of the liquid crystal CuPc derivative leads to imbolilization of BSA. Basova et al., 2008 employed a peripherally octathiohexyl-substituted dysprosium phthalocyanine derivative for detection of the biological cofactor, nicotinamide adenine dinucleotide hydrogen (NADH). One of the aims of the current project is to use electrochromic phthalocyanines as biosensing membranes for NADH and vitamin C (ascorbic acid), based on the method developed by Basova et al., 2008.

NADH acts as an electron exchanger in mitochondrial respiration. The NAD^+/NADH ratio for the normal metabolic state of a human body should be in the range of 1 to 0.1 (Lin and Guarente et al., 2003). Deviation from the ratio indicates disruption of the normal metabolic process in the cell, and oxyradicals produced are detrimental to brain proteins, thus causing age-related diseases like Alzheimer's and Parkinson's diseases, brain ischemia and Leigh syndrome. (Ghosh et al., 2012 ; Hattori et al. 2010 ; Hadzsiev et al. 2010). Vitamin C acts as a useful antioxidant and neurotransmitter, and contributes to the development of bone structure and the immune system of body. A deficiency of vitamin C may cause scurvy and bone homeostasis (Gabbay et al. 2010). Therefore, detection of these two biological cofactors has potential applications in medical diagnosis.

The use of magnetic chitosan microspheres/poly(thionic) modified glass electrode, polycatechol/ordered mesophorous carbon composite film modified electrode, biometric membrane which have detection limit in the μM range has been reported in the literature (Liu et al. 2010; Bai et al. 2010; and Lee et al. 2010). Detection in the range of 20 μM - 80 nM concentration of NADH has been achieved by a voltammetric process using a modified carbon nanotube electrode (Salimi, Lasghariand Noor-bakhash, 2010). In addition to these, development of electrochemical sensors employing a host of carbon based nanomaterials including graphene has been reported by a number of authors (Radoi and Compagnone, 2009; Shao et al., 2010; Kuila et al., 2011). Like NADH, vitamin C determination has been carried out by electrochemical procedures using modified graphene electrodes. The minimum detection level is reported as 0.12 mM (Keeley et al., 2010).

Liquid crystal display (LCD): The liquid crystal property of the long-chain phthalocyanines enables them to have potential applications in digital watches, TV, calculators and many other display devices. Formerly, cathode ray tubes with fluorescent screens were mainly in use as display devices. Recently, research has been going on the fabrication of LCDs with miniaturisation, better display properties, more durability, and cost effectiveness by the solution-processible phthalocyanine chromophores. Halogenated CuPc derivatives and phenoxy-substituted metal-free phthalocyanines have been reported to be used as the active matrix in LCD filters by Lee et al., 2012 and Wöhrle et al., 2012, respectively.

Nonlinear optics (NLO): Frequency modulation is an important function of the LC phthalocyanines. They have the property that the frequency of an incident light beam is converted to a double or triple harmonic state after passing through the polarising material. Long-chain LC phthalocyanines with extensive self-assembly by intermolecular π-π interactions, polarizable d-orbital electrons and the metal–ligand charge transfer mechanism exhibit second and third order nonlinear activity by induced scattering of light or photo refraction. The non-linear optics of phthalocyanines have been mainly employed in optical limiting devices like eye protection against intense light, signal processors, and optical switches (Nalwa and Miyata, 1997; Huang et al., 2008; Manjunathaa, Umesha and Bhat, 2013).

Photodynamic therapy (PDT): The principle of this photodynamic method is to generate reactive singlet oxygen species (ROS) by the photosensitizer which destroy the tumour cells. The energy required to produce ROS is nearly 22 kcalmol^{-1} (1274 nm) which match with the NIR absorption of phthalocyanines. The amphiphilic zinc metallated derivatives have potential use as photosensitisers in cancer therapy (Cook et al., 2002).

Chapter 3 Hybrid Nanocomposite and Phthalocyanine

Recently, it has been an encouraging idea of doping phthalocyanines extrinsically with fullerene, inorganic nanoparticles like lead sulphide (PbS), cadmium sulphide (CdS) and cadmium selenide (CdSe) to develop advanced phthalocyanine-based devices with faster response times, larger capacities in memory storage or better clarity in display. To meet these targets, nanocomposites are one of the most emerging and interesting topics of research.

The nanomaterials were discovered in 1960 by Feynman who predicted that manipulating the size of a material causes modifications of its physical and chemical properties relative to its bulk properties. Therefore, the blending of nanoparticles with phthalocyanines develops interesting properties in the composite with advanced electronic applications. Among the inorganic/organic hybrid nanocomposites, silica gel (SiO_2)/lead phthalocyanine,titanium dioxide (TiO_2)/copper phthalocyanine, and zinc oxide (ZnO)/nickel phthalocyanine nanocomposite hybrid materials have found potential applications in the fields of medicine, energy storage and optics (Guo et al., 2006; Mekprasart, Jarernboon and Pecharapa, W., 2010; Saglam, 2013).

For appropriate device applications, it is important to understand the origin of the novel characteristics of quantum dots compared to the bulk material. In this chapter, a brief review of quantum confinement effects in PbS nanoparticles, the advantage of solid state synthesis over other traditional methods, and the development of PbS nanocomposites and their various properties have been presented.

3.1 Lead sulfide nanoparticles and quantum confinement

In Figure 3.1 the energy levels of the PbS bulk material are very close to each other and are considered as a continuous band. The energy gap between the conduction and valence band is also very small. The band gap has been reported to be 0.41 eV at room temperature with an exciton Bohr radius of 18 nm (Machol et al., 1993; Patel et al., 2004). As the particle size is reduced the gap between adjacentenergy levels is increased, which confines the particle transitions. In this stage, the levels with low energy and with higher probability of electron density are called bonding orbitals and the higher energy levels with low electron density are called antibonding orbitals. The band gap between the bonding and antibonding orbitals also becomes wider, causing a quantum confinement effect and the particles are called quantum dots. For PbS nanoparticles the effect of confinement starts when the Bohr exciton radius is less than 10 nm (Liu et al., 2008).

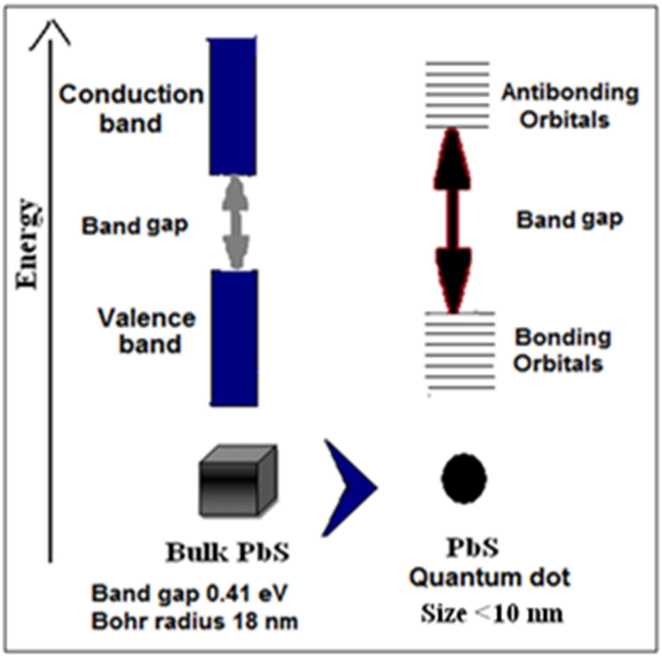

Figure 3.1: Quantum confinement in lead sulfide nanoparticles

3.2 Synthesis of PbS quantum dots and hybrid nanocomposites

Synthesis of PbS quantum dots (QDs) is comparatively easier than that of other semiconductors like ZnO, PbSe, CdSe and CdS. This is because of the large exciton Bohr radius (18 nm) of PbS. The QDs have been reported to show size dependent property when the radius is smaller than the exciton Bohr radius (a*). The relation between exciton Bohr radius and dielectric constant (ε_r) of a material can be expressed as follows (Tripathi and Mitra, 2014):

$$a^* = \frac{\varepsilon_r h^2}{\pi m^* q^2} \tag{3.1}$$

where, m* is the reduced mass of nanoparticle , h is the Planck's constant, q is the elementary charge. In CdS, for example, the exciton Bohr radius can be calculated as 5.4

nm from Equation 3.1 considering the value of m* is 0.16 atomic mass unit and dielectric constant 5.7 for bulk CdS (Arellano et al., 2010). In this case, the quantum confinement effect starts when the particle size is less than 2 nm. The larger excitonic Bohr radius of 18 nm in PbS bulk lead to the start of quantum confinement effect at 10 nm. The easier synthesis of comparatively larger QDs of PbS is one of the reasons for PbS being the dominant material in the field of nanotechnology.

In addition to this, PbS has a larger band gap than those of the other lead-containing chalcogenides PbSe, PbTe. The tuneable property of the PbS quantum dots makes it suitable for use in a broad range of applications, from thermal photovoltaics and telecommunication, to solar cells and biological imaging (Kane and Evans, 1996; Sargent, 2005; Sun et al., 2007; Choudhury, Song and So, 2010).

There are several methods described in the literature for the synthesis of nanocomposites. The common problem inherent with the solution-phase synthesis is the aggregation of the nano-sized particles due to their high surface energy (Godovsky, 2001). The aggregation makes the surface imperfect and also traps the electrons resulting in a decrease of mobility. The problems have been tried to be solved by coating the nanocrystals with surfactants. The surfactants prevent the nanoparticles from adhesion by making a physical barrier outside the particles (Wanga et al., 2001). However, the disadvantage of coating is that the surfactant acts as an insulating layer and affects the charge transport.

The chemical solid-state technique is a well-known synthetic route for nanocomposite preparation. The preparation of a PAM-PbS nanocomposite with simultaneous polymerisation of acrylamide has been reported by Nair et al., 2005. Warner and Watt, 2006, synthesised a nanocomposite PbS on conductive polymer poly-(3-hexylthiophene-2,5-diyl) (P3HT) with a potential application in optoelectronic devices. There are reports of phthalocyanine-based nanocomposites in solution phase, for example multiwall carbon nanotube (MWCNT)-copper phthalocyanine by Pu et al., 2013; iron phthalocyanine/graphene micro/nanocomposites have been reported by Cui et al., 2013. Recently, a graphene-based composite has been produced by Zhang et al., 2013, through a one-step solid state reaction between iron phthalocyanine (FePc) and silicon nanoparticle (SiNPs) precursors. In this case the aggregation was used to help in improving the performance of Lithium ion batteries.

Nabok et al. 2004 produced an inorganic/organic hybrid nanocomposite *in situ*. A non-planar hexyl-substituted lead phthalocyanine and H_2S gas were used as precursors to produce lead sulfide quantum dots on a metal-free phthalocyanine matrix in a one-step and cost-effective method. Also, the aggregation of the quantum dots was avoided to a considerable extent by this solid state synthesis. The band gap and size were estimated as 1.91 eV and 2.24 nm respectively. Following similar steps, structurally distorted octa-(benzo-15-crown-5)-substituted phthalocyaninato Cd(II) was exploited to form a CdS quantum dots based hybrid /metal-free phthalocyanine by Basova et al., 2010.

3.3 Developments of phthalocyanine nanocomposites in organic electronics

Now, it is important to know the types of possible interaction between the molecular conjugates to improve device performance. As reported, the interaction can be various types like surface passivation of the matrix by the quantum dots or electrostatic interaction, hydrogen bonding, and Van der Waal interaction. Photophysical influence of CdSe quantum dots inside a substituted silicon phthalocyanine matrix has been investigated by Dayal et al. 2006. Steady-state and femtosecond time-resolved photoluminescence showed electron transfer between the two components. Cadmium telluride (CdTe) quantum dots capped with thioglycolic acid (TGA) on positively charged zinc phthalocyanines cause quenching of luminescence intensity of the compound in a solvent mixture of water and pyridine. This phenomenon was interpreted as fluorescence resonance energy transfer between the electropositive zinc phthalocyanine and CdTe by Moeno et al. 2009.

In the case of organic photovoltaic (PV) cells the nanocomposites act as charge carriers by different intra- and intermolecular interactions. For instance, a PbS/MEH-PPV based device showed an improvement in quantum efficiency of three orders of magnitude with respect to a MEH-PPV solar cell (Mcdonald et al., 2005).

The first phthalocyanine-based organic solar cells were designed in 1983 with very small power conversion efficiency (η) even less than 0.01% (Chamberlain, 1983). This is because the photogenerated electrons and holes in the low mobility phthalocyanines cannot travel very far before recombination and consequently power conversion efficiency drops, but in a PV cell with nanoscale heterojunctions, every photogenerated charge carrier needs to travel less distance and the problem of recombination can be greatly reduced. Figure 3.3 illustrates a hybrid inorganic/organic nanocomposite PV cell. The efficiency of the cell is improved due to the consecutive four processes as follows:

1. Photogeneration of excitons by nanoparticles
2. Exciton diffusion
3. Dissociation of exciton into hole and electron
4. Transfer of charges into appropriate electrodes

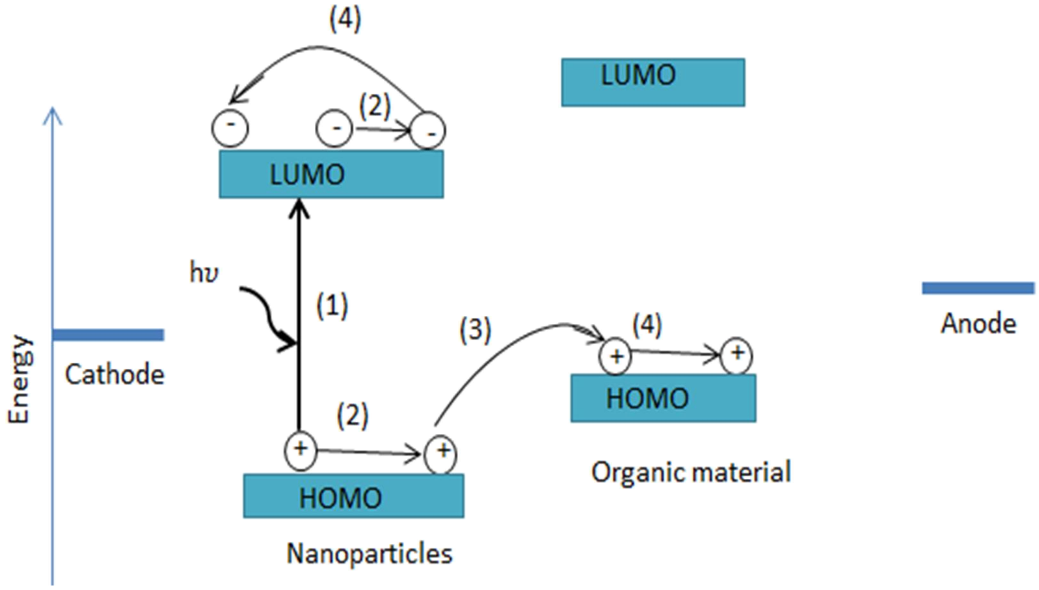

Figure 3.2: **Working principle of hybrid nanocomposite photovoltaic cell (Khozaee, 2012)**

An electrostatic interaction between photosensitive phthalocyanine and conjugated quantum dots coupled assemblies leads to the charge transfer between the components being much faster than the recombination rate, with potential application in photovoltaic cells (Sykora et al. 2006).

PbS quantum dots of modified band gap have already been proved to be a good light absorbing material according to Shockley-Queisser limit of the maximum efficiency of solar cell (Mcdonald et al., 2005). Therefore, PbS nanoparticles combined with photoconductive phthalocyanine is a promising candidate for the fabrication of hybrid solar cells. Recently, Guchhait et al., 2013 have presented a near infrared sensitive heterojunction solar cell based on lead sulfide (PbS) quantum dots and a metallated phthalocyanine derivative.

The electron mobility through the quantum dots is dependent on the distribution of the nanoparticles in the matrix. Charge Carrier Transport in Poly (N-vinylcarbazole) with

CdS Quantum Dot has been investigated by Roy Choudhury et al., 2004. With increasing concentration of CdS nanoparticles the mobility of nanocomposite was found to be increased, and it is enhanced up to 6 times at a concentration of 1.7% of volume fraction of CdS. Figure 3.3 shows a conductive pathway of the charge carriers through the nanoparticles of average diameter D and the average path length L_t. Increasing the number of charge particles in the conductive pathway helps to increase transport mobility. When the intermolecular distance is the same as the diameter of the particles it reaches the percolation limit, the best situation for charge transportation. But even below the percolation limit improvement in the conductance takes place to some extent.

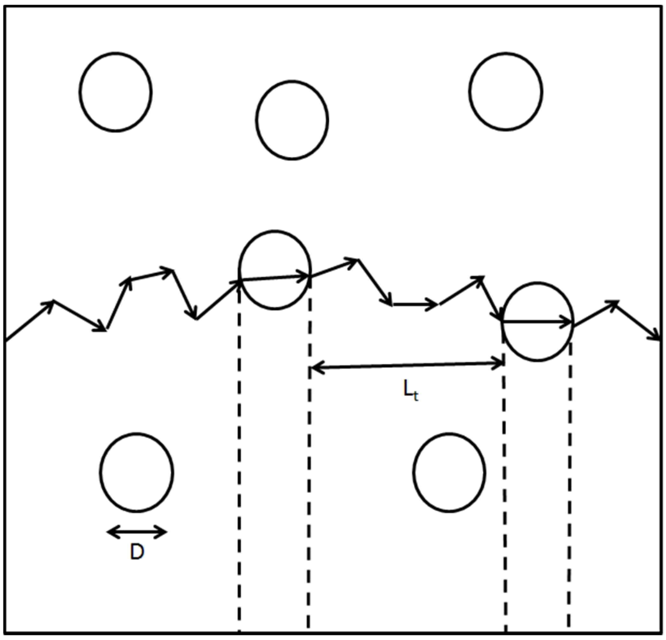

Figure 3.3: Scheme of conductive pathway through the nanocomposite (Roy Choudhury et al., 2004)

Isolated quantum dots are often useful in trapping and storing injected charge. The trapping and consecutive detrapping result in a hysteresis of current, which is an ideal condition for the fabrication of memory storage devices.

Phthalocyanines have already been proved to be promising candidates for these devices. As semiconductor films these molecules have a region with a high concentration of dopants with a high current or “on” state, and the remainder has a low (essentially zero) dopant concentration and lower current or “off” state. Also, the capacity of the devices can be tailored by a selective change of the molecular structure or doping.

An investigation with a lead phthalocyanine-based device showed the reproducible on/off ratio as much as 10^3 (Mukherjee et al., 2008). This result is considerably higher than zinc oxide-based memristors (Choi et al., 2012). Existence of a depletion barrier at the electrode/Pc interfaces and trapping-detrapping of the Pc film were found to be responsible for the advanced performance of phthalocyanine-based memristors.

The switching and retention time factors control the rate of internal state variable changes, which is especially important for non-volatile memory applications involving fast writing and reading time scales and also in those cases where long-term data retention capability is required.

Equation (3.2), developed by Strukov et al., 2008, shows the relationship between the charge flux ($M(t)$) and the width of the doped region ($W(t)$) in memristors as follows:

$$M(t) = \frac{W(t)}{D_0} R_{\mathrm{on}} + \left(1 - \frac{W(t)}{D_0}\right) R_{\mathrm{off}} \qquad (3.2)$$

Where D_0 is the overall thickness, R_{on} is the resistance when the active region is completely doped ($W = D_0$) and R_{off} is the resistance of the region which is mostly undoped ($W \rightarrow 0$). Considering $R_{\mathrm{on}} << R_{\mathrm{off}}$, the decreasing value of size increases the on/off ratio. This explains the importance of nanomaterials in memristors. A gold Nanoparticle/ 1,8-octanedithiol Organic hybrid memresistive device has been produced by Alibart et al., 2012, for neuroinspired biological information coding circuits. To date there is no report of nanocomposite phthalocyanine-based memristors.

Chapter 4 Basic Solid State Principles

The characteristic optical and electrical processes in the phthalocyanines are due to the electronic transitions between the molecular orbitals in the presence of electromagnetic radiation or an applied potential. Therefore, the energy gap between the two transition states is a crucial factor in determining the physical and chemical behaviour. The molecular orbital (MO) theory has often been used to explain the origin of the band gap in these compounds. In semiconductors the charge transportation is dependent upon the electrodes and the properties of the bulk materials. In the amorphous phase localized states appears near the band edge due to weak overlap between the wavefunctions. Different mechanisms have been found to be responsible for the charge conduction at different temperatures. This chapter is focussed on the theoretical models used in the analysis of the phthalocyanine materials in Chapters 6, 7, and 8.

4.1 Phthalocyanine band gap - A molecular orbital approach

Molecular orbitals (MOs) are formed due to the interaction between the atomic orbitals of reacting molecules or atoms. The origin of the formation of the highest occupied molecular orbital (HOMO) and the lowest unoccupied molecular orbital (LUMO) can be explained using a simple model of ethylene ($H_2C=CH_2$). Figure 4.1a shows the ethylene molecule with four hydrogen atoms bound to a pair of sp^2 hybridised carbon atoms. When the molecular orbitals of the two isolated carbon atoms are brought close together, they eventually overlap giving rise to bonding and antibonding π orbitals (Figure 4.1b). The interaction between the orbitals of two ethylene molecules in the same phase which is either fully bonding or fully antibonding forms the HOMO. In the LUMO, some of the bonding interactions are compensated by the antibonding orbitals and form higher energy orbitals than HOMO (Brédas et al., 2002). The band gap between the HOMO and LUMO is considered as a band of forbidden energy. The Fermi energy level (E_F) lies in this gap (Mott and Davis, 1971).

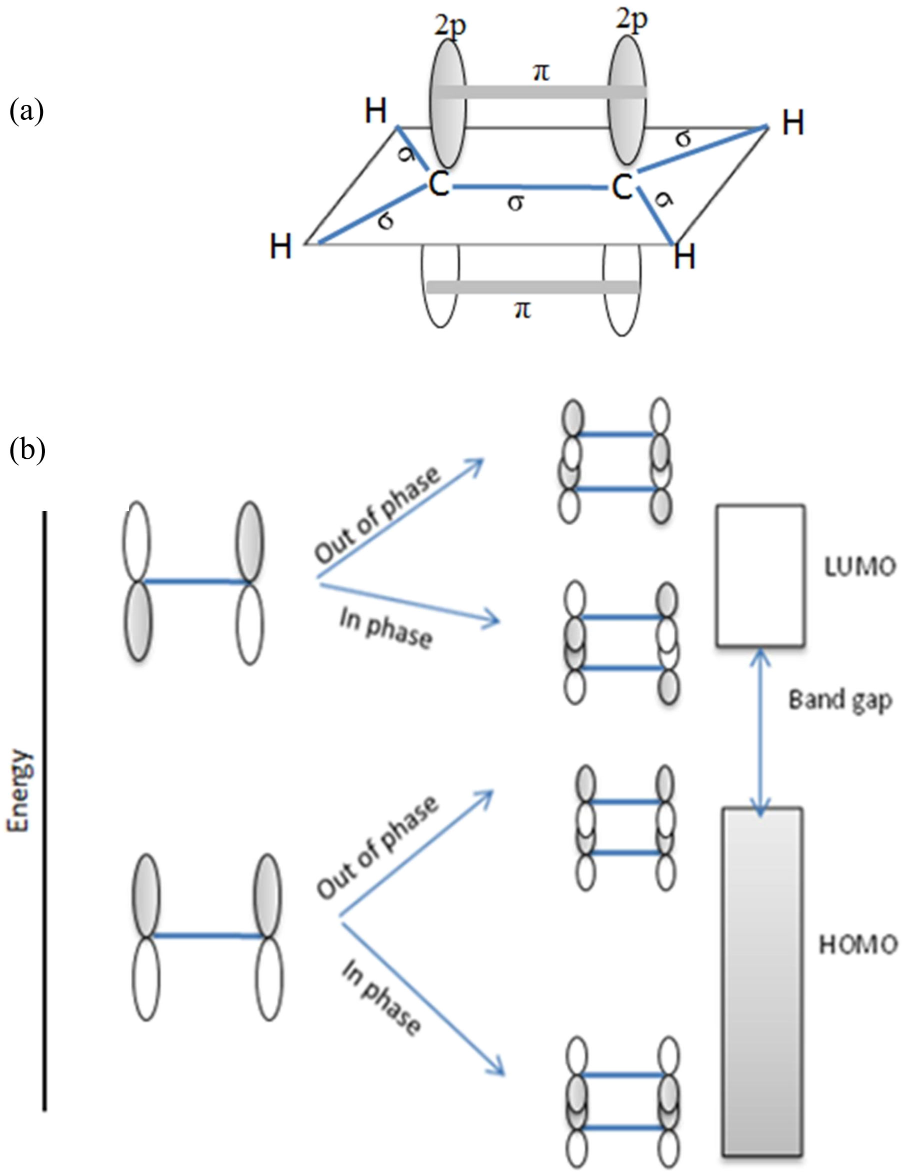

Figure 4.1: (a) Bonding scheme of ethylene (b) the formation of HOMO and LUMO in ethylene dimer due to π-π interaction. The different shades show wave function phases (Brédas et al., 2002)

The densities of states in the HOMO and LUMO bands increase when the electrons are delocalized over a large length scale. In these cases, the extended conjugation causes stronger splitting between the MOs. A series of theoretical studies of the lanthanide bisphthalocyanines ($LnPc_2$) MOs have been reported (Orti, Brédas and Clarisse, 1990; Ishikawa et al., 1992). Rousseau, Aroca, Rodriguez-Mendez, 1995 employed extended Hückel molecular orbital model to establish the formation MOs of a lanthanide bisphthalocyanines from two Pc rings (Figure 4.2). The interaction between the a_{1u} orbitals of two Pc ligands creates a HOMO consisting of an antibonding a_2 orbital with an unpaired electron and a filled bonding b_1 orbital. The doubly-degenerate e_g orbitals form the e_1 and e_3 orbitals of the LUMO. The dots in the Figure represent the electrons. According to the Pauli exclusion principle each orbital may contain a maximum of two electrons. A semi-empirical quantum chemical study by Ishikawa, Ohno, and Kobayashi, 1992, showed that the HOMO-LUMO are associated π-π^* interactions depending upon the inter-ring distance. In the case of phthalocyanines, the HOMO-LUMO energy gap is relatively small (~1 to 3 eV) and the molecules can be doped to adopt n- or p-type character. Thus, these conjugated molecules can act as semiconducting channels in organic devices.

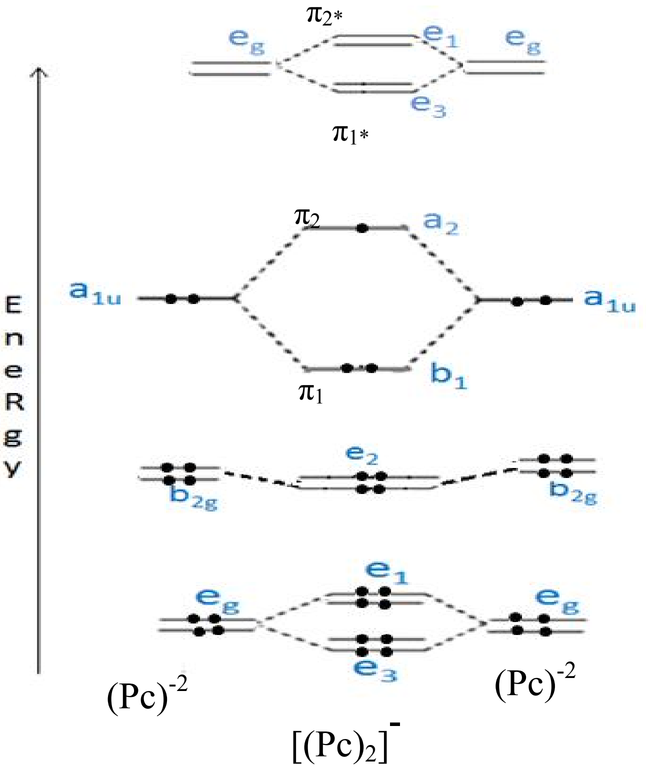

Figure 4.2: **Schematic representation of energy levels of lanthanide bisphthalocyanines by the interaction of two Pc rings (Redrawn from Rousseau, Aroca, Rodriguez-Mendez, 1995)**

4.2 Charge transport through metal-semiconductor contact

There are mainly two types of phthalocyanines depending upon the nature of charge particles taking part in carrying the current. In the p-type semiconductors holes are the major charge carrying particles whereas in n-type semiconductors, the electrons take the leading role. Most of the phthalocyanine molecules have been observed as p-type (Jafari, Azim-Araghi and Gholami, 2012). Some phthalocyanines with electron withdrawing moiety like CN or F exhibit n-type semiconductivity (Li et al., 2008). Now, on applying voltage on the electrode at first charge carriers are injected from the metal electrode. The magnitude of the energy to be applied depends upon the work function of the electrode and the semiconductor. The electrode-material contact is an important factor to determine the performance of the electric circuit. In this section, the two types of contacts for the p-type single-crystal semiconductor have been discussed.

Schottky Contact: In this case the Fermi level (E_{FM}) of the metal stays higher than the semiconductor Fermi level (E_{F}) before contact is made and the difference between the vacuum work function (Φ_{m}) of the metal in comparison to the vacuum work function of the semiconductor (Φ_{s}) is large (Figure 4.3a). To equalise the Fermi level with the metal, the semiconductor's Fermi level shift upward upon contact. Consequently, the valence and conduction bands of the p-type semiconductor also shift upward, resulting in band bending as illustrated in the Figure 4.3b. The band bending results to drifting of holes to the top of valence band. This causes a 'depletion region' at the junction which referes to the region devoid of holes. Therefore, an extra potential of $q(\Phi_s - \Phi_m)$ has to be applied for the current flow from metal to semiconductor. The charge transport in the Schottky contact is said to be electrode limited (Streetman, 1980). Phthalocyanines with the HOMO energy levels at around 5.2 eV form a Schottky contact with comparatively low work function metals like aluminium and lead with work functions 4.14 eV and 4.05 eV, respectively (Kwong et al., 2003; Saleh et al., 2003).

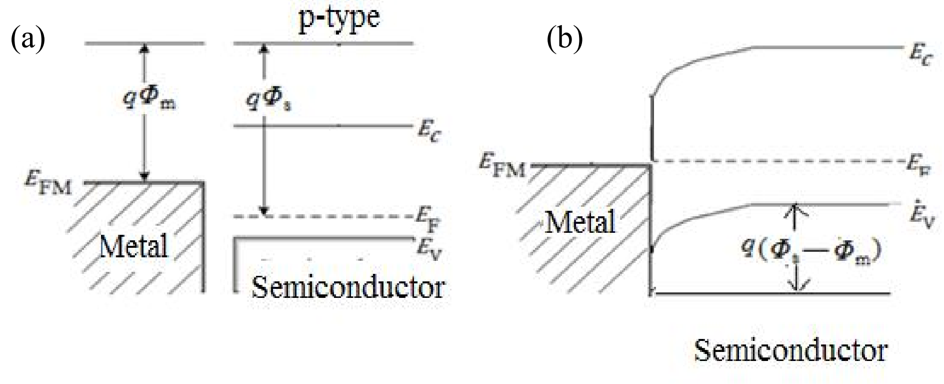

Before contact **After contact**

Figure 4.3: (a) a metal-vacuum contact and (b) The metal and p-type semiconductor contact for a Schottky contacts without any applied voltage (Streetman, 1980)

Ohmic Contact: In this case, the Φ_{m} stays at slightly lower energy level than that of the Φ_{s} ($\Phi_{\mathrm{m}} > \Phi_{\mathrm{s}}$). To align the Fermi levels, the valence and conduction bands of the semiconductors need to bend downwards to some extent. However, the small potential barrier at the metal-semiconductor contact is crossed in low or even zero applied potential with an easy hole flow across the junction. In this type of interface an Ohmic contact is said to be established between the semiconductor and electrode material (Figure 4.4b). A bulk-dominated linear relationship between current and voltage following Ohm's law has been found to occur in these cases (Streetman, 1980). Gold and indium tin oxide with high work functions of 5.1 eV and 4.7 eV respectively form an Ohmic contact with the phthalocyanines (Kwong et al., 2003, Kilinc et al., 2012).

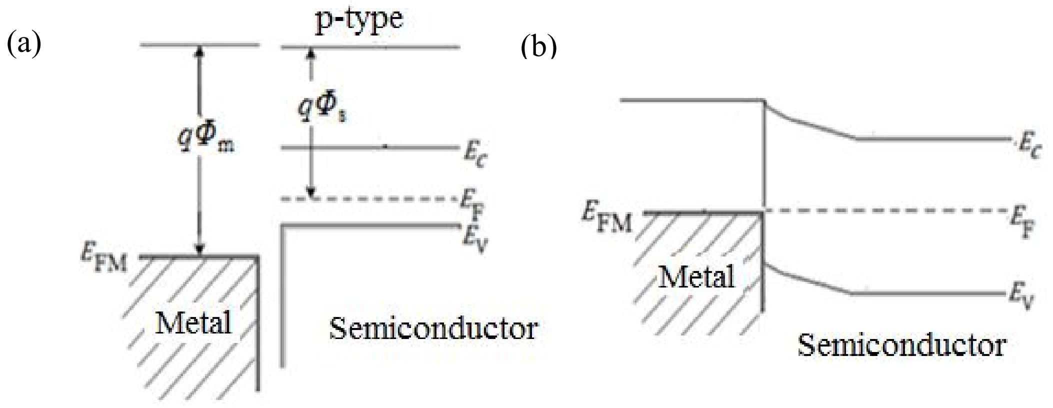

Before contact **After contact**

Figure 4.4: (a) a metal-vacuum contact and (b) The metal and p-type semiconductor contact for an Ohmic contact without any applied voltage (Streetman, 1980)

In the present research work, an interdigitated gold planar electrode has been used for the investigation of the dc conductivity of the phthalocyanine films. Therefore, the conduction mechanism was Ohmic type. In practical cases, the films are in amorphous or polycrystalline state rather than ideal single crystal. The following topic is regarding the charge transport in between metal and p-type phthalocyanine Ohmic conduct in the films.

4.3 Conduction mechanism in amorphous and polycrystalline films

The charge transport of a semiconductor is governed by the concentration of charge carriers injected from the metal contact and the mobility of the carrier through the band gap. The conductivity σ can be expressed from the electron sea model developed by Drude and Lorentz in 1905 as following Equation 4.1 (Hussein, 1990).

$$\sigma = n_0 q \mu \qquad (4.1)$$

where, n_0 is the free carrier density, μ is the charge carrier mobility and q is the unit charge.

A crystalline solid has a conduction and valence band with well-defined Fermi level, E_F (Figure 4.5a). On the other hand in semiconductors a range of weakly localized states exist below the conduction and above the valence bands due to the weak wave function overlap between two adjacent molecules (Figure 4.5b). In this case, the density of states displays an exponential tail in the forbidden band gap. While fabricating the amorphous thin film, a number of traps are generated in this band tail area due to the presence of impurities or defects in the film. There is always a tendency for the charge carriers to be immobilized in the forbidden zone, reducing the mobility of the carriers.

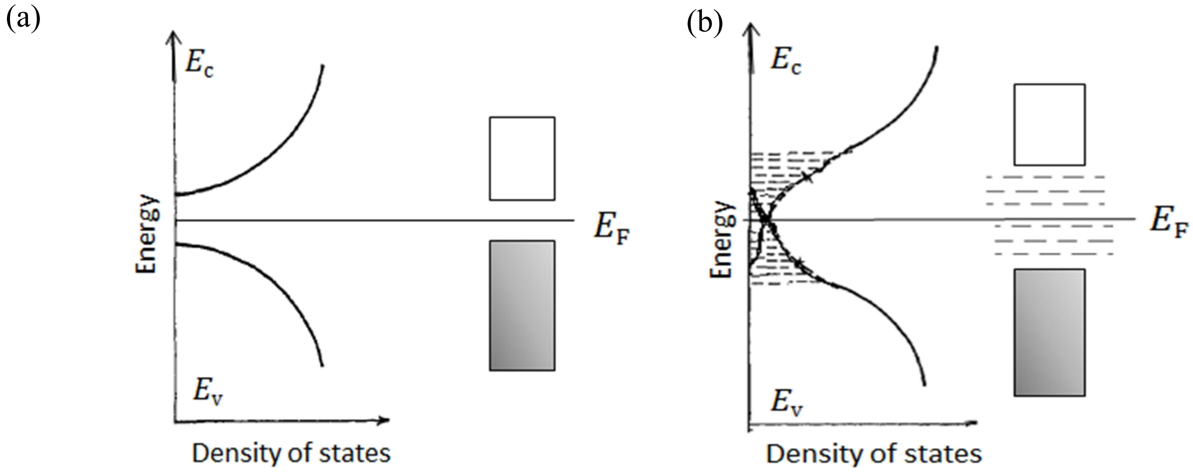

Figure 4.5: Density of states for (a) crystalline solid (b) amorphous solid (redrawn from Simmons, 1971).

Ohmic conduction: In an Ohmic contact between metal and p-type phthalocyanine, at low voltage the number of thermally generated carriers is enough for them to free the trapped charge carriers injected by the metal. Therefore, trap-free Ohmic conductivity can be observed.

Under these conditions, the conductivity, σ, with resistance R can be described as the relationship between the current (I), and the applied voltage, V_a by Ohm's law,

$$\sigma = \frac{L}{RA} = \frac{I\,L}{V_\mathrm{a}A} \qquad (4.2)$$

At high voltage a non-linear behaviour of current voltage (I-(V_a)) characteristics is found which might be due to Space charge limited conduction (SCLC) or Poole-Frenkel (PF) conduction.

Space charge limited conduction (SCLC): At high voltage holes are generated by the electrodes. They start to accumulate at the metal-semiconductor interface and eventually their numbers overcome the thermally generated carriers. This form of space charge applies a potential in the opposite direction to that of the injected charge, thereby limiting the current passing through the bulk. This is the origin of space charge limited conductivity (SCLC) which is characterized by a power law dependence in the form $I \propto V_\mathrm{a}^\mathrm{n}$ where the index n has values ≥2.The Figure 4.6 illustrates the metal-semiconductor contact in presence of localized traps, at levels E_tp1 and E_tp2., for holes as charge carrier.

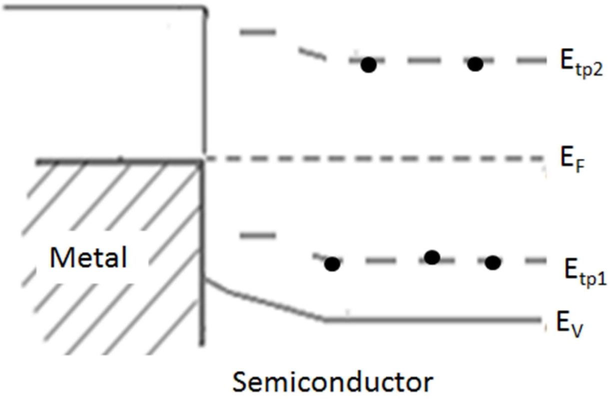

Figure 4.6: The metal-semiconductor contact for the SCLC conductivity (adapted from Lampert 1965)

Poole-Frenkel (PF) conduction: Sometimes the trapped charge in the SCLC regime is released by the application of potential. This may happen by lowering of the Coulombic potential barrier (Φ_t) between carriers at impurity levels and the edge of the valence bands on the application of high electric fields. As the electric field increases, the potential barrier decreases, making it easier for the holes to vacate the trap by thermal emission. Figure 4.7 presents, under the applied electric field, the amount of ionization energy of trapping center decreases in the direction of applied electric field by $\beta_{PF}\mathbf{E}^{1/2}$where β_{PF} is the Poole-Frenkel coefficient. Braun, 2003 gives the relationship between current and potential as

$$I = A\mathbf{E}\exp[\frac{\beta_{PF}\boldsymbol{E}^{1/2} - \Phi_t}{k_B T}] \qquad (4.3)$$

Where k_B is the Boltzmann constant, T is the temperature.

The parameter β_{PF} is the related to the dielectric constant (ε_r) of the medium according to the following equation (Gould and Safai, 2000)

$$\beta_{PF} = \sqrt{\frac{q^3}{\pi\varepsilon_0\varepsilon_r}} \qquad (4.4)$$

where, q is the unit charge, ε_0 is the permittivity of vacuum. The theoretical value of β_{PF} can be estimated as 3.84×10^{-5} eV $m^{1/2}$ $V^{-1/2}$ from the Equation 4.4 using the value of $\varepsilon_0\varepsilon_r=3.54\times10^{-11}$ Fm^{-1} for lead phthalocyanine (Gould and Safai, 2000).

The electric field (**E**) is defined as the applied voltage per unit distance over which the V_a is applied (V_a/L). Therefore, the Equation 4.3 can be also be written as

$$I = \frac{AV_a}{L}\exp\left[\frac{B_{PF}V_a^{\frac{1}{2}} - \Phi_t}{k_B T}\right] \qquad (4.5)$$

where, B_{PF} is equal to $\frac{\beta_{PF}}{\sqrt{L}}$.

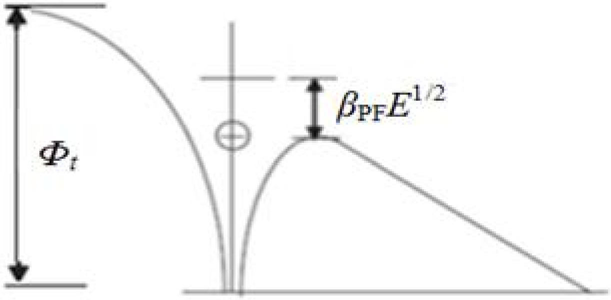

Figure 4.7: Coulombic potential distribution in semiconductor in presence of applied electric field showing the Poole-Frenkel effect for a single trap (redrawn from Gupta, Singh, Akhtar, 2012)

4.4 Temperature dependence of conduction

The study of [I-(V_a)] characteristics as a function of temperature gives an idea about the localized states which control the electronic transitions. Hurd, in 1985 proposed the 'particle in a box' model to explain the localised state hopping. In this case a vibrating wall of potential V, width S_0 was assumed as the width of potential barrier between two localised states (Figure 4.8). Also, an oscillating particle of mass m was considered to be trapped in the well.

The hopping conductivity, σ during thermally assisted coincidence of the states with activation energy U can be written in the following expression (4.4) derived by Hurd, (1985).

$$\sigma = c\ T^{-1}\exp\left(-2\alpha_0 S_0\right)\exp\left(-\frac{U}{k_B T}\right)\exp\left(\frac{2{\alpha_0}^2 k_B T}{m\omega^2}\right) \qquad (4.6)$$

Where U is the activation energy for the site displacement, α_0 is the inverse of the site localization parameter or penetration of the wavefunction in the site localization parameter, ω is the frequency of the barrier oscillation, k_B is the Boltzmann constant.

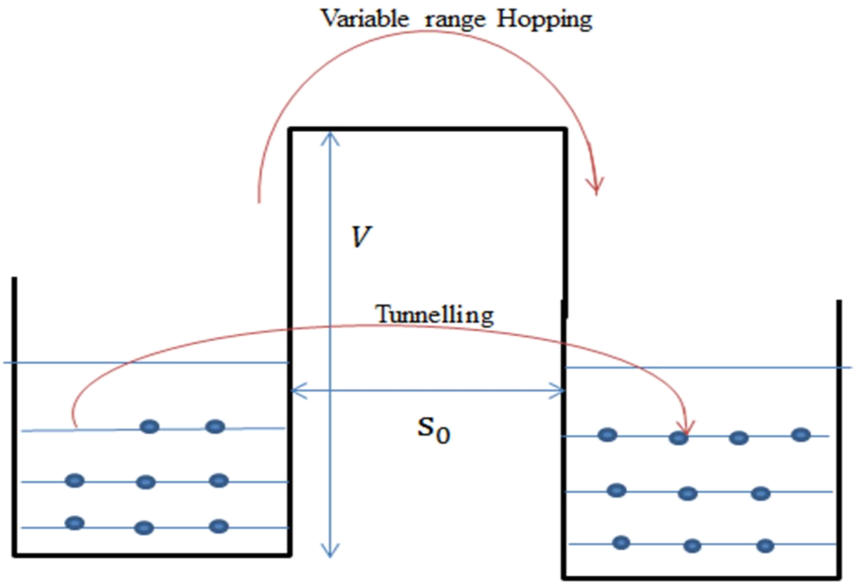

Figure 4.8: Vibrating barrier model by Hurd, 1985 for charge transport in the localized state

Tunneling: At very low temperatures the activation energy to cross the barrier is comparatively higher than the thermal energy at that temperature ($U>>k_BT$). The particle shows some temperature independent conduction in the same localised energy state through the wall, which is called tunnelling. Therefore, the σ is dependent on the extent of overlap between the wavefunctions and the tunnelling term, $(\frac{2\alpha_0{}^2 k_B T}{m\omega^2})$. In a real case the lattice parameters of the crystal control the tunnelling term and follow the equation log (σT) = constant $\times T$ at constant temperature derived from the above Equation 4.4.

Variable range hopping (VRH): As the temperature increases the charge carriers acquire enough energy for hopping through the potential barrier (Figure 4.5). In this case $\alpha_0 S_0 >> 1$ and $U << k_B T$. Upon application of an electric field the charge carriers will hop from one localized state to another. However, the thermal activation energy is still much lower than the activation energy required for the transition for to the valence band level where conduction takes place. This hopping process may not be only fixed range or between the nearest neighbours, rather it can be variable range. The probability of hopping depends upon the spatial separation, S_o and energy separation between two states.

The variable range hopping model current (I_{VRH}) was found to be proportional to $T^{-1/4}$developed by Mott and Davis 1971 (Pope and Swenberg, 1999). Therefore,

$$I_{\mathrm{VRH}} = \frac{2AV_{\mathrm{a}}}{L}\sqrt{\frac{9N_0}{8\pi\alpha_0 k_B T}}\ \upsilon_{ph} e^{(\frac{T_0}{T})^{1/4}} \qquad (4.7)$$

where, $T_0 = \frac{16\alpha_0{}^3}{k_B N_0}$. The parameter is called the υ_{ph} Debye frequency and its value is equal to 10^{13} Hz. The term T_0 is the characteristic temperature, N_0 is the density of localized states at the Fermi level, A is the area of the electrodes, V_{a} is the applied voltage, L is the length of the electrodes. The optimum VRH hopping distance S_{H} can be calculated from the knowledge that

$$S_H = (\frac{3}{2\pi\alpha_0 k_B N_0 T})^{\frac{1}{4}} \qquad (4.8)$$

Band edge conduction: At higher temperatures, the conductivity mechanism is mainly determined by hopping of carriers from valence to conduction band as the charge carriers have sufficient energy to do so (Khan et al., 1995).

The conductivity (σ) in this case can be described by the Arrhenius relation

$$\sigma = \sigma_0' \exp(-\frac{\Delta E}{k_{\mathrm{B}} T}) \qquad (4.9)$$

Where ΔE is the activation energy for the conduction and σ'_0 is the pre-exponential factor. Essentially this process is a fixed range hopping process.

There is the possibility of different activation energies at high temperature conduction. El-Nahaas et al., 2006, mentioned the activation energy in the range 308K ≤ T ≤ 350K as 0.12 eV, and in the range 350K ≤T ≤ 423K as 0.76 eV for a thermally evaporated nickel phthalocyanine thin film. This is because the thermal activation energy at comparatively lower temperatures is associated with impurity conduction. The increase in the activation energy above 350K is attributed to a change from extrinsic to intrinsic conduction, which probably results from the removal of impurity states.

Chapter 5 Experimental Techniques

This chapter describes the various experimental methods employed. This includes cleaning of the substrates, thin film deposition of phthalocyanine derivatives and their post deposition heat treatment. The solid state synthesis of nanocomposite lead sulfide (PbS)/ metal free phthalocyanine has been demonstrated with the experimental set up. Structural, optical, and electrical studies of thin films were carried out by the spectroscopic, microscopic, thermogravimetric and electrical measurements. The working principle of instruments and sample preparation methods used for each of the analysis are also discussed.

5.1 Phthalocyanine materials

In this research work, five different novel solution processible phthalocyanines were used. The International Union of Pure and Applied Chemistry (IUPAC) names and symbols of the compounds are as follows:

1. Bis[1,4,8,11,15,18,22,25-octakis(octyl)phthalocyaninato]lutetium(III),C_8LuPc_2,
2. Bis[1,4,8,11,15,18,22,25-octakis(octyl)phthalocyaninato]gadolinium(III),C_8GdPc_2,
3. Bis[1,4,8,11,15,18,22,25-octakis(hexyl)phthalocyaninato]gadolinium(III),C_6GdPc_2,
4. 1, 4, 8, 11, 15, 18, 22, 25-octaoctyl phthalocyaninato lead (II) (C_8PbPc),
5. 1, 4, 8, 11, 15, 18, 22, 25-octaoctyl metal free phthalocyanine (C_8H_2Pc).

The 99.9% pure phthalocyanines in powder form were supplied from the University of East Anglia. All The compounds were reported to have liquid crystalline (LC) properties in the temperature range -50° to 250°C. The differential scanning calorimetric (DSC) plots are presented from Figure A1.1 to A1.5 in Appendix 1. The compounds were stored in the dark to eliminate the aerial artefacts.

Studies of optical absorption, self-assembly, electrical properties in the as-deposited and a LC mesophase were carried out withcompounds 1, 2, and 3. Compound 4 was used for the synthesis of the nanocomposite containing lead sulfide (PbS) quantum dots and octyl substituted metal free phthalocyanine (C_8H_2Pc). The pristine metal free phthalocyanine (compound 5) was used for comparison with the nanocomposite component.

5.2 Preparation of thin films

Spin-coating was used for the fabrication of thin films of the solution processible phthalocyanines. The advantages of spin-coating over the other techniques such as vacuum deposition, jet-spray coating, Langmuir-Blodgett (LB) method have been discussed in the Section 2.7, Chapter 2.

Prior to the preparation of the film, the glass surface was cleaned in the ultrasonic bath (Ultrawave U50, UK). The substrates were sonicated in distilled water of resistivity 18.2 MΩ, acetone, and isopropyl alcohol, in sequence for 15 minutes each.The cleaned substrates were then dried with nitrogen gas before film deposition.The cleaning is very crucial factor to produce a homogeneously coated impurity free surface. Any particulate or greasy substance the film affects the alignment and electrical properties. A KW-4A spin coater (as shown in Figure 5.1) from the Chemat Technology Inc., USA was used to produce thin films of the phthalocyanine compounds. About 50 µl of the 5 $mgml^{-1}$ spreading solution in chloroform (99.9% anhydrous) was dispersed on ultrasonically clean glass/quartz/ITO/interdigitated gold coated glass substrate according to requirement and left for 30 second. The spin coater was connected to a vacuum pump creating a pressure more than 2.1 CFM in the vacuum chuck. Using the stage 2 timer and speed controller of the spin coater, the dispersed solution was allowed to spin at 2000 rpm for 30 second. The coated sample dried for at least 4hours inside vacuum desiccator.

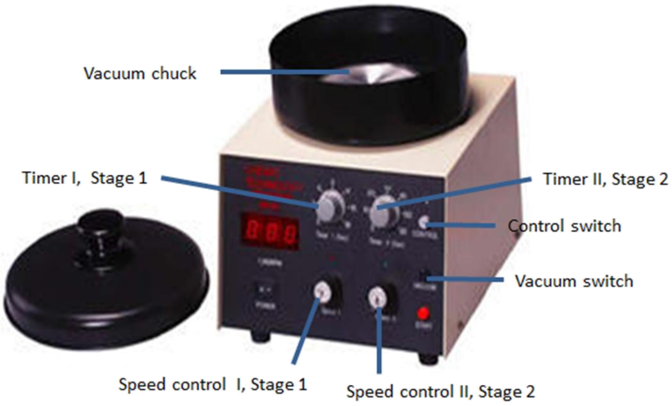

Figure 5.1: The Ultrawave U50 spin coater (Chemat Technology Inc., 2014)

The thickness was measured as 74 ± 15 nm, 60 ± 15 nm, and 80±15 nm for C_8GdPc_2, C_8LuPc_2, and C_6GdPc_2, respectively. A Zygo NewView 5000 interferometer with white laser was used for the thickness measurement. Measurements were repeated on five different areas of the film and an average value of the thickness was used for further analysis. C_8PbPc and C_8H_2Pc were spin coated on quartz/interdigitated gold coated glass substrates following the same method. In this case, toluene (99.8% anhydrous) was used to prepare the 5 $mgml^{-1}$ solution. The thickness was measured as 20 ±5 nm for both of C_8PbPc and C_8H_2Pc.

The solvents were chosen according to stability of the material and the quality of the film. Chloroform evaporates very fast which helps to form an evenly coated film and reduces sample drying time. Toluene solvent was used for the deposition of lead phthalocyanine as the stability of Pc molecule was found to be more in toluene than chloroform (Sosa-Vargas, personal communication, 5 February, 2012).

It was noticed that the C_8PbPc and C_8H_2Pc produce much thinner films than the bisphthalocyanines. The difference in thicknesses (*d*) may be attributed to the viscosity of the solvent (η_L) and the material (η_S) according to the power law proposed by Sahu, Parija and Panigrahi, 2009 (equation 5.1)

$$d = [\frac{3C(t)^3\eta_0\phi_S}{2\{1-C_0(t)\}\omega_S^2}]^{1/3} \qquad (5.1)$$

where, liquid evaporation rate ϕ_S, concentration of the solid at time *t* is $C(t)$, ω_s is the speed of rotation of the material, $\eta_0=\eta_L+\eta_S C^\gamma(t)$ and $\gamma = 2.5$.

Therefore, $$d \propto \eta_0{}^3 \qquad (5.2)$$

The viscosity of toluene and chloroform are 0.62 cP and 0.51 cP, respectively at 20°C (Dean, 1967).

The relationship between the viscosity of a material (η_s) with the molecular weight (*M*) is

$$\eta_S=K[M]^a \qquad (5.3)$$

The constants'a' and '*K*' are known as Mark–Houwink, parameters which depend on the particular material-solvent system(Hiemenz and Lodge, 1984).

If η_0 in Equation5.2 is replaced by η_s in Equation 5.3, it can be mentioned as

$$\eta_0=\eta_L + K[M]^a C(t)^\gamma \qquad (5.4)$$

The molecular weights of the C_8GdPc_2, C_8LuPc_2, and $C_6GdPc_2$are 2525.5 g/mol, 2542 g/mol and 2496 g/mol, respectively. The molecular weights of C_8PbPc and C_8H_2Pc are 1391 g/mol and 1186 g/mol, respectively. The equation 5.4 explains the lowerviscosity of the compounds C_8PbPc and C_8H_2Pc is due to their lower molecular weight.

To investigate the interaction mechanism between the C_8LuPc_2/C_8GdPc_2 spun films and NADH, a 100±15 nm film was prepared by spin coating 10 $mgml^{-1}$ solution on glass/indium tin oxide coated glass (ITO) at a rate of 1500 rpm for 30 seconds. A higher concentration of the solution was used to make the film thick enough so that the change of colours is visible to the naked eye.

5.3 Preparation of drop cast coating

To prepare samples for photoluminescence, Raman, thermogravimetric analysis, XRD and XPS, drop casting method was employed. 0.5 ml of the 5 $mgml^{-1}$ solution was dispersed on top of the cleaned silicon/glass substrate and then placed in the dark, low vacuum and moisture free dessicator for 24 hours to be fully dried. The substrates were cleaned thoroughly as described in the method in the previous Section 5.2 of this chapter. The thickness of the film was estimated to be ~3 μm.

5.4 Thermal annealing

To investigate the molecular organisations and its effect on charge transport properties, the as-deposited spun thin films of the bisphthalocyanines were heated to 80°C. The heat-treatment was done in an oven in presence of air. The phthalocyanine conductivities have been found to be improved after exposure in oxygen by Anthopoulos and Shafai, 2003 and El-Nahass, Atta and El-Zaidia, 2011. The samples were left at high temperature for 1 hour, followed by slow cooling to room temperature at 5°C min^{-1}. At the high temperature the molecular lattices recrystallize and some of the orientations were maintained at room temperature.

The required annealing temperature was chosen according to the phase transition exhibited by differential scanning calorimetric (DSC) data of the bisphthalocyanines. The DSC plots wereobtained from East Anglia University and are displayed in appendix 1. For C_8LuPc_2 crystal (K) to discotic mesophase (D) was noted as 61.5°C and C_8GdPc_2 showed the K-D transition at 64.2°C which were maintained till 120°-130°C (Figure A1.1 and A1.2 in Appendix 1). For C_6GdPc_2, transition was found peak at 66°C on heating which can be noticed in the DSC plot of Figure A1.3. Therefore, 80°C for the three bisphthalocyanines were considered between in the range to study the characteristics in discotic phase.

5.5 Oxidation of thin films for *in situ* biosensing

In order to investigate the interaction mechanism between the chemichromic lutetium and gadolinium phthalocyanine spun films and NADH, the as-deposited neutral films on glass were oxidized by exposure to saturated bromine (Br_2) vapour for 2 minute in a glass conical flusk (Figure 5.2a). As Br_2 is a toxic gas, the excess gas was passed through an aqueous solution of sodium thiosulfate ($Na_2S_2O_3$) (Figure 5.2b) to neutralise the gas. The reaction between $Na_2S_2O_3$ and Br_2 produces water soluble non-toxic sodium tetrathionate and sodium bromide. The set up was placed in the fume cupboard during the experiment.

$$2Na_2S_2O_3 + Br_2 \rightarrow Na_2S_4O_6 + 2NaBr \qquad (5.5)$$

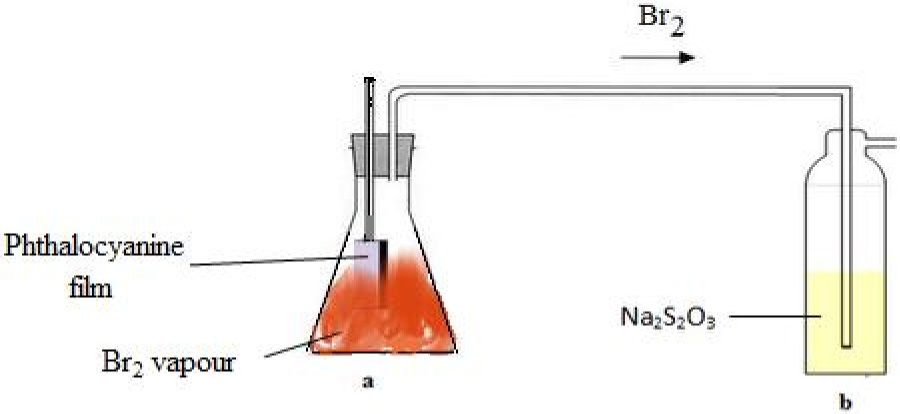

Figure 5.2: The set up for the Br_2 exposure of the thin films

The oxidized films were then reduced by NADH freshly dissolved in an aqueous solution of 1.5 M $LiClO_4$ in a 1 cm path length quartz cuvette. The kinetics of chemichromic modification of the spun films were monitored by recording spectral changes using a

UV–visible spectrophotometer described in Section 5.7 of this Chapter. Measurements were repeated at19°C for NADH and vitamin C at different concentrations.

For electrochemical oxidation, a GiIIAC potentiostat was used in a three-electrode configuration (Figure 5.3a). A high purity platinum wire as counter electrode, an Ag/AgCl/Cl$^-$ as reference electrode and the phthalocyanine coated on ITO glass acted as working electrode (Figure 5.3b). A 1.5 M aqueous solution of LiClO$_4$ (pH = 7.2) was used as the electrolyte. The Ag/AgCl/Cl- reference electrode was enclosed in a Luggin capillary, filled with the solvent and electrolyte mixture. The capillary tip was placed close to the platinum working electrode with a view of minimizing the undesirable electrical resistance.

The steady state cyclic voltammogram curves were recorded at room temperature in the aqueous medium of 1.5 M LiClO$_4$ by potentiodynamic sweep between 0 and 1.5 V at a rate of 100 mVs^{-1} with respect to the reference electrode. An ACM's software of version 5 was employed for the data analysis. An oxygen-free environment was maintained by the constant flow of pure N$_2$ gas during the voltammetric experiments.

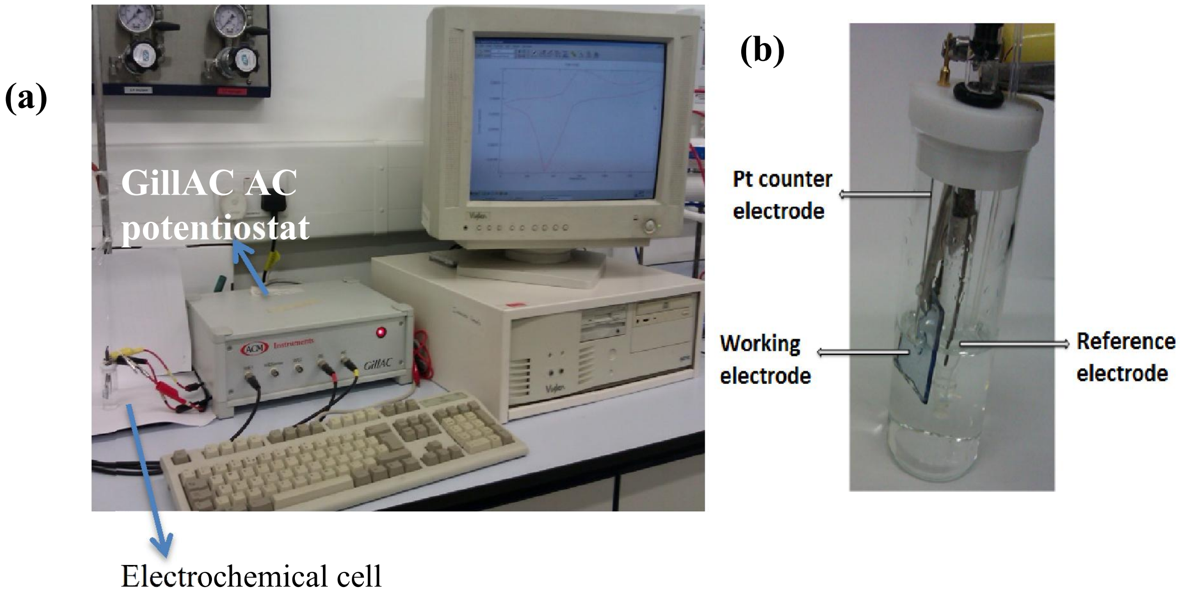

Figure 5.3: (a) Set up for the electrochemical experiment (b) the electrodes in the cell

5.6 Preparation of hybrid PbS/C_8H_2Pc nanocomposite film

In this research PbS/C_8H_2Pc nanocomposite material was produced in a single solid step technique. The first time *in situ* solid state monodispersed nanocomposite synthesis was carried out by Nabok et al., 2004. A thin film of octahexyl lead phthalocyanine was exposed to H_2S gas to form PbS QDs/ C_6H_2Pc nanocomposite. Our present study stems from their report. In this case a non-peripherally octaoctyl substituted LC lead phthalocyanine (C_8PbPc) was used following the study on the demetallation rate of lead phthalocyanines containing alkyl substituents of C_6 to C_8 carbon atoms (Sosa-Vargas et al., 2013). The *in situ* UV-Vis spectra as a function of time are plotted in Figure 5.4. On a 25 minute time scale the C_6 and C_7 lead phthalocyanines remained intact (a) and (b) whereas C_8PbPc in Figure (c), was readily de-metallated. The choice of C_8PbPC was based on the time factor of nanocomposite formation.

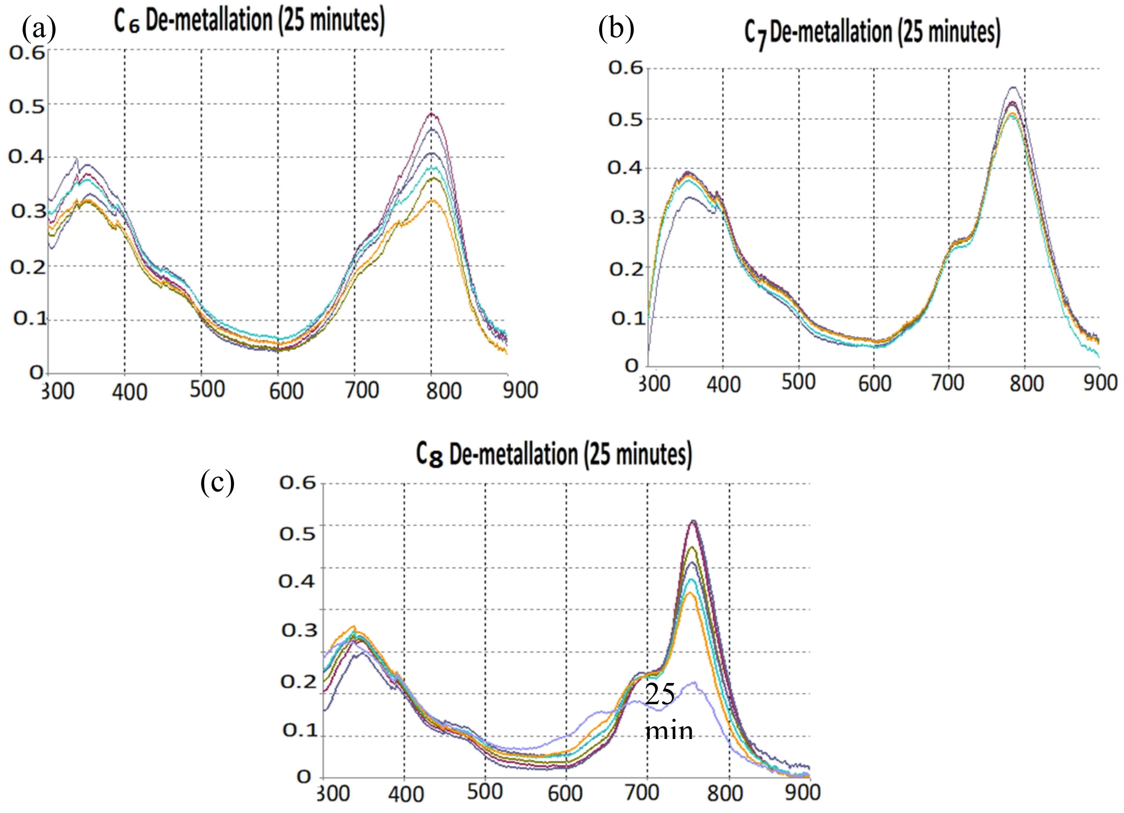

Figure5.4: **De-metallation of (a) C_6PbPc, (b) C_7PbPc, and (c) C_8PbPc as function of time in 25 minute time scale (Courtesy of Lydia Sosa-Vargas, East Anglia University)**

PbS quantum dots/octyl substituted phthalocyanine nanocomposite films were produced in the process as described by Nabok et al., 2004. Figure 5.5 illustrates the set up that was used for the de-metallation of lead phthalocyanine. A gas cylinder filled with 99.5% pure H_2S gas in (a) was connected to a sample chamber (b), and two sodium hydroxide (NaOH) filled gas jars (c). At first gas was allowed to flow through the glass chamber for 5 minutes to ensure a complete atmosphere of H_2S in the chamber (b). To prevent environmental exposure, excess gas was allowed to pass through two gas-jars partially filled with saturated solution of NaOH. NaOH reacts with H_2S and produce sodium hydrosulfide (NaHS) and the sodium sulfide (Na_2S) by the following reactions.

$$H_2S + NaOH \rightarrow NaHS + H_2O \qquad (5.6)$$

$$NaHS + NaOH \rightarrow Na_2S + H_2O \qquad (5.7)$$

NaHS and the sodium sulfide Na_2S are both non-toxic materials and soluble in water. The outlet of the H_2S gas cylinder as well as inlet and outlet of the sample chamber were closed after 5 minutes of the H_2S exposure of the sample. Then C_8PbPc films were left in the closed chamber for about 24 hours for complete conversion of C_8PbPc into nanoparticle PbS and metal free phthalocyanine analogue.The reaction between the C_8PbPc and H_2S has been already explained in Section 1.1 of Chapter 1. This set-up was located inside a laboratory fume hood to prevent exposure to H_2S.

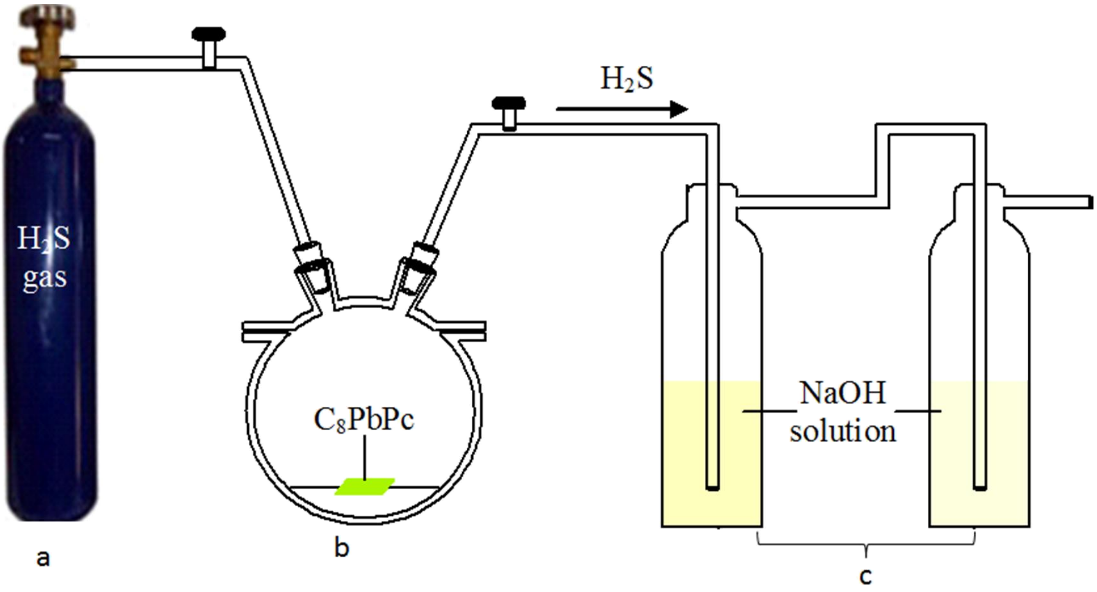

Figure 5.5: The set up for the H_2S exposure in C_8PbPc

The completion of reaction was indicated by a colour change from green to bluish-green. Figure 5.6 shows the drop cast C_8PbPc, before and after reactions. The black spots on the film after reaction were most likely PbS nanoparticle. The detail physico-chemical analysis of the reaction products will be described in the Chapter 8.

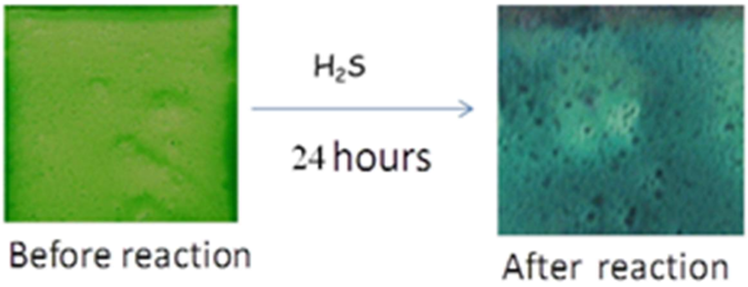

Figure 5.6: A colour change from green to bluish green with black spots on exposing dropcast film of C_8PbPc in H_2S

5.7 UV-Visible or absorption spectroscopy:

The optical properties of the compounds C_8LuPc_2, C_8GdPc_2, C_6GdPc_2 in both solution and solid phase were studied using the UV-Vis spectroscopy. This technique was also used to characterise PbS QDs in the thin film of the nanocomposite compound. Absorption spectroscopy is employed as an analytical chemistry tool to determine amount of energy absorbed by a valence electron for transition to higher energy electronic levels. The amount of energy for the electronic transitions is few hundreds kilojoule per mole and falls in UV or visible region. The spectral changes were recorded using Perkin Elmer LAMBDA 650 UV–Visible spectrophotometer.

A schematic diagram of a UV-Vis spectrophotometer is shown in Figure 5.7. A tungsten halogen lamp was used which emit light in the range 200-1100 nm wavelength. Then the light was allowed to pass through a double holographic grating monochromatic filter with intensity of incident light (I_0) and the phthalocyanine sample consecutively. The electronic spectra of the phthalocyanines were measured in both of solution and solid phase. In case of solution phase absorption spectra, the compound was dissolved in appropriate solvent and kept in a standard 1 cm quartz cell. A reference 1 cm quartz cell filled with the solvent was used simultaneously throughout the experiments in order to avoid the effect of background absorbance. To monitor solid film spectra a spin-coated sample on glass/quartz slide was used with a reference glass/quartz slide.

As the phthalocyanine is a colour absorbing material, the intensity of the transmitted light (I_t) was less than the incident light (I_0). Lambert-Beers law states I_t is dependent on

I_0 and product of the absorption coefficient of the substance (α_a), the path length (d_a) with exponentialfunction as follows (Tkachenko, 2006).

$$I_t = I_0 \exp(-\alpha_a d_a) \qquad (5.8)$$

The absorption coefficient (α_a), in turn, can be expressed as a product of an extinction coefficient of the absorber, $\in$, and the concentration c_a of absorbing species in the material expressed in the following equation,

$$\alpha_a = \in c_a \qquad (5.9)$$

The logarithm of the intensity ratio between the I_0 and I_t is called absorbance (A_t) and can be expressed as follows

$$A_t = \log_{10}\frac{I_0}{I_t} = \in c_a d_a \qquad (5.10)$$

The absorbance of the phthalocyanines was measured by a detector, which consists of a combination of a photomultiplier tube, 3-stage Peltier cooled In GaAs and a temperature stabilized PbS detectors. The scanning rate was 654.92 nmmin^{-1} over the range 300–850 nm of incident wavelength of light.

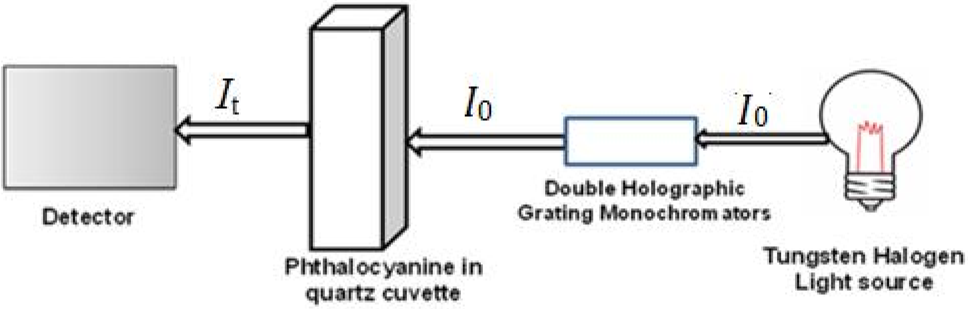

Figure 5.7: Instrumentation of optical absorption spectrophotometer (Perkin-Elmer, April 2, 2014)

5.8 Photoluminescence Emission (PL) spectroscopy

Photoluminescence emission spectroscopy was used to monitor the intensity of emitted light by the PbS QDs/ C_8H_2Pc nanocomposite. In this case, when a molecule is excited from the ground state to the higher molecular orbital, a set of photophysical phenomenon occurs before returning to the ground state. The emitted radiation while coming back to ground state is called photoluminescence.

Figure 5.8 shows the instrumentation of a typical Perkin Elmer Fluorimeter LS5, employed for the study. A450 W pulsed Xenon lamp, emitting light in the wavelength range 250-850 nm was used as the light source. The light was allowed to pass through a monochromator filter for the selection of exciting light wavelength (λ_0). After passing through the phthalocyanine, the emitted wavelength of light (λ) was found to be significantly different from the incident light (λ_0). Both of the spin-coated, and dropcast film of PbS/phthalocyanine nanocomposite and the pristine metalfree phthalocyanine compound were used for the study. In addition to this, the solution phase photoluminescence spectra were collected for the metal free phthalocyanine in 0.01 mgml^{-1} concentration of toluene solution in a 1 cm quartz cell. An emission monochromator was used to get high resolution PL spectra. The intensity and wavelength of emitted light was analysed by a detector. A S5 type photomultiplier tubes were used as detectors for the scanning range of 365-865 nm of wavelength.

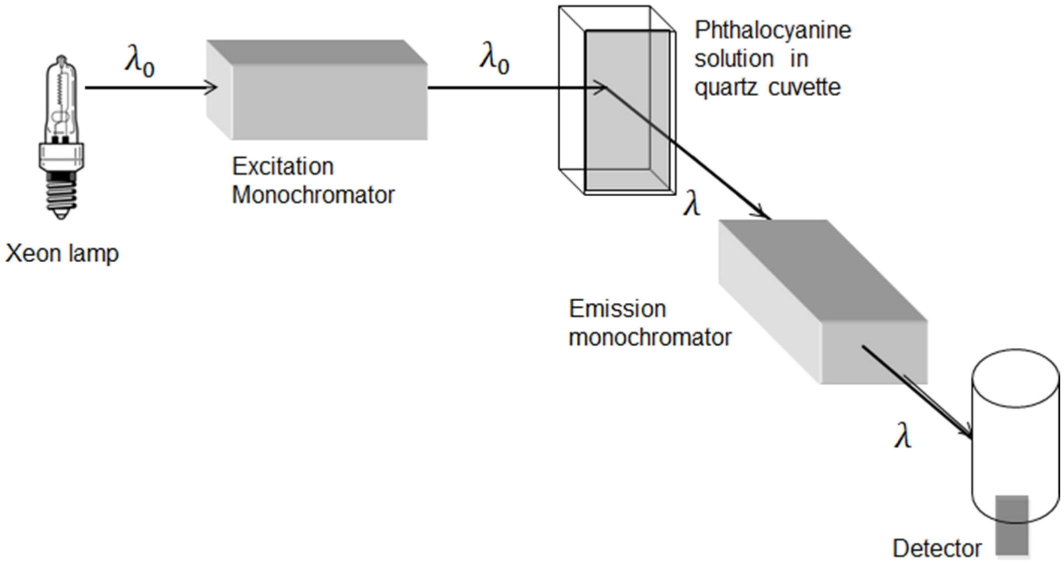

Figure 5.8: The typical diagram of how a fluorometer works (redrawn from, molecular fluorescence spectroscopy, 2014)

5.9 Resonance Raman spectroscopy

Raman spectroscopy was used to give an insight into the molecular vibrations of the phthalocyanine molecules on structural changes or chemical reactions. The technique in resonance Raman spectroscopy is based on the energy exchanged between the molecule and photon during inelastic collision. If the molecule gains energy due to the change of vibrational and rotational energy level, the scattered light energy frequency will be less than the incident one. These lines are called anti-Stokes radiation. In other cases, the scattered light might have lower frequency than the incident because of the molecule emitting some energy, is called Stokes radiation. This phenomenon with certain discrete frequencies above and below is the incident beam is called Raman Scattering (Ferraro, Nakamoto, and Brown, 2002).

Raman spectra phthalocyanines were examined using LabRam Raman spectrometer from Horiba Jobin Yvon. The spectrometer was equippedwith a laser source, an 1800 groove mm^{-1} holographic grating, a holographic super-notch filter, and a Peltier-cooled CCD detector (Figure 5.9). A He–Ne laser provided the exciting radiation at 632.8 nm to study the vibration spectra of C_8LuPc_2, C_8GdPc_2, and C_6GdPc_2 molecules dropcast on glass substrate. The samples were placed on a Olympus BX40 microscope slide using a microscope objective of × 100 magnifications to focus the laser beam. The laser beam was attenuated by a 10% neutral density filter (D1 filter), resulting in a laser power of 0.8 mW at the sample. This is to avoid the sample degradation under the heat generated by the laser. Raman measurements of the bisphthalocyanines were involved acquisition of multiple spectral windows in the range 200–3500 cm^{-1} (Stokes shifts only) accumulation of 5 scans, each in 30 seconds. The spectral width was 3 cm^{-1}.

A green Nd:YAG laser, wavelength of 532 nm was employed to study the vibration spectra of dropcast films of C_8PbPc before and after H_2S treatment. The measurements consisted of the acquisition of multiple spectral windows in the range 500–1700 cm^{-1} (Stokes shifts). The other parameters were kept as the previous ones. Raman spectrum of pristine C_8H_2Pc was also collected in the same region for comparison with the C_8H_2Pc formed after H_2S treatment of C_8PbPc. To identify the presence of PbS nanoparticle in the nanocomposite, Raman spectra were also obtained for H_2S treated films of lead phthalocyanine and galena powder from 300 to 700 cm^{-1} (40 scans, each in 5 sec and spectral width 3.5 cm^{-1}). Very slow scan rate was chosen as PbS is a second order Raman scatterer (Etchegoin et al., 2000). A reduced power of 11.8 μW (D3 filter) was used in this case to stop oxidation of PbS at high laser power. Formation of oxy-sulfates by laser-induced degradation of PbS has been reported by Deng et al., 2010.

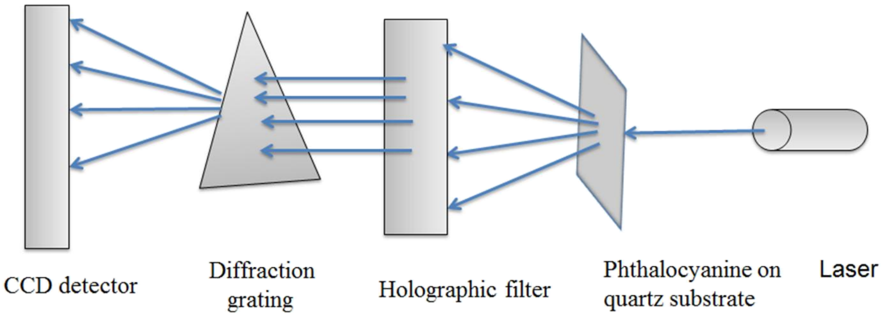

Figure 5.9: **Schematic representation of the instrumentation of Raman Spectrometer (redrawn from University of Cambridge, 2014)**

5.10 Electrical measurements

The electrical measurements were carried out for the characterisations of the bisphthalocyanines as well as the nanocomposite material. The interdigitated gold electrodes on top of a glass substrate (Figure 5.10a) were used to measure the in-plane direct current (DC) conductivity measurements by the two-probe method. A number of authors have studied the charge transport of the phthalocyanines on planar electrode especially asgas sensing devices. The large surface areas of the planar electrodes are more suitable as gas sensors than the sandwich electrodes (Guillaud, Simon, and Germain, 1998; Sen et al., 2011).

Figure 5.10b is the sketch of the enlarged view of the electrodes. The channel length (*L*), width (*W*), and number of fingers (*N*) of the interdigitated electrodes were measured as 45µm, 0.716 cm and 24, respectively using a microscope objective of×5 magnification.

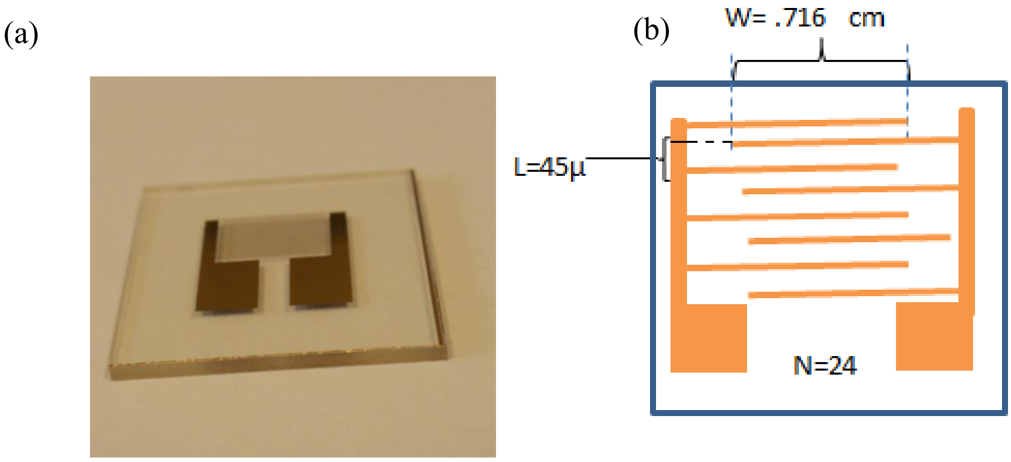

Figure 5.10: **(a) Interdigitated electrodes used in the current-voltage measurements (b) Schematic diagram of the electrodes.**

When the length of the electrode is L, the in-plane conductivity (σ_{x}) of the phthalocyanines can be measured using the mathematical expression explained in Equation 4.2 as $\sigma_{\mathrm{x}} = \frac{L}{\mathrm{R}A}$. As the material was coated on top of the gold coated substrate, approximately (N-1) number of resistors can be assumed between the two electrodes, where N is the total number of fingers in the electrode. The total conductivity of the material can be expressed as $\sigma_{\mathrm{x}} \approx \frac{L}{(N-1)RA} \approx \frac{IL}{(N-1)V_{\mathrm{a}}A}$ where, I is the current under applied voltage V_{a}. Using the area (A) of the interdigitated electrode as Wd, σ_{x} is written as follows,

$$\sigma_{\mathrm{x}} \approx \frac{I}{V_{\mathrm{a}}} \frac{L(N-1)}{Wd} \qquad (5.11)$$

Figure 5.11 shows the electrometer and cryostat set up used for the dc conductivity study of the films.The in-plane current-voltage characteristics of the phthalocyanines were studied by microprocessor controlled Keithley 617 electrometer, (a) and data were analysed using a LABVIEW programme. Samples were kept in high vacuum of $\geq 10^{-4}$ mbar in an Oxford instrument cryostat, (c). Contacts between the cryostat pin and electrodes were made with silver paste. The low temperature was maintained by liquid N_2. Temperature was controlled and measured by an Oxford instrument ITC 601 temperature controller, (d).

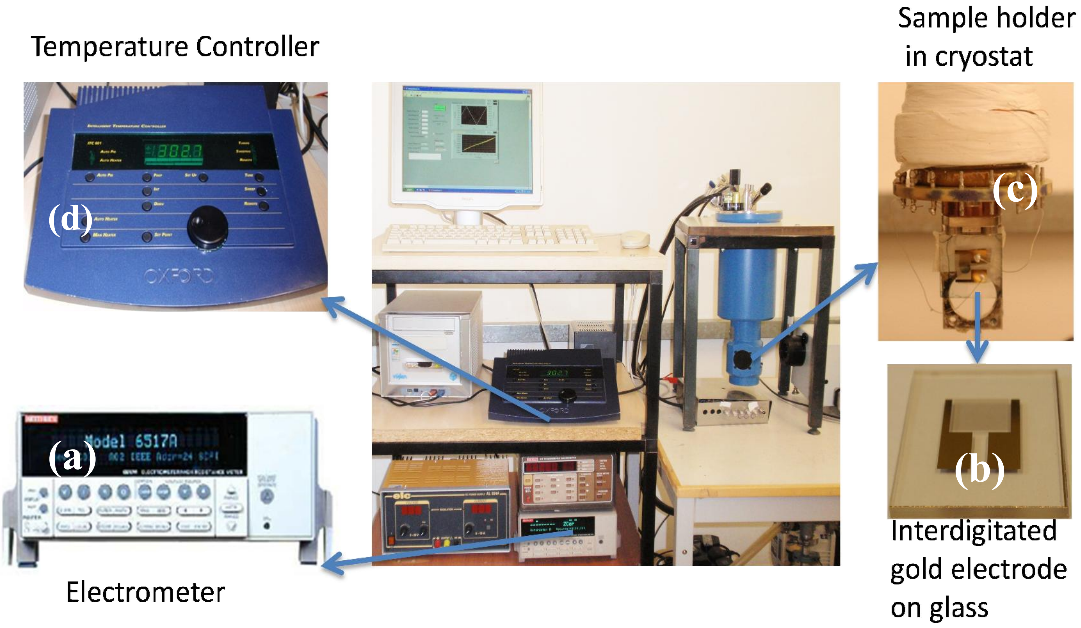

Figure 5.11: **Set up for the electrical measurements in high vacuum and different temperatures from 87K to 430K**

5.11 X-Ray diffraction (XRD) study

In this research work, the XRD study of the nanocomposite PbS/C_8H_2Pc was carried out for the identification of the components as well as to examine the structural changes in C_8H_2Pc due to the incorporation of PbS quantum dots. The XRD technique for determination of the bulk molecular structure was first discovered by William Bragg in 1912. This is well-known that a crystal is a repetitive, three dimensional arrays of the atoms, ions or molecules. Each face of the crystals has planes parallel to itself. X-ray can penetrate to the crystal planes as it has similar wavelength of the atom size approximately 1Å. Figure 5.12 is the diagram of reflection of X-rays from crystal planes. Bragg established the relation between the Angle of diffraction (θ) and crystal planes (d) as follows (Cullity and Stock, 2001)

$$n_{\mathrm{x}}\lambda_{\mathrm{x}} = 2d\sin\theta \qquad (5.12)$$

Where n_x is an integer 1,2,3,……..and so on, which is called the order of reflection.

λ_x = Wavelength of X-ray. For Cu-Ka radiation, the value of λ_x is 0.154178 nm the interplanar distances between the crystal planes. Therefore, coordinate of the planes of single crystal, film or powder can be calculated by using X-ray diffraction study.

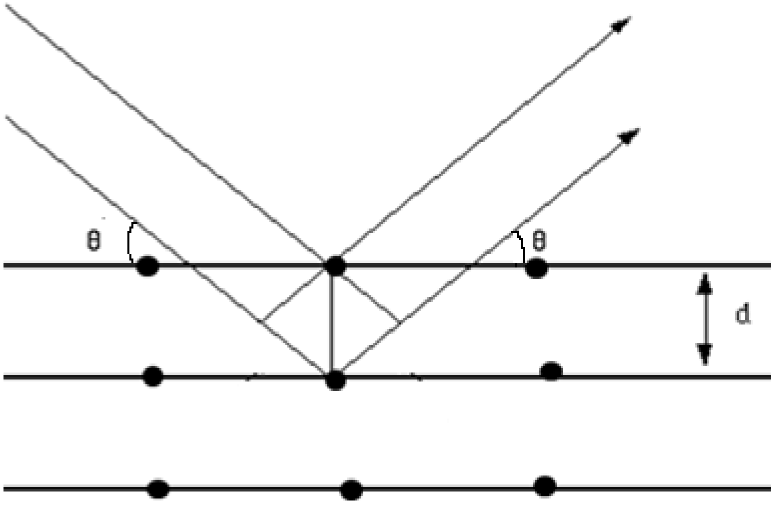

Figure 5.12: Reflection of X-rays from lattice planes (Rakshit, 2001)

XRD patterns of the nanocomposite drop cast films on silicon wafers were acquired with a Bruker D8 Advance instrument with Bragg-Brentano geometry. The instrument consists of three main parts: X-ray source, detector and the sample holder. The sample holder and the detector were allowed to rotate with θ and 2θ angles, respectively keeping the X-ray source fixed. The value of 2θ was varied in the range of 10˚ to 60˚ at the rate of 0.16° per minute.

Topas software was used to perform the profile fitting and crystal data analysis for PbS quantum dots to estimate the lattice parameters and the crystallite size. In appendix 3, the detail of the fitting parameters and the results for PbS QDs and bulk phase has been described. The calculation of the crystallite size in the software was based on the well-known Debye-Scherrer equation (Iwatsu, Kabayasi and Udeyta, 1980). The Bragg peak broadening in the pattern-ray diffractogram is caused by the size of the crystals (D) and the lattice strain. Measuring the half width of Bragg peak (β) and the diffraction angle of the most intense peaks (θ) gives the value of crystallite size by Debye-Scherrer equation after neglecting the lattice strain.

$$D \approx \frac{k\lambda_x}{\beta cos\theta} \tag{5.13}$$

Here, *k* is the Scherrer constant where the value of *k* is typically 0.9.

5.12 Transmission electron microscopy (TEM)

TEM is an imaging technique with high magnification of up to one million times and employed to observe materials down to nanometre level. TEM has been used to characterise the PbS QDs in the nanocomposite. JEOL, EM 13005, TEM instrument using an accelerating voltage of 200 kV was applied for that purpose. TEM is widely used by a number of authors (Wang et al., 2001; Sarma and Datta, 2010; Chakrabarty and Moulik, 2005) to determine the size and shape of nanosized PbS. In TEM analysis, very high energy electrons were produced by a tungsten filament (Figure 5.13). The electron beam was accelerated to the nanocomposite sample through vacuum using electromagnetic objective lens. The incident electrons, after passing through the specimen either transmitted or scattered by a new angle. The transmitted beam of electrons was focussed on the image plane by allowing them to pass through the projection lens.

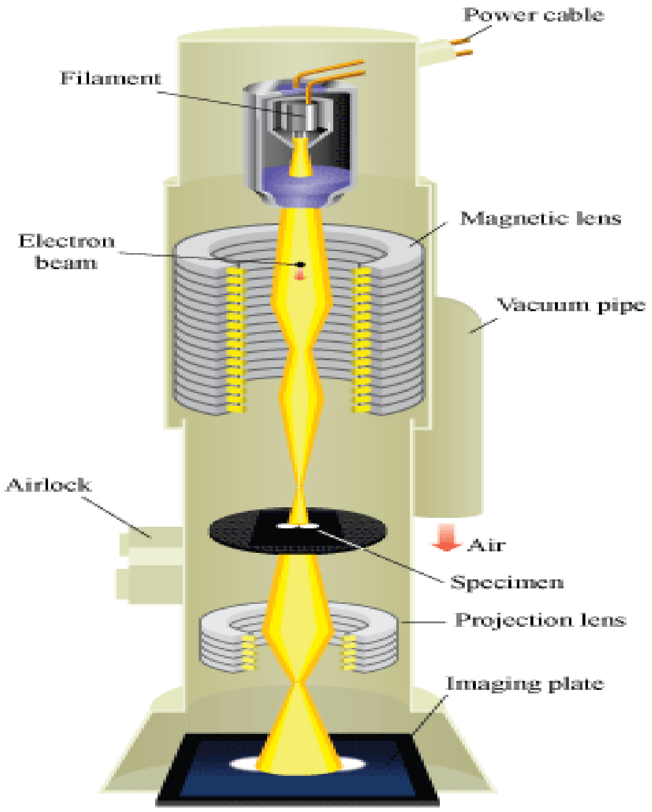

Figure 5.13: **Schematic diagram of how TEM Works [EDN Network, April 5, 2014]**

The specimen was prepared by scratching little amount of nanocomposite material from the dropcast substrate and dispersing the material in anhydrous alcohol (99.9%). Then the specimen was transferred to a sample holder, made of Cu grid. The image of the sample was dependent on how many electrons had transmitted through it. The darker region of image indicates a low number of transmitted electrons whereas the lighter regions are due to transmission of electrons in a large number.

SAED (selected area electron diffraction) of TEM was used to find out the crystal planes of the PbS QDs. In this case, when the high energy electrons collide with the atoms in the molecule, the diffraction angle of the electrons gives information about the crystal lattice planes and interplanar distances.

Values of the interplanar spacing (d_s) of PbS QDs was estimated using the formula

$$L_c.\lambda_{\mathrm{tem}} = d_s.\, r \qquad (5.14)$$

L_c = camera constant, λ_{tem}= wavelength of the electron beam, d_s= interplanar spacing, r= radius of SAED pattern. $L\lambda_{\mathrm{tem}} = 1.9815 \times 10^3$ is known as the camera constant (Azimirad et al., 2009). The electron scattering at the limited number of particles results in different diffraction spots which are arranged in the diffraction ring pattern.

5.13 Thermogravimetric analysis (TGA)

Thermogravimetric analysis is a thermal study of a material which determines the mass loss with temperature. In this work, TGA was used to find out the weight fraction of the PbS in the nanocomposite PbS/ C_8H_2Pc. PbS is an ionic compound which has a very high melting point of 1118°C (Kullerud, 1969).Phthalocyanines as organic compound shows comparatively lower melting point (Lawton, 1958; Garcia-Sanchezand and Campero, 2000).

To prepare the sample for the thermal analysis, around 2 mg of dropcast nanocomposite material was mechanically scratched from the glass substrate and placed in the TA Instruments TGA500. This instrument has an inbuilt balance to weigh the sample precisely upto 1/10th of a milligram. Equivalent amount of pristine metal-free phthalocyanine was also placed in the instrument for comparison. Both of the samples were heated up to 700°C at a heating rate of 10°Cmin^{-1}. The analysis was carried out under a nitrogen flow of 50 mlmin^{-1} to prevent any lead sulfide oxidation occurring at high temperature. As the temperature increases, the mass change was measured and plotted against temperature. The Universal Analysis 2000 V4.3 software was used for the data analysis.

5.14 X-ray photoelectron spectroscopy (XPS)

In X-ray photoelectron spectroscopy, when an X-ray beam is allowed to hit on an atom or molecule, electrons from core or valence orbitals are ejected leaving behind an ion. The ejected electrons have different velocities depending upon their binding energy (Barr et al., 1994).

Obeying the energy conservation rule, the following expression can be written,

$h\nu$ = Binding energy + Kinetic energy

Therefore, Binding energy = $h\upsilon$ - Kinetic energy

Here h is the Planck's constant and υ is the frequency of the incident X-ray beam.

X-ray photoelectron spectroscopy was used to measure the binding energy of the N_{1s} and Pb_{4f} electrons in the components of nanocomposite material. Each element has specific characteristic binding energy associated with a particular atomic orbital. Based on the fact, this technique is frequently used to examine the chemical composition and electronic state of different composites (Wells et al., 2004, Asunskis and Hanley, 2007, Asunskis et al., 2008)

XPS measurements were made with the nanocomposite PbS/C_8H_2Pc and pristine C_8H_2Pc dropcasted on silicon wafer using a VG ESCALAB 210 Photoelectron Spectrometer. The X-ray source was a non-monochromated Al Kα source (1486.6eV), operated with an X-ray emission current of 20 mA and an anode high tension (acceleration voltage) of 12 kV. The software Casa XPS 2.3.13 was used to fit the XPS spectral peaks. All spectra were charge-corrected to saturated hydrocarbon at 285.0 eV. The take-off angle was fixed at 90° relative to the sample plane. The area corresponding to each acquisition was of 1 mm^2. Each analysis consisted of a wide survey scan (pass energy 50eV, 1.0eV step size) and high-resolution scans (pass energy 50eV, 0.05eV step size) for component speciation. 10 scans were taken for the survey spectra, and 5 scans were taken for each one of the expansions.

Chapter 6 Liquid Crystalline Lutetium and Gadolinium Bisphthalocyanines: Characterisations

This chapter describes optical and electrical studies on thin films of three different types of novel non-peripherally substituted liquid crystalline (LC) lanthanide bisphthalocyanines (Pc) shown in Figure 1.2. All of these three compounds exhibit a discotic liquid crystalline mesophase on annealing the film at 80°C. The results of optical and electrical characterisation of as-deposited and annealed films have been interpreted in terms of the molecular rearrangements with an emphasis on the role of central metal ion and substituents.

6.1 UV-Vis or Optical absorption spectroscopy

Optical absorption spectra are presented for three bisphthalocyanine molecules in the solution and solid thin film (both as-deposited and annealed) phases and individual characteristics have been analysed in terms of molecular arrangements.

6.1.1 Bis[1,4,8,11,15,18,22,25-octakis(octyl)phthalocyaninato]lutetium(III), C_8LuPc_2

A sharp Q-band arising from the 0.01 mgml^{-1} neutral solution of C_8LuPc_2 inchloroformappears at 714 nm (Q_y band) in the absorption spectrum (a) in Figure 6.1. An additional band of comparatively lower intensity is situated at 653 nm (Q_x band). The peaks are sharp in this spectrum as the screening effect of the solvent prevents the molecular aggregations. The small shoulder at 473 nm is a characteristic band for the neutral rare-earth bisphthalocyanines attributable to the radical nature of the molecules. The Q_y-band for the compound in an as-deposited spun film on quartz substrate was found to be broad and red shifted to 718 nm, indicating this small redshift of the band with respect to Figure 6.1a. According to Kasha molecular exciton theory (in Section 2.3 in Chapter 2), the redshift of optical band is caused by the interactions between the transition dipoles situated parallel to the molecular profile. The crystal packing patterns of the molecules C_8LuPc_2 in Figure A2.3 in Appendix 2 show the J-aggregated or head-to-tail arrangement between the neighbouring molecules. This is believed to be responsible for the redshift in this case. Similar crystal packing has been observed for peripherally substituted thioalkylated Cerium derivatives by Nekelson et al., 2007.

The spectrum of the annealed film of C_8LuPc_2 is also included in Figure 6.1c. The Q band positions in the discotic LC mesophase upon annealing show significant differences from the as-deposited film. There is a further redshift of the Q_y and Q_x bands now situated at 730 and 655 nm, from the as-deposited solid phase spectrum at 718 nm and 653 nm. The redshift may be attributed to the long-range staggered slipped stacking arrangements of the transition dipoles in form of stacks (Basova et al., 2007)

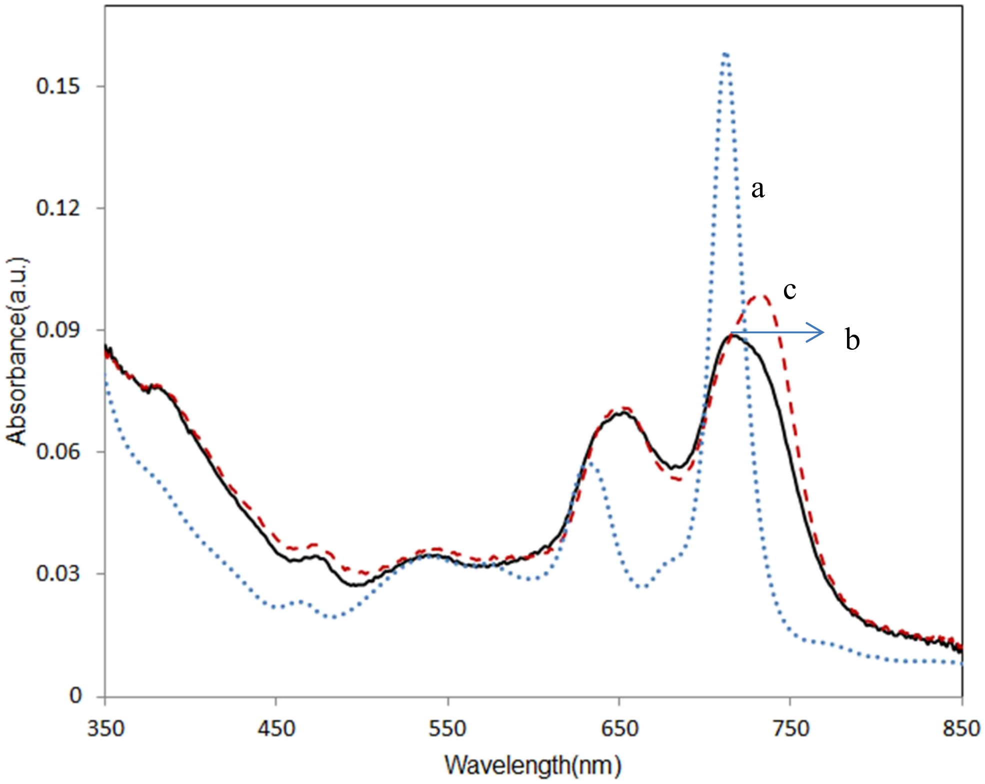

Figure 6.1: **UV-Vis spectra of (a) 0.01 $mgml^{-1}$ chloroform soliution of C_8LuPc_2 (dotted line), (b) as-deposited thin film (solid line), (c) annealed film (dash line)**

Both Valence effective and extended Hückel Hamiltonian calculations have shown that the characteristic Q-band transitions in the absorption spectrum arise after transition of an electron between the molecular orbitals under optical excitation (Orti, Brédas and Clarisse, 1990; Rousseau, Aroca and Rodriguez-mendez, 1995). The molecular orbitals (MOs) from Figure 4.2 of Chapter 4 have been redrawn in Figure 6.2 in simple form to assign the electronic transitions of C_8LuPc_2 in the solution phase. The a_2 and e_3^* form the highest occupied molecular orbital (HOMO) and lowest unoccupied molecular orbital (LUMO). The Q_y band can be assigned as the electronic transitions from the a_2 to e_1^*corresponding to the optical transitional energy (ΔE_0) value of 1.73 eV. The additional band at 653 nm (1.89 eV) is generally associated with the transition from the $b_1 \rightarrow e_3^*$(Orti, Brédas, and Clarisse, 1990). The radical band at 473 nm (2.62 eV) is the charge transfer band from the inner orbital of e_1 to half-filled a_2 orbital (Mendonca et al., 2000). An electron spin resonance (ESR) signal of neutral bisphthalocyanine for the radical character of the compound is consistent with the band found in the optical absorption spectra. The free radical is stabilised by delocalisation through conjugated double bonds of the two phthalocyanine rings which can be represented as $[Pc^A(-2)Lu^{3+}Pc^B(-1) + Pc^B(-2)Lu^{3+}Pc^A(-1)]$. On one-step oxidation the radical band disappears along with the absence of the ESR signal (Ishikawa, 2001). The electronic transitions in the as-deposited and annealed film with assignments have been summarised in Table 6.1.

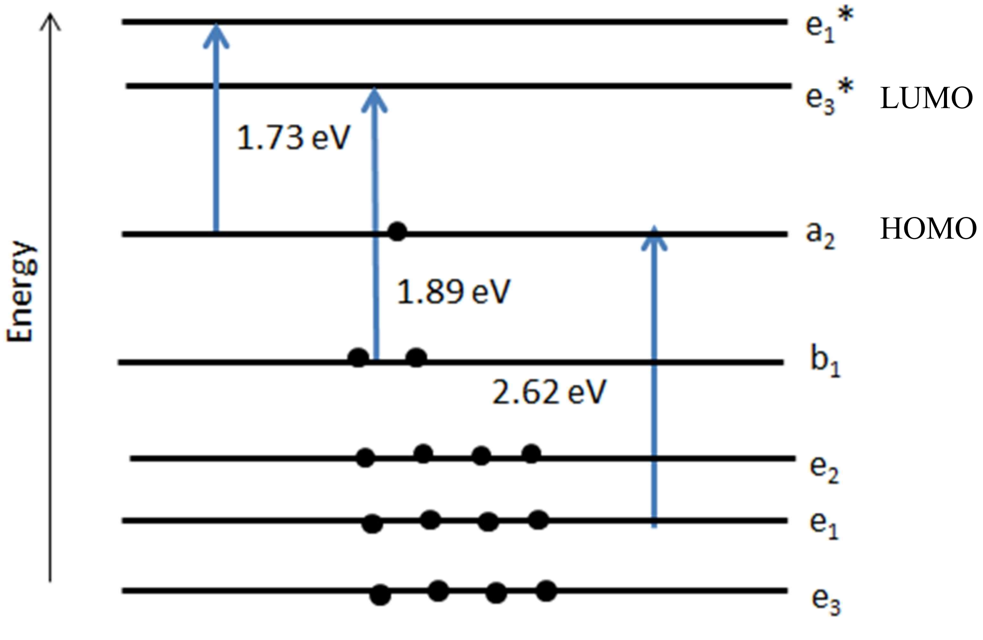

Figure 6.2: Optical transitions of 0.01 mgml^{-1} solution of C_8LuPc_2 in $CHCl_3$

6.1.2 Bis[1,4,8,11,15,18,22,25-octakis(octyl)phthalocyaninato]gadolinium(III), C_8GdPc_2

C_8GdPc_2 in the solution phase of 0.01 mgml^{-1} chloroform also shows two Q bands at 724 nm and 640 nm (Figure 6.3a). Similar to the C_8LuPc_2, the Q band positions in the spectrum (b) for the solid thin film are broadened and the Q_y and Q_x bands are red shifted to 728 nm and 643 nm, respectively in relation to the solution spectrum. As before, this is due to the formation of J-aggregation of the transition dipoles. The radical band is present at 473 nm. The electronic transitions in solution phase with assignments have been listed in Table 6.1.

The stacking arrangements of transition dipoles in discotic LC mesophase lead to significant red shifts of Q_y and Q_x band to 750 from 724 nm and 648 nm from 640 nm, respectively in the spectrum (c).

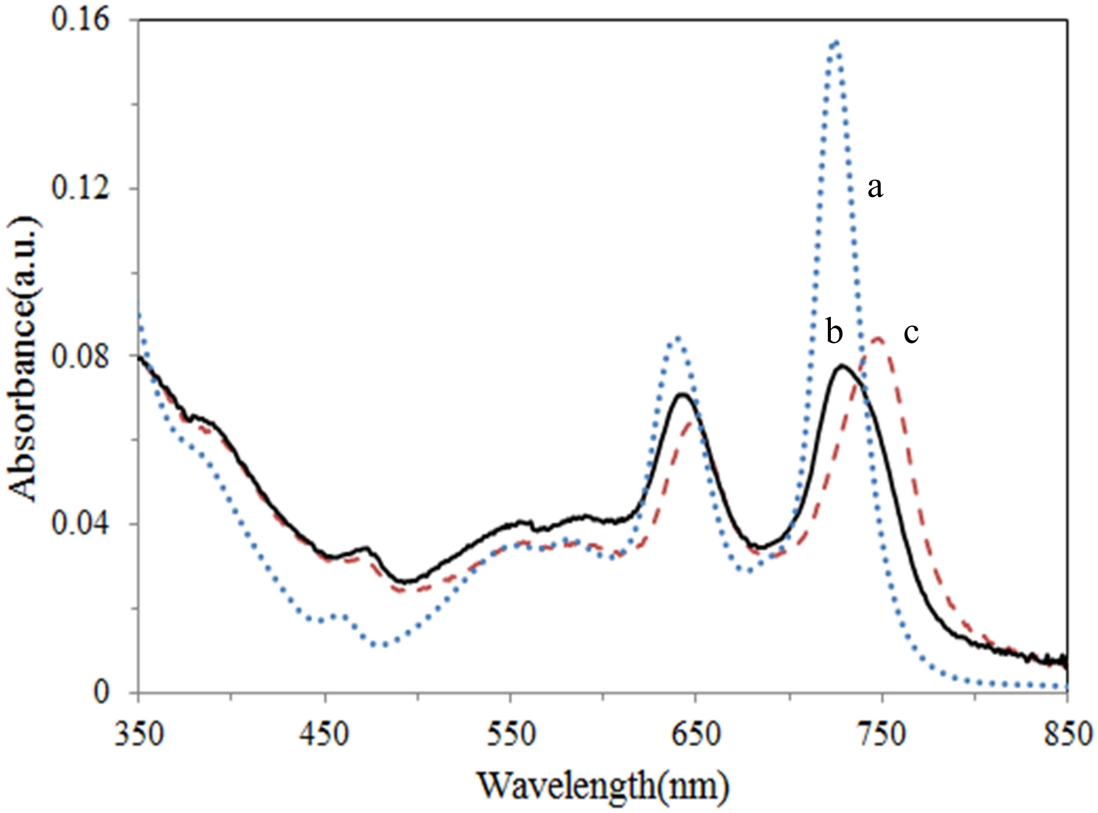

Figure 6.3: **UV-Vis spectra of (a) 0.01 mgml^{-1} chloroform soliution of C_8GdPc_2(dotted line) (b) as-deposited thin film (solid line), (c) annealed film (dash line)**

As it is evident from Figure 6.1 and 6.3, the Q_y band in C_8GdPc_2 is redshifted by 10 nm relative to the Lu-derivative in both solution and solid phase spectra. The band shifting can be correlated to the different types of central metal ions in the two compounds. The ionic radius of Gd (III) is 0.94 Å in lieu to the Lu(III) as 0.86 Å has been reported by Lide, 2007. The Q band shifts to higher energy is usually observed when there is additional π-π interaction between phthalocyanine molecules with the rare-earth contraction. The smaller size of Lu (III) leads to additional interactions between the Pc rings and this can be understood from the single crystal structure determination of the molecules. The side view of the isostructural single crystal of the two octyl substituted derivativesis given in Figure A2.1 in Appendix 2. In both cases, all the eight substituents in each ring are organised approximately in the 'planes' of the two Pc rings. Steric hindrance of the long octyl chains causes twisting of the phthalocyanine core and the angle between 'top' ring and the lower ring was estimated as comparable 38-39 degrees with D_4 point group symmetry. Slight changes in the bond angles, bond lengths and distance between the two rings can be noticed with changing the central metal ion from Lu to Gd which have been listed in Table A2.1 in Appendix 2. The average Pc ring-ring distance increases from 2.39 Å to 2.92 Å on changing the metal ion from Lu to Gd. The larger intramolecular distance in C_8GdPc_2 leads to smaller π-π interaction between the rings resulting in a small redshift of the Q bands with respect to C_8LuPc_2.

6.1.3 Bis[1,4,8,11,15,18,22,25-octakis(hexyl)phthalocyaninato]gadolinium (III), C_6GdPc_2

No significant difference was noticed between the solution phase spectra of C_6GdPc_2 in Figure 6.4a with the octyl substituted gadolinium derivative in Figure 6.3a. The chain length of alkyl groups does not affect the main electronic transitions in monomeric form in the solution phase as the distance of the side chain from the molecule centre is relatively large. However, the Q_y and Q_x bands of thin solid film spectra were found at 721 nm and 637 nm in comparison to the 728 and 643 nm bands of C_8GdPc_2. The band shifts and the energy associated with them are included in Table 6 .1. Unlike the redshifts in other two Pcs C_8GdPc_2 and C_8LuPc_2, the blueshift of the Q bands in C_6GdPc_2 with respect to the solution phase Q bands may be related to the differences in molecular arrangements in the solid phase. The molecular packing in Figure A2.4, Appendix 2 suggests the formation of H-aggregated or face-to-face arrangements between two adjacent C_6GdPc_2 molecules in the solid phase. According to the Kasha model the blue shifted exciton is usually observed when there is π-π interaction between the transition dipoles in the direction perpendicular to the Pc ring (Section 2.3 in Chapter 2).

The Q bands of the C_6GdPc_2 film in discotic LC phase are further blueshifted from 721 nm and 637 nm to 715 nm and 625 nm, respectively due to long range face-to-face stacking arrangements of the monomers. The blueshifts in the as-deposited and LC phases are comparable to those of tetra-substituted nickel phthalocyanines reported by Basova et al., 2009. However, the radical band was situated at 473 nm irrespective of metal ion, side chain, or single crystal structure.

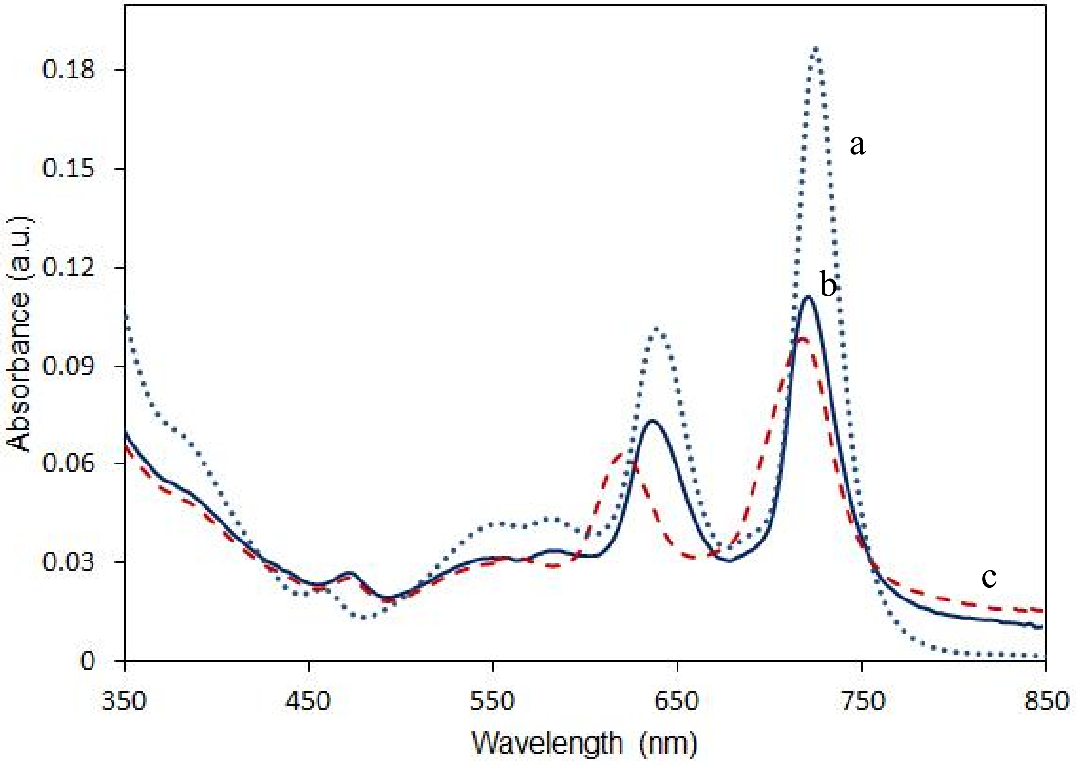

Figure 6.4: **UV-Vis spectra of (a) 0.01 $mgml^{-1}$ chloroform soliution of C_6GdPc_2 (dotted line) (b) as-deposited thin film (solid line) and (c) annealed film (dash line)**

Table 6.1: Variations in the absorption maxima of the main visible region bands for the solution, as-deposited, and annealed film of C_8LuPc_2, C_8GdPc_2 and C_6GdPc_2.

Molecule	**Positions of bands of optical absorption spectra**																	
	Solution in chloroform						**As-deposited Film**						**Annealed Film**					
	Q_y ($a_2 \rightarrow e_1^*$)		**Q_x ($b_1 \rightarrow e_3^*$)**		**Radical band ($e_1 \rightarrow a_2$)**		**Q_y ($a_2 \rightarrow e_1^*$)**		**Q_x ($b_1 \rightarrow e_3^*$)**		**Radical band ($e_1 \rightarrow a_2$)**		**Q_y ($a_2 \rightarrow e_1^*$)**		**Q_x ($b_1 \rightarrow e_3^*$)**		**Radical band ($e_1 \rightarrow a_2$)**	
	λ_p (nm)	**ΔE_0 (eV)**	**λ_p (nm)**	**ΔE_0 (eV)**	**λ_p (nm)**	**ΔE_0 (eV)**	**λ_p (nm)**	**ΔE_0 (eV)**	**λ_p (nm)**	**ΔE_0 (eV)**	**λ_p (nm)**	**ΔE_0 (eV)**	**λ_p (nm)**	**ΔE_0 (eV)**	**λ_p (nm)**	**ΔE_0 (eV)**	**λ_p (nm)**	**ΔE_0 (eV)**
C_8LuPc_2	714	1.73	653	1.89	473	2.62	718	1.72	652	1.90	473	2.62	730	1.70	655	1.89	473	2.62
C_8GdPc_2	724	1.71	640	1.93	473	2.62	728	1.70	643	1.93	473	2.62	750	1.65	648	1.91	473	2.62
C_6GdPc_2	724	1.71	640	1.93	473	2.62	721	1.72	637	1.95	473	2.62	715	1.73	625	1.98	473	2.62

6.2 Resonance Raman spectroscopy

The Raman spectra of neutral bisphthalocyanines were recorded in 200-1650 cm^{-1} range for a drop cast film on glass substrate. The excitation wavelength was chosen as 632.38 nm which is close to the Q-band absorptions. The Figure 6.5 displays the Raman spectra of (a) C_8LuPc_2 (b) C_8GdPc_2 (c) and C_6GdPc_2**.** Similar to the optical absorption, the resonance Raman bands are significantly dependent on structural geometry such as staggering angles between the two Pc rings, Pc-Pc distance, bond lengths and bond angles (Bao et al., 2006). It can be noted from Table A2.1 in Appendix 2, that the equilibrium geometry of three of the molecules are of D_4 symmetry with the comparable twist angles as 39.10, 38.31, and 39.71 for C_8LuPc_2, C_8GdPc_2, and C_6GdPc_2, respectively. Due to similar basic features of the molecular structure, this series of the Pc rings show identical Raman spectra. Some shifting of the band positions with different central metals can be observed as a function of the ionic radii of the ions.

The qualitative assignment of the vibrations of the compounds was carried out on the basis of comparison with Raman spectra of different bisphthalocyanine derivatives in literature (Bao et. al. 2006; Jiang et al., 2006; Basova et al., 2008). The peaks occurring at 1325−1603 cm^{-1} are, therefore, attributed to C=C pyrrole, isoindole ring, and C=N aza stretching. The most intense band in the range 1505-1510 cm^{-1} is called the marker band for the radical species attributed to nearly equal contribution from C=C pyrrole and aza stretching (Tran-thi et al., 1994). The macrocycle ring breathing is responsible for the 500−840 bands, and the 748 and 777 cm^{-1} bands are related to aromatic bonding and aza C=N stretching, respectively. The metal−nitrogen (M-N) bond stretching vibrations have caused the occurrence of Raman peaks at frequencies in the range from 200 to 500 cm^{-1}.

Table 6.2 illustrates a blue shift of C_8LuPc_2 Raman spectrum in comparison to both of the gadolinium derivatives, more prominently in case of M-N stretching in the 200-500 cm^{-1} region and isoindole and aza group stretching at 1325-1603 cm^{-1} region. The Raman frequency differences in the two bisphthalocyanine compounds with different central metal ions are due to the effect of ionic radii. This result agrees well with the blueshifts in the Q band absorption with lanthanide contractions of optical absorption spectra. Jiang et al., 2006 have reported a linear relationship of blueshift of the isoindole and aza band stretching with the lanthanide contraction of a series of unsubstituted rare-earth bisphthalocyanines from La to Lu.

However, Raman bands of C_6GdPc_2 (Figure 6.5 c) do not show any significant difference from those of C_8GdPc_2. As the substituents are away from the core of the phthalocyanine rings, the vibrational characteristics of the bonding are not influenced by the chain lengths of the substituents. The similar positions of optical absorption bands of the monomeric octyl and hexyl substituted Gd-derivatives in solution phase is consistent with the Raman spectroscopic study. The identical Raman band positions of these two derivatives indicate that the resonance Raman spectroscopy is not affected by the molecular orientations of the phthalocyanines.

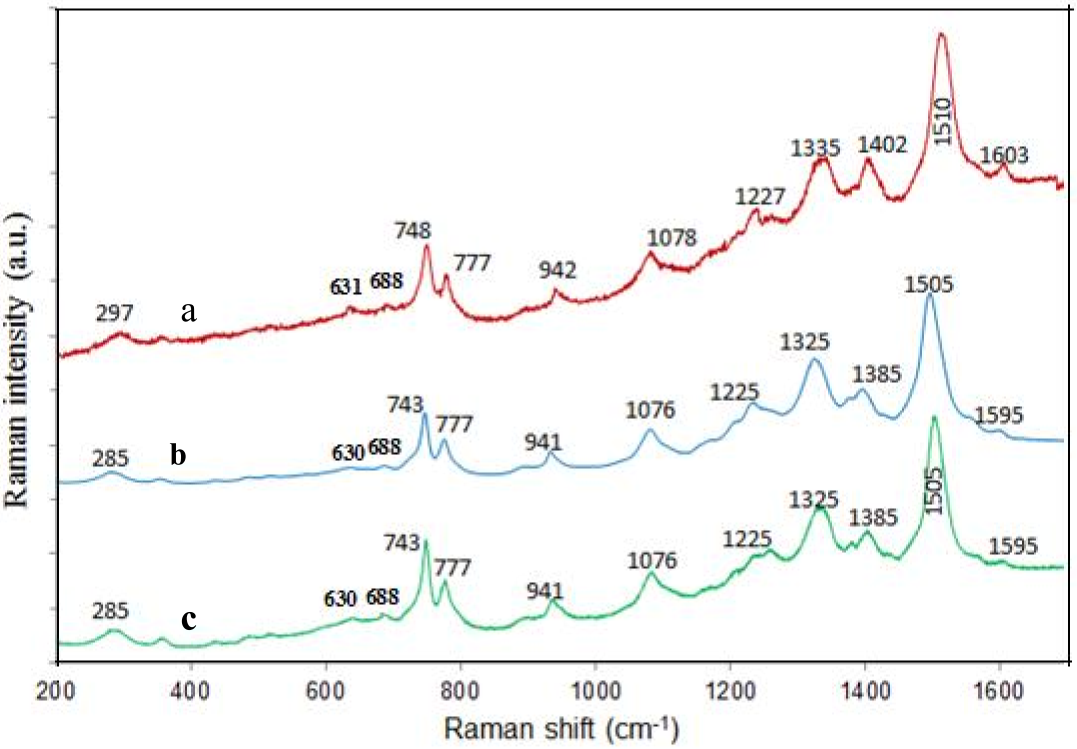

Figure 6.5: **Raman spectra of (a) C_8LuPc2 (b) C_8GdPc_2 (c) and C_6GdPc_2 dropcast as-deposited film on glass substrate**

Table 6.2: Raman shifts of characteristic bands of neutral C_8LuPc_2, C_8GdPc_2, C_6GdPc_2.

C_8LuPc_2	C_8GdPc_2	C_6GdPc_2	Raman shifts (cm^{-1})	
			Assignment	**References**
297	285	285	Metal-Nitrogen str.	Jiang et al.,2006
631	630	630	Pc ring breathing	Jiang et al.,2006
688	688	688	Pc ring breathing	Jiang et al.,2006
748	743	743	Aromatic C-H wag.	Jiang et al.,2006
777	777	777	aza C=N str.	Bao et al.,2006
942	941	942	Benzene ring breathing	Jiang, Rintoul, and Arnold, 2000
1078	1076	1075	Aromatic C-H bending	Jiang et al.,2006
1227	1225	1225	Aromatic C-H bending	Bao et al., 2006
1335	1325	1325	Pyrrole C=C stretching	Jiang et al.,2006
1402	1385	1385	Isoindole C-N stretching	Bao et al.,2006
1510	1505	1505	Coupling of C=C pyrrole and aza C=N stretching	Tran-Thi et al., 1994; Bao et. al.,2006
1603	1603	1603	C=C Benzene stretching	Bao et al.,2006

6.3 Electrical characteristics

The in-plane DC charge transport studies of the spun films of C_8LuPc_2, C_8GdPc_2, C_6GdPc_2 were performed using a two probe method on interdigitated gold electrodes in dark and under vacuum conditions ($\geq 10^4$Pa). The applied voltage was swept from 0 to 100 V at the scan rate of 0.5 Vs^{-1}. The device was annealed in ambient air at 80°C for 1 hour and the experiments were repeated with the annealed films.

6.3.1 Bis[1,4,8,11,15,18,22,25-octakis(octyl)phthalocyaninato]lutetium(III), C_8LuPc_2

The current-voltage [I-(V_a)] characteristics of the as-deposited C_8LuPc_2 were found to be linear on sweeping the voltage from 0 to 100 V (Figure 6.6a). Ohmic contacts were formed between gold and phthalocyanines as given in Section 4.2 in Chapter 4. The slope of the linear current-voltages logarithm plot was 0.96 in Figure 6.6b obeying the Ohm's law of $I \propto V_a$ (I= net current, V_a= applied voltage). The value of in-plane Ohmic conductivity (σ_x) was calculated as 67.55 μScm^{-1} for the as-deposited film from the intercept of the Figure (b) using the following mathematical expression modified from Equation (5.11) of Section 5.7, Page 75 in Chapter 5.

$$\log I = \log V_a + \log \frac{\sigma_x W d}{L(N-1)} \qquad (6.1)$$

where, the number of fingers (N) in the interdigitated electrode is 24, the length of electrodes (L) is 45μm, and the thickness of the C_8LuPc_2 film is 74 nm. The trap-free charge carrier density (n_0) was found to be 2.87×10^{17}cm^{-3} for as-deposited film using Equation (4.1) in Page 56, Chapter 4. The mobility for this calculation was assumed as 1.5×10^{-3} cm^{2}V^{-1}s^{-1} derived by Chaure et al., 2010 for a C_8LuPc_2 based organic thin film transistor (OTFT).

The annealed structure shows two different mechanisms of conduction (Figure 6.6b). Region I: Ohmic conduction is dominant in the low voltage range of $0V \leq V_a \leq 30V$. The slope of the linear plot for annealed device in the Figure 6.6b was found to be 1.01. Slightly higher Ohmic conductivity of 79.51 Scm^{-1} was estimated for the discotic LC film. The conductivities agree well with the non-peripherally octylthio-substituted lutetium (III) bisphthalocyanine published by Atilla et al., 2009. As reported by

Chaure et al., 2010, annealing removes the defects from the surface of the film and increases mobility of the charge carrier to 8×10^{-3} $cm^2V^{-1}s^{-1}$. Therefore, the $n_0$value of the LC phase was estimated as 6.21×10^{16} cm^{-3}.

Region II: In the higher voltage range of 30V≤V_a≤100V, the current increases with an exponential nature in the figure 6.6a. The slope of the log$I$ - logV_a plot with value of 1.3 in Figure 6.6b is steeper than that in the Ohmic region 1.01. This can be associated with Child's law of $I \propto V_a^n$ (where n>1) which takes place in the materials containing traps and defect states (Phan et al., 2007).

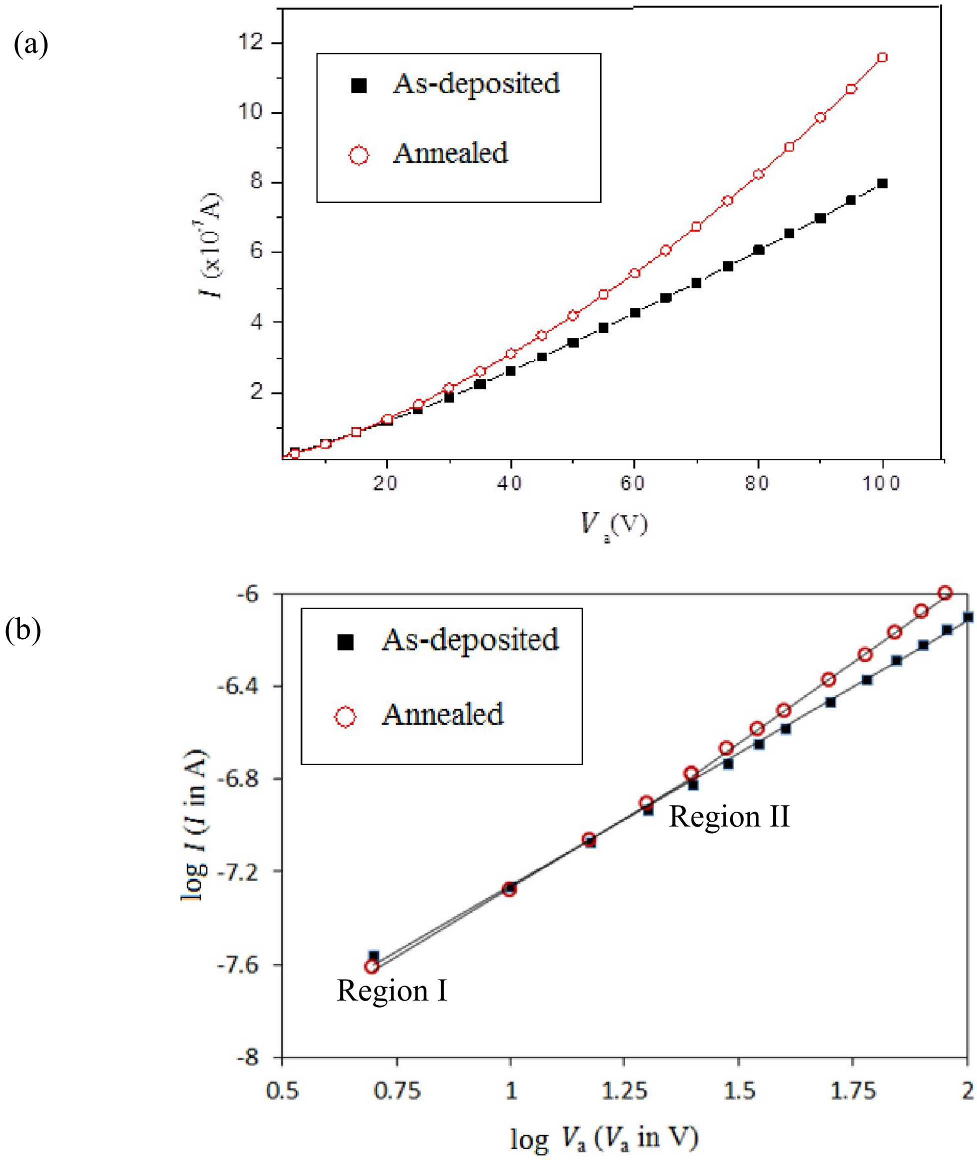

Figure 6.6: **(a) Current–Voltage characteristics of C_8LuPc_2 at room temperature 302K, (b) logarithm of current and voltage plot for as-deposited and annealed film**

From the Ohmic region of conduction it is evident that the number of trap free charge carriers was decreased on annealing by one order of magnitude. As the annealing of the films were carried out in an oxygen (O_2) environment, it is possible that the adsorbed O_2 ions in the grain boundary act as defect states and produce a columbic potential barrier (Φ_t) and trap the charge. Under high applied potential, the barrier is reduced by a factor $B_{PF}\sqrt{V_a}$ as explained in Section 4.3 of Chapter 4 (B_{PF}=Poole-Frenkel lowering coefficient). The decreasing gap between the conduction or valence bands under electric field is responsible for the increased conduction from 30 V to 100 V by detrapping the charge carriers. Hence, the conduction can be predicted as Poole-Frenkel dominated bulk conduction (Orwa et al., 2005). Similar conduction mechanism at high voltage has been explained for lead phthalocyanine (PbPc) with aluminium electrodes by Gould and Safai, 2000. Figure 6.7 is the plot of $\ln\left(\frac{I}{V_a}\right)$versus square root of voltage from the same data as in Figure 6.6a in the voltage range $30\text{V} \leq V_a \leq 100\text{V}$. The data fit well with straight lines validating the following Equation 6.2 derived from Equation 4.5 in Page 58, Chapter 4 of bulk-limited Poole-Frenkel effect.

$$\ln\left(\frac{I}{V_a}\right) = \ln\frac{A}{L} + \frac{B_{PF}V_a^{1/2} - \Phi_t}{k_B T} \qquad (6.2)$$

where, k_B is the Boltzmann constant, T is the temperature.

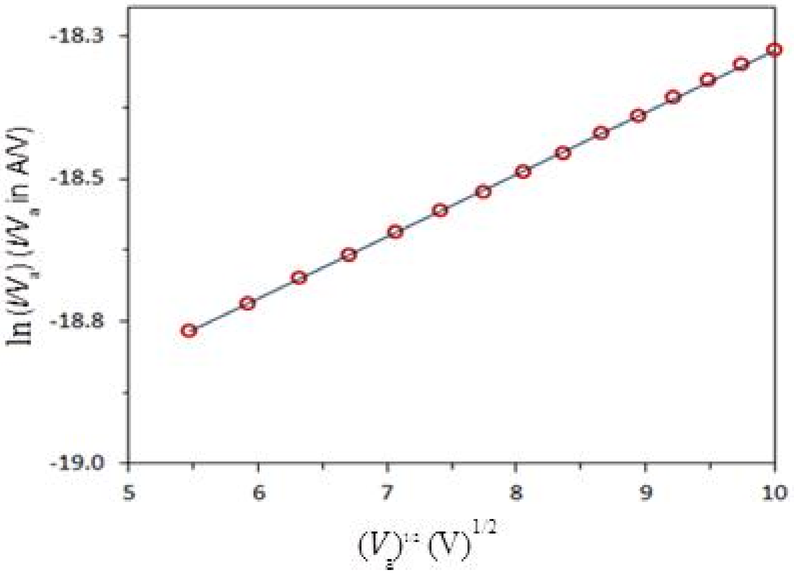

Figure 6.7: **Plot of ln (I/V_a) versus square root of voltage in the range of $30\text{V} \leq V_a \leq 100\text{V}$ for annealed film of C_8LuPc_2**

In order to estimate the activation energy (ΔE) for conductions, the measurements were repeated for both as-deposited and annealed films at different temperatures from 302K-360 K. The I-(V_a) characteristics in logarithmic scale for the as-deposited films are shown in figure 6.8a. As expected for organic semiconductors, the conductivity was found to be increased because the trapped charge carriers are released on thermal excitation and contribute to the charge transport. The conductivities at different temperatures were estimated and listed in Table 6.3.

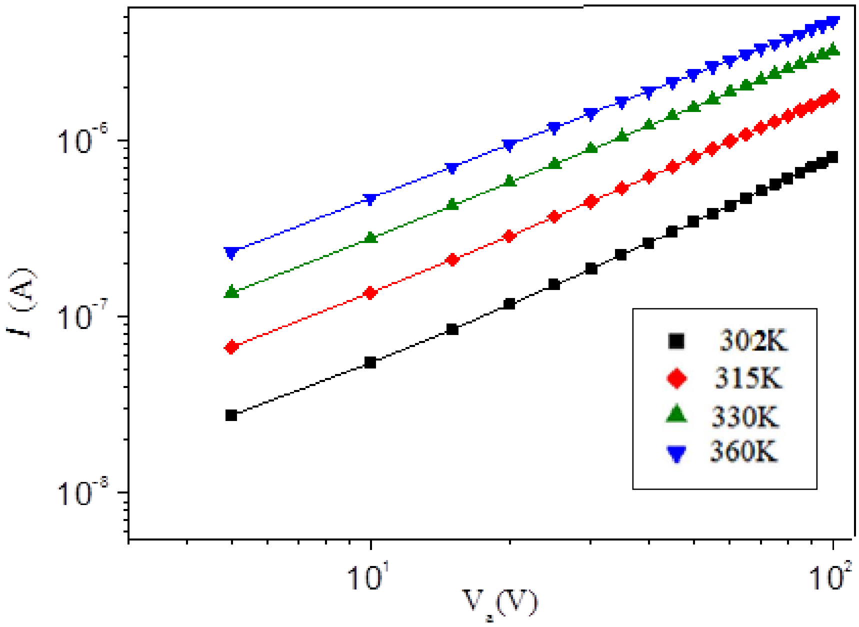

Figure 6.8: **Plot of current-voltage characteristics at different temperatures for as-deposited film from 302K to 360K**

The logarithm of current is inversely proportional to the temperature according to the Arrhenius Equation as follows (from Equation 4.9 in Page 61, Chapter 4).

$$\ln I = \ln I_0' - \frac{\Delta E}{k_B T} \qquad (6.3)$$

where I'_0 is the pre-exponential factor. Therefore, the plot of ln I versus $1/T$ in the Ohmic region gives a straight line and the slope was estimated as 3329 (Figure 6.9). The activation energy required for the electronic transitions between band edges was calculated from the slope of the value as 0.29 ±0.03 eV in the temperature range of 302-360K.

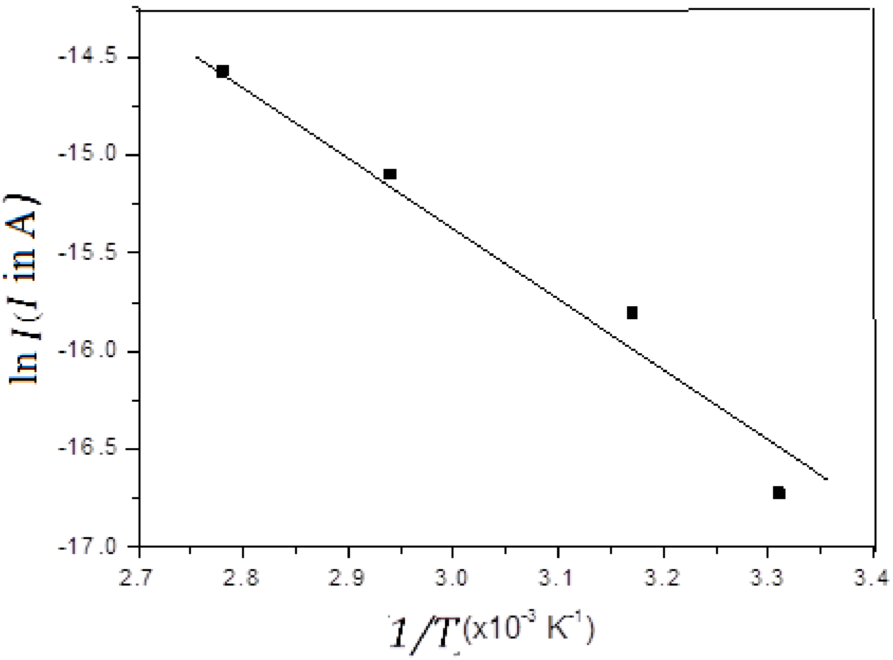

Figure 6.9: Logarithm of Current versus inverse of temperature plot at 10 V for as-deposited film of C_8LuPc_2

The influence of post-deposition annealing on DC electrical properties of C_8LuPc_2 was studied by monitoring the I-(V_a) characteristics in the same range of temperatures as the non-annealed one and reproduced as a logarithmic plot of I-(V_a) in Figure 6.10. Two different slopes can be noticed in all of the four plots incating Ohmic conduction following by Poole-Frenkel effect in high voltage. However, a decrese in the gradient of slopes from can be noticed in the Figure 6.10 from 1.3 at 302K to 1.1 at 360K. This is due to fact that the higher thermal energy makes detrapping of charge carriers easier and conduction mechanism approaches towards Ohmic. The activation energy was estimated as 0.25±0.03 eV in the Ohmic region from the logarithm of current versus temperature inverse plot (Figure 6.10b). Table 6.3 shows the activation energies of the C_8LuPc_2 thin films before and after annealing in the temperature range of 302K-360K.

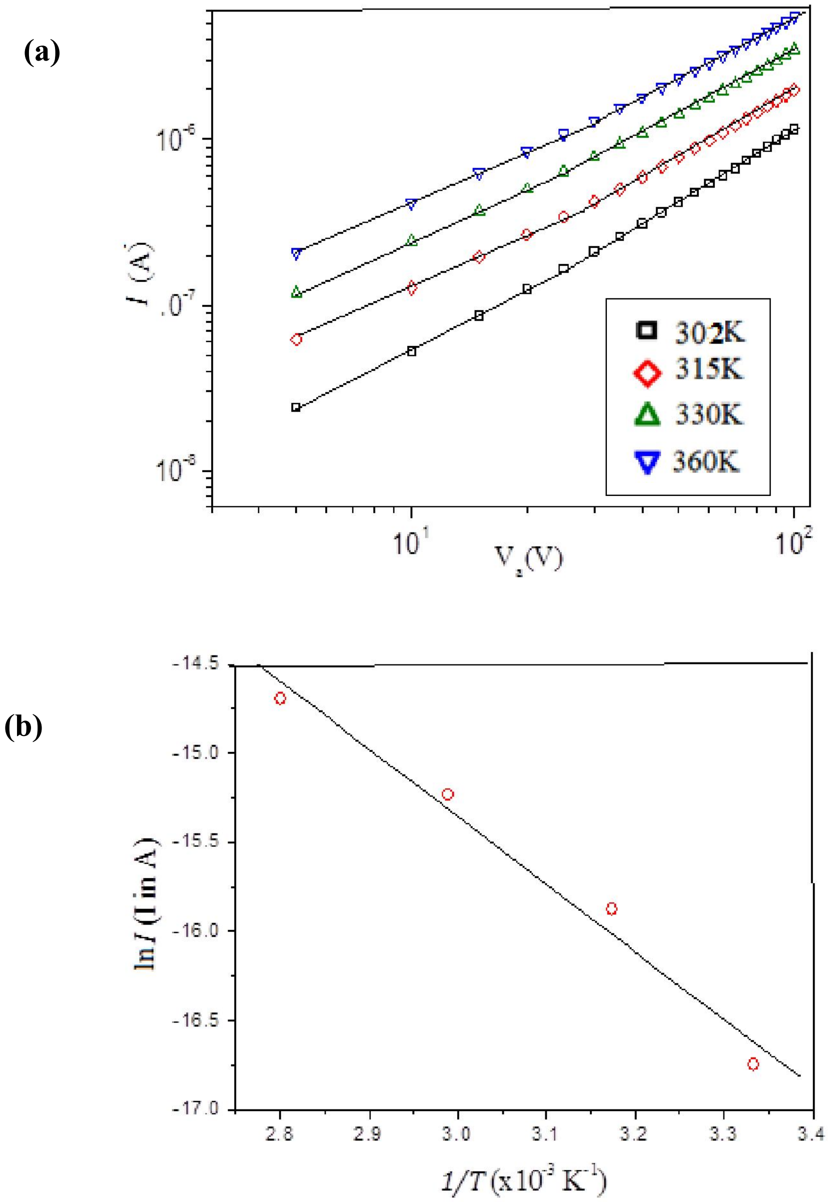

Figure 6.10: (a) Current–Voltage characteristics at different temperature in the range of temperature 302K-360K, (b) logarithm of current versus temperature inverse plot for annealed film C_8LuPc_2

To determine the trap energy levels in the annealed film, the logarithm of current versus temperature inverse was plotted in the Poole-Frenkel region. A set of straight lines were produced which has been displayed in Figure 6.11a. It is possible to correlate the slopes of the lines d ln*I*/d(1/*T*) with the activation energy of the molecules from Arrhenius equation. Hence, combining Equation 6.2 and 6.3, the following relationship can be established as,

$$\frac{\mathrm{d}\ln I}{\mathrm{d}(\frac{1}{T})} = \Delta E = B_{PF}V_{\mathrm{a}}^{1/2} - \Phi_t \qquad (6.4)$$

The activation energies for conduction were found to be decreasing with increasing voltage in Figure 6.11b which agrees with the Equation 6.4. This is because with increasing the electric field the density of detrapped charge carriers increses which move to the conduction band. The barrier lowering coefficient (B_{PF}) of the value 8.42×10^{-3} eVV$^{-1/2}$ and 0.33 eV for the zero field potential barrier height coefficient was calculated from the activation energy against square root of voltage plot in Figure 6.11b.

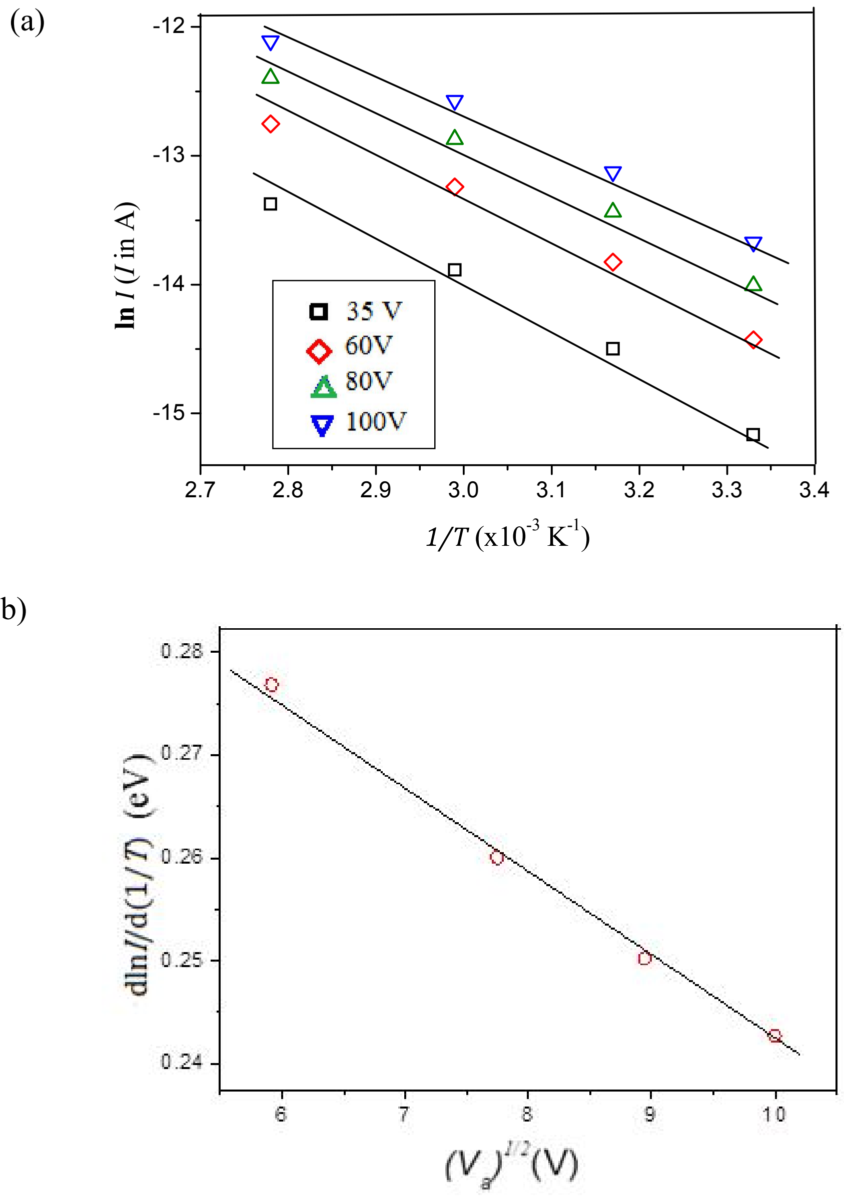

Figure 6.11: **(a) Logarithm of current versus temperature inverse plot at different voltages in region II for annealed thin film of C_8LuPc_2 at different temperature in the range of 302-360K. (b) Plot of d (ln *I*)/d(*1/T*) versus square root of voltage for annealed film**

The Poole-Frenkel coefficient (β_{PF}) per unit distance (L) of applied voltage V_a was calculated as 5.65×10^{-4} eVcm$^{1/2}$V$^{-1/2}$ from the relationship $\beta_{PF} = B_{PF}\sqrt{L}$, explained in Equation 4.5 in Page 58 of Chapter 4. This value agrees well with the theoretical value of 3.54×10^{-4} eVcm$^{1/2}$V$^{-1/2}$ using the Equation 4.4 as $\beta_{PF} = \sqrt{\frac{q^3}{\pi\varepsilon_0\varepsilon_r}}$ in page 58, Chapter 4. Comparable values of β_{PF} and Φ_t as C_8LuPc_2 have been reported by Daira et al., 2011; Azim-Araghi and Sahebi, 2014 for bulk-limited Poole-Frenkel conduction in thin film form. Table 6.4 displays the values of $B_{PF,}$ β_{PF} and Φ_t at room temperature. Till this date, there are no reports on thecharge transport mechanism of phthalocyanine planar structure in high electric field.

6.3.2 Bis[1,4,8,11,15,18,22,25-octakis(octyl)phthalocyaninato]gadolinium(III), C_8GdPc_2

The I–(V_a) characteristics of the C_8GdPc_2 on gold planar structure were carried out in the same manner as the Lu-derivative. On sweeping the voltage from 0 to 100 V, both of the as-deposited and annealed films exhibited non-linear characteristics in Figure 6.12a. The as-deposited film showed considerably different characteristics than the as-deposited Lu-derivative in the voltage region $30\text{V}\leq V_a\leq100\text{V}$. This may be correlated to factors like surface defects, impurity level at the edge of the conduction or the valence band (Donley et al., 2004). The annealed film of C_8GdPc_2 showed a sharp increase of current in the high voltage region. Two distinct slopes of trap-free Ohmic charge conduction in the range of $0\leq V_a\leq30$ V and Poole-Frenkel effect by field-assisted thermal detrapping of carriers in the range of $30\leq V_a\leq100$ V was noticed in the logarithmic I-(V_a) characteristics at room temperature (Figure 6.12b). The Ohmic conductivity and total trap free charge density (n_0) at room temperature was calculated with the 60 nm thick film from the region (I), as 0.40 μScm^{-1} and 1.66×10^{15} cm^{-3}, respectively. The mobility of the charge carriers were taken as 1.5×10^{-3} cm^{2}V^{-1}s^{-1} for the n_0 calculation, equivalent to the C_8LuPc_2 mentioned in Section 6.3.1. On annealing, the conductivity was found to be increased to 0.91 μScm^{-1}. On the other hand, the n_0 value was decreased to 7.03×10^{14} cm^{-3} for the annealed film with mobility 8×10^{-3} cm^{2}V^{-1}s^{-1}. The 3.5 times enhancement of the Ohmic conductivity in annealed film with respect to the as-deposited one can be attributed to the long-range staggered slipped stacking arrangements of the Pc monomers in the discotic LC film. However, the value of n_0 in LC phase went down by 5 times in comparison to the as-deposited one due to probable trapping of charge at the grain boundary in presence of O_2. It is obvious from the Figure 6.12b that the slope of the linear log$I$-logV_a plot for annealed films in region (II) is steeper (slope 2) than the as-deposited films(slope 1.5) indicating rate of increasing current per unit applied voltage is higher in the annealed film. The higher field lowering factor $B_{PF}\sqrt{V_a}$ in the annealed film may imply the release of more trapped charges (Orwa et al, 2005).

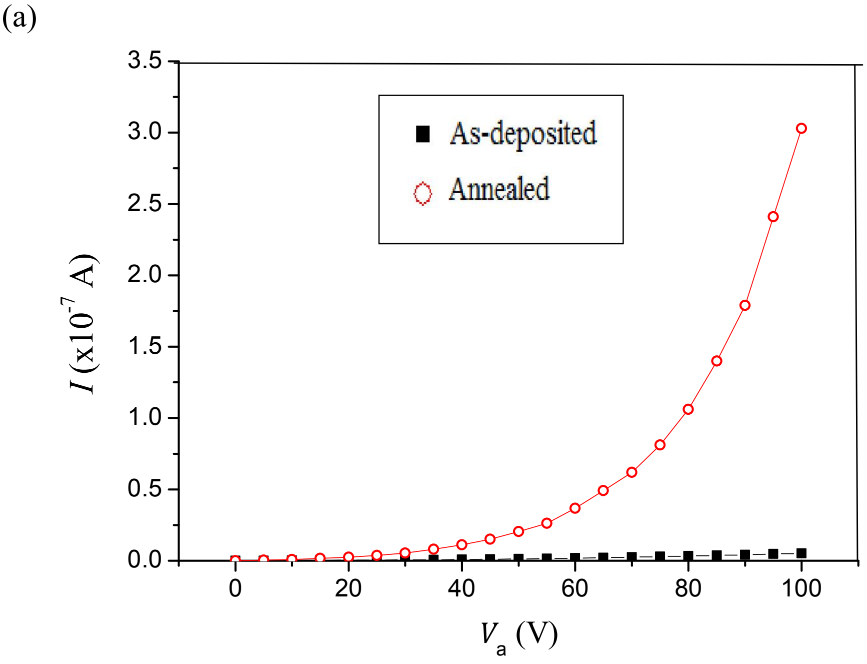

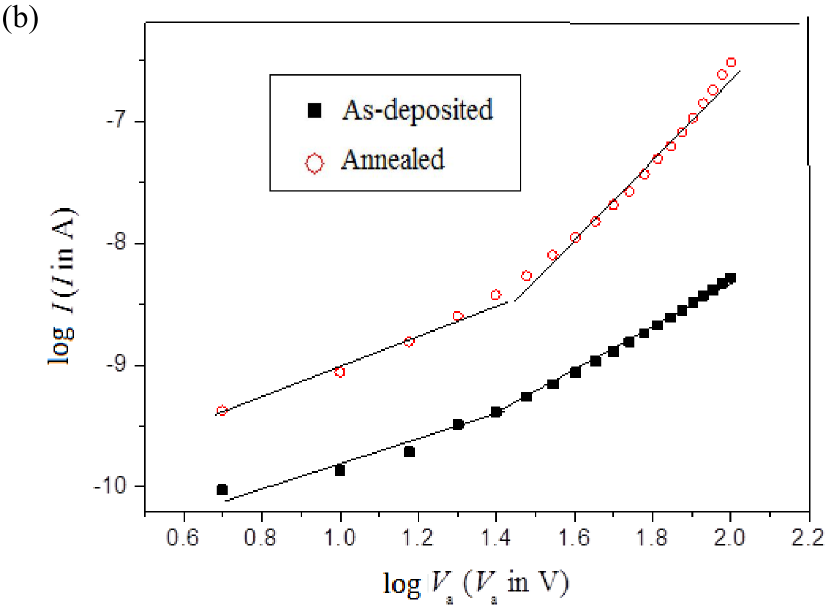

Figure6.12: (a) Current–Voltage characteristics, (b) logarithm of current and voltage plot for as-deposited and annealed film of C_8GdPc_2 at room temperature 300K

The ln (I/V_a) versus $\sqrt{V_a}$ was plotted in Figure 6.13 in the region II. The straight lines produced for both of as-deposited and annealed films further approve the bulk limited Poole-Frenkel charge conduction.

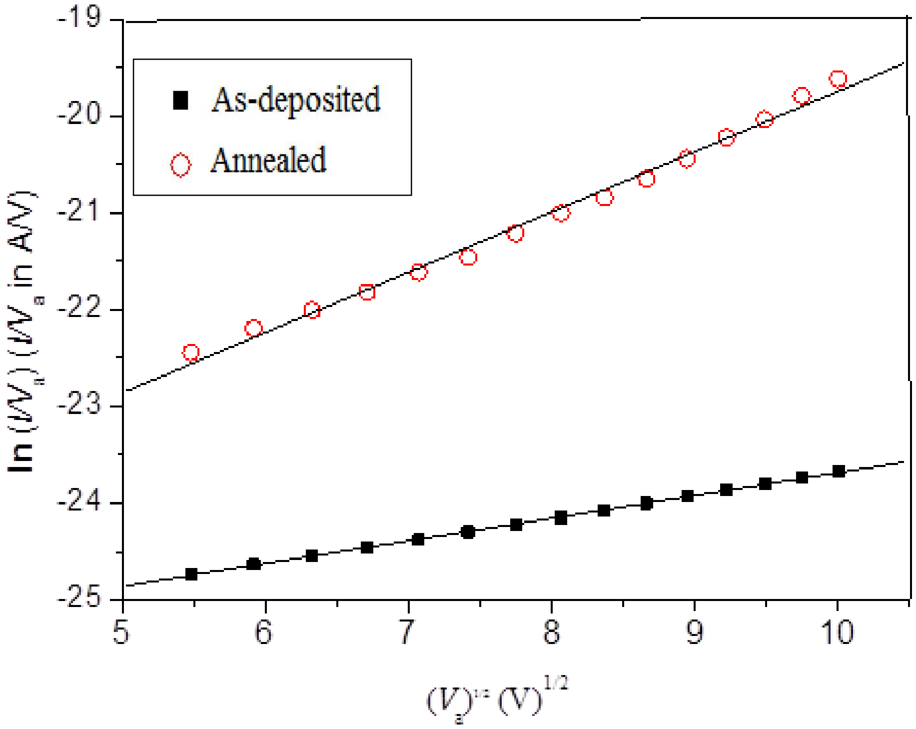

Figure 6.13: ln (I/V_a) versus square root of voltage in the voltage range of 30V≤V_a≤100 V for as-deposited and annealed films of C_8GdPc_2

Figure 6.14 displays the increasing current with temperature rise in the logarithmic I–(V_a) characteristics of C_8GdPc_2 as-deposited and annealed films in the range of temperature 302K-360K. The conductivity at 360 K was estimated as 51.50 μScm^{-1} which is three orders of magnitude higher than the room temperature conductivity. Similarly, the conductivity of the annealed thin film was measured as the value of 89.11 μScm^{-1} at 360K. Table 6.3 shows the conductivity values of the as-deposited and annealed film of C_8GdPc_2 at different temperatures.

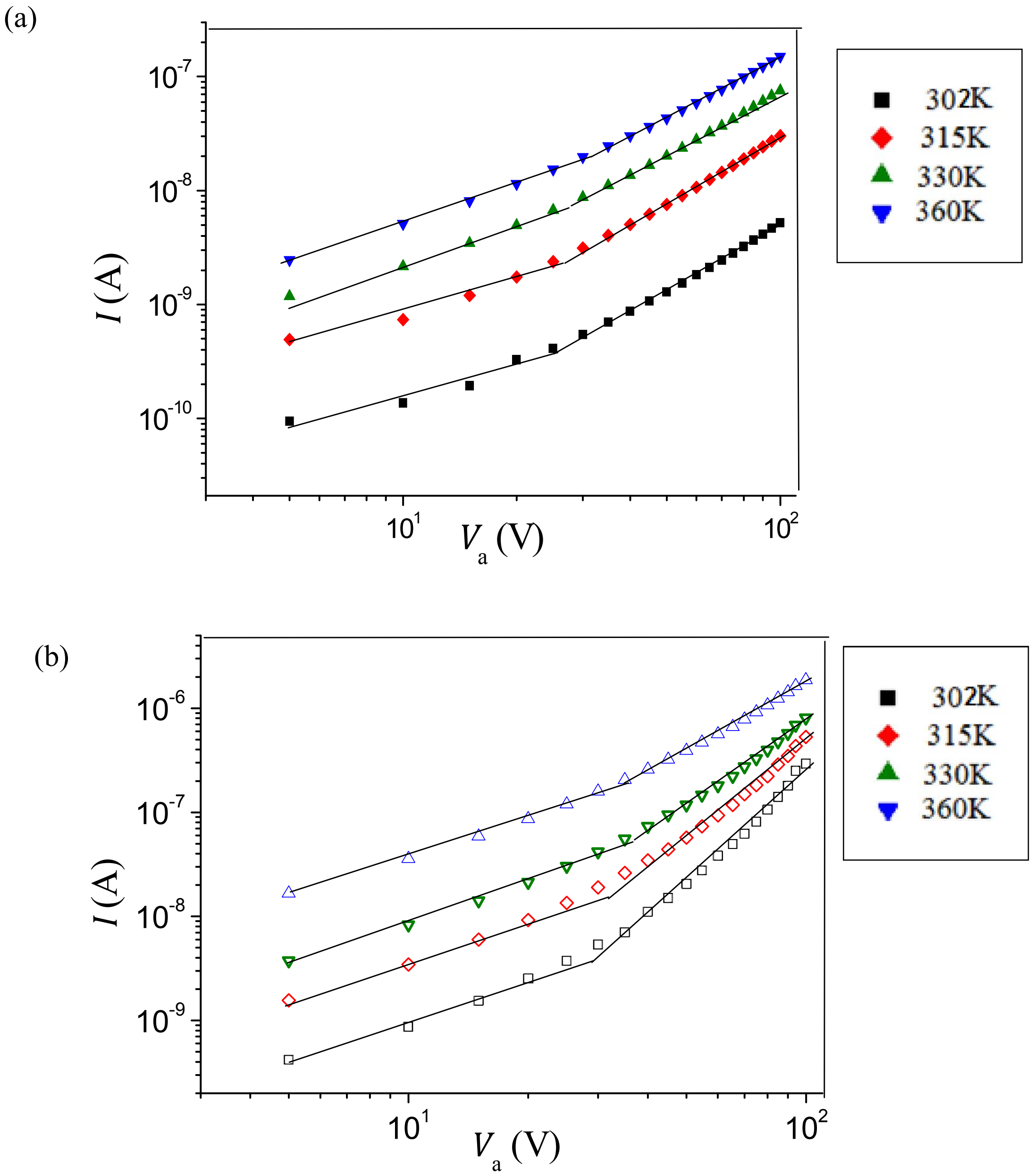

Figure 6.14: Current versus voltage characteristics in the range of temperature 302K-360K for (a) as-deposited and (b) annealed film of C_8GdPc_2

In order to calculate the activation energy in the trap-free Ohmic region, logarithm of current at 10V and inverse temperature for as-deposited and annealed films were plotted in Figure 6.15. Two straight lines with slopes of 9054 and 7884 gave the activation energy of 0.78±0.03 eV and 0.68±0.03 eV of as-deposited and annealed films, respectively. The standard error (SE) of the value 0.03 was calculated from the formula $SE = \frac{1-r^2}{\sqrt{(n-1)}}$ where, r is the correlation coefficient, n is the number of points (Gorsuch and Lehmann, 2010). The π-π stacking interactions between the well-ordered monomers in the discotic liquid crystals can be corresponded to the lowering of the activation energy required for electrical conduction. Hence, the self-assembling properties of the phthalocyanines in the LC phase is promising for designing advance organic thin-film electronics such as memory diodes, organic field-effect transistors, and organic photovoltaics (Chaure et al., 2009; Chaure et al., 2010; Lu et al., 2012).

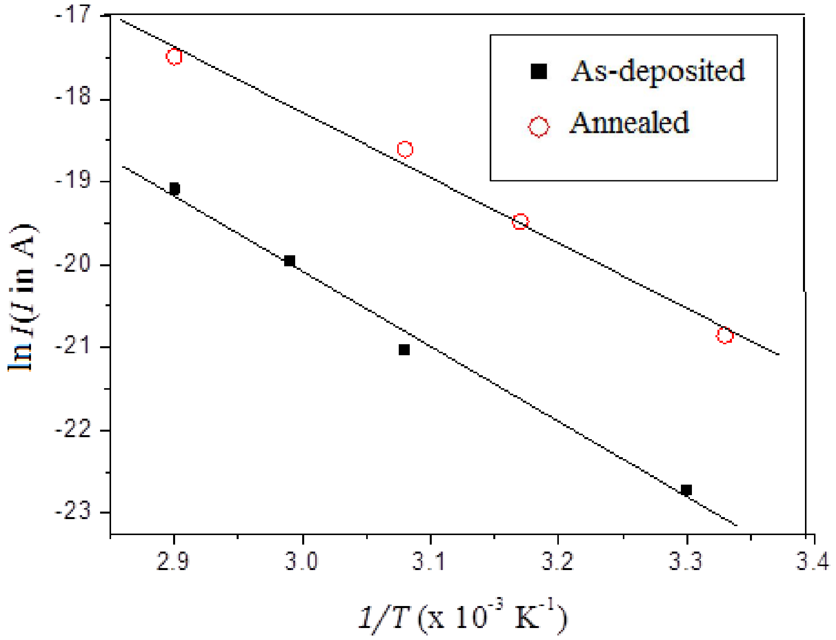

Figure 6.15: Logarithm of current at 10V versus inverse of temperature plot for as-deposited and annealed C_8GdPc_2 film

In the Poole-Frenkel region, slopes of ln *I* versus 1/*T* plots at different voltage were employed to evaluate the activation energies in both as-deposited and annealed films (Figure 6.16a). As can be seen from the Figure 6.16b, the activation energies decrease with the square root of voltage in both cases as the higher electric field de-traps the charge carriers. The intercept of the plots or the zero field columbic barriers was found to be increased from 0.82 eV to 0.99 eV on annealing due to the traps incorporated in the grain boundary by O_2 (Orwa et al., 2005). However, the slopes of the plots yielded the coulombic field lowering coefficients (B_{PF}) in an as-deposited film as 9.95×10^{-3} eVV$^{-1/2}$ and as 6.43×10^{-2} eVV$^{-1/2}$ in the annealed film. The corresponding β_{PF} values were estimated as 6.74×10^{-4} eVV$^{-1/2}$cm$^{1/2}$ and 43.12×10^{-4} eVV$^{1/2}$cm$^{-1/2}$. The 6.5 times increase in β_{PF} in the well-ordered LC phase explains the higher current in the annealed film of C_8GdPc_2 in comparison to the as-deposited one. The parameters regarding the electrical characteristics have been included in Table 6.3.

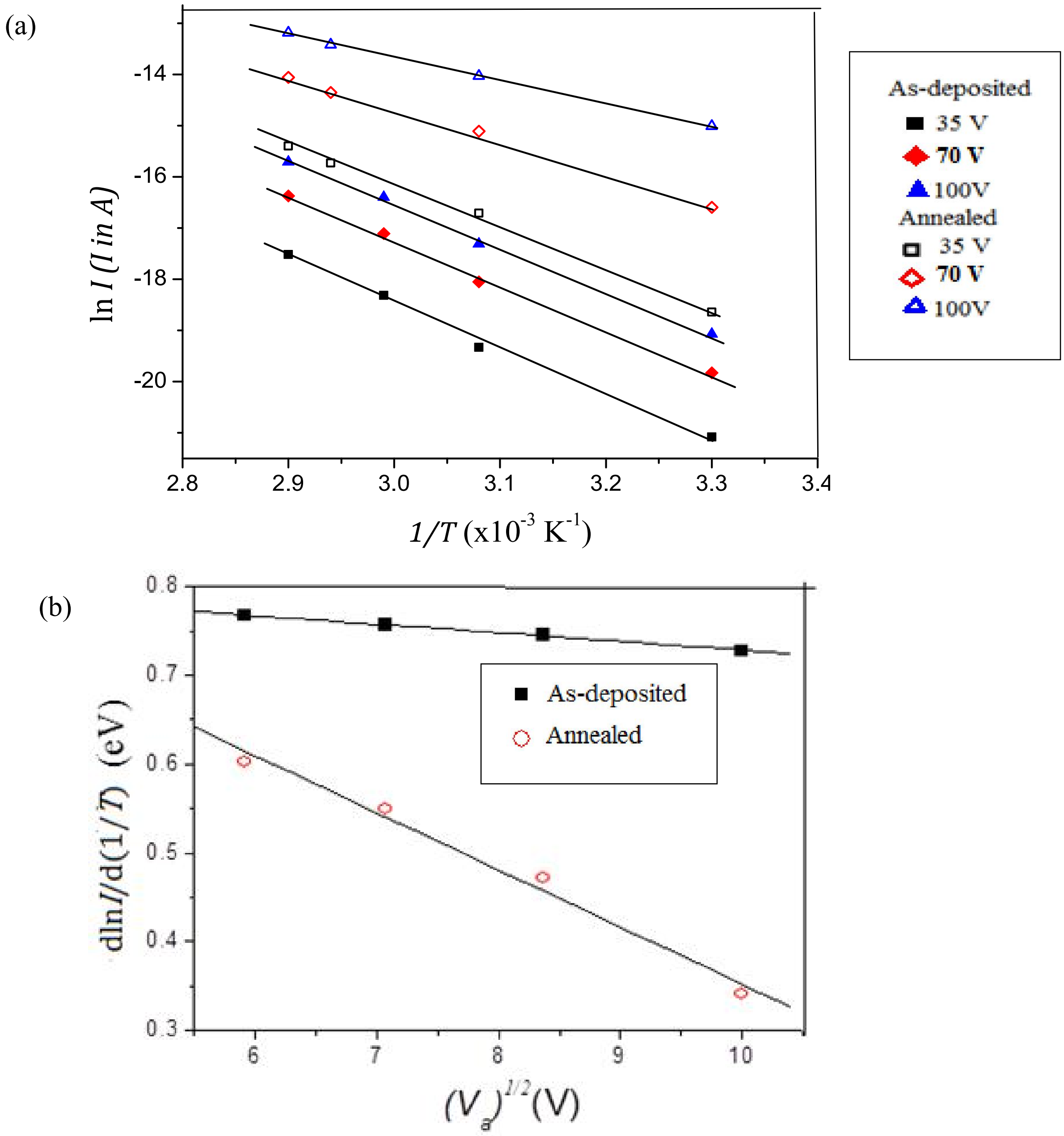

Figure 6.16: **(a) Logarithm of current versus temperature inverse plot at different voltages in the range of temperature 302K-360K, (b) plot of dln*I*/d(1/*T*) versus square root of voltage for as-deposited and annealed thin film of C_8GdPc_2**

6.3.3 Bis[1,4,8,11,15,18,22,25-ctakis(hexyl)phthalocyaninato]gadolinium(III), C_6GdPc_2

The I-(V_a) curves, as presented in Figure 6.17a and b for as-deposited and annealed thin films of C_6GdPc_2 also exhibited Ohmic charactersistics in the range 0-30 V with slope of nearly 1 in region I in $\log I$-$\log V_a$ plot. Region II, in the range of $30V \leq V_a \leq 100V$ was dominated by Poole-Frenkel field lowering mechanism with slopes of 1.59 and 2.04, for as-deposited and annealed films, respectively. The Ohmic characteristics were analysed and the conductivity and the trap-free charge density were estimated as 42.31 μScm^{-1} and 1.76×10^{17} cm$^{-3,}$ respectively from Figure 6.16b assuming the mobility of charge carrier as 1.50 ×10^{-3} cm^{2}V^{-1}s^{-1}. The thickness of the film was taken as 80 nm for the conductivity calculation. When the film was annealed, the current was decreased by about one order of magnitude in comparison to the as-deposited sample. The conductivity and trap density was calculated as 1.5 μScm^{-1} and 6.25×10^{15} cm^{-3} for the annealed film with mobility 8 ×10^{-3}cm^{2}V^{-1}s^{-1}.

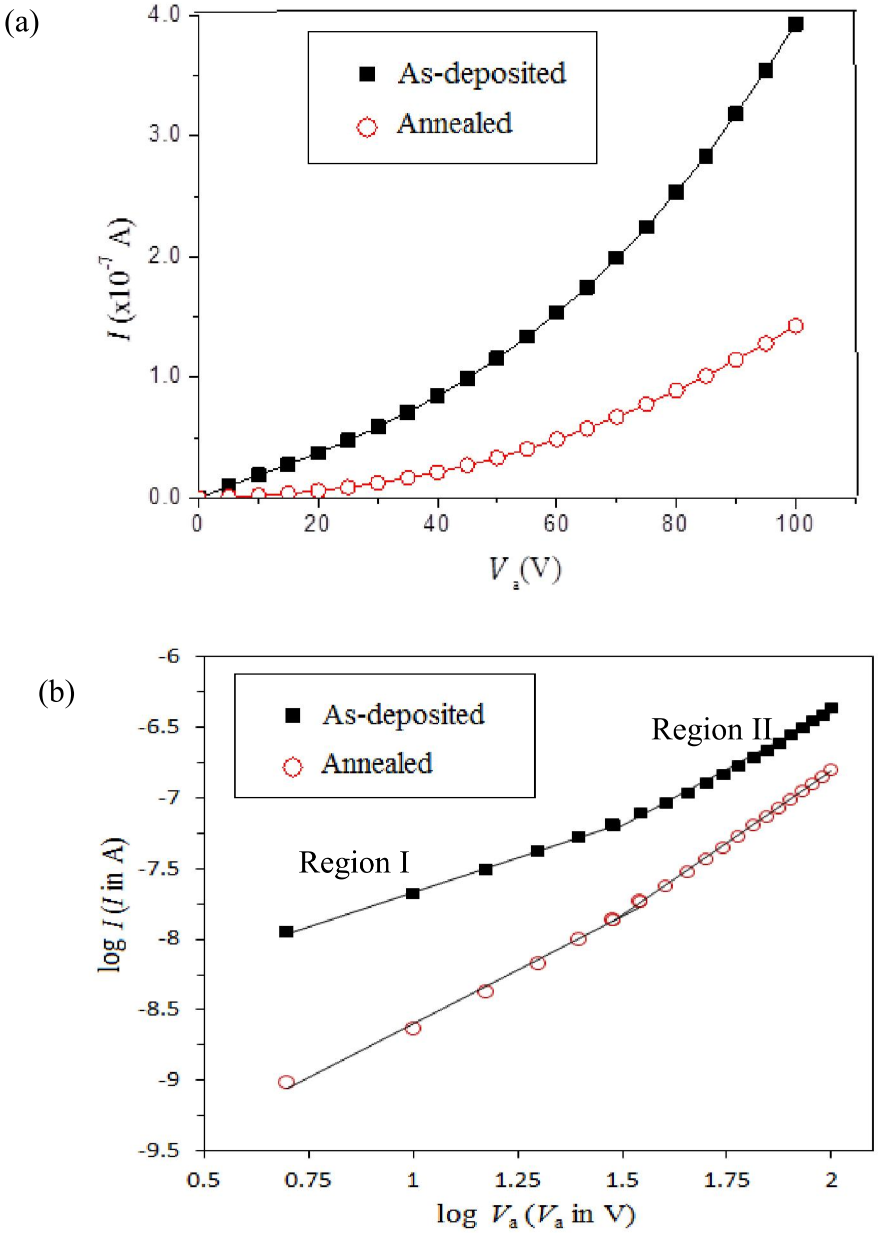

Figure 6.17: **(a) Current–Voltage characteristics at room temperature (302K), (b) logarithm of current and voltage plot for as-deposited and annealed films of C_6GdPc_2 at room temperature**

It can be noticed from Table 6.3 that the decrease of conductivity on annealing in the case of C_6GdPc_2 film is in contradiction with respect to the increasing conductivity for the other two octyl substituted compounds. The combined interpretation of UV–Vis spectra and the electrical characteristics suggest the formation of H-aggregated or face-to-face arrangements of the Pc units in the LC phase. The stacking of Pc units is expected to enhance the conductivity of the material. But the different directional anisotropic property of the aggregated molecules as explained in Section 2.5 in Chapter 2 may be the reason for the decrease of film conductivity on annealing.

Figure 6.18 shows the Poole-Frenkel dominated conduction in the region II from above Figure 6.17. The higher slopes in the as-deposited compound indicated higher field-assisted thermal detrapping of carriers due to lowering of the gap between conduction and trap level.

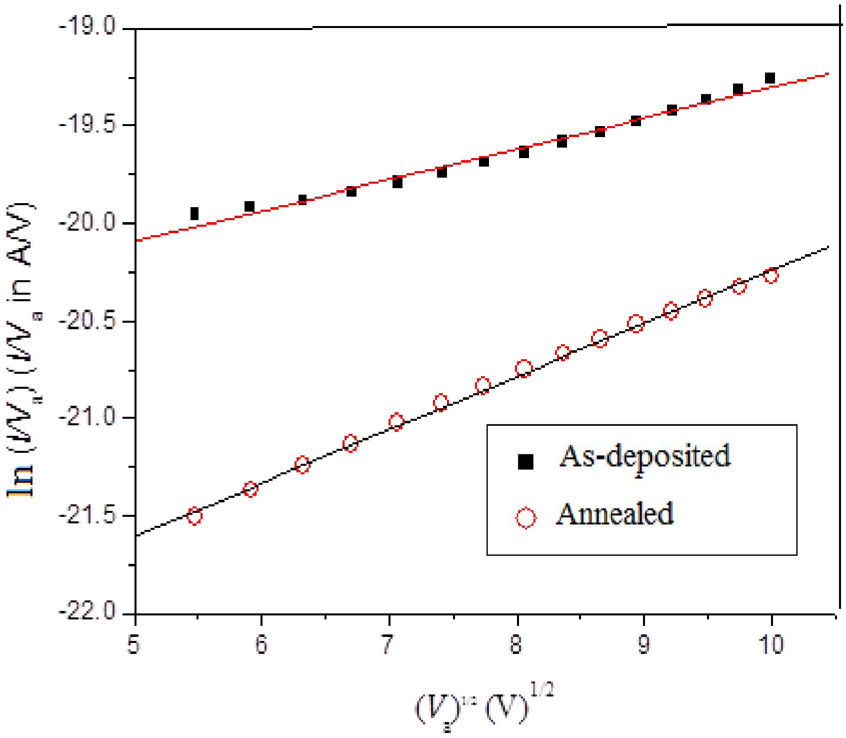

Figure 6.18: ln (I/V_a) versus square root of voltage in the range of $30V \leq V_a \leq 100$ V for as-deposited and annealed films of C_8GdPc_2

The current voltage characteristics in Figure 6.19 are the as-deposited and annealed films of C_6GdPc_2. The conductivities were calculated and listed in Table 6.3.

Comparing the values shows the anealed film show lower current than the as-deposited one at the same temperature.

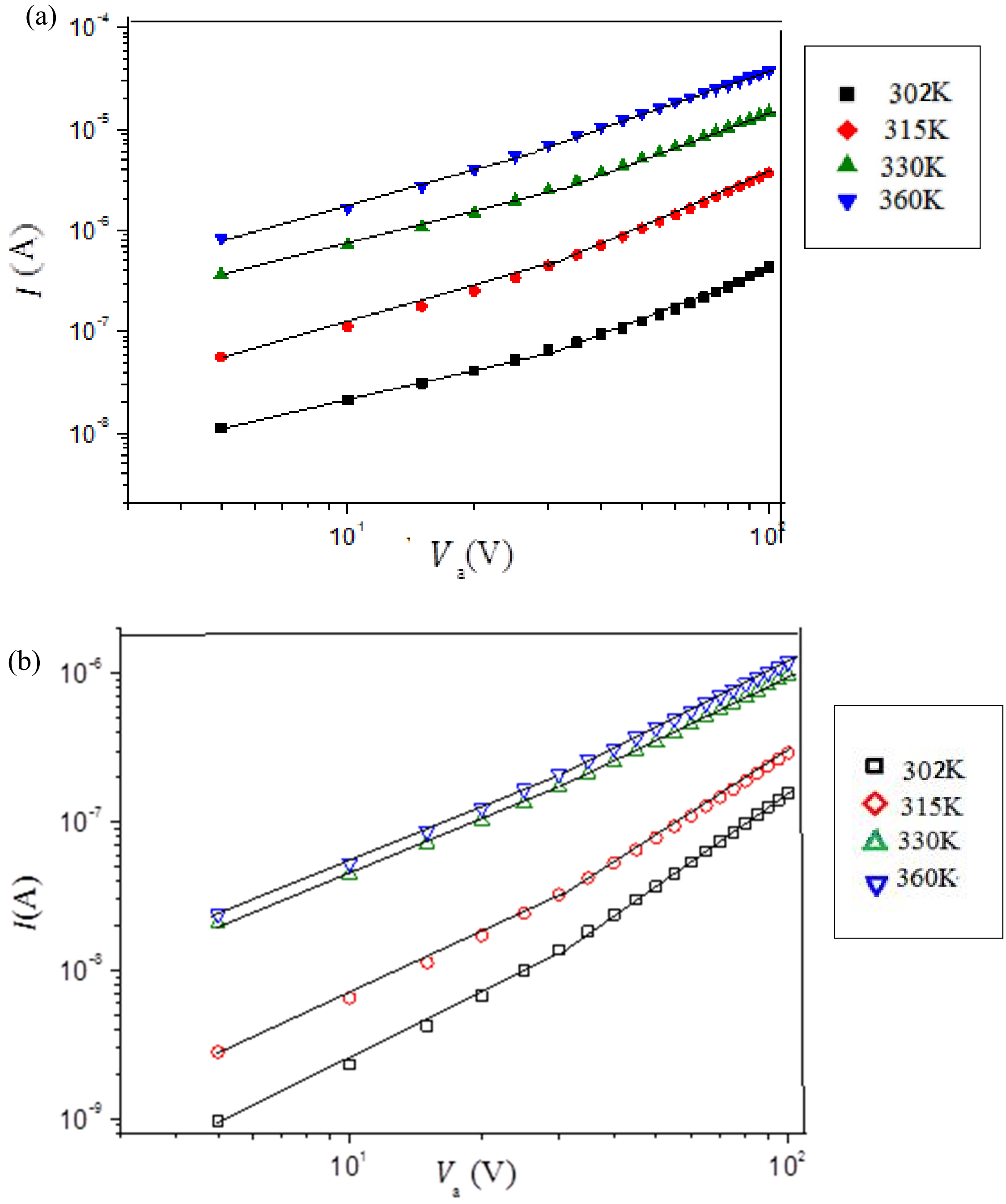

Figure 6.19: **Current-voltage characteristics for C_6GdPc_2 at different temperature in the range of 302K-360K for (a) as-deposited and (b) annealed film**

The activation energy required for the trap free charge flow through the band edge was found to increase from the 0.78±0.03 eV in the as-deposited film to 0.88±0.03 eV in the annealed phase recognized as responsible for lower the conductivity value (Figure 6.20).

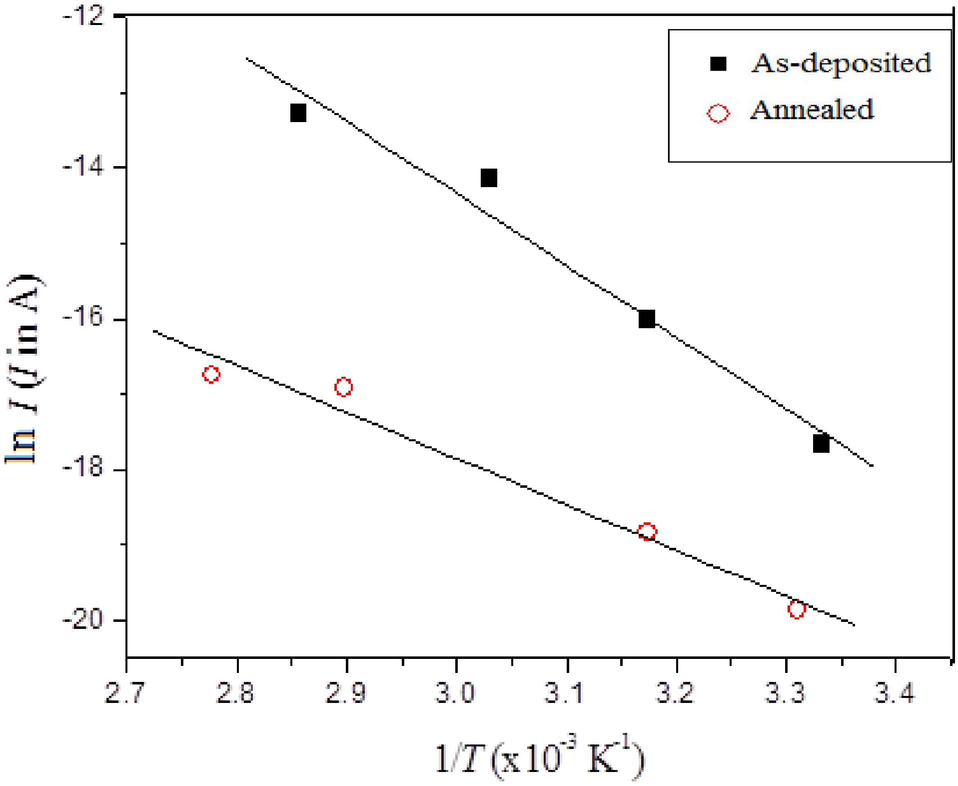

Figure 6.20: **(a) Conductivity versustemperature plot, (b) logarithm of current at 10 V versus temperature inverse plot for as-deposited and annealed films of C_6GdPc_2**

The intercept and slope of the Figure 6.21b provided the values of B_{PF} and Φ_t for as-deposited and annealed films which are tabled in 6.3. As expected, the barrier potential increased to 0.88 eV in the annealed film from 0.63 eV of the as-deposited one. The values of B_{PF} were calculated as 2.73×10^{-2} $eVV^{-1/2}$ for the as-deposited and 1.24×10^{-3} $eVV^{-1/2}$for the annealed film. The β_{PF} values were estimated to be 18.25×10^{-4} $eVV^{-1/2}$ $m^{1/2}$and 8.35×10^{-4} $eVV^{-1/2}$, consistent with the theoretical values calculated from Equation 4.4 in page 58. Table 6.4 displays all the parameters related to the Poole-Frenkel effect in the range of voltage $30V\leq Va\leq100V$.

(a)

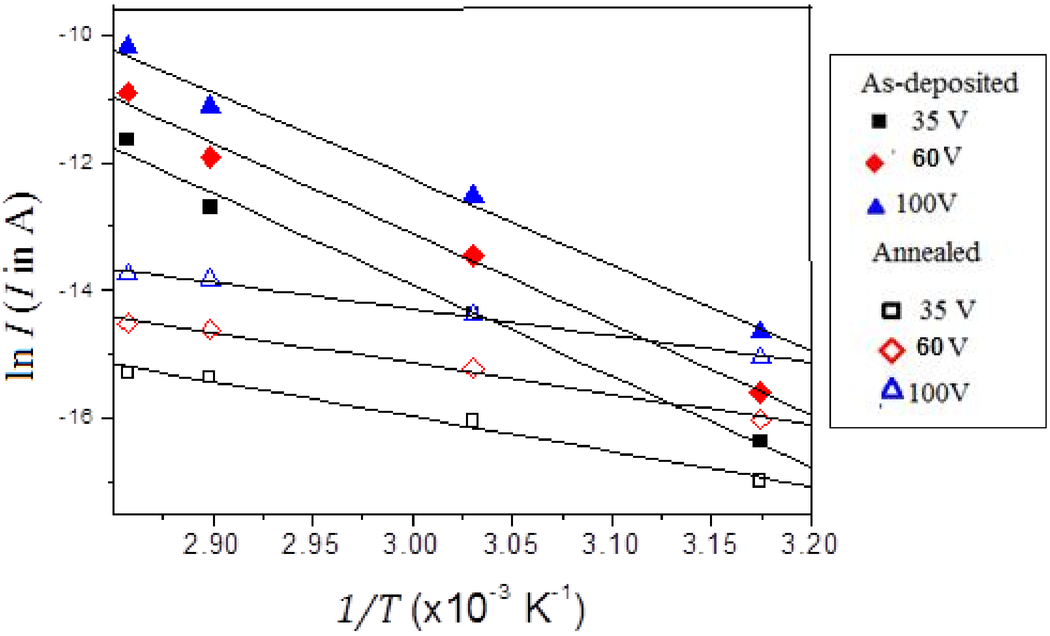

(b)

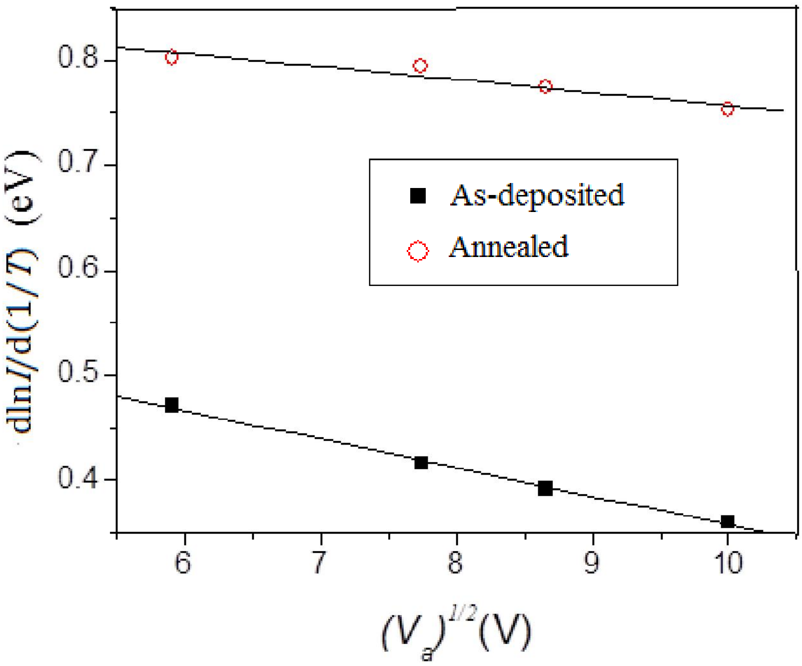

Figure 6.21: **(a) Logarithm of current versus temperature inverse at different voltages at different temperature in the range of temperature 302K-360K, (b) d(ln*I*)/d(1/T) versus squre root of voltage plot for as-deposited and annealed films of C_6GdPc_2**

Table 6.3: Comparative study of the electrical characteristics of the three compounds C_8LuPc_2, C_8GdPc_2, C_6GdPc_2 in the voltage range $0V \leq V_a \leq 30$ V

Compound	Thickness (±15 nm)	Ohmic conduction									
		As-deposited					Annealed				
		σ_x ($\times 10^{-5}$ Scm^{-1})				ΔE (eV) (±0.03)	σ_x ($\times 10^{-5}$ Scm^{-1})				ΔE (eV) (±0.03)
		302 K	315K	330K	360K		302 K	315K	330K	360K	
C_8LuPc_2	74	6.75	21.42	42.71	76.46	0.29	7.95	21.6	48.01	91.46	0.27
C_8GdPc_2	60	0.04	0.05	0.85	8.91	0.78	0.09	0.11	0.98	5.15	0.68
C_6GdPc_2	80	4.23	17.4	51.65	86.51	0.56	0.15	0.53	5.4	5.98	0.88

Table 6.4: Comparative study of the electrical characteristics of the three compounds C_8LuPc_2, C_8GdPc_2, C_6GdPc_2 at room temperature in voltage range $30V \leq V_a \leq 100$ V (302K)

Compound	Thickness (±15 nm)	Poole-Frenkel Conduction					
		As- deposited			Annealed		
		B_{PF} ($\times 10^{-3}$ $eVV^{-1/2}$)	β_{PF} ($\times 10^{-4}$ $eVV^{-1/2}cm^{1/2}$)	Φ_t (eV)	B_{PF} ($\times 10^{-3}$ $eVV^{-1/2}$)	β_{PF} ($\times 10^{-4}$ $eVV^{-1/2}cm^{1/2}$)	Φ_t (eV)
C_8LuPc_2	74	-----	----	-----	8.42	5.65	0.33
C_8GdPc_2	60	9.95	6.74	0.82	64.30	43.12	0.99
C_6GdPc_2	80	27.22	18.25	0.63	12.4	8.35	0.88

6.4 Chapter summary

Characterisations of newly synthesised liquid crystalline C_8GdPc_2, C_8LuPc_2, and C_6GdPc_2 were accomplished on the basis of UV-Vis, Raman spectroscopy, and electrical methods. The comparatively low energy optical absorption of the solution phase hexyl and octyl substituted gadolinium phthalocyanines derivatives compared to the octyl substituted Lu-derivative have revealed that the larger ionic radius of the central metal ion leads to a weaker π–π interaction. The alignments of the side chains were also found to have an important role in the crystal packing of the compounds. Hence, the different direction of splitting with respect to the monomeric solution phase spectra was interpreted in terms of the different directional anisotropic property of the aggregated molecules.

Similar to the electronic transitions, the stretching and bending vibrational frequencies of pyrrole, isoindole, and metal-nitrogen bonds were controlled by the size of the central metal ion. However, the substitution chain length does not have any role in the Pc ring vibrations. This interpretation of weaker π–π interaction between the Pc rings with decreasing metal ion size using optical and Raman spectroscopywas further supported by the DC conductivities of the phthalocyanines. The in-plane conductivity value of the C_8LuPc_2, was found to be two orders of magnitude higher than the larger in size Gd-derivative with same chain length substituents. In fact, being the smallest rare-earth atom, lutetium contained compounds show assembly of highest carrier density of the material from its homologues. Consequently the intrinsic conductivities of Lu-compounds are highest among the rare earth. It may be possible that the long-chain substitution inhibits the charge flow inside the aromatic core of the Pcs. The two order of magnitude higher value of hexyl substituted Gd-derivative with respect to the octyl one can be related to this circumstance. The annealing promoted the alignment of the Pc units in more organized way influencing the optical and electrical properties of the films. Increase of Ohmic conductivity was noticed in case of octyl substituted lutetium and gadolinium phthalocyanines. A 3.5 times decrease of Ohmic conductivity in the annealed film in comparison to the as-deposited one was believed to be due to directionalanisotropy from preferential charge flow across the stacks. During annealing in the air traps were incorporated near the conduction band edge caused lowering the number charge carriers. The detrapping of the carriers was found to have occurred at high electric field giving rise to the Poole-Frenkel type of conduction.

Chapter 7 Biosensing Applications of Bisphalocyanines

The results of *in situ* kinetic optical absorption measurements of the interactions between octyl substituted lutetium/gadolinium bisphthalocyanines with the biological cofactors at varying concentrations are reported in this chapter. The methods were optimised with C_8LuPc_2. The similar methods were adopted for biosensing using the octyl substituted gadolinium derivative at the lowest concentration of 0.05 mM**.** Cofactors such as nicotinamide adenine dinucleotide hydrogen (NADH) and vitamin C are catalytic agents for many important biological activities in the human body. During mitochrondrial respiration, the electron transfer takes place through the NADH producing sufficient adenosine triphosphate (ATP) enzymes for cellular energy supply. The concentration of NADH varies in different parts of the body depending on the energy requirements. For example, heart cells have 90 μg/g; brain and muscle cells contain 50 μg/g tissues; liver cells contain 40 μg/g and red blood cells contain 3 μg/g tissues in human body (Lehninger, 1975; Albert et. al., 1994). This is equivalent to the $0.14\text{-}5.71\times10^{-3}$ mM in solution. Vitamin C promotes in development of bone structure and immune systems in the body. In scurvy patients the vitamin level in human serum is observed to be reduced up to 0.006 mM, compared to minimum 0.036 mM in healthy body (Raynaud-Simon et al. 2010).

7.1 Oxidation of thin films:

Preparation of the films for the biosensing of NADH and Vitamin C has been described in the experimental techniques chapter (Section 5.2).The oxidation was carried out by exposing the spun film of thickness ca. 100 nm to bromine vapour. Due to its chemichromic property, when the spun film of C_8LuPc_2 was exposed tithe oxidising gas Br_2 for 2-3 minutes, its colour changed from green to purple possibly owing to the change in oxidation state of the Pc ring. However, the colour change was not visible on oxidation of C_8GdPc_2 by the same method (Figure 4.1).

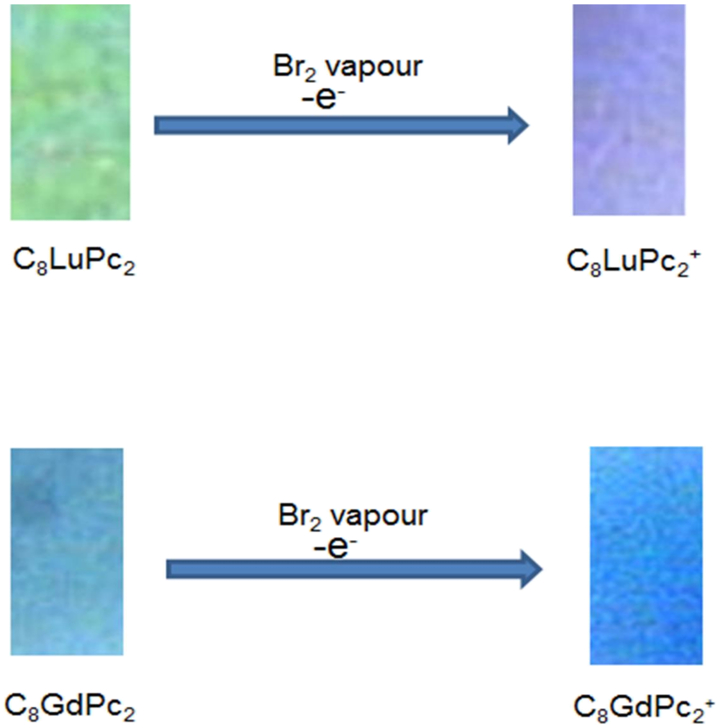

Figure 7.1: Microscopic images of C_8LuPc_2 and C_8GdPc_2 films before and after oxidation (5 times magnified)

The UV-Vis spectra of the C_8LuPc_2display bathochromic shift of Q band from 618 nm to 778 nm, 60 nm with respect to the neutral film (Figure 7.2 a, c). In case of $C_8GdPc_{2,}$ the shift was found to be 66 nm, from 628 nm to 796 nm (Figure 7.2 b, d). The broad bands of the oxidised films in the range 540-640 nm are indicative of radical cations, possibly owing to the presence of charge-transfer Br_2–C_8LuPc_2/C_8GdPc_2 adducts (Aroca et al.,1993). Thus, the fully oxidized films presumably balanced by Br_2 anions trapped in the film. The red shifts of the Q-band are due to the removal of the electrons in the antibonding HOMO resulting of relatively short Pc−Pc inter-ring distance. This result agrees well with the prediction of the density functional model for lanthanide bisphthalocyanines (Takamatsu and Ishikawa, 2007). The disappearance of the radical band at 473 nm is another indication of the oxidation of the film which has been explained in Section 6.1.1 of Chapter 6.

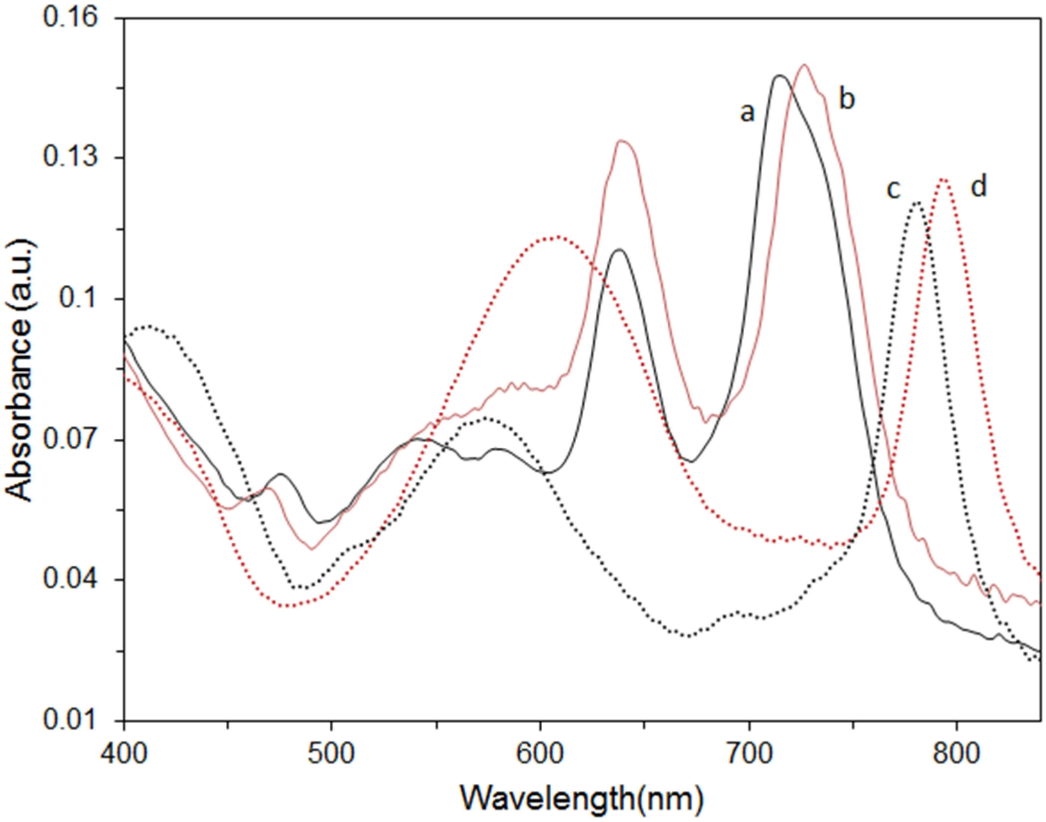

Figure 7.2: **Electronic absorption spectra of (a) C_8LuPc_2 neutral, (b) C_8GdPc_2 neutral, (c) Br_2-oxidized film of C_8LuPc_2, and (d) Br_2-oxidized film of C_8GdPc_2**

7.2 Stability of oxidised species in air

It is important that the oxidation state of the films stayed long enough for biorecognition of NADH and vitamin C. The degree of stability of the Br_2-oxidized C_8LuPc_2 film was examined by monitoring the position of the Q-band for fully oxidized films stored in different environments. Details of the oxidation procedure are given earlier in Section 5.5.The film was kept in a closed container for about two weeks and the UV–visible spectra in Figure 7.3 recorded at different times exhibited no shift of the Q-band. It took about two weeks for the film to be reduced back to neutral state in air (Figure 7.3d). This indicates that the oxidized film is stable enough for the biosensing study. A similar slow reduction was observed for vacuum sublimed lutetium bisphthalocyanine bromine-oxidized films by Passard, Blanc and Maleysson, 1995. A period of at least two months was required for complete reduction.

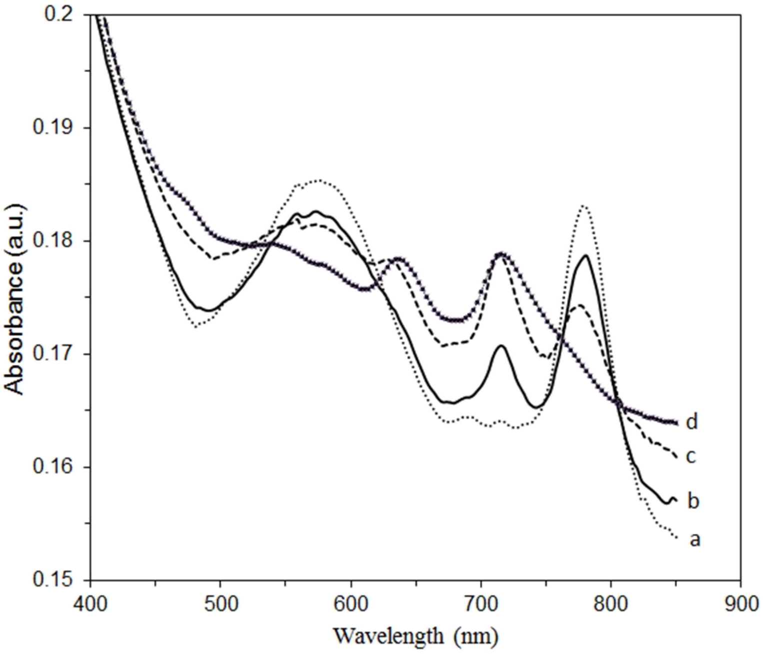

Figure7.3: **Plots of stability of Br_2-oxidized film of C_8LuPc_2 after (a) 3 h, (b) 1 day, (c) 5 days, (d) 13 days of oxidation**

In order to ascertain the required time for complete oxidation, the C_8LuPc_2 film was exposed to Br_2 vapour for 3 seconds and 7 minutes. Figure 7.4 shows the oxidation was nearly complete within 3 seconds after exposure to Br_2 vapour whereas a period longer than 7 minutes did not produce additional oxidation. This oxidation is reversible and the initial state can be reverted by NADH and vitamin C as the reducing agents.

The following chemical reaction is responsible for the oxidation of phthalocyanines (De Sajaand Rodriguez-Mendez, 2005):

$2C_8Pc(-1)MPc(-2) + Br_2 \rightarrow 2C_8Pc(-1)MPc(-1) + 2Br^-$ (7.1)

where M= Lu/Gd

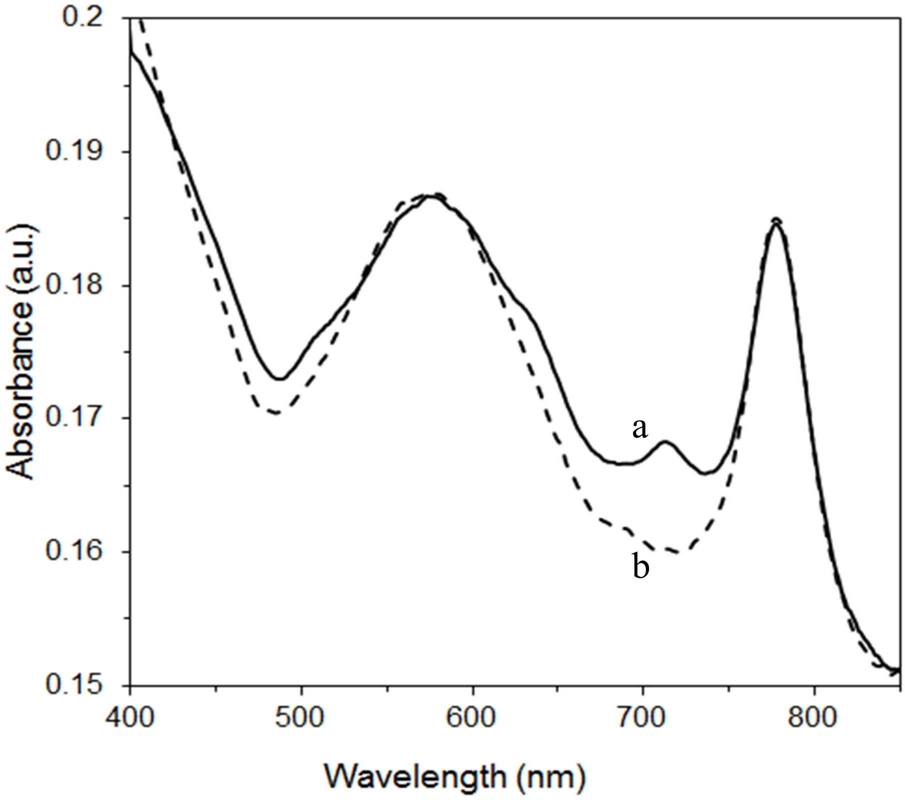

Figure 7.4: **Oxidation for (a) 3 s and oxidation for (b) 7 min for the film of C_8LuPc_2**

7.3 Electrochemical oxidation of films

For electrochemical oxidation a three electrode potentiostat was used with phthalocyanine coated ITO as working electrode, Ag/AgCl/Cl^- as reference electrode, pure Platinum wire as auxiliary electrode. Aqueous solution of 1.5 M$LiClO_4$ was employed as the electrolyte. Figure 7.5a shows a typically reproducible cyclic voltammogram of the C_8LuPc_2 molecules in the solid phase, displaying the presence of an anodic potential peak E_{pa} at +0.70 V and a cathodic potential peak at -0.41 V in the voltage sweep between 0 to 1.5 V. The ratio of the anodic (i_{pa}) to cathodic (i_{pc}) peak currents is estimated to be 0.35, implying that only about one-third of neutral C_8LuPc_2 on the forward sweep becomes oxidized to $C_8LuPc_2^+$ compared to those reduced on the reverse sweep. The electron transfer is therefore, a quasi-reversible process. In similar conditions on sweeping the voltage from 0 to 1.5 V an anodic peak at +0.80 V and a cathodic peak at +0.43 V were obtained for C_8GdPc_2. The ratio of current due to anodic and cathodic oxidation peaks were measured as 0.3 as it was found in the case of C_8LuPc_2 (Figure 7.5b). Values of oxidation potentials were 0.88 V for C_8LuPc_2 and 0.96 V for C_8GdPc_2, calculated using a Fortran based programme, CATSIM (Fyson, personal communication, 31 May, 2013).Values of heterogeneous electron transfer rate constant, diffusion coefficient, and charge transfer coefficient were used for the calculation as 2.20×10^{-3} cm s^{-1}, 1.0×10^{-5} cm^2 s^{-1}, and 0.5 respectively from the numerical solution of the Tafel equation by Neudeck et al., 1999.

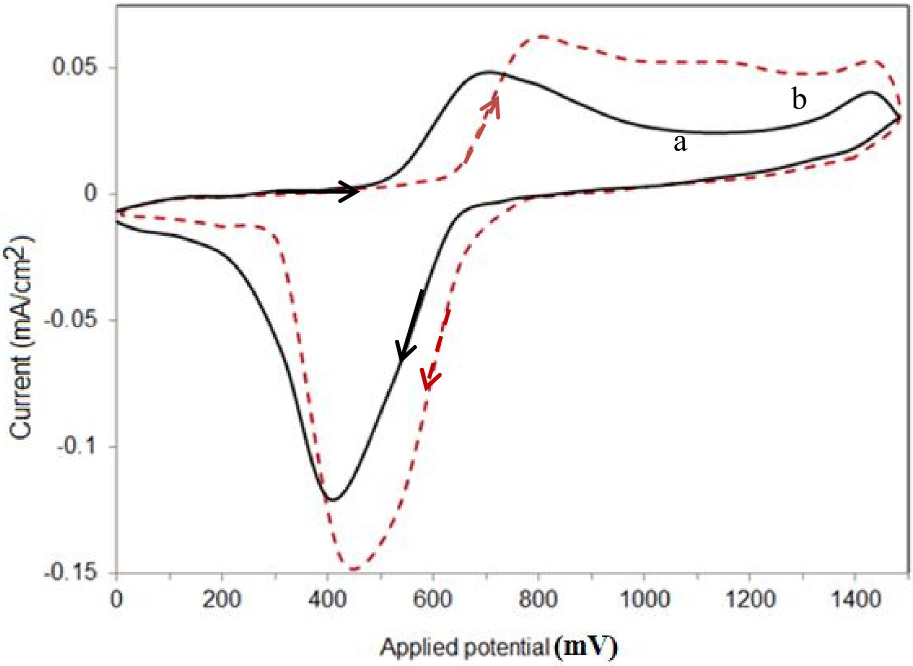

Figure 7.5: Cyclic voltammogram of (a) C_8LuPc_2 and (b) C_8GdPc_2 spun film on an ITO electrode in 1.5 M $LiClO_4$ aqueous solution at 19 °C. Scan rate 100 mVs^{-1}

The overall reaction equilibrium depends upon the ion transfer energetics. Therefore, the stability of redox species in the electrolyte during the electrochemical process is important for an observable electron transfer in the polarisation domain (Zhu et al., 2004). An experiment was carried out with C_8LuPc_2 to find out the stability of oxidised species in the 1.5 M $LiClO_4$ electrolyte solution up to 10 cycles. Figure 7.6a shows the cyclic voltammograms of C_8LuPc_2 after 1st, 4th, 6th and 10th cycles. The anode peak currents from Figure 7.6a have been replotted in Figure 7.6b. The constant value of i_{pa} within the error limit of ±0.001 with respect to the number of cycles indicates the invariant nature of ion pairing with supporting electrolyte anions according to Nakanishi et al., 2003.

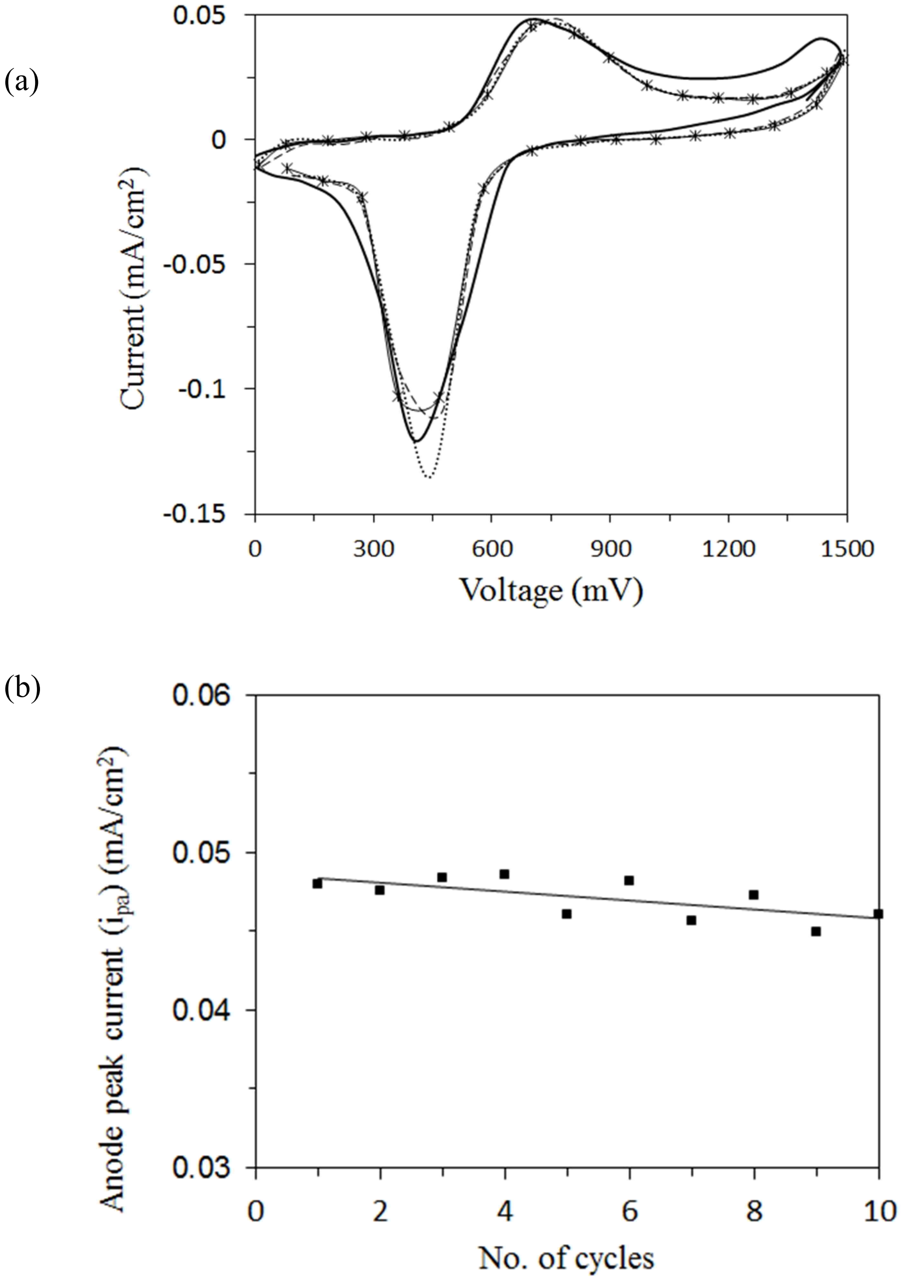

Figure7. 6: (a) **Cyclic voltammogram of C_8LuPc_2 in an aqueous solution of 1.5 M $LiClO_4$ after 1st (solid line), 4th (dash line), 6th (dotted line) and 10th (starred line) cycles. (b) Dependence of the anodic peak current obtained with number of cycles**

The current–time transient curves of C_8LuPc_2 and C_8GdPc_2 were recorded under the application of a constant oxidizing potential of 0.88 V and 0.96, respectively. As shown in Figure 7.7a and b, a sharp spike in current density of 11 μA/cm^2 and 5 μA/cm^2 were observed which is due to the accumulation ClO_4^- near the working electrode at the start for C_8LuPc_2 and C_8GdPc_2, respectively. The oxidation of the thin films was found to be complete within the period of 60 seconds. After this time, the rate of diffusion of the ions to the interface between the film and the electrolyte was much slower than that of the oxidation process, giving rise to the rapid drop of current.

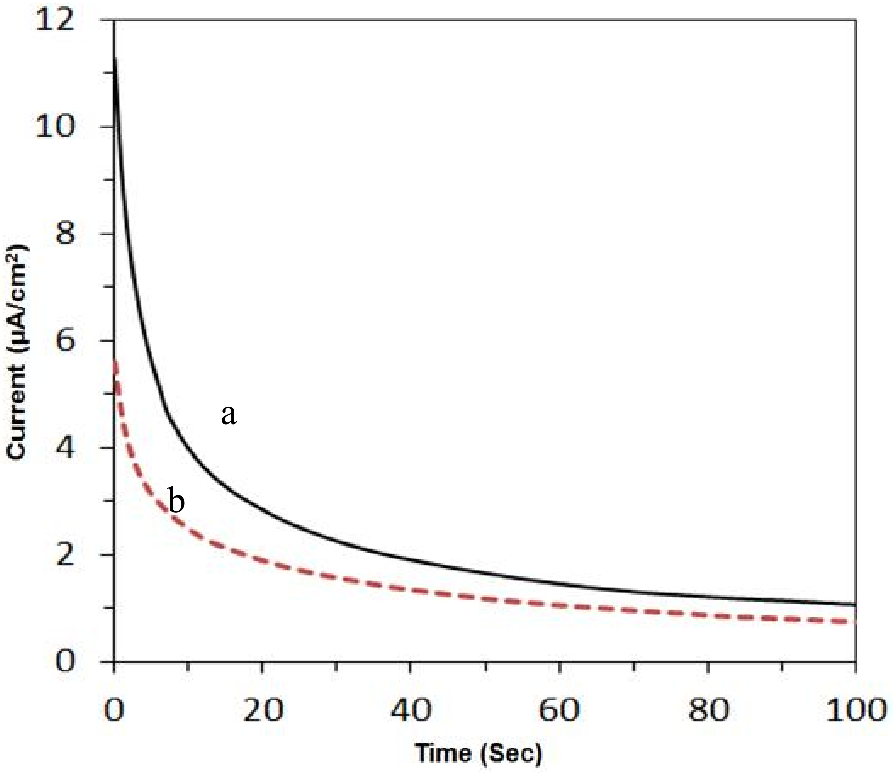

Figure7.7: Current density versus time transients at applied oxidizing potential on an ITO electrode for 100 seconds in 1.5 M $LiClO_4$ (a) C_8LuPc_2 and (b) C_8GdPc_2

The plot in the Figure 7.8 of the current density against time on logarithmic scales is linear for $t < 60$ second, giving a value of 0.53 for the slope for C_8LuPc_2 and 0.43 for C_8GdPc_2. This implies the validity of the Cottrell law according to the following Equation 7.2 (Li et al., 2003).

$$I_e = \frac{n_e F A_{\mathrm{p}} c_j^0 \sqrt{D_j}}{\sqrt{\pi}} t^{-1/2} \qquad (7.2)$$

Considering I_e = current through electrolytic solution in Amp, n_e = number of electrons to reduce/oxidize one molecule of analyte j, for example), F = Faraday constant, 96,485 Cmol^{-1}, A_{p}= area of the ITO electrode in cm^2, c_{j}^0 = initial concentration of the analyte j in molcm^{-3}, D_{j} = diffusion coefficient for species j in cm^2/s.

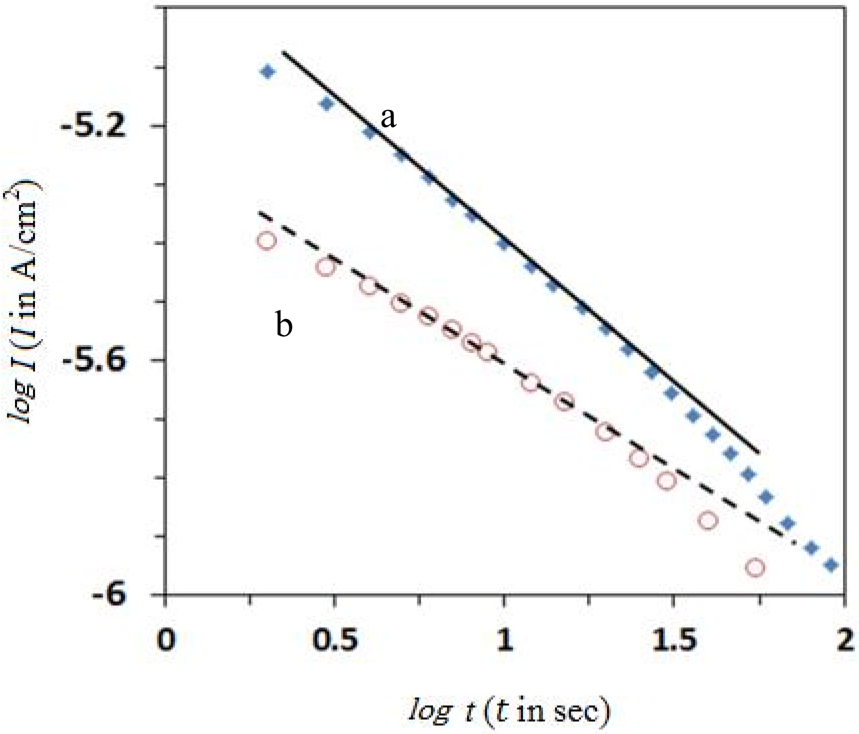

Figure 7.8: **Logarithmic plots of current density versus time at the same applied potential (a) C_8LuPc_2 and (b) C_8GdPc_2**

7.4 UV-Vis Spectroscopy of oxidised film

Figure 7.9 shows the electronic absorption spectra for Br_2 vapour and electrochemically oxidised films of C_8LuPc_2 and C_8GdPc_2 for comparison. The positions of the Q-bands after electrochemical oxidations of the thin films show similar pattern as the chemically oxidised one. The Q bands were found to be at 778 and 560 nm for C_8LuPc_2, and 796 nm and 610 nm for C_8GdPc_2. Therefore, the oxidation states obtained by chemical and electrochemical procedures were inferred as the same.

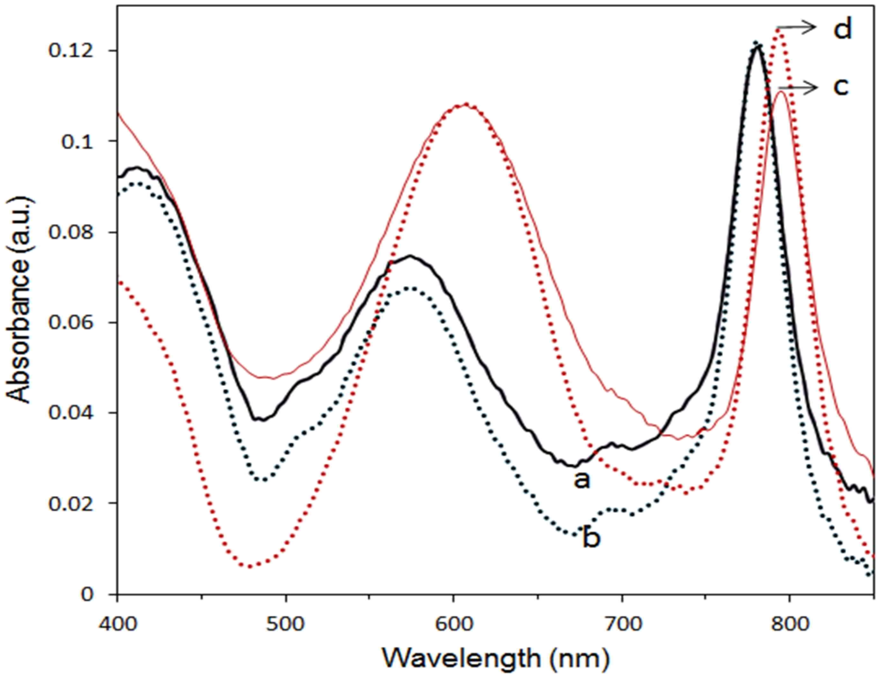

Figure 7.9: UV-Vis spectra of (a) C_8LuPc_2 of the Br_2 oxidised film (black solid line), (b) C_8LuPc_2, the electrochemically oxidized film (black dotted line) and (c) C_8GdPc_2, Br_2 oxidised film (red solid line), (d) C_8GdPc_2, electrochemically oxidized film (red dotted line)

7.5 Lithium perchlorate ($LiClO_4$) aqueous solution as stabiliser

The kinetics of the reduction of the oxidised spun films was monitored by recording the spectral changes using a UV–Visible spectrophotometer over the range of 400–850 nm. Figure 7.10 shows the spectral changes of the Br_2-oxidized C_8LuPc_2 film in 1.5 M aqueous $LiClO_4$ solution over a period of more than 3 hours. The isosbestic point observed at 763 nm in Figure 7.10 indicates the charge-transfer band in the near infrared region associated with the free radical bisphthalocyanines (Rodriguez-Mendez, 2009). The Q-band at 778 nm progressively decreased in intensity accompanied by an increase intensity of the 718 nm band. Similar electronic transitions were evident in photo-assisted reduction of lutetium bisphthalocyanines in the presence of thionyl chloride (Nesala and Nyokong., 1998).

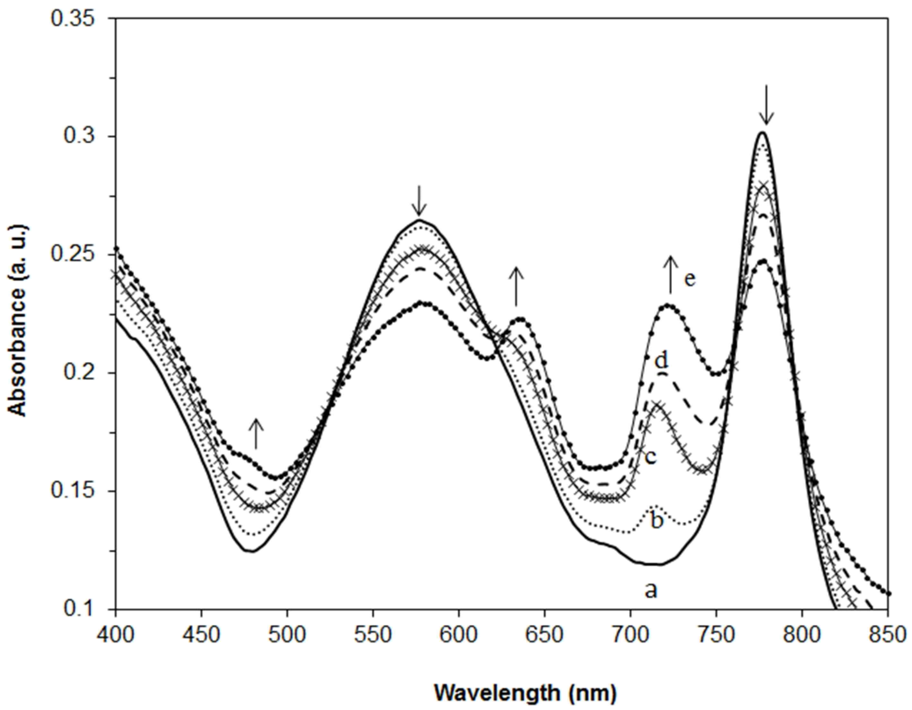

Figure 7.10: Electronic absorption spectral changes as a function of time (indicated by arrows) during neutralization of $C_8LuPc_2^+$ by water in the presence of a 1.5 M $LiClO_4$ aqueous solution. Data recorded after (a) 2, (b) 17, (c) 64, (d) 110, and (e) 198 min

The oxidised C_8GdPc_2 film presented a similar graph as the one shown in Figure 7.10. The peak at 796 nm for the oxidised C_8GdPc_2 film in the presence of 1.5 M $LiClO_4$ was found to decay gradually with simultaneous increase of the 727 nm peak. The isobestic point was noted at 778 nm. According to the Laws of reaction kinetics, the first order rate of reaction (R_t) can be expressed as follows (Castellan, 2010).

$$R_{\mathrm{t}} = \frac{\mathrm{d}C_t}{\mathrm{d}t} = k_{\mathrm{obs}}C_t \qquad (7.2)$$

Where C_t is the concentration of the reactant at time *t*, k_{obs} is the rate constant

If the reaction continues for t time and C_0 is the concentration at initial time, the following eqn. 7.2 can be written

$$c_{\mathrm{t}} = c_0 \mathrm{e}^{-k_{\mathrm{obs}}t} \qquad (7.3)$$

When the reaction kinetics is monitored by UV-Vis spectrophotometry, considering the absorbance of the completely reduced film for A_∞, the absorbance of the oxidised film for A_0, the Equation7.3 can be written as following Equation 7.4 by (Nesala and Nyokong, 1998).

$$\frac{(A_t - A_\infty)}{(A_0 - A_\infty)} = e^{-k_{obs}t} \qquad (7.4)$$

The half-life of the reaction ($t_{1/2}$) is defined as when 50% of the reaction is completed. For 1st order reaction this is independent of the concentration (Castellan, 2010).

From Equation 7.3 when C_t=0.5 C_0,

$$t_{1/2} = \frac{0.693}{k_{obs}} \qquad \textbf{(7.5)}$$

Half-life is a significant parameter for 1st order reaction to envisage the speed of reaction as according to Equation 7.3, these reactions never completes.

The linear plot of ln($A_t - A_\infty$) versus time t (where A_t of absorbance at 778 nm at time t) follows the Equation 7.4 showing a first order kinetics reaction. The value of k_{obs} was estimated to be 2.8×10^{-3} $min^{-1}$from the slope of the graph 7.11a. The half-life of the reduction reaction was calculated as giving a value of 4 hour following Equation 7.5. In an aqueous solution C_8LuPc_2 molecules became less stable with a smaller concentration of $LiClO_4$. Only 17 per cent of oxidized phthalocyanine was reduced in 1 h in the presence of 1.5 M $LiClO_4$ solution whereas reduction as large as 76 per cent took place in 0.7 M $LiClO_4$ over the same length of time. The oxidized film was reduced to a neutral state in water within 10 min. The addition of $LiClO_4$ was to control the rate of reduction of C_8LuPc_2 film.

The value of k_{obs} and $t_{1/2}$ were estimated to be 3.6×10^{-3} min^{-1} and 3 hour, respectively for C_8GdPc_2 from the slope of the graph 7.11 b.

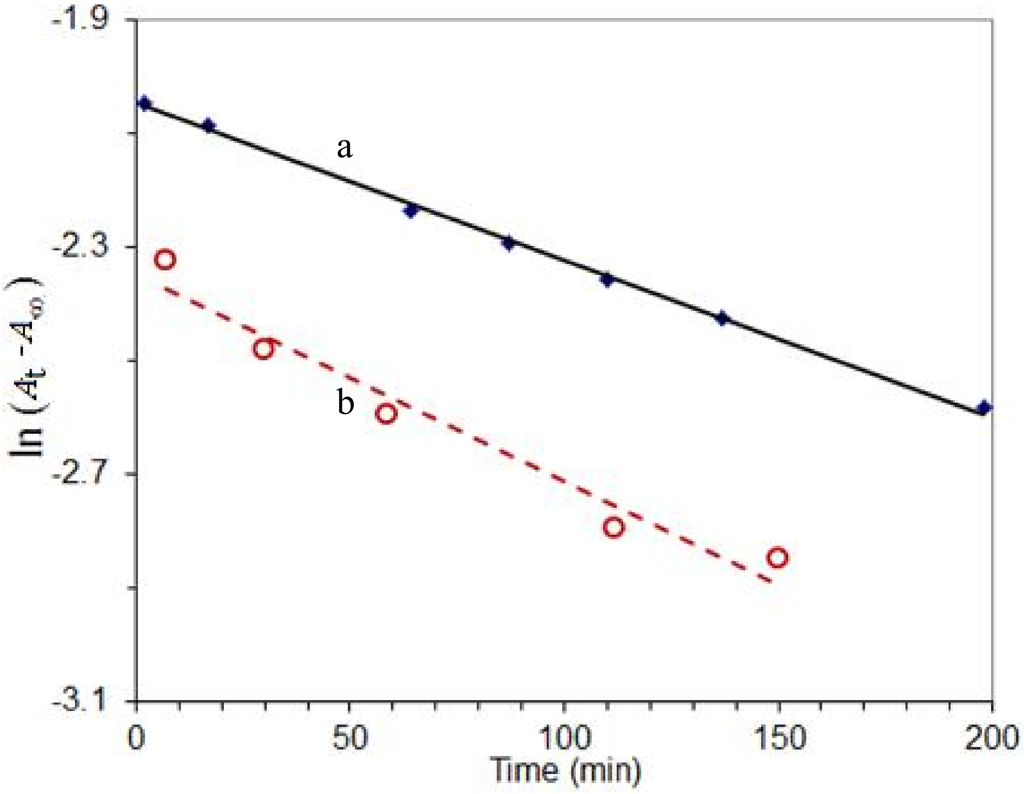

Figure 7.11: Plot of ln (A_t-A_∞) versus time for 1.5 M $LiClO_4$ (a) C_8LuPc_2 and (b) C_8GdPc_2

7.6 *In situ* detection of NADH and vitamin C

In order to carry out controlled reduction, experiments for in situ detection of the cofactors, the aqueous solution containing 1.5 M $LiClO_4$ was chosen in preference to the aqueous solution as a medium for recording the optical absorption in C_8LuPc_2 film. Figure 7.12 shows the spectral changes of C_8LuPc_2 film in the presence of 3 mM NADH in the 1.5M $LiClO_4$ aqueous solution in the time interval of 2 min., 7 min., 10 min. and 90 min. from the time reaction started. A decreasing absorbance of 778 nm peak with increasing absobance of 718 nm peak can be observed from the figure. After 90 minutes the film returns to its original neutral state.

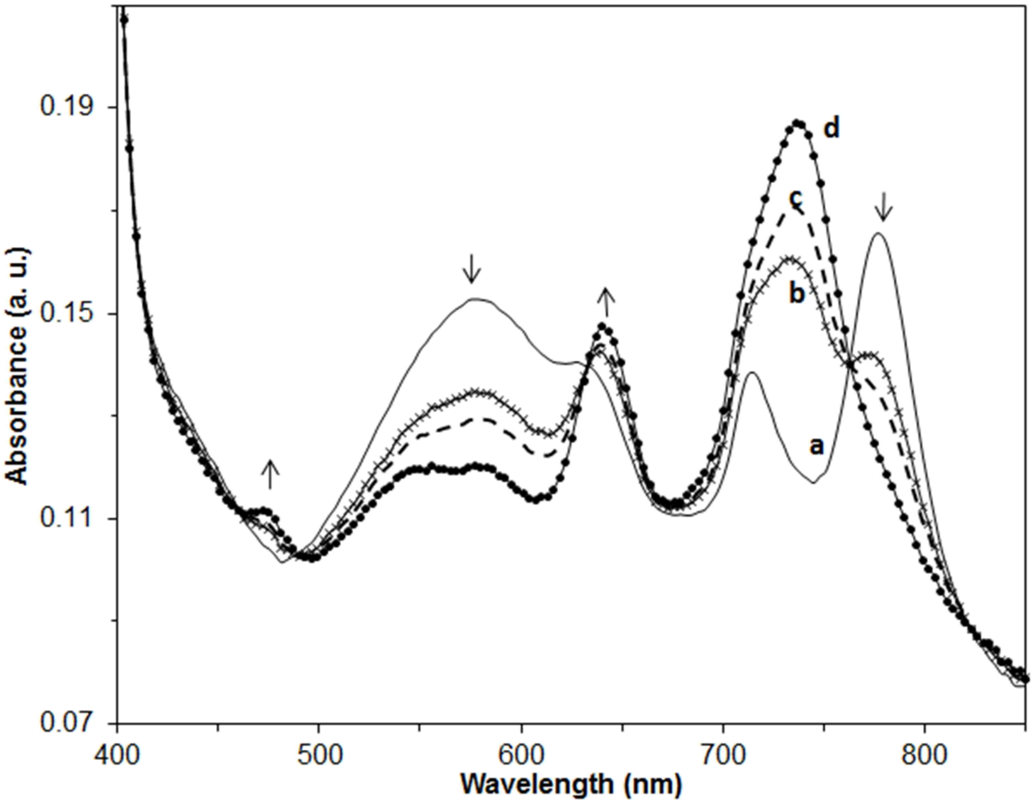

Figure 7.12: **Electronic absorption spectral changes as a function of time (indicated by arrows) of C_8LuPc_2 in 3 mM NADH dissolved in 1.5 M $LiClO_4$ aqueous solution. Data recorded after (a) 2, (b) 7, (c) 10 and (d) 90 min**

Figure 7.13 shows the results of similar kinetic measurements of the oxidized film in the presence of 3.5 mm vitamin C in 1.5 M $LiClO_4$ aqueous solution in the 1 min., 3 min., 5 min., 9 min. and 90 min. time interval. As in the case of NADH, the presence of an isosbestic point at 763 nm was observed during reduction over 90 min. The isobestic point indicates the presence of only two species is taking part in the reaction. Therefore, in can be concluded that the compounds are stable in the reaction medium.

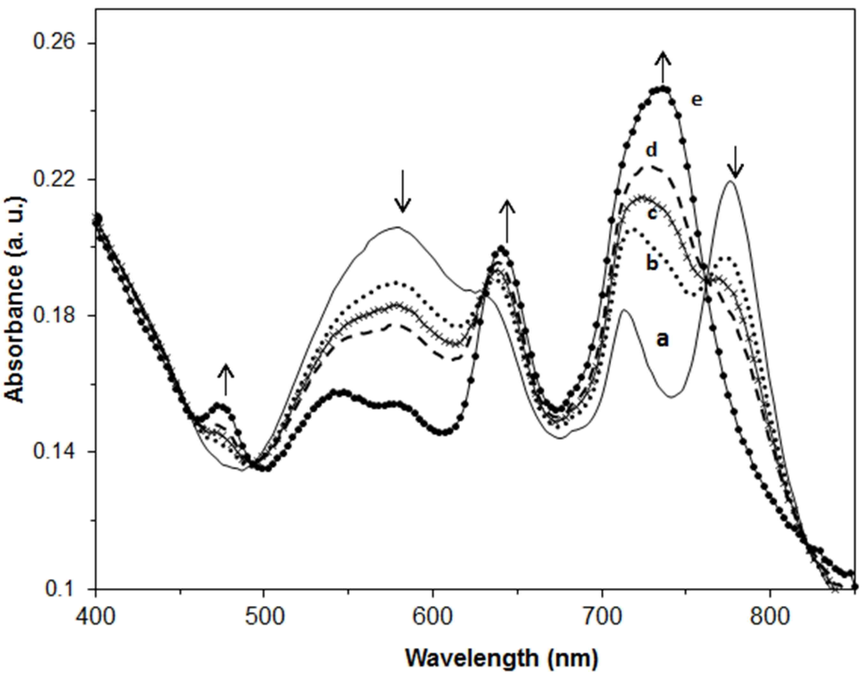

Figure 7.13: **Electronic absorption spectral changes as a function of time of $C_8LuPc_2^+$ in 3.5 mM vitamin C in a 1.5 M $LiClO_4$ aqueous solution. Data recorded after (a) 1, (b) 3, (c) 5, (d) 7 and (e) 90 min**

Figure 7.14 shows the logarithm–linear plots of (A_t –A_∞) against time for 3 mM NADH and 3.5 mM vitamin C. The resulting graphs were found to be linear implying 1st order reaction taking place in the medium.

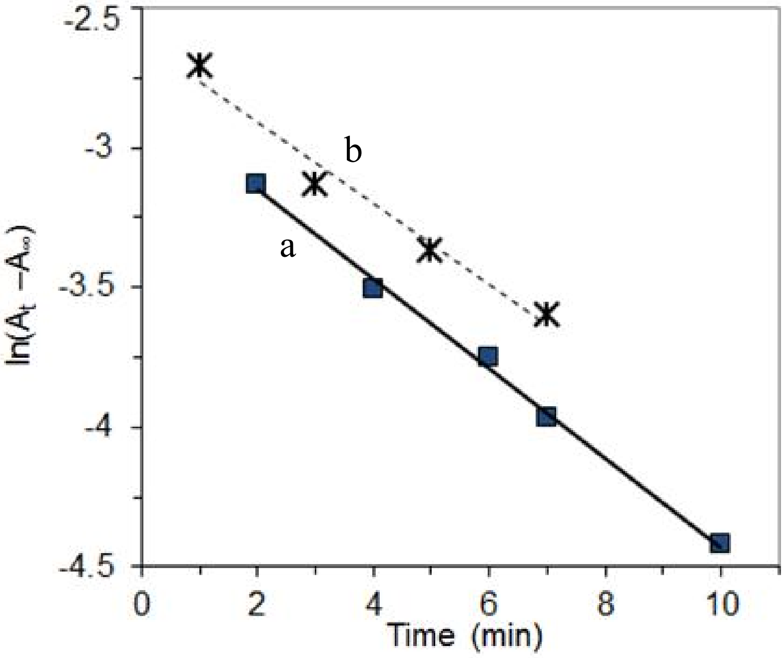

Figure 7.14: **Plot of $\ln(A_t - A_\infty)$ versus time for (a) 3 mM NADH (solid line) and (b) 3.5 mM vitamin C (dash line) in a 1.5 M $LiClO_4$ aqueous solution using thin film of C_8LuPc_2**

Value of 4.3 was determined from the slope corresponding to neutralization by NADH and vitamin C, respectively from the Equation 7.4 in page 120 of this chapter. Similarly, the half-life ($t_{1/2}$) of the reduction of vitamin C by thin film of C_8LuPc_2 was estimated as 4.8 min

The reducing power of both redox agents can, therefore, be taken to be equal for practical purposes. Measurements were repeated for different lower concentrations of both NADH and vitamin C and the resulting plots in Figure 7.15a of k_{obs} versus the concentration were found to be linear implying the validity of Equation 7.4 (Adhikamsetty and Jonnalagadda, 2009). The correlation coefficients were found to be 0.96 for NADH and 0.90 for vitamin C. The Lewis basicity of NADH and vitamin C became dominant in reducing the C_8LuPc_2 film to the neutral state over the ability of $LiClO_4$ to counteract the neutralizing effect of water molecules. The half-lives of the neutralization of the Br_2-oxidized C_8LuPc_2 films in1.5 M $LiClO_4$ became shorter, predictably showing the inverse dependence in the Figure 7.15b on the increasing concentrations of NADH and vitamin C.

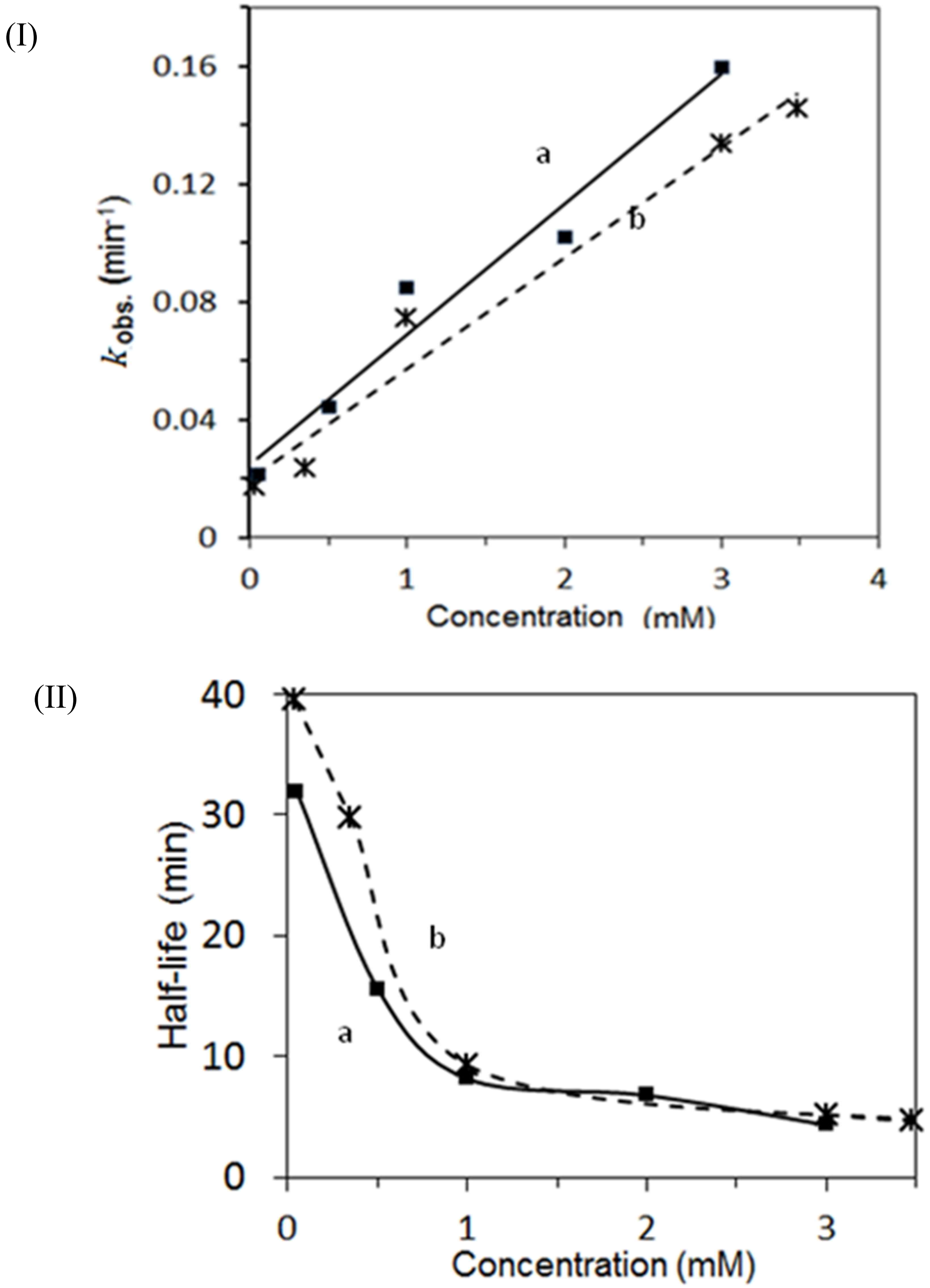

Figure 7.15: **(I) Plot of k_{obs} versus concentration of (a) NADH (solid line) and (b) vitamin C (dash line) in a 1.5 M $LiClO_4$ aqueous solution. (II) Dependence of half-life of the reaction on concentration (a) NADH (solid line) and (b) vitamin C (dash line) for C_8LuPc_2**

Similar kinetic study of the oxidized C_8GdPc_2 film was carried out at the lowest detection limit of 0.05 mM NADH in the 1.5 M $LiClO_4$ aqueous solution.

The presence of an isosbestic point at 778 nm was observed during reduction over 3 hour (Figure 7.16).

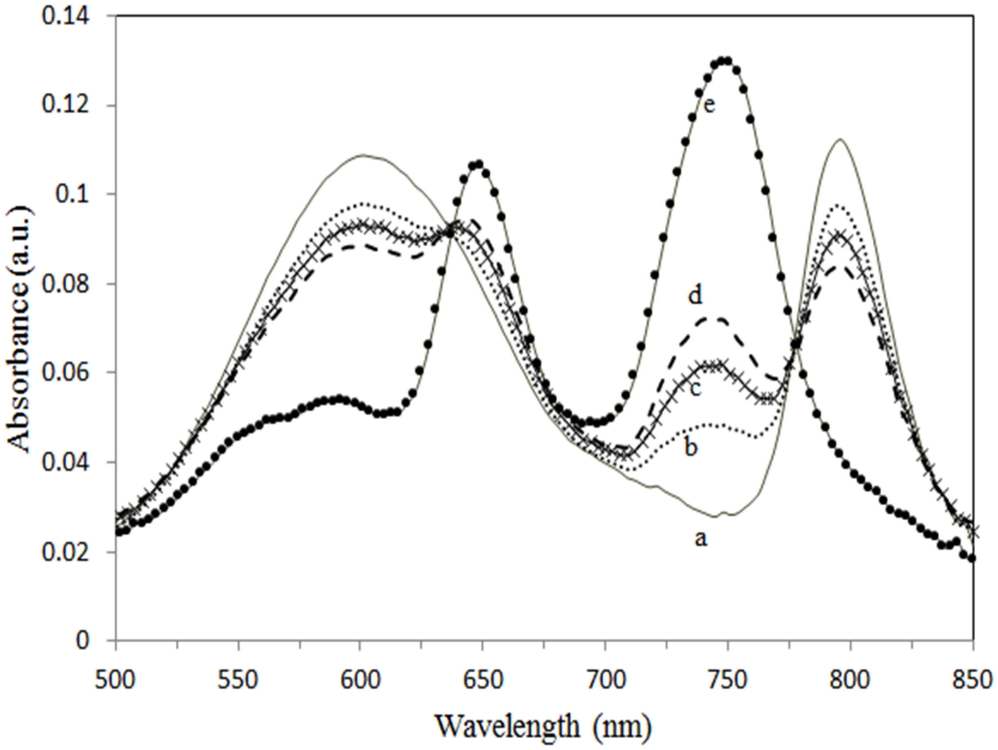

Figure 7.16: Electronic absorption spectral changes as a function of time of $C_8GdPc_2^+$ in 0.05 mM NaDH in a 1.5 M $LiClO_4$ aqueous solution. Data recorded after (a) 1, (b) 20, (c) 37, (d) 54 and (e) 90 min

A straight line was obtained on plotting $\ln(A_t - A_\infty)$ against time over the time of 90 minutes of reaction. Similar to the previous cases of NADH and vitamin C reduction by $C_8LuPc_2^+$, the straight line indicates a 1st order reaction mechanis taking place during the reduction of NADH by oxidised species of C_8GdPc_2. The value of reduction rate constant was estimated to be 1.03×10^{-2} min^{-1} from Figure 7.17 of the the linear logarithm plot of $\ln(A_t - A_\infty)$ against time.

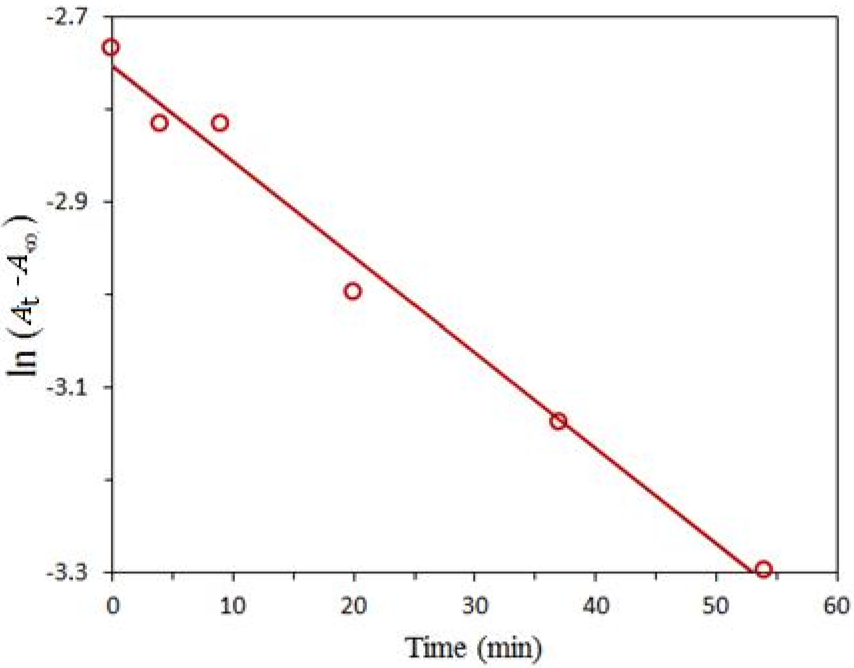

Figure 7.17: Plot of $\ln(A_t - A_\infty)$ versus time for 0.05 mM NADH in a 1.5 M $LiClO_4$ aqueous solution using thin film of C_8GdPc_2

7.7 Aging effect of C_8LuPc_2 thin film on biosensing of NADH

To determine the effect of aging, the spectra were recorded for C_8LuPc_2 samples which had been left in air for 3 months. As shown in Figure 7.18, the solution of C_8LuPc_2 in chloroform appears not to suffer from any aging effect with the Q-band peaks at almost the same positions of 714 and 653 nm. On the other hand, the two Q-bands of the 3 month old neutral spin coated film spectrum exhibited two different types of wavelength shifts: a small red shift from 718 to 736 nm and a blue shift from 653 to 643 nm. It is possible that some relaxation of the molecular packing distortion occurs over time. When this film was oxidized by exposure to bromine vapour, the main Q-band peak of the oxidized film underwent a redshift to 772 nm from 736 nm. However, this is smaller than that exhibited by a fresh film upon oxidation. The bromine-oxidized $C_8LuPc_2^+$ film remained stable for at least 3 hour, long enough to examine its interaction with freshly prepared biological cofactor NADH in 1.5 M $LiClO_4$ aqueous solution.

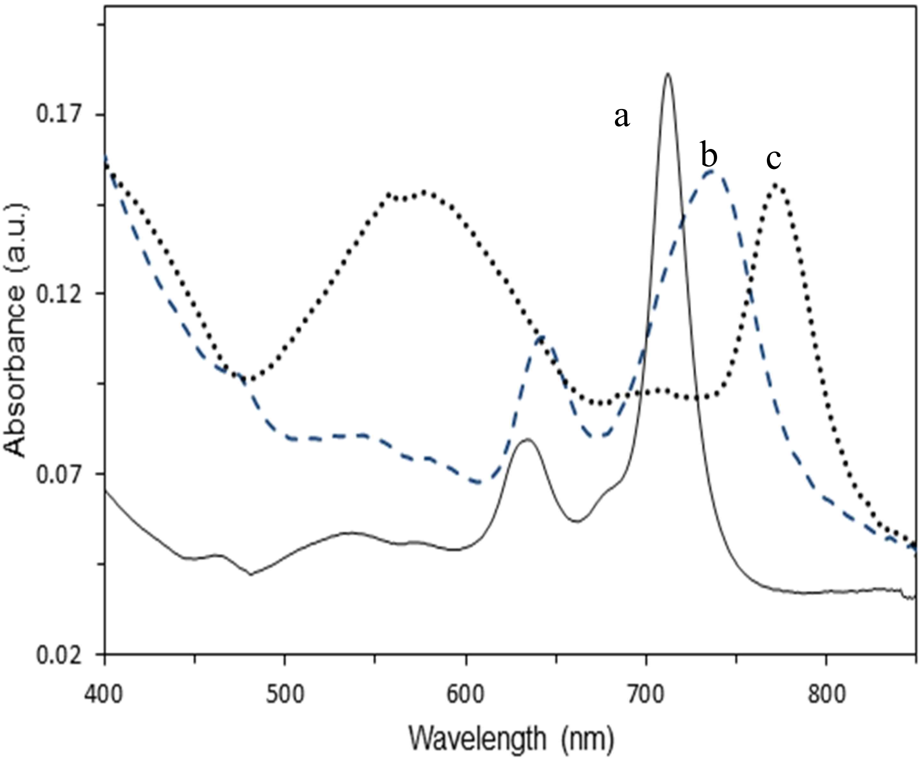

Figure 7.18: Electronic absorption spectra of three month old C_8LuPc_2 (a) neutral solution (solid line) (b) neutral film (dash line) and (c) Br_2-oxidized film (dotted line)

To study the effect of aging, the *in situ* kinetics was monitored with varying concentration of freshly prepared NADH from 0.05 to1 mM in aqueous solution of 1.5 M $LiClO_4$. Figure 7.19(I) shows the time-dependent neutralization process of a $C_8LuPc_2^+$ film on interaction with 0.5 mM NADH over 90 min. The isobestic points are well-defined with the monotonic decrease in the absorption intensity at the 772 nm peaks and simultaneous increase in the peak intensity of the 718 nm bands with time. The lowering of the intensity of the 772 nm peak was found to be exponential as evident from the linear plot of absorption intensity against time on a logarithmic-linear scale 7.19(II). The reduction rate constant was found to be 1.12×10^{-2} min^{-1} from the slope. Absorption spectra were recorded for the reduction of a $C_8LuPc_2^+$ film by 0.5 and 1 mM NADH is shown in 7.19(II).

(I)

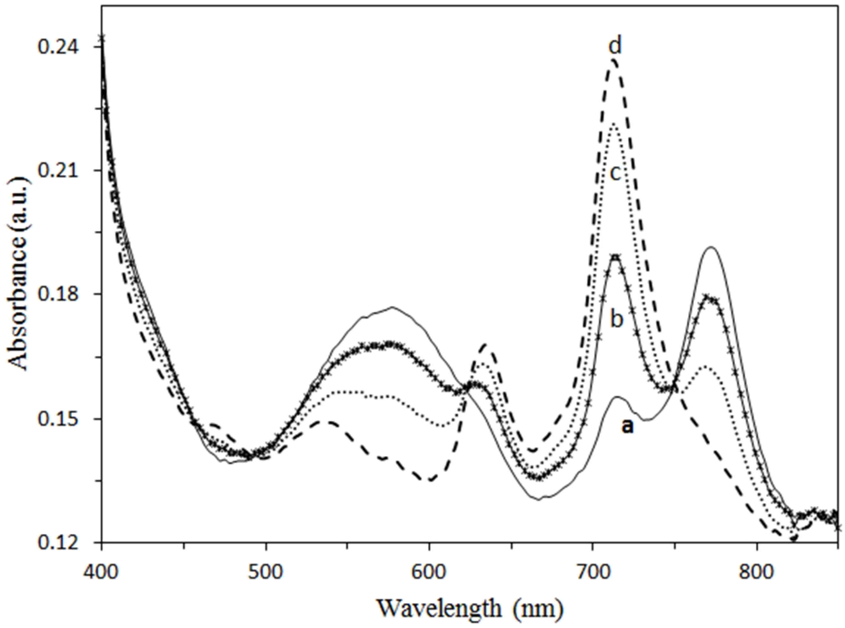

(II)

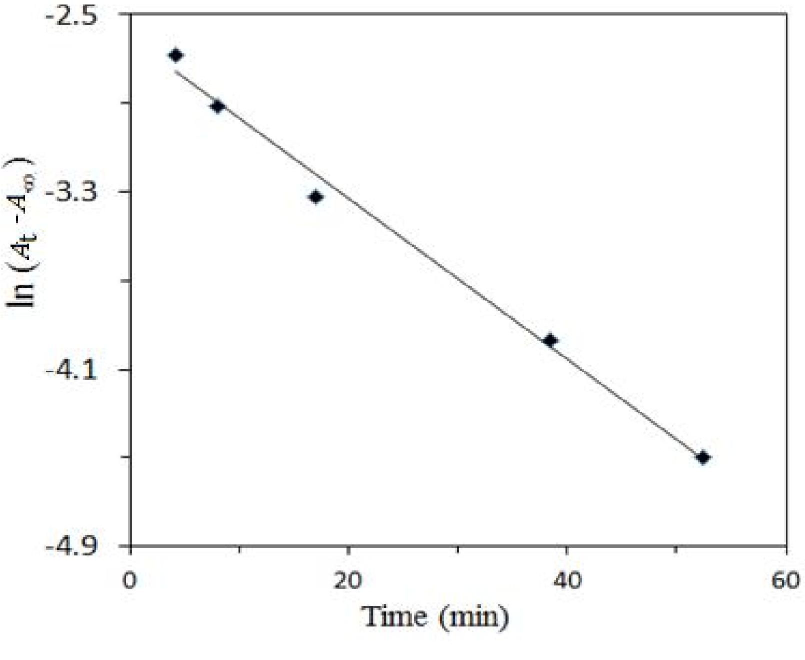

Figure 7.19: **(I) The change of optical absorption spectra of 3 month old $C_8LuPc_2^+$ film in 0.5mM NADH dissolved in 1.5 M $LiClO_4$ with time (a) 4 min, (b) 17 min, (c) 38 min and (d) 90 min. (II) the plot of decrease in intensity of the Q_y-band against time of reduction on logarithm-linear scale**

Values of the half-life of the oxidation of $C_8LuPc_2^+$ were found to be decreasing with the concentration of NADH. The NADH reduction of the 3 month old film is consistently slower than a similarly oxidized fresh film, giving a percentage change from 94% for 0.05 M to 6% for 1 mM concentration of NADH. This detection limit is smaller than the reported value of 8 mM NADH, detected with different types of modified electrodes for enzyme-based electrocatalytic systems (Deore and Freund, 2005). The table 7.1 summarises the rate constant and half-life values of *in situ* interactions of C_8LuPc_2 fresh film and 3 months left film with NADH and vitamin C.

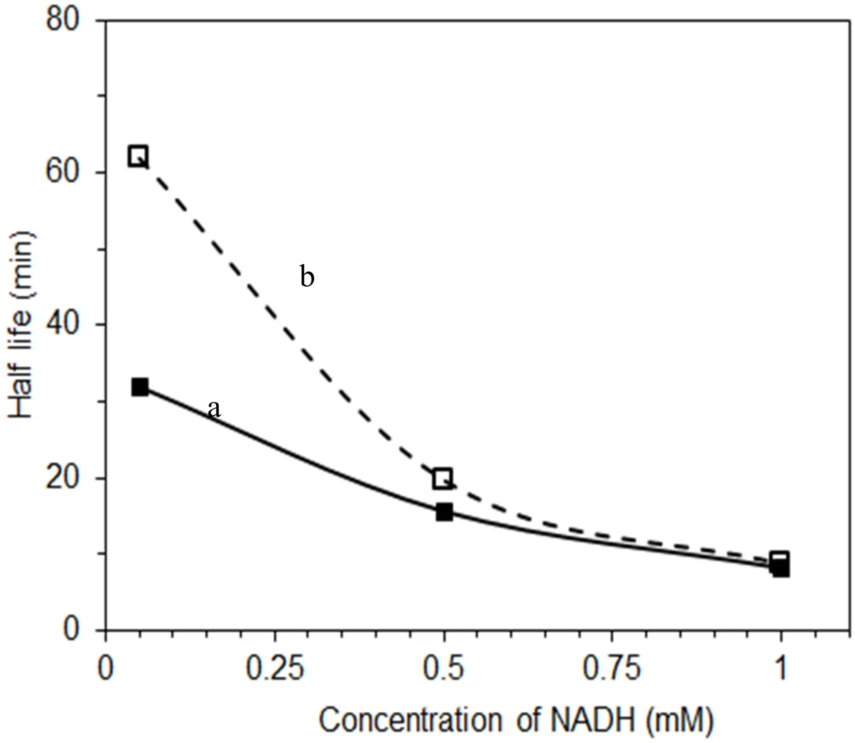

Figure 7.20: **Dependence of reduction reaction half-life on NADH concentration for (a) freshly prepared (solid line) and (b) 3 months old films (dash line) for C_8LuPc_2**

Table 7.1: **Aging effect of lutetium phthalocyanine on the reduction rate constant and half-life of NADH at different concentrations**

Concentration of NADH (mM)	**Aging effect of C_8LuPc_2 film on biosensing**			
	Rate constant ($\times 10^{-2}$ min^{-1}) (±0.005)		**Half-life (min) (±3)**	
	Fresh	**3 Months old**	**Fresh**	**3 Months old**
0.05	2.17	1.12	31.94	61.88
0.5	4.44	3.52	15.61	19.69
1	8.48	7.97	8.17	8.69

7.8 Raman Spectroscopic study of NADH biosensing and aging effect on C_8LuPc_2 film

The electrochromic changes of C_8LuPc_2 drop cast films and the aging effect on the vibrational characteristics in the bonding were studied using Raman spectroscopy. Figure 7.21b shows the Raman modes of lutetium bisphthalocyanineare sensitive to the removal of an electron from their π–π* conjugation on phthalocyanine rings after one-electron oxidation with a resulting shift in the redox-sensitive vibrational modes. The positive charge (hole) becomes localized on the Pc ring (Jiang et al. 2006).The neutral C_8LuPc_2 has been replotted here from Figure 6.5 in Chapter 6 for the sake of comparison. The hole is delocalized throughout the two macrocycles of a neutral C_8LuPc_2 film. It is evident from Figure 7.21 that there is a general tendency of vibrational modes moving to higher frequencies on oxidation, possibly due to the hole confinement. The maximum shift is observed in the frequency region between 1320 and 1650 cm^{-1}. The NADH interaction is believed to reduce the C_8LuPc_2 film almost completely to the neutral form as judged by the Raman spectra in Figure 7.21d which is similar to those of the film prior to chemical oxidation (Figure 7.21a).

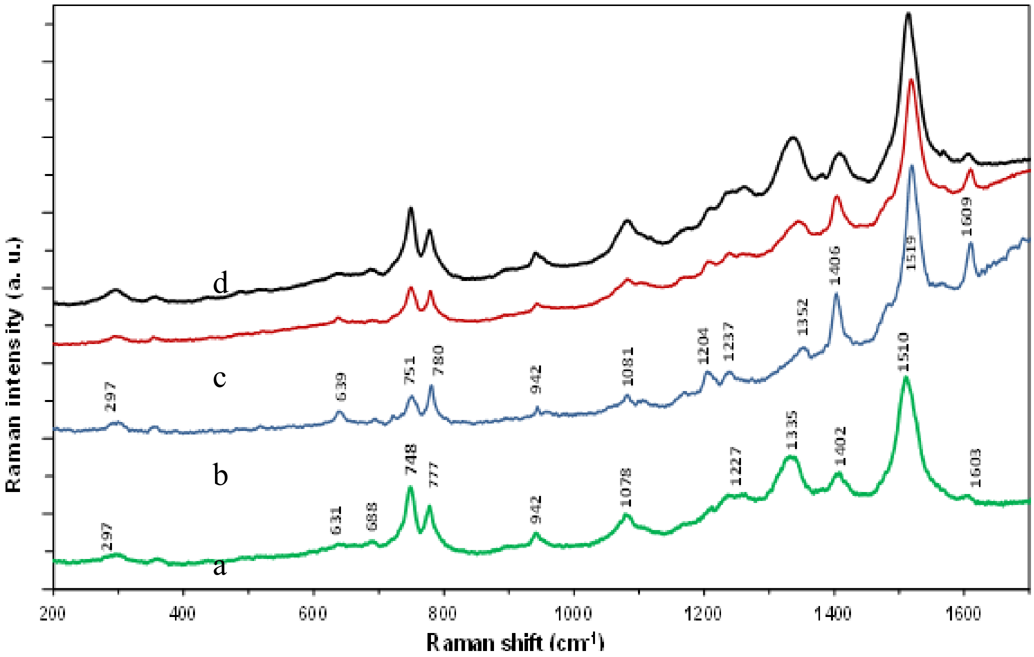

Figure 7.21: **Raman spectra of drop cast C_8LuPc_2films on glass substrates: (a) neutral, (b) Br_2-oxidised, (c) partially reduced by NADH reaction and (d) completely reduced by NADH reaction. The excitation wavelength was equal to 633 nm in each case**

Therefore, the processes of reduction and oxidation of C_8LuPc_2 films may, therefore, be considered reversible from the figure 7.21.

The drop cast film was left in air for 3 months, and Raman spectra in Figure 7.22 were recorded for neutral and oxidized films. Figure 7.22a represents the Raman spectra of 3 months old neutral film of C_8LuPc_2 and Figure 7.22b represents the corresponding oxidised film by using the film left in air for 3 months. Comparing with the Figure 7.21, it can be said that the basic features of the spectra remains same as the fresh film indicating no degradation took place over the months. However, the peak positions are included in Table 7.2, showing very small shifts in frequencies through aging the film over 3 months. Shifts of the positions due to oxidation are similar to those obtained for the freshly prepared film. The differences between the peak positions of the fresh and the film left for 3 months are estimated in the Table 7.2 for both the neutral and oxidised species.

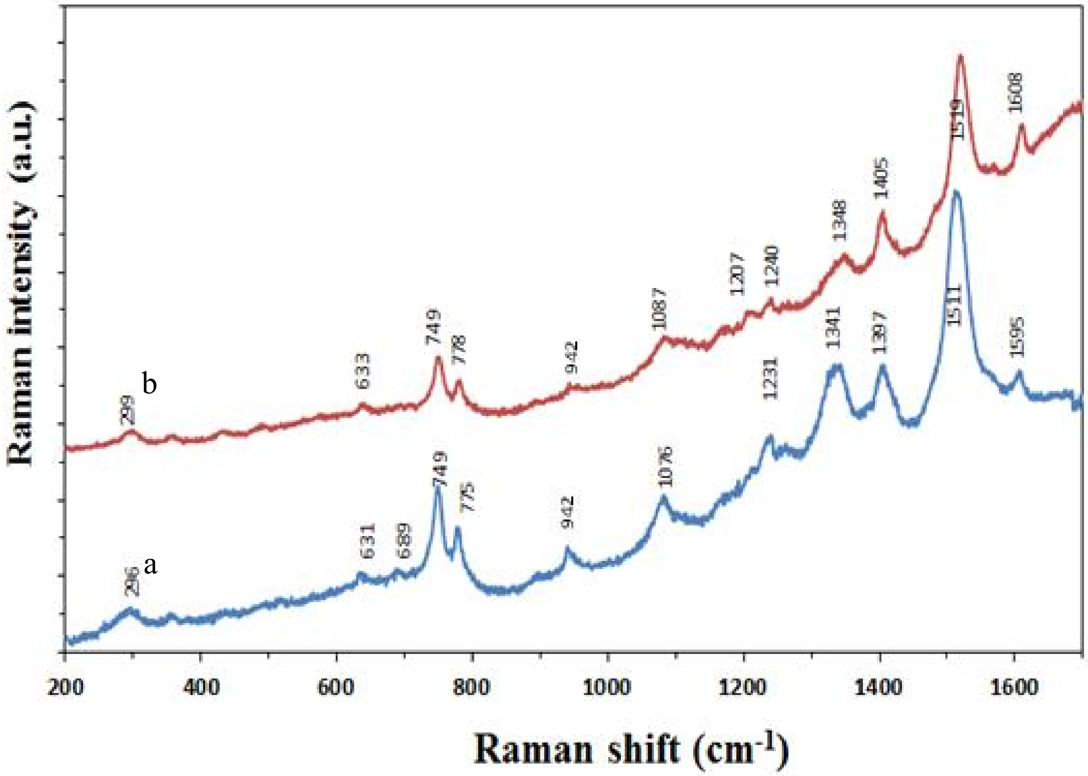

Figure 7.22: Raman spectra of 3 months old drop cast film on glass (a) neutral and (b) oxidised film of C_8LuPc_2

Table 7.2: Raman shifts of neutral and oxidised C_8LuPc_2

Position of Raman peaks of the fresh and 3 months left film(cm^{-1})		Difference of 3 months old Raman peak position from fresh film(cm^{-1})	
Neutral state	**Oxidised state**	**Neutral state**	**Oxidised state**
297 (296)	297 (299)	**-1**	2
631 (631)	639 (633)	0	-6
688 (689)	683 (---)	1	---
748 (749)	751 (749)	1	-2
777 (775)	780 (778)	-2	-2
942 (942)	942 (942)	0	0
1078 (1076)	1081 (1087)	-2	-6
----	1204 (1207)	----	-1
1227 (1231)	1237 (1240)	4	3
1335 (1341)	1352 (1348)	6	-4
1402 (1397)	1406 (1405)	-5	-1
1510 (1511)	1519 (1519)	1	0
1603 (1595)	1609 (1608)	-8	-1

Values in parenthesis are the peak positions for 3 months old film.

The histograms in Figure 7.22 show the changes in relative intensities of two adjacent bands within the ranges of 748−780 cm^{-1} and 1335−1406 cm^{-1}. The interaction between the macrocycles changes due to change of electron density, affecting the relative intensities of the bonds. The pyrrole and isoindole stretching vibrations in the range 1300−1530 cm^{-1} are believed to be strongly affected by change of electronic distribution due to oxidation of the freshly prepared sample. The hole localization and delocalization on the phthalocyanine rings due to oxidation are believed to be comparable for both the freshly prepared and 3 month old samples.

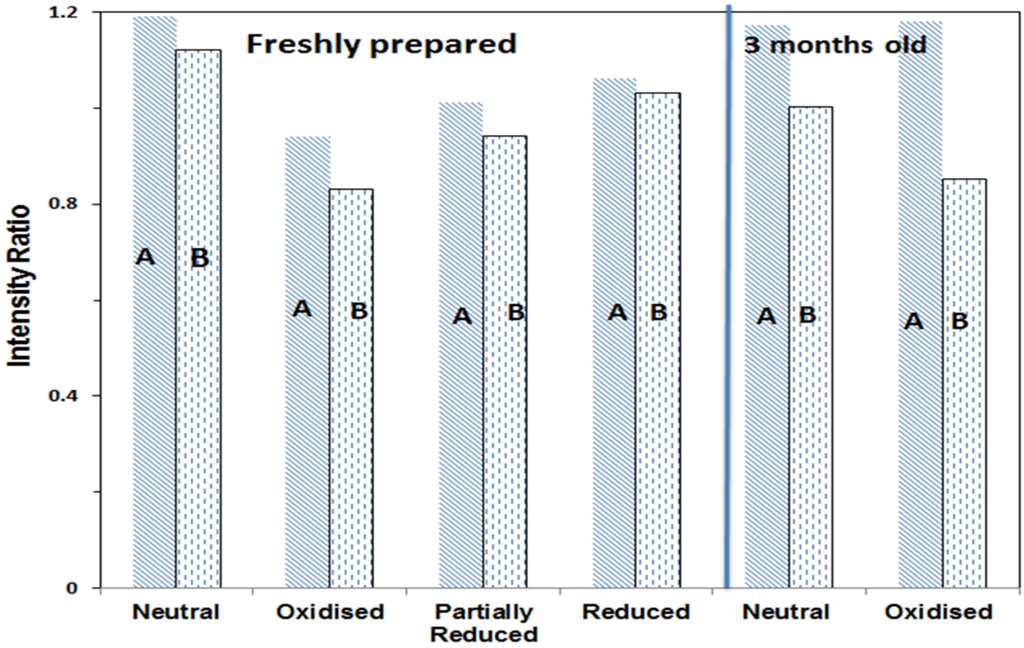

Figure 7.23: Histograms showing relative intensities at two peaks occurring in the range of (A) 748cm^{-1} -780cm^{-1} (B) 1335 cm^{-1} - 1406 cm^{-1} for thin film of C_8LuPc_2

7.9 Chapter summary

Neutral C_8LuPc_2 and C_8GdPc_2 films were oxidised chemically or electrochemically. The electrochromic behaviour of the films was examined by cyclic voltammetry establishing the value of 0.88V bias potential for oxidation in the case of C_8LuPc_2**,** and for C_8GdPc_2 it was 0.96 V. A slightly lower value of oxidation potential in C_8LuPc_2 (0.88V) shows comparatively easier oxidation of the compound. Being the smaller rare-earth atom, lutetium contained compounds show low oxidation potentials associated with lower band gaps (ΔE), which also explains the higher conductivities of the Lu-compounds compared to their C_8GdPc_2 analogues. The comparative electrical dc conductivity of these materials has been checked and reported in Section 6.3 of Chapter 6. These findings support the studies by Zhu et al., 2004, who found that in a series of unsubstituted rare-earth bisphthalocyanines there is a linear drop of electrochemical potential with lanthanide contraction. Using UV-Vis spectroscopy, a simple method was developed to detect NADH and vitamin C in a solution wetting the surface of an ITO coated glass substrate modified with spin coated electrochromic films. The addition of 1.5 M $LiClO_4$ was found to be satisfactory for supplying ClO_4^- ions in order to maintain a stable C_8LuPc_2/C_8GdPc_2 film in aqueous media for biorecognition. The reduction rate was greatly increased when redox biomolecules were added tithe aqueous medium of water and $LiClO_4$. The reduction of the oxidized film in the presence of NADH and vitamin C was described in terms of first-order kinetics. The kinetics study of NADH using thin films of C_8GdPc_2 also follows a first order kinetics with reduction. A reference plot of the rate constant versus concentration of NADH and ascorbic acid may be employed to determine an unknown concentration under similar ambient conditions. The detection limit for NADH and Vitamin C was found to be 0.05 mM. The sensing was found to be reproducible. The C_8LuPc_2 film remains sensitive for at least three months even when left in an open space. However, the reduction rate was slower in the films left in an open space. The spun film of C_8GdPc_2 exhibited a biosensing property with a rate constant of value 1.03×10^{-2} min^{-1} and half-life 53.03 min for 0.05 mM concentration of NADH. These are half the values recorded for thin films of C_8LuPc_2.

The observation from Raman spectroscopic measurements of the complete recovery of the oxidized bispthalocyanine film to its neutral form via NADH reduction approves the observations in UV−Visible absorption. This study leads to the realization of reusable membranes to be incorporated in practical biosensors for medical diagnosis.

Chapter 8 Hybrid Nanocomposite of Lead Sulfide Quantum Dots/Metalfree Phthalocyanine

This chapter presents the properties of a nanocomposite material consisting of lead sulfide (PbS) quantum dots (QDs) embedded in a matrix of octyl substituted metal-free phthalocyanine (C_8H_2Pc). This work was motivated by the first report of the synthesis of PbS quantum dots in hexyl substituted metal free phthalocyanine (C_6H_2Pc) by Nabok and coworkers in 2004. In this research, their work was carried forward for the characterisation and the compositional analysis of PbS/ C_8H_2Pc. The modified band gap and size of the PbS quantum dots have been estimated. Also, the interfacial interactions between the components of the nanocomposite material have been analysed. A special emphasis was given on the current hysteresis properties for applications in memristors. Analysis of pristine metalfree phthalocyanine was also carried out simultaneously for comparative studies.

8.1 Nanocomposite formation: Calculation of PbS QDs size and volume percentage

The preparation of the inorganic/organic hybrid nanocomposite containing PbS QDs/C_8H_2Pc matrix using octyl substituted liquid crystalline lead phthalocyanine (C_8PbPc, compound **1**) and H_2S precursor has been explained in Section 5.6 in Chapter 5.

To find out the components of the nanocomposite material, XRD patterns of H_2S treated drop cast film of Compound **1** was compared with the pristine C_8H_2Pc (compound **2**) and galena powder. The results of the XRD measurements are summarised in Table 8.1. The X-ray diffractogram in Figure 8.1a was obtained for the investigation into structural consequences of exposing drop cast films of compound **1** to H_2S gas for 24 hours. The peak positions at 25.98, 30.02, 43.04 and 50.87 are similar to those observed for powdered galena in Figure 8.1b. According to the JCDF cards No. 1-880, these peaks may be identified with the planes (111), (200), (220) and (311) corresponding to d-spacings of 0.34 nm, 0.29 nm, 0.21 nm and 0.18 nm of the face centred cubic lead sulfide (PbS) with the lattice parameter a = 0.59 nm (Machol et al., 1993). This value of the lattice parameter is in good agreement with the value of 0.59 obtained for powdered galena from Figure 8.1b. A comparison with the pattern-ray diffractogram of Figure (b) with (c) for the pristine spun film of Compound **2** implies the formation of hybrid nanocomposite films containing PbS quantum dots embedded in the matrix of Compound **2**, due to the removal of out-of-plane lead atom from Compound **1** by the reaction with H_2S. Values of the intensity ratio I_{111}/I_{200} were found to be 0.82 and 0.85 from Figure 8.1a and b, respectively. These compare well with the theoretical value of 0.80. The corresponding ratios of I_{220}/I_{200} are, on the other hand, estimated to be 0.40 and 0.63 from Figure 8.1a and b, respectively. The comparison with the theoretical ratio of 0.60 implies that the preferred orientation of PbS quantum dots is along the (200) plane (Patel et al., 2000). The average size of the PbS particles was estimated from Figure 8.1a to be 7.1±1.6 nm using the TOPAS software (see Section A3.1 in Appendix 3). This value is much smaller than its exciton Bohr radius of 18nm and the threshold size for the quantum confinement is reported to be less than 10 nm for ester capped PbS quantum dots (Liu et al., 2008). The broadening of the XRD peaks in Figure 8.1a is, therefore, believed to be caused by the quantum confinement. Spectra obtained at low angles of incidence 2θ from 10° to 20° presented in the inset indicate the structure of the phthalocyanine films (Baybliss, 1999; Zhang et al., 2004). As shown in Inset 8.1(i), the ratio of the peaks at 12.6° to the one at 13.5° is estimated to be 1 for the pristine film of Compound **2**, whereas this ratio becomes much higher for the nanocomposite film (inset 8.1 (ii)). The ratios of comparatively low intensity peaks at larger angles are significantly different between the two spectra. This observation is consistent with possible changes in the crystal orientation in the metal-free phthalocyanine matrix, perhaps due to the incorporation of PbS in the film (Deng et al., 2010).

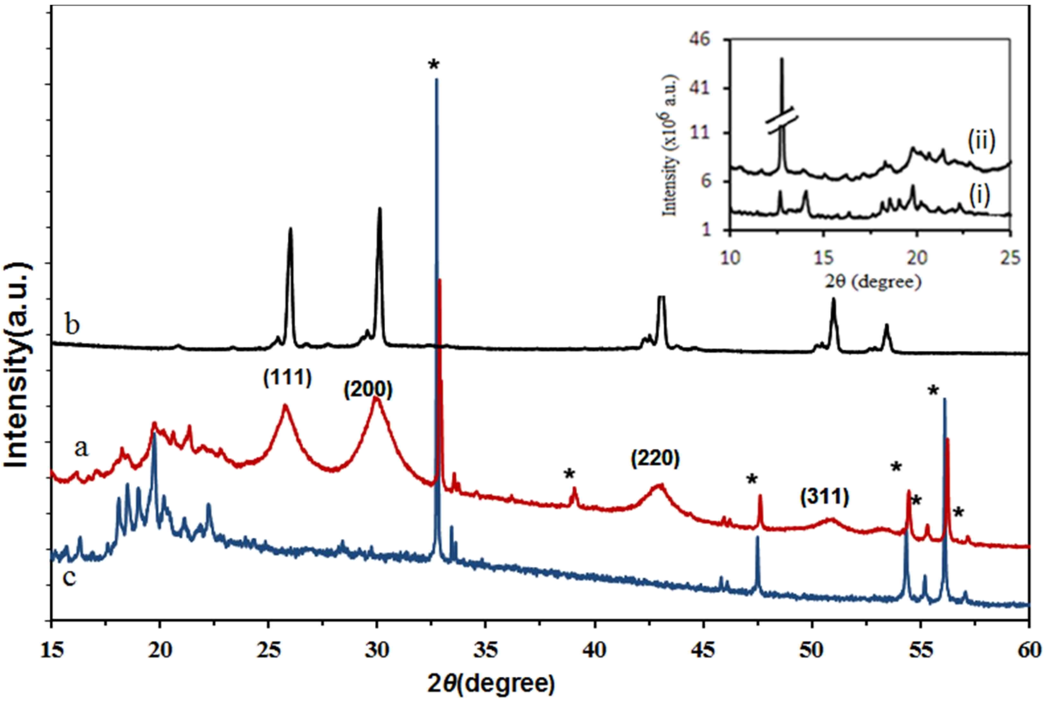

Figure 8.1: **X-ray diffractograms of (a) H_2S treated dropcast film of compound 1, (b) galena powder and (c) dropcast film of compound 2. (Inset) zoomed XRD of (i) compound 2, (ii) H_2S treated film of compound 1 in the low gazing angle**

Table8.1: **d-spacings and lattice indices of dominant reflections and peak orientation as featured in Figure 8.1**

2*θ* (°)		***d* (nm)**		**Intensity ratio**	
Compound 2	**H_2S treated Compound 1**	**Compound 2**	**H_2S treated Compound 1**	**Compound 2**	**H_2S treated Compound 1**
12.40	12.68	0.70	0.69		
13.98	13.29	0.62	0.66	1.00	0.27
18.07	14.51	0.48	0.60	0.83	0.26
18.48	15.85	0.47	0.55	0.89	0.26
19.58	18.21	0.45	0.48	1.09	0.29
19.84	19.68	0.44	0.44	0.85	0.32
21.08	20.11	0.41	0.43	0.76	0.31
22.22	21.31	0.39	0.41	0.84	0.32

The TEM image in Figure 8.2 was recorded for the H_2S treated films of Compound **1**. The dark spots marked in circles indicate the presence of PbS quantum dots, showing no obvious aggregation. Their average size was found to be 5.8±1 nm. This value agrees satisfactorily with one that previously obtained from XRD to within the experimental error. This correlation indicates a good degree of non-aggregation of the PbS quantum dots produced by this method for their synthesis (Nabok et al. 2004). The inset of figure 8.2 is the selective-area electron diffraction (SAED) pattern of the PbS QDs. The distances between the centre spot and the peripheral rings were found to be 6.75 µm and 9.25 µm as the radius of the SAED pattern. Values of the interplanar spacing *d* were estimated to be 0.29 nm and 0.21 nm for the crystal planes (200), (220) using the Formula 5.14 mentioned in Chapter 5. Both XRD and the selective-area electron diffraction pattern show that PbS quantum dots are polycrystalline.

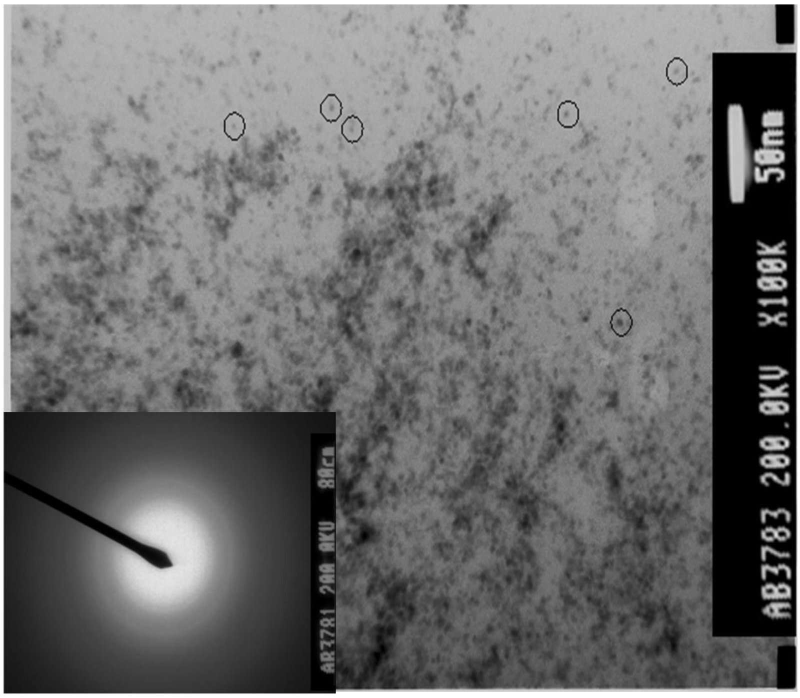

Figure 8.2: TEM images of H_2S treated dropcast film of Compound 1 withPbS quantum dots marked in circles and selective-area electron diffraction pattern of a PbS quantum dot

In order to determine their thermal stability, the thermogravimetric analysis (TGA) was carried out on the powdered samples under a nitrogen flow of 50 $mlmin^{-1}$ using a TA Instrument. Thermogravimetric analysis in figure 8.3 a and b shows the initiation of thermal decomposition of the H_2S treated films of Compound **1** at 200°C. Compound **2**, on the other hand, underwent thermal decomposition with a sharp drop in mass loss between 364°C and 442°C which has been reported to be the typical decomposition temperature of phthalocyanines (Bilgin, Ertem, and Gok, 2009).

The residue mass after heat treatment of the hybrid nanocomposite and compound **2** was found to be 17.2% and 6.1%, respectively at 700°. The PbS content in the H_2S treated film (g) was, estimated to be 11.1%. This is a reasonable observation in light of the fact that PbS as an ionic compound has a very high melting point. The volume fraction (x) of PbS quantum dots was estimated to be 2% from the following Equation 8.1 reported by RoyChoudhury et al., 2004.

$$x = \frac{\frac{g}{\rho_Q}}{\frac{g}{\rho_Q} + \frac{(1-g)}{\rho_o}} \tag{8.1}$$

The densities of PbS QDs (ρ_Q) and Compound **2**(ρ_o) are 7.60 g/cm^3 and 1.43g/cm^3, respectively (Patnaik, 2003; Erk and Hengelsberg, 2003; RoyChoudhury et al., 2004).

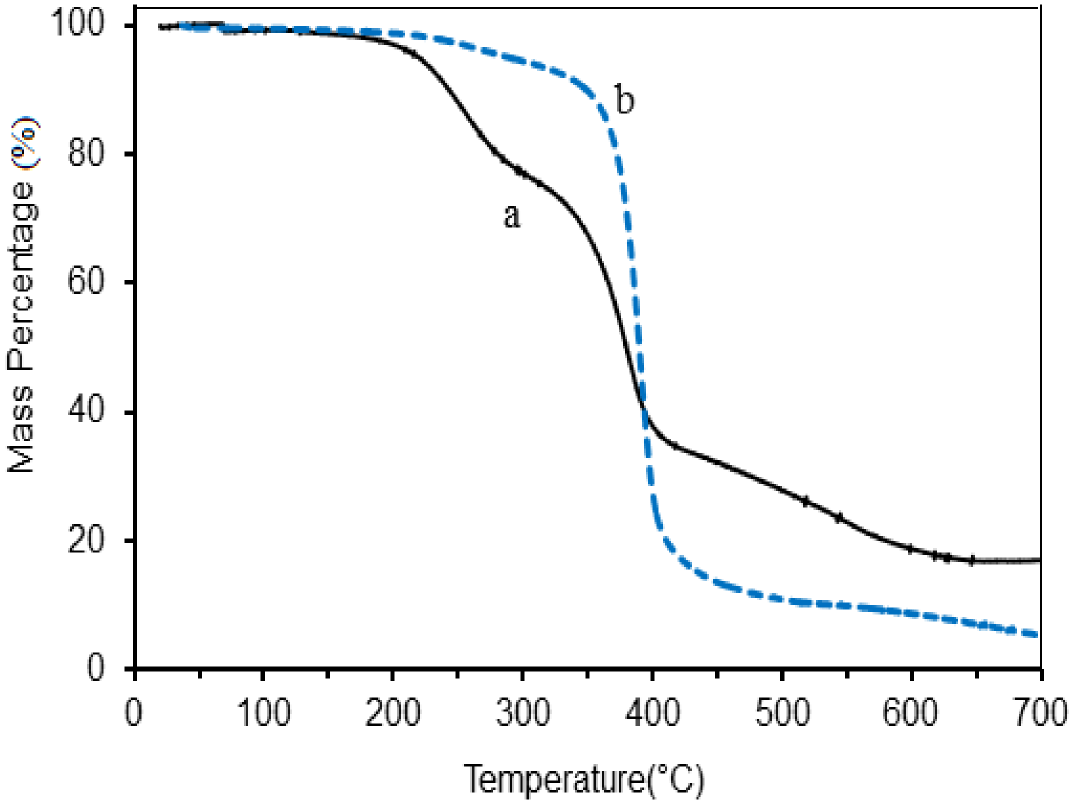

Figure8.3: TGA plots of (a) H_2S treated films of Compound 1 (soild line) and (b) pristine fim of Compound 2 (dash line)

Determination of band gap:

The UV-Vis spectra of H_2S treated compound **1** and compound **2** were recorded using a quartz at room temperature in the range from 300 nm to 850 nm. The spectrum of the H_2S treated film of Compound **1** in Figure 8.4a exhibits the peak positions of the split phthalocyanine Q band at 763 nm and 640 nm with a shoulder at 688 nm. The splitting is the characteristics for the metal-free phthalocyanines. The splitting is attributable to the Davidov splitting corresponding to the herringbone molecular structure of the film. The details about the origin of splitting have been explained by Kasha exciton theory in Section 2.3 of Chapter 2.

This absorption behaviour corresponds very well to that observed in Figure 8.4b for the pristine film of Compound **2**. However, enhanced absorbance was observed in the spectrum of the H_2S treated film of Compound **1** over the wavelength range from 300 nm to 400 nm which is attributable to the absorption by lead sulfide. The absorption in PbS in Figure 8.4c was obtained from the difference between spectra shown in Figure 8.4a and 8.4b for the wavelength range between 300 nm and 550 nm displaying the characteristic features of absorption in PbS nanoparticles (Yofee, 2001; Wang et al., 2001).

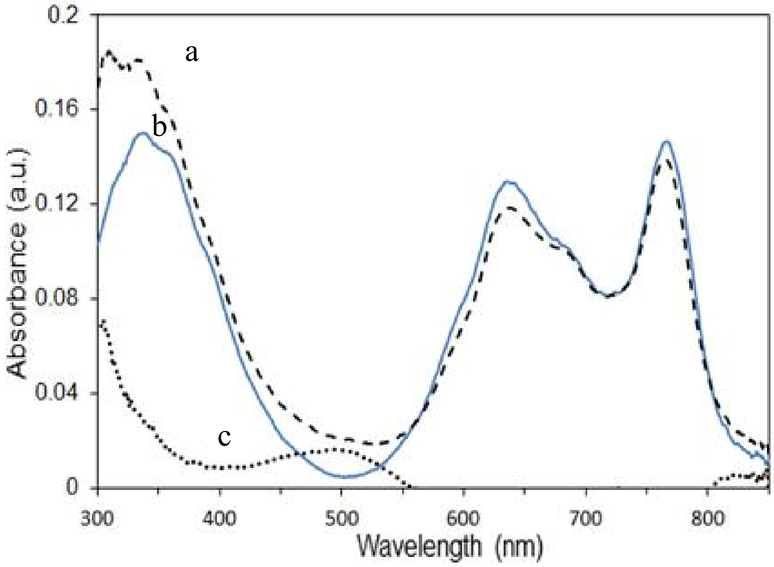

Figure 8.4: Optical absorption spectra of (a) H_2S treated spun film of Compound 1 (dash line) (b) spun film of Compound 2 (solid line) (c) PbS after subtracting (dotted line) (a) from (b)

The band gap of the PbS QDs was calculated using Tauc law. In 1972, the relationship between the band gap and absorption coefficient was derived by Tauc and Menth as follows.

$$\alpha_{\mathrm{a}} = \frac{C}{hv}(hv - \Delta E)^{\mathrm{m}} \qquad (8.2a)$$

where, α_{a} is the absorption coefficient, C is a constant, hv is the photon energy and ΔE is the band gap energy. The symbol m signifies the nature of electronic transitions associated with optical processes. The value of m was reported to be equal to ½ where the electronic transitions associated with the direct optical transitions. In this case, the momentum energy of electrons does not change by excitation from valence band to conduction band. The value of m is equal to 2 for indirect transition (Streetman, 1980). PbS has been reported to be a direct band gap material (Wang et al., 1987). Considering $A_t = \alpha_{\mathrm{a}} d_{\mathrm{a}}$, where A_t is the absorbance of the film, d_{a} is the path length. Equation (8.2a) can be rewritten as

$$(A_{\mathrm{t}} hv)^2 = C'(hv - \Delta E) \qquad (8.2b)$$

Where C' is a constant.

Therefore, to estimate the band gap the plot of $(A_t hv)^2$ versus hv was drawn in the figure 8.5. The plot was found to be linear. The ratio of the slope to the intercept of the ordinate extrapolated to produce a value of 2.22 eV for the optical band gap for PbS quantum dots. This value is significantly larger than that obtained for the bulk PbS band gap of 0.41eV at 298 K with an absorption onset at 3200 nm (Patel et al., 2000). This arises from the quantum confinement of charge carriers in PbS quantum dots with the relatively small effective mass of electrons (Zhang, Zhang, and Jiang,2003) and is dependent upon the size, stoichiometric ratio and passivating ligands of PbS quantum dots (Moreels et al., 2009; Kim et al., 2013).

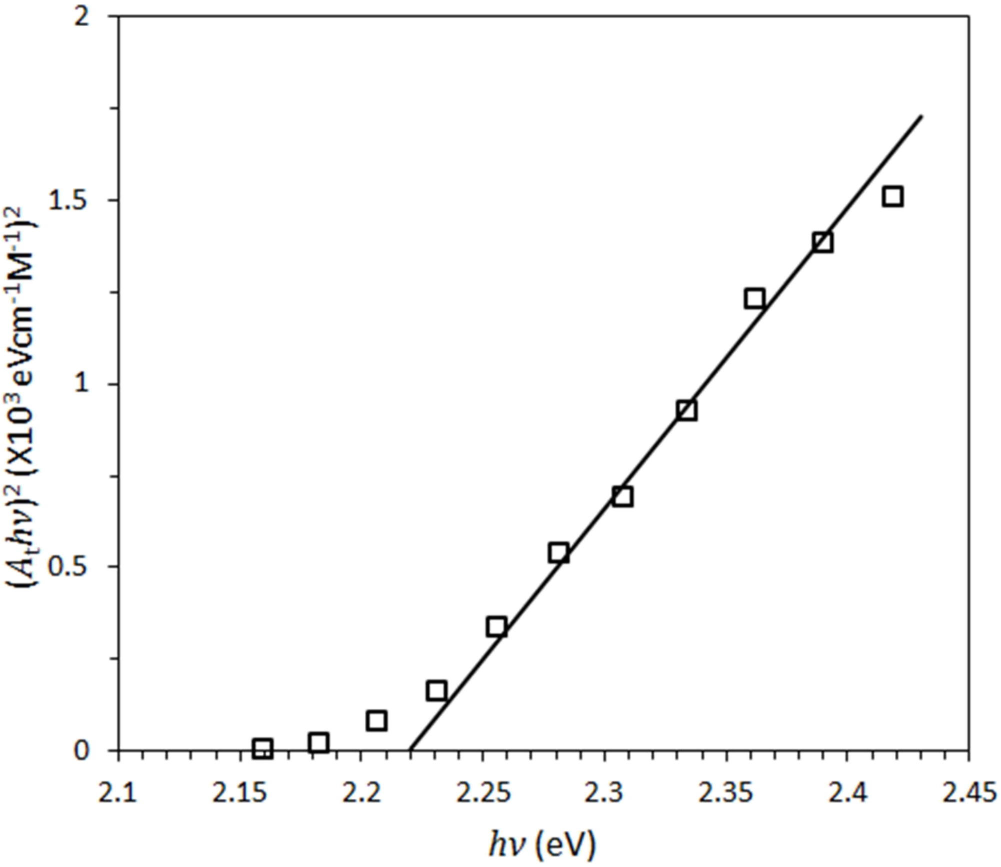

Figure 8.5: Tauc plot of $(A_t h\nu)^2$ versus $h\nu$ to calculate the band gap energy

8.2 Interfacial interactions

Raman spectra of compound **1**, H_2S treated dropcast films of Compound **1** and Compound **2** are presented in figure 8.6(I). Raman active bands for Compound **1** with a C_{4v} symmetry, are A_1, B_1 and E as reported by Zhang et al., 2006. The Raman bands between 734-1000 cm^{-1} in this compound are related to Pc ring vibrations in (a). The bands at 1010 cm^{-1} and 1235 cm^{-1} can be assigned as C-H bending of the benzene rings while the range of the spectrum in 1350-1600 cm^{-1} is linked to the isoindole and aza stretchings (Zhang et al., 2006). This region is considered as marker band of phthalocyanines which is sensitive to the central ion present (Tackley, Dent, and Smith, 2001). The highest intensity peak was noted at 1379 cm^{-1}.

Significant changes were noticed in the bands of compound **1** between 1350-1600 cm^{-1} after exposure in H_2S gas (Figure 8.6(I) a and b). An XRD result has already revealed one of the products after the reaction as compound **2** which is C_8H_2Pc. Pristine C_8H_2Pc

is regarded to have A_g and B_{1g} Raman active modes as being a D_{2h} symmetric molecule (Zhong, Zhang, and Bian, 2010). The assignments of the compound **2** Raman active bands have been summarised in Table 8.2. From figure 8.6 it can be noted that the band at 1379 cm^{-1} of compound **1** is absent in compound **2**. This is most probably owing to the change of symmetry from C_{4v} to D_{2h} after removal of Pb(II) from lead phthalocyanine . A similar result was reported with unsubstituted zinc phthalocyanine (ZnPc), before and after methanol exposure. An investigation of low temperature ZnPc Raman spetroscopy showed an increase in the intensity of 1331 cm^{-1} peak during the course of reaction between ZnPc and methanol. This was explained as lift of planarity from D_{4h} to C_{4V} symmetry of ZnPc (Szybowicz et al., 2007). The absence of 1326 cm^{-1} band in H_2S treated compound **1** indicates the complete reaction and absence of compound **1** in the nanocomposite.

On comparing the Raman bands of H_2S treated compound **1** and pristine compound **2**, it was confirmed that Figure (b) and (c) are showing no appreciable shifts of peak positions. The peak positions with their Raman vibrational assignments of both the compounds are summarised in Table 8.2. The bands at 1097 $cm^{-1}$and 1522 cm^{-1} which remain relatively more defined from adjacent peaks are identified with non-totally symmetric B_{1g} and totally symmetric Ag active modes (Murrey et. al., 2010). A_g modes are not sensitive to charge-transfer effect while B_g modes are highly sensitive to charge-transfer contributions (Fu et al., 2011). The relative intensity change between these two peaks is higher for H_2S treated Compound **1** than for Compound **2**. The degree of charge transfer is estimated to be 0.39 for H_2S treated Compound **1** and 0.29 for compound **2**, respectively from the ratio of the intensities. As reported by Fu et al., 2011 the degree of charge-transfer depends upon the excitation wavelength and the PbS quantum dot size.

As PbS being a weak Raman scatterer it undergoes degradation under high laser power. A lower scan rate experiment with low laser power was carried out for Raman band of PbS. The Figure 8.6(II)a and b shows Raman peak at 480 cm^{-1} for both bulk PbS and PbS QDs, respectively. This peak is attributed to the vibration of longitudinal optical phonons by Upadhyaya, Yadav and Upadhyaya, 2002.

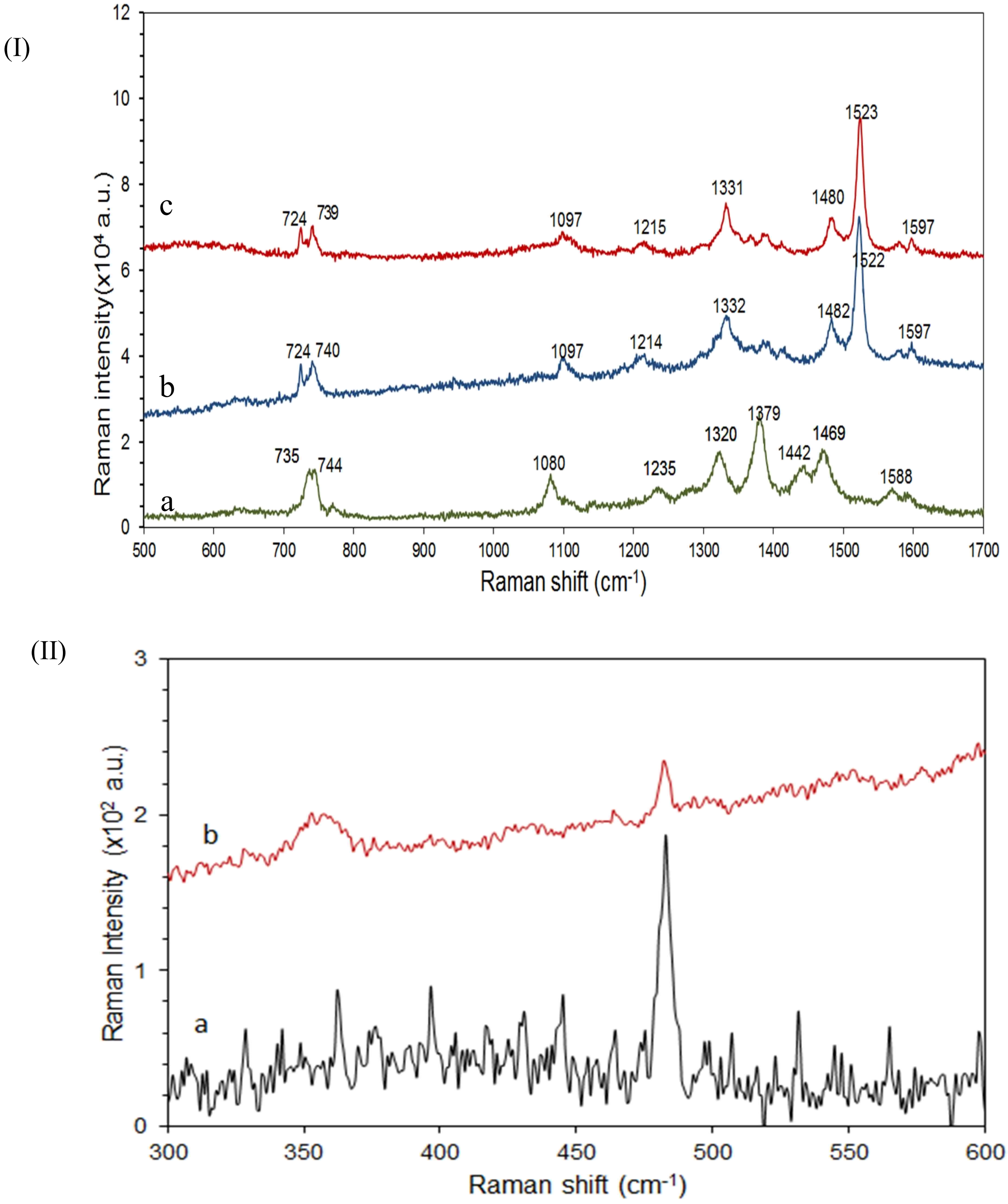

Figure8.6: **(I) Raman spectra of dropcast films on glass of (a) compound 1, (b) H_2S treated Compound 1 (c) compound 2 (II) (a) Galena (b) H_2S treated Compound 1**

Table 8.2: Raman shifts (cm^{-1}) for Raman spectroscopy using 532nm laser illustrated in Figure 8.6

Raman shifts (cm^{-1})		Symmetry	Vibrational assignment	References for vibrational assignment
Compound 2	H_2S Treated Compound 1			
724	724	A_g	C-H, N-H bending	Zhang, Zhang, and Jiang,2003
739	740	A_g	Pc ring defs., N-H bending, isoindole str.	Zhang, Zhang, and Jiang,2003
1097	1097	B_{1g}	N–H and C–H bending, isoindole str., Pc ring def.	Zhang, Zhang, and Jiang,2003
1215	1214	B_{1g}	C-H def.	Murray et al., 2010
1331	1332	A_g	Pyrrole and isoindole str.	Murray et al., 2010
1480	1482	A_g	Pyrrole and isoindole str.	Murray et al., 2010
1523	1522	A_g	N–H bending, C–N (aza) str.	Zhang, Zhang, and Jiang,2003
1597	1597	A_g	Benzene str.	Murray et al., 2010

Str.=Stretching,def.=deformation

XPS data in Figure 8.7 show peaks corresponding to different atomic orbitals. The binding energies were estimated from Figure 8.7a to be 138.7 eV and 143.4 eV for $Pb4f_{7/2}$ and $Pb4f_{5/2}$ orbitals, respectively for PbS within the spun films of H_2S treated Compound 1. The Figure 8.7b shows the binding energy of $S2p_{3/2}$ and $S2p_{1/2}$ at 159.5 eV and $S2p_{1/2}$ at 162.8 eV. Similar values were obtained for PbS quantum dots produced by precipitation of methanolic lead acetate–thiourea (Patel et al., 2012). These values also compare well with the corresponding standard values of 137.2 eV and 142.1eV for Pb4f including 159.2 and 161.9 for S2p in case of bulk galena (Wagner et al., 1979). The broad peak at around 169 eV in Figure 8.7b can be associated to the presence of sulphur dioxide (SO_2) on the surface (Nabok et al., 2004). The binding energy of the N1s signal of the organic component of H_2S treated compound 1 was found to be 399.6 eV, slightly higher than 398.4 eV obtained for Compound **2**. The peaks of Pb4f and S2p show an increase of binding energy compared to the bulk PbS. This observation supports the conclusion from Raman spectroscopy regarding the charge transfer between the nanocomposite components (Murray et. al., 2010).

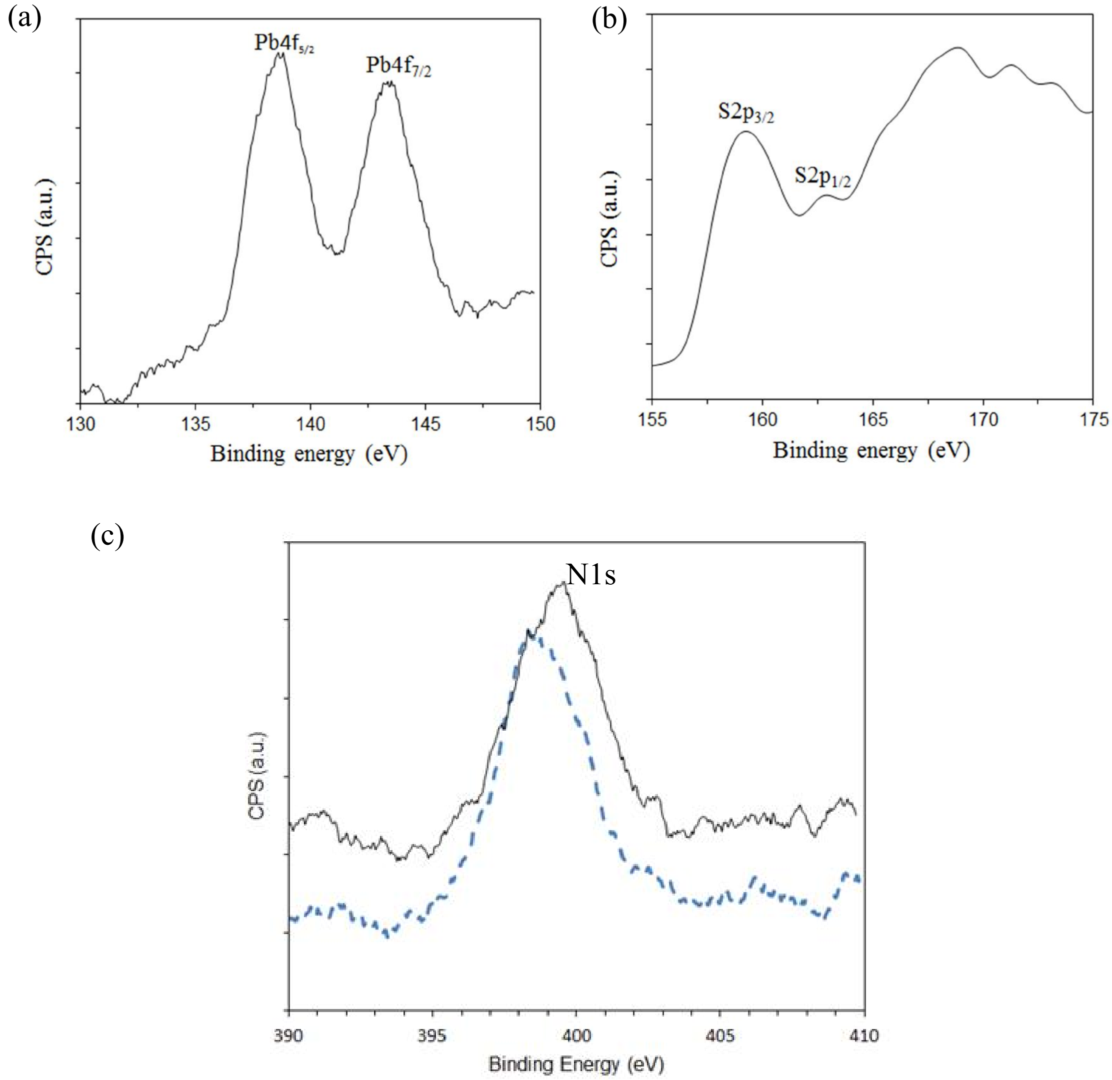

Figure 8.7: XPS spectra of (a) Pb-4f orbital of PbS QDs (b) S-2P orbital of PbS QDs and (c) N-1S orbital of H_2S treated Compound 1 (solid line) and pure H_2Pc (dash line)

8.3 Photoluminescence property of the nanocomposite material

Figure 8.8a and b shows the photoluminescence (PL) emission spectra of ca. 3µm thick films of pristine Compound **2** and H_2S treated Compound 1 in the range 365-800 nm at excitation wavelength 300 nm. Three emission bands were observed at around 446 nm, 665 nm and 776 nm for the films of Compound **2**in (b). The position and relative intensities of these PL bands correlate well with the corresponding phthalocyanine B and Q absorption bands respectively (Sun, Ma, and Jiang, 2003; Yosino et. al., 2000). Presence of a single band at 380 nm with splitting and disappearance of 662 nm bands were observed for the films of H_2S treated Compound 1 in (a). A shoulder at 526 nm and a peak at 821 nm were also observed in this case. However, the thin film (ca.20 nm) of H_2S treated compound 1 did not show any considerable differences from pristine compound **2**.

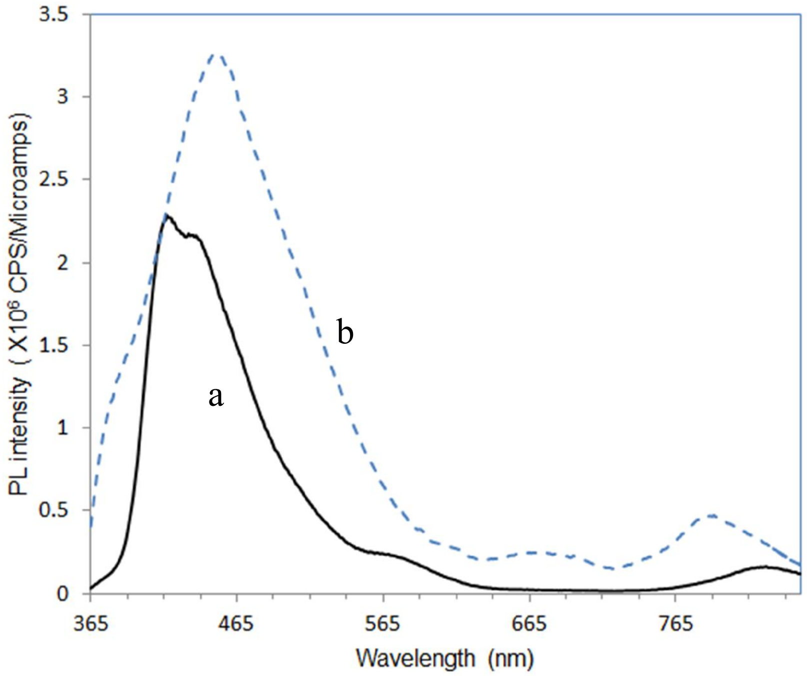

Figure 8.8: PL emission spectra of the dropcast film of (a) H_2S treated Compound 1 (solid line) and (b) Compound 2 (dash line)

To explain the origin of splitting and quenching of photoluminescence, PL spectra was obtained for Compound **2** as a solution in toluene at different concentrations from 0.007 $mgml^{-1}$ to 0.6 $mgml^{-1}$. In comparison to the solid phase, two broad and blue-shifted PL emission bands at 345 nm and 745 nm were observed for the lowest concentration of 0.007 $mgml^{-1}$. These bands became broader and suffered greater quenching with the rise in concentration. The latter can be attributed to increasing aggregation of the Pc molecules (Freyer, Neacsu and Raschke, 2008). Therefore, it can be suggested that the splitting in the 300-400 nm emission bands appears in the presence of less aggregated species or monomers. From the solution phase study, the splitting in the H_2S treated compound 1 in the figure 8.8 of thin film spectra can be attributed to the less Pc-Pc interaction of the incorporated PbS quantum dots in the Pc matrix (Figure 8.9 inset). Nabok and coworkers suggested a similar result by studying the optical absorption spectra of the octahexyl substituted lead phthalocyanine film after exposure in H_2S (Nabok et al., 2004).

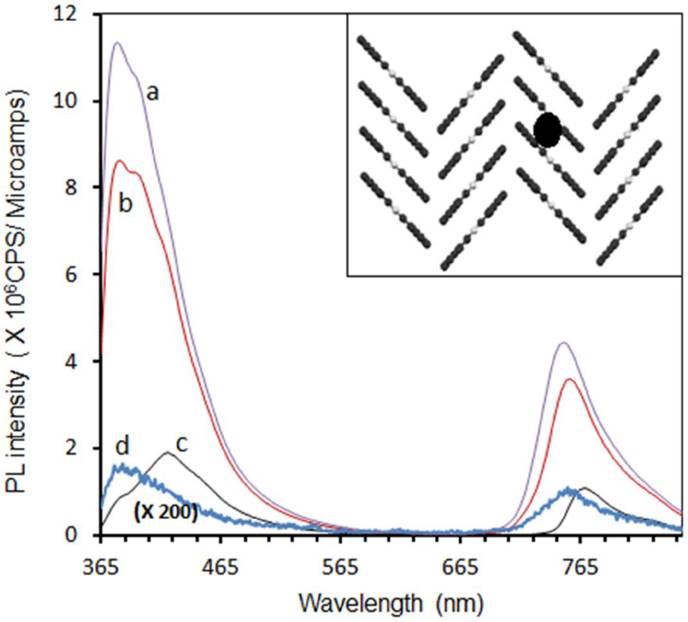

Figure 8.9: **PL emission spectra of solution of Compound 2 in toluene at different concentration in mgml^{-1} (a) 0.007 (purple line), (b) 0.018 (red line), (c) 0.071 (black line), (d) 0.6 (blue line). Excitation wavelength λ_o is 300 nm. (Inset) C_8H_2Pc film structure with PbS quantum dots**

Current hysteresis

For electrical measurements, the films were deposited on an interdigitated gold electrode system. Figure 8.10a shows a set of reproducible room temperature in plane current-voltage [I-(V_a)] characteristics of H_2S treated Compound 1 deposited on gold electrodes when the applied voltage V_a was swept over the voltage range of ±50V at four different scan rates from 5 mVs^{-1} to 5000 mVs^{-1}. In all cases, the direction of the current in the forward voltage sweep (0V → 50V and -50V →0V) is reversed in the backward sweep

(0V ← 50V and 0V ← -50V), and shows a scan rate dependent hysteresis. For the sake of clarity, the forward characteristics are given in Figure 8.10b, showing a rise in current with increasing scan rate for all values of the applied voltage V_a.

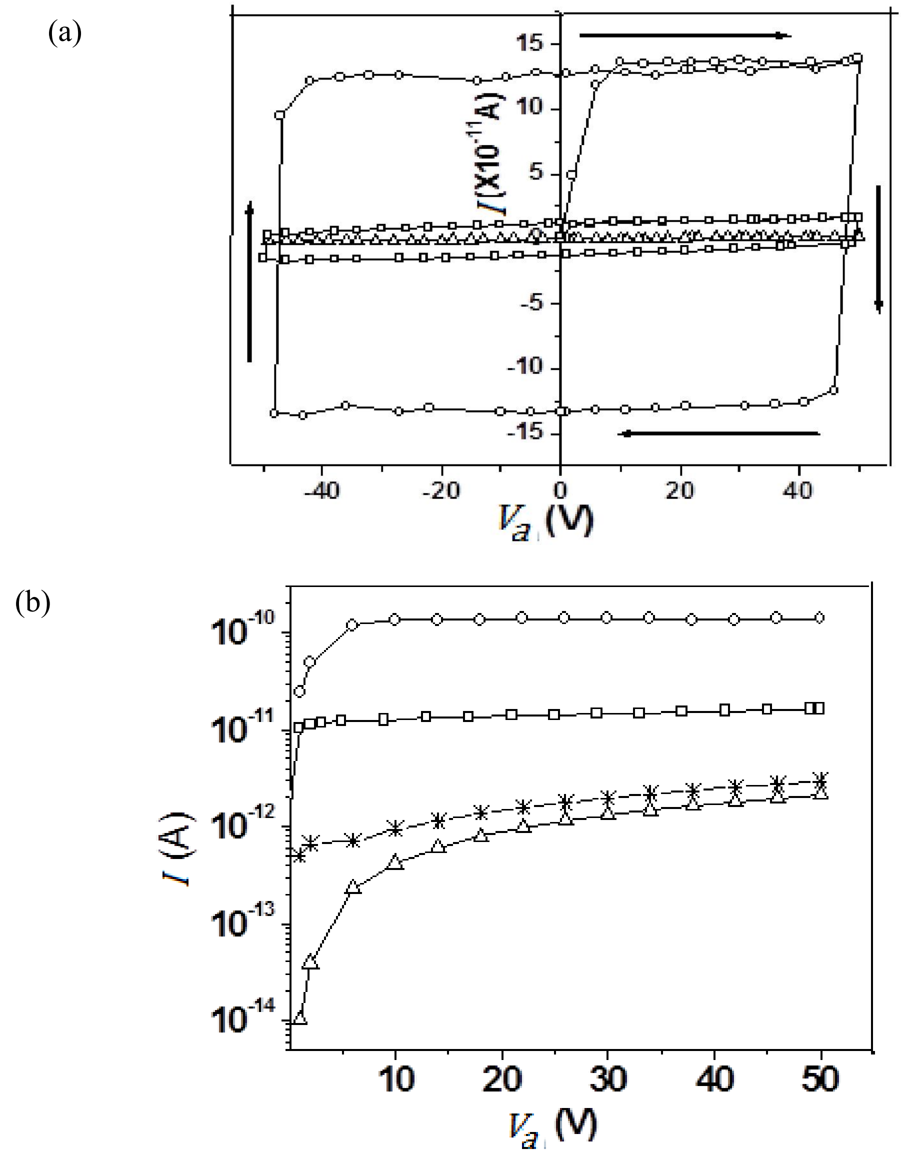

Figure 8.10: (a) Current versus applied voltage [I-(V_a)] graphs of H_2S treated compound 1 as the applied voltage V_a is swept from 0 to 50V in the forward and backward directions at the scan rate of 5mVs^{-1} (triangle), 500mVs^{-1} (square) and 5000mVs^{-1} (circle), arrows show the voltage sweep; (b) Forward [I-(V_a)] characteristics of H_2S treated compound 1 at the scan rate of 5mVs^{-1} (triangle), 500mVs^{-1} (square) and 5000mVs^{-1} (circle)

The current level is, however, of the same order of magnitude as the one obtained for Langmuir-Blodgett films of bis-hydroxyl hexaoctyl metal free phthalocynine (Ray et al., 1999). Similar scan rate dependent hysteresis loop has been reported by Majumdar, Bandyopadhyay, and Pal 2003 for nickel phthalocyanine based memory storage device.

Measurements were also performed on the spin coated films of Compound **2** in a similar device configuration and the results are shown in Figure 8.11 for the scan rate of 500 mVs^{-1}. The hysteresis is found to be more pronounced in the I-(V_a), characteristic of H_2S treated Compound 1 than Compound **2**. The hysteresis loop area for the compound **2** was calculated as 1.43×10^{-9} watt whereas the H_2S treated films of Compound 1 the value was 2.25×10^{-9} watt by the numerical integration method. The two well defined high and low conducting states are common characteristics of the memristors devices as described in Section 3.3 in Chapter 3.

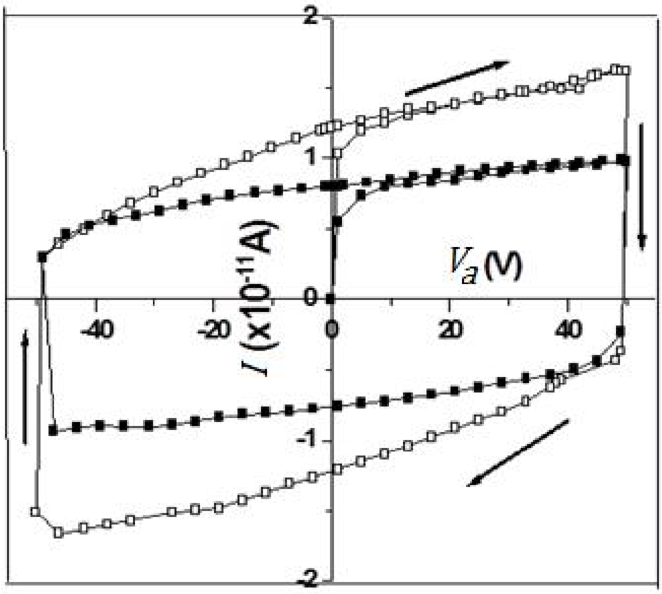

Figure 8.11: Current versus voltage [I-(V_a)] of H_2S treated compound 1 (open square) and compound 2 (solid square) for 500 mVs^{-1}, arrows show the voltage sweep

The effect of the scan rate on the planar charge transport in both films can be interpreted in an equivalent circuit model. The circuit consists of two passive electrical components, resistor *R* and capacitor *C*, connected in parallel as displayed in figure 8.12.

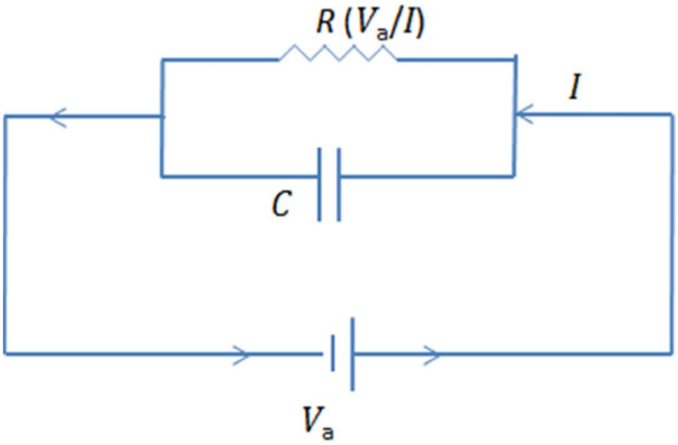

Figure 8.12: Equivalent circuit model for planar charge transport

The net current is the sum of the circulating current and displacement components in the form:

$$I = \frac{V_a}{R} + \frac{dV_a}{dt}\left[V_a \frac{dC}{dV_a} + \frac{\tau}{R}\right] \qquad (8.3)$$

Where$\tau = CR$ is the charging and discharging time constant.

Figure 8.13a shows the dependence of the short circuit current I_{sc}, open circuit voltage V_{oc} and the hysteresis loop on the scan rate of the applied voltage V_a. The linear increase of I_{sc} with the scan rate$\frac{dV_a}{dt}$ for both samples is in consistent with the observation from Equation (8.3) that $I_{sc} = \frac{\tau}{R}\frac{dV_a}{dt}$ corresponding toV_a=0.The open circuit voltageV_{oc} can be written as $V_{oc} = \left[\dfrac{-\frac{\tau}{R}\frac{dV_a}{dt}}{\frac{1}{R} + \frac{dV_a}{dt}\frac{dC}{dV_a}}\right]$ for I=0 . The gold forms an Ohmic contact with metal free phthalocyanine (Fan and Faulkner, 1978) and the value of the capacitance C may thus be taken to be determined by the geometry, dimension and dielectric constant of the compounds, making$\frac{dC}{dV_a} = 0$. Therefore, the linear rise of V_{oc} with the scan rate in Figure 8.13 (b) is also expected from Equation (8.3). Values of time constant τ for films of H_2S treated compound **1** and compound **2** are estimated to be 95 seconds and 78 seconds from the slopes of the graphs. The area of the hysteresis loop also increases with the scan rate as shown in Figure 8.13c for both the compounds. Values of room temperature Ohmic conductivities are estimated to be 1.66 μSm^{-1} and 2.74 μSm^{-1} for Compound **2** and H_2S treated Compound 1, respectively. The sweeping time decreases with the increasing scan rate and this time for the fast scan rates becomes shorter than the time constant τ. Under these circumstances, the majority of the carriers are swiftly swept from the injecting gold electrode finger to the counter electrode contributing largely to the circulating current $\frac{V_a}{R}$. The trap-detrapping mechanisms become progressively slow as the scan rate is increased.

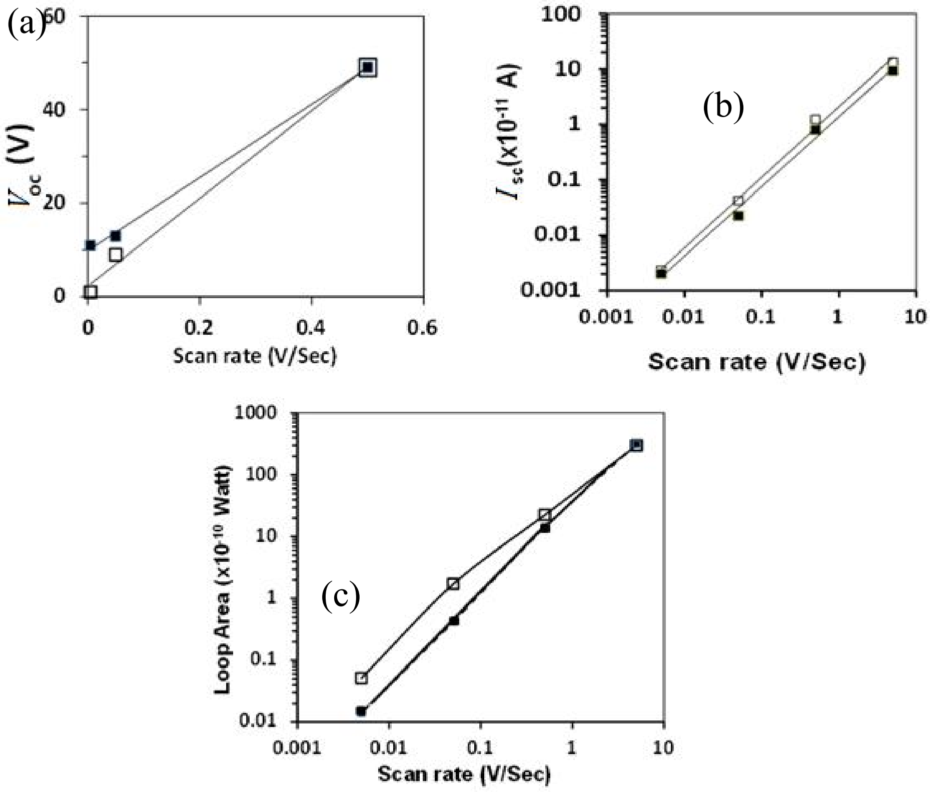

Figure 8.13: Dependence of (a) open voltage, (b) short circuit current for H_2S treated compound 1 (open squares) and compound 2 (solid squares). (c) area of hysteresis loop with scan rate for H_2S treated compound 1 (open squares) and compound 2 (solid squares)

8.3 Charge transport in nanocomposite compound

To find out the conduction mechanism in the H_2S treated compound **1**, *I-(V*$_a$*)* characteristics were monitored in the temperature range of 87K-430K. The current at voltage 50 V was noted in the entire temperature range for H_2S treated compound **1** and plotted in Figure 8.14. Three different mechanisms were responsible for charge transport over the entire temperature range. Almost temperature-independent behaviour was noted in the temperature range 87K≤T≤220K in region (i). At higher temperature 220K≤T≤302K, the region (ii) indicates temperature dependent conduction behaviour. Region (iii) shows a sharp rise of current with increasing temperature in the range 330K≤T≤ 430K.

From the slope of the Arrhenius plot in the inset of figure 8.14, activation energy was determined as 0.4± 0.1 meV in region (i) which is much below the thermal energy, $k_B T$ (Where k_B is the Boltzmann constant and T is the temperature). This can be attributed to the tunnelling through the quantum barriers between the molecular domains (Hurd, 1985).

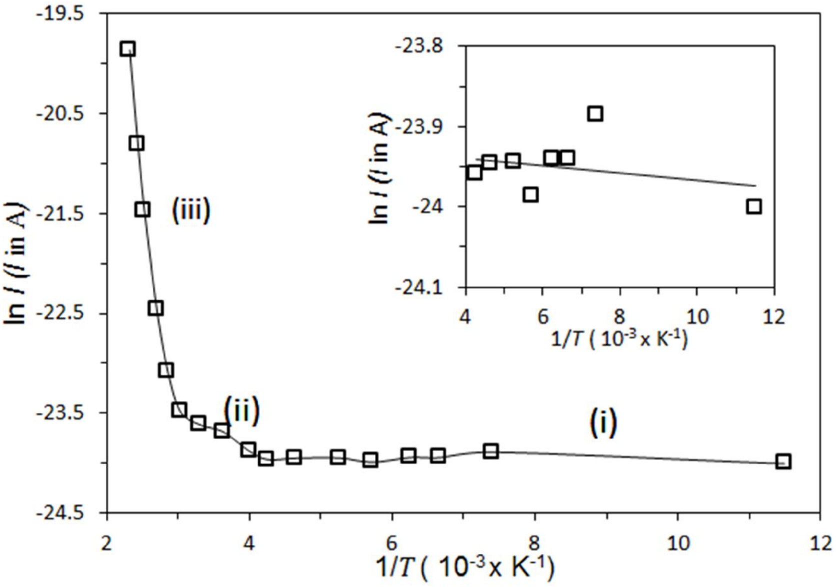

Figure 8.14: ln *I* versus 1/*T* in the temperature range 87K-430K for H2S treated compound 1 at applied voltage 50 V. (Inset) Zoomed plot of ln *I* versus 1/*T* in the temperature range 87K-220K for H_2S treated compound 1 at applied voltage 50V

At higher temperature 220K≤T≤302K, the region (ii) the plot of $\ln(I\sqrt{T})$ versus $T^{-1/4}$ at 50V applied voltage in Figure 8.15 shows straight line behaviour which can be designated as hopping in the localized band-tail states. Mott and Davis, 1971 described this charge transport as Variable range hopping (VRH) which is a common phenomenon for non-crystalline semiconductors like phthalocyanine with large band gap. In this case, weakly localized states exist below the conduction and above the valence bands due to the weak wave function overlap between adjacent molecules. In low temperature, on application of potential the charge carriers hop from one localized state to another in the band edge (Figure 4.4 in Page 59, Chapter 4). Khan et al., 2004 have studied the conduction mechanism in amorphous $Se_{75}In_{25-x}Pb_x$ (x=0 to 10). The band gap of the Se-In complex has been reported to be 1.3 eV which is in order of the phthalocyanines (1 to 3 eV).

Employing the Equations (4.7) explained in Chapter 4 in Page 60, the slope of the graph can be expressed as $(T_0)^{1/4}$ where, T_0 is $\frac{16\alpha_0^{3}}{k_B N_0}$. The value of intercept is $\ln\left(\frac{2AV_a\upsilon_{ph}}{L}\right) + \frac{1}{2}\ln(\frac{9N_0}{8\pi\alpha_0 k_B T})$. Here, T_0 is the characteristic temperature, N_0 is density of states, A is area of electrodes, υ_{ph} is the Debye frequency, α_0 is the inverse of the site localization parameter. The values of T_0, N_0 were measured as 1.05×10^{6} K, 6.11×10^{18} cm^{-3} eV^{-1} from Figure 8.15. The optimum hopping distance (S_H) was determined as 9.05 nm from Equation (4.8) in Page 60.

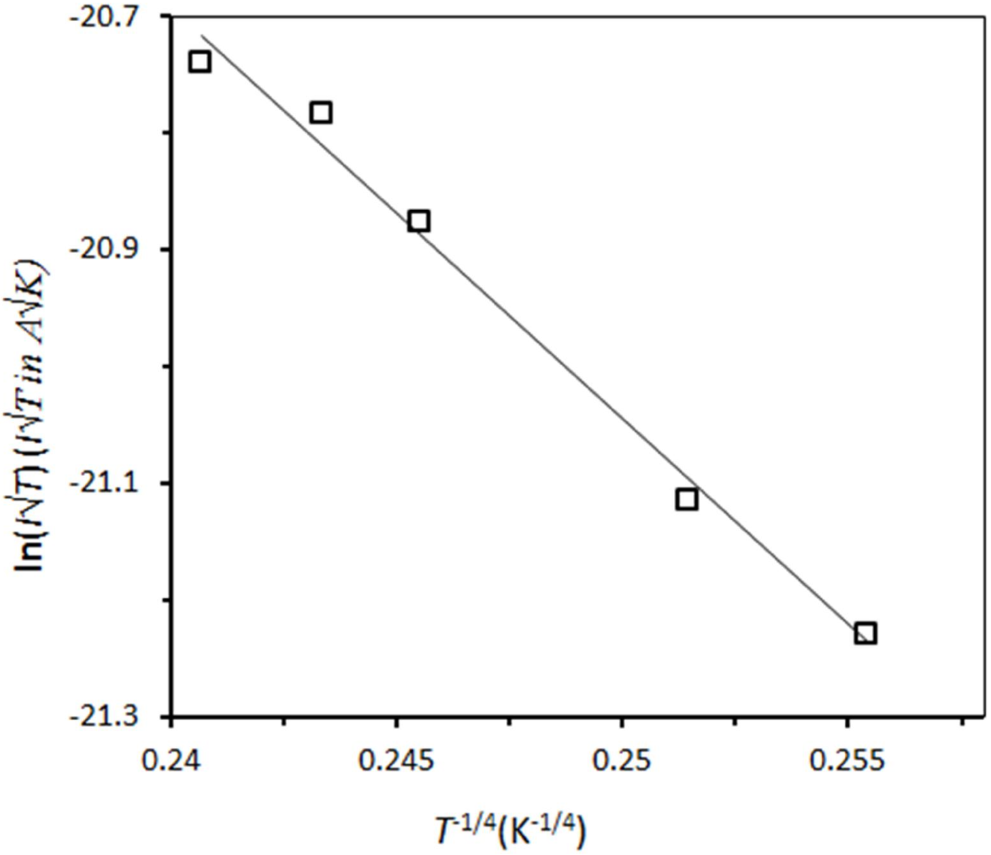

Figure 8.15: ln($I\sqrt{T}$) versus $T^{1/4}$ for H_2S treated compound 1 in the temperature range 235K-302K at applied voltage 50V

From figure 8.16 ln *I* versus 1/*T* was plotted corresponding to the region (iii) of plot 6.13. A sharp rise of current can be observed with changing the temperature from 302-430 K. The activation energy for the conduction was calculated as 0.43±0.02 eV using the Arrhenius equation mentioned in Equation 4.8, Page 61, Chapter 4. This activation energy is related to the charge carrier transition between the valence and conduction band which is also called as band edge conduction.

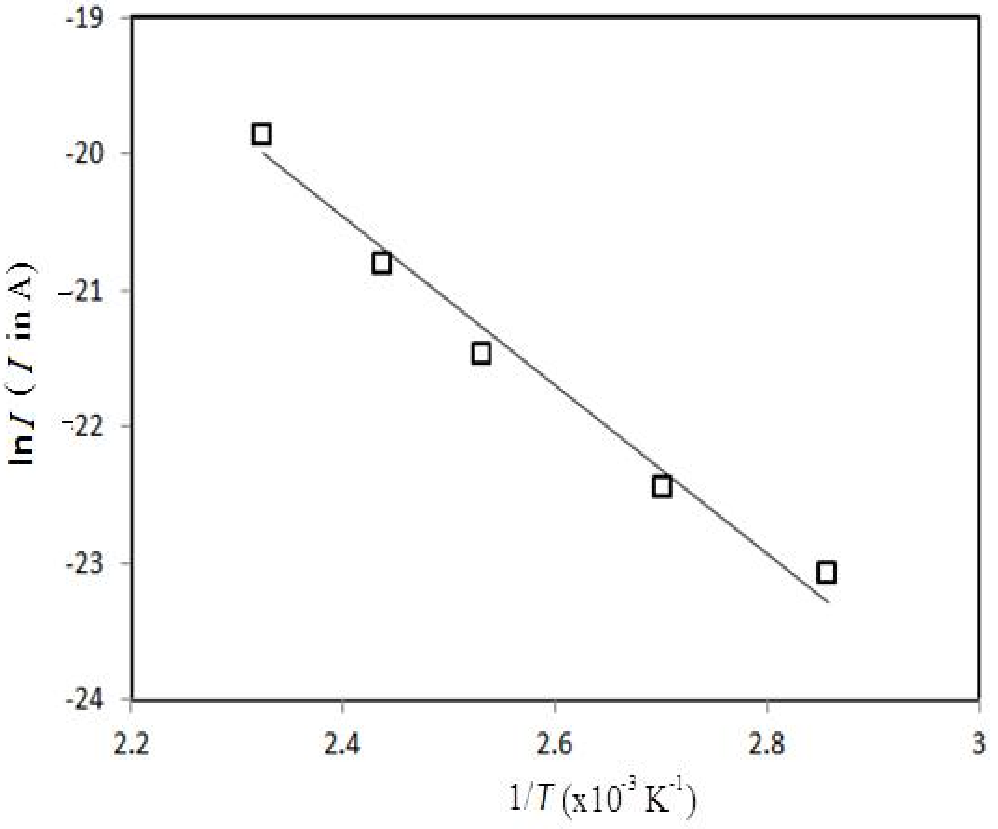

Figure 8.16: **ln I versus 1/T in the range of temperature 330K-430K for H_2S treated compound 1 at applied voltage 50 V**

8.4 Chapter summary

Nanocomposite PbS quantum dots of an average size of 5.8 nm and band gap of 2.22 eV were successfully produced on metalfree phthalocyanine matrix exploiting the non-planar structure of C_8PbPc. The XRD and TEM studies confirmed the presence of PbS QDs. The particle size calculated by TEM was well in agreement with the crystallite size from XRD study. A very low aggregation of the QDs in the film can be inferred. The volume fraction was estimated as 2% in the matrix.The increasing concentration of the QDs is useful for device applications as it makes a conductive pathway and helps carrier to flow (RoyChoudhury et al., 2004).

Photophysical quenching was found in the presence of quantum dots, indicating the incorporation of the QDs in the lattice structure of the metalfreephthalocyanine matrix.

In addition to the distribution of QDs in the host matrix, the interfacial interactions between the components also help to enhance the charge flow between the materials. The opencircuit voltage, short circuit current and Ohmic conductivity increased with the 2% of volume PbS quantum dots in the matrix. In Table 8.3 the compositional analysis and electrical parameters for the planar electrodes of H_2S treated compound 1 and pristine compound 2 have been summarised.

Table 8.3:Electrical parameters of H_2S treated compound 1 and compound 2 on gold interdigitated electrode at room temperature and dark

Materials	Composition analysis			Electrical parameters on gold interdigitated electrode at scan rate 0.5 Vs^{-1}				
	PbS (%)	***D*** **(nm) (±1)**	**ΔE (eV)**	**Loop area (Watt)**	**σ_x (μSm^{-1})**	**τ (seconds)**	**I_{sc} (A)**	**V_{oc} (V)**
H_2S treated Compound 1	2	5.8	2.22	2.25×10^{-9}	2.74	95	1.22×10^{-11}	50
Compound 2	0	---	---	1.43×10^{-9}	1.66	75	8.00×10^{-12}	50

The hopping distance of charge was measured as 9.05 nm by temperature study of I-(V_a) characteristics. In the case of H_2S treated compound **1**, the value of 9.05 nm is still below the percolation limit 5.8 nm for PbS QDs. However, the gap between the particles may have contributed to the displacement current in the hysteresis loop in figure 8.11 by trapping and de-trapping of charge. This behaviour of the nanocomposite compound has potential application in memristors.

Chapter 9 Conclusions and future work

9.1 Conclusions

Four non-peripherally substituted liquid crystalline (LC) phthalocyanine (Pc) compounds, viz. C_8LuPc_2, C_8GdPc_2, C_6GdPc_2, and C_8PbPc were studied in this research work. The experiments for the characterisation of liquid crystalline bisphthalocyanines C_8LuPc_2, C_8GdPc_2, C_6GdPc_2enhance our understanding of the structure-property relationship by introducing different metal ions, or substituents and the post deposition heat treatment of the films. The compound C_8PbPc was used to produce a hybrid nanocomposite comprising of lead sulphide and octyl substituted metal-free phthalocyanine analogue (C_8H_2Pc).

The solution-processible liquid crystalline phthacolyanines were deposited by easy and cost-effective spin-coating methods suitable for fabricating stretchable or bendable circuit boards. A smaller Pc-Pc distance was found in C_8LuPc_2 with respect to the Gd-derivatives due to the smaller size of the central metal ion. The blueshift of electronic and Raman spectra in C_8LuPc_2 in comparison to the other two compounds C_8GdPc_2 and $C_6GdPc_2$was attributed to the size effect of the central metal ion. The conduction of the three molecules on gold interdigitated electrodes was mainly bulk limited. Ohmic conduction was followed by Poole-Frenkel conduction at high voltage. An increase of conductivity in the discotic liquid crystalline mesophase of the octyl substituted compoundswas explained as slipped stack columnar alignments of the monomers. On the other hand, the molecular arrangement in the discotic mesophase of C_6GdPc_2 was explained as face-to-face stacking. The two orders of magnitude decrease of conductivity in mesophoric C_6GdPc_2 with respect to the as-deposited state may be associated with the direction of the molecular orientation on the substrate.

Oxidation of octyl substituted lutetium and gadolinium bisphthalocyanine films using Br_2 vapour or applying certain potential was proved to be effective by redshifts in optical absorption spectra. The quasi-reversible one-electron redox processes in cyclic voltammetry investigation of the lutetium and gadolinium derivatives were independent of the central ion but associated with ring-based processes during oxidation and reduction. The oxidised species can be useful not only for biosensors but sensors can be fabricated for different kinds of gas by using the electrochromism property of phthalocyanines. The semiconducting and electrochromism behaviour have already been reported in the literature for the development of certain gas sensing electronic devices upto ppb level and also for biosensing.

Solid thin films of lutetium bisphthalocyanine were successfully employed for sensing the redox active biomolecules NADH and vitamin C in desirable concentration. The study showed satisfactory response times, and linear concentration ranges up to two orders of magnitude: 0.05–3 mM for NADH and 0.03–3.48 mM for vitamin C. The method of sensing NADH and Vitamin C works well up to a concentration of 10^{-5} M and the complete recovery of the neutral bispthalocyanine from the oxidized film via NADH reduction leads to the realization of developing reusable membranes. This method can be adapted for the development of practical reusable biochemical devices to monitor NADH and vitamin C levels in plasma, serum, red cells, urine and other accessible tissues for biochemical and functional status. The film remains sensitive for at least three months even when left in open space. However the reduction rate is slow, but developing well-designed calibration protocols may overcome the limitations. Freshly prepared C_8GdPc_2 filmwas examined for biosensing NADH and found to be active in the low concentration of 0.05 mM.

It is shown in this research work that phthalocyanines have the advantage of producing solid state non-aggregated inorganic/organic hybrid nanocomposites in a very simple and economical method. In PbS quantum dots of modified size to 5.8 nm, a band gap of 2.22 eV were produced on ocyl substituted metal-free phthalocyanine matrix. Charge transport in the H_2S treated quantum dots obeys the $T^{-1/4}$ law of the variable range hopping mechanism predicted by Mott at room temperature. At very low temperatures isoenergic tunnelling of charges takes place with temperature independent current-voltage characteristics. The exploration of the current hysteresis properties of the new nanocomposites will be a base for fabricating hybrid nanocomposite based memory storage devices.

9.2 Future work

The applications of liquid crystals in electronic devices have been found to be dependent on their anisotropic behaviour. Investigations into the structural alignments and crystal parameters can be undertaken using polarised optical microscopy, polarised Raman spectroscopy and X-Ray diffraction. Thickness of the organic layers is an important factor to determine the mobility of the materials as well as the efficiency of the devices. As for example, for the organic light emitting diodes, recombination of electron and holes in the emissive layer is important to produce light. In addition to this, to increase the efficiency of photovoltaic devices the charge transfer rate between the components needs to be faster than the recombination rate. Therefore, controlling the thickness of the layers with variable solvent viscosity and concentration of solution would be a useful study.

The biosensing of redox active NADH and vitamin C was focused on a UV-Vis spectroscopic study of their interaction with the phthalocyanines. It has already been established in this research that electrochemical oxidation of the phthalocyanines is possible by applying the required potential in an aqueous solution of $LiClO_4$. An *in situ* electrochemical kinetics study of the interaction between the phthalocyanines and the designated biosensor can be carried out to develop electrochemical biosensors. In this work, the biosensing application was limited to the isostructural octyl substituted lutetium and gadolinium phthalocyanines. It would be interesting to assess the biosensing property of the hexyl substituted derivative as it shows different structural features in single crystal as well as molecular packing. The memory behaviour of the C_8H_2Pc /PbS nanocomposite was studied by the hysteresis in the current-voltage obtained at different scan rates. As the memory loop was found to decrease with the decreasing scan rate, the effect was attributed to trapping and detrapping mechanisms. It could be interesting to study the capacitance-voltage characteristics of PbS/C_8H_2Pc on gold interdigitated electrode at different frequencies to investigate the bistable switching efficiency. Also, the distribution of the quantum dots in the composite matrix can control the performance of the device. More investigations can be performed to achieve the optimum condition for the device fabrication to control the thickness of the film.

Appendix 1- Differential scanning calorimetric (DSC) data of phthalocyanines

The DSC investigations of the liquid crystalline phthalocyanines were performed by Dr. Isabelle Fernandes and Dr. Lydia Sosa-Vargas at East Anglia University.

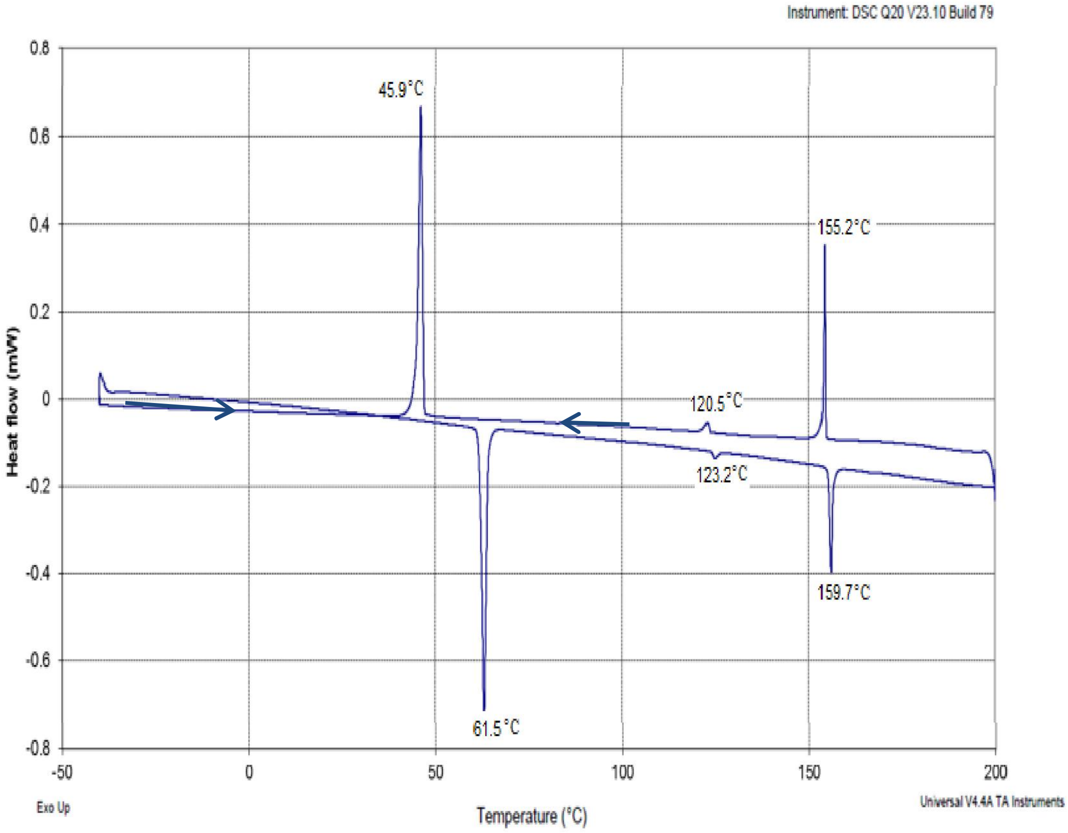

Figure A1.1: **DSC thermogram of C_8LuPc_2.**

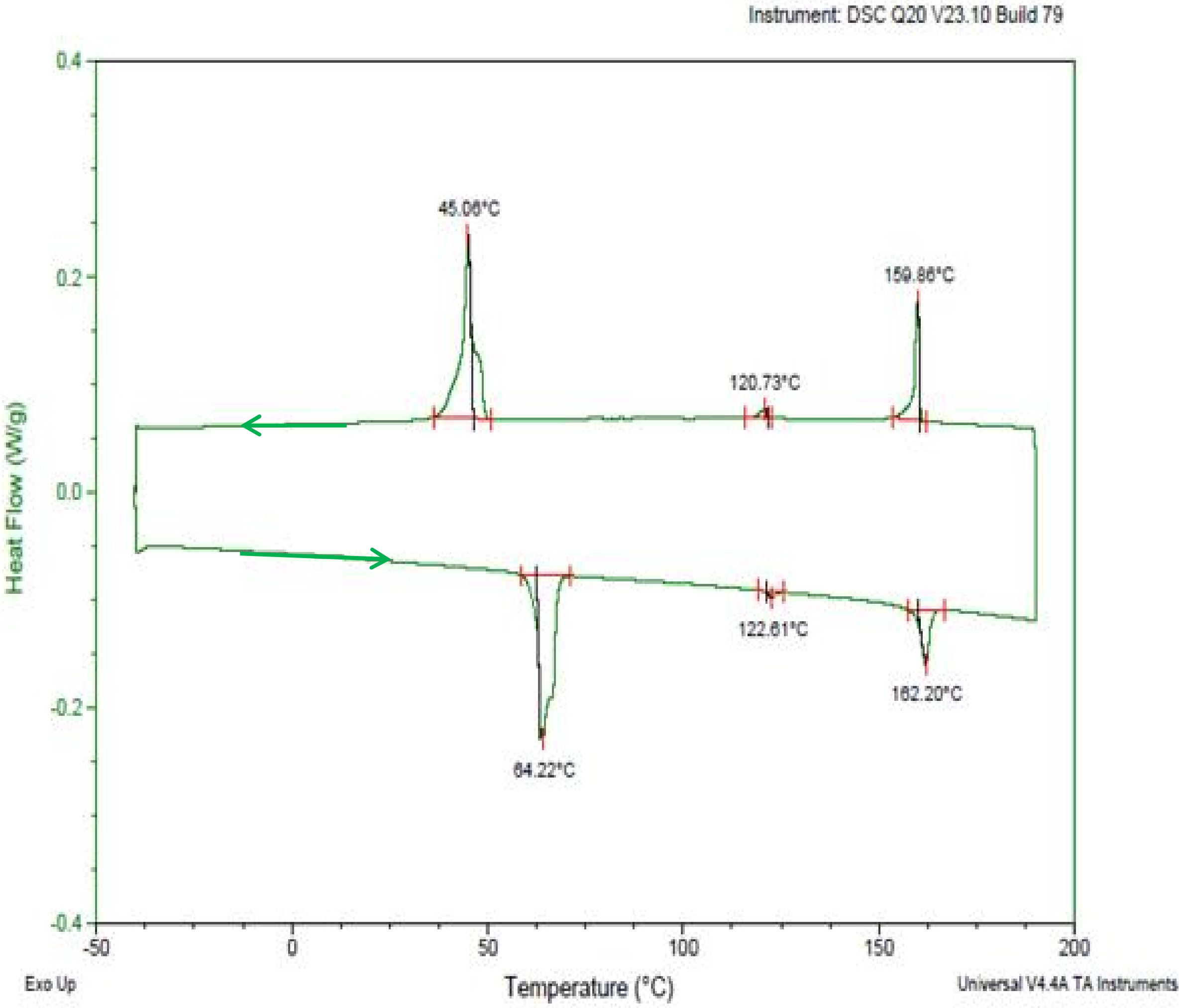

Figure A1.2: DSC thermogram of C_8GdPc_2.

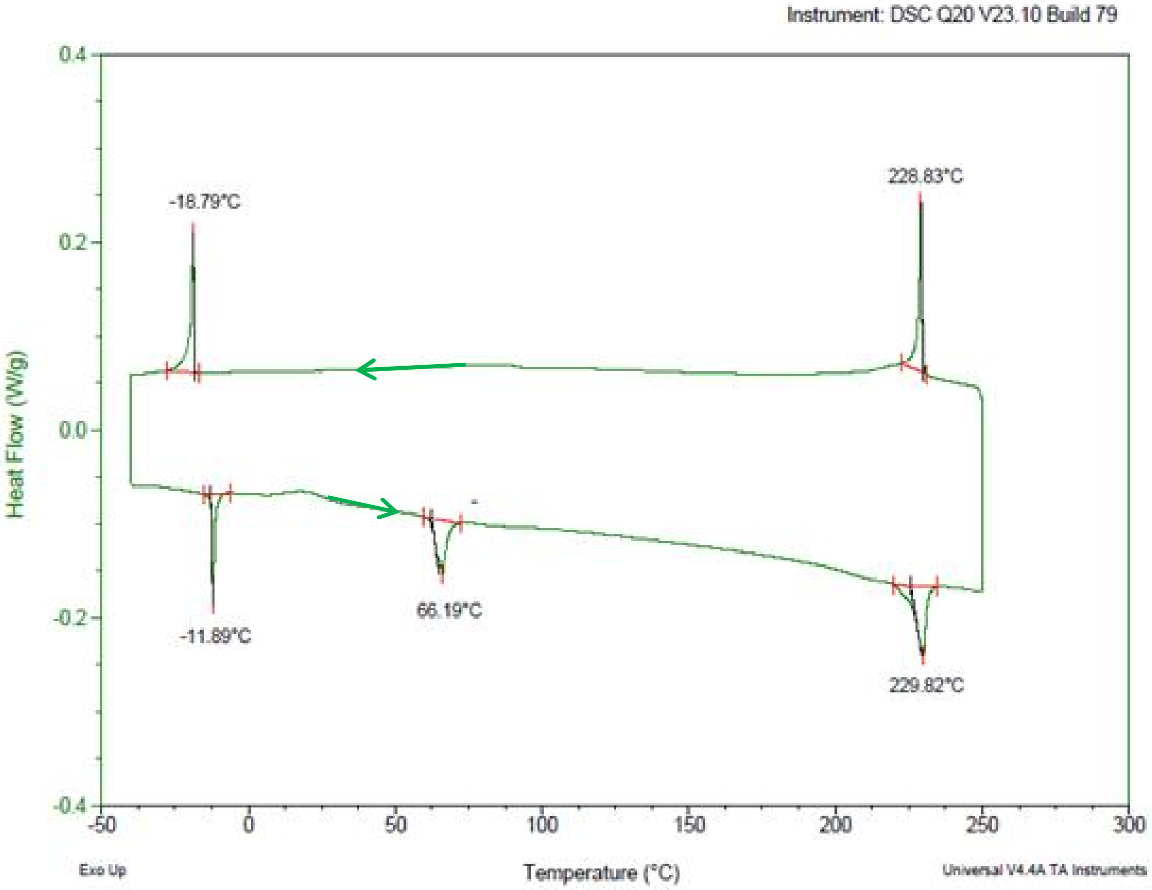

Figure A1.3: DSC thermogram of C_6GdPc_2.

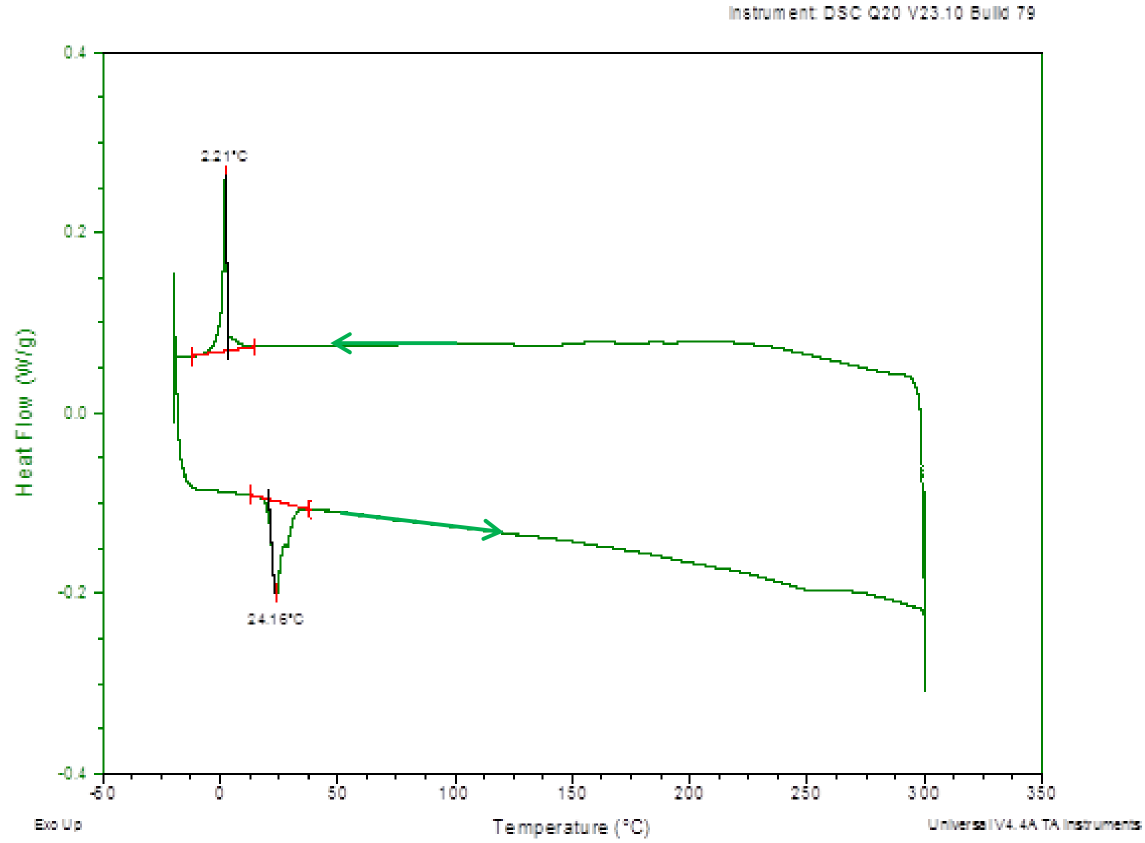

Figure A1.4: DSC thermogram of C_8PbPc.

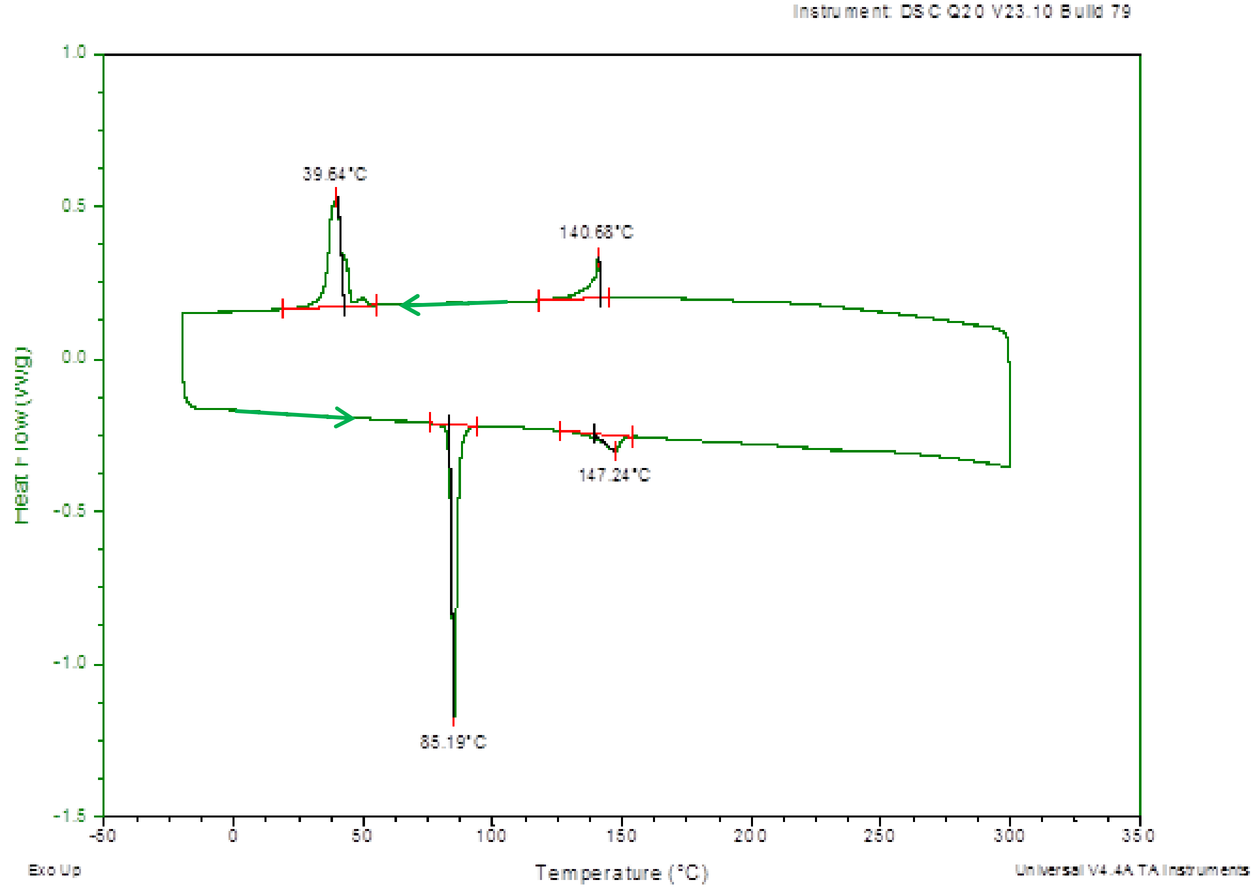

Figure A1.5: **DSC thermogram of C_8H_2Pc.**

Appendix 2 - Single crystal structure and molecular packing of the bisphthalocyanines

The single crystal X-ray crystallographic studies were done by Dr. David Hughes at the University of East Anglia. The structural parameters were evaluated using crystal structure visualisation software, mercury 3.0.

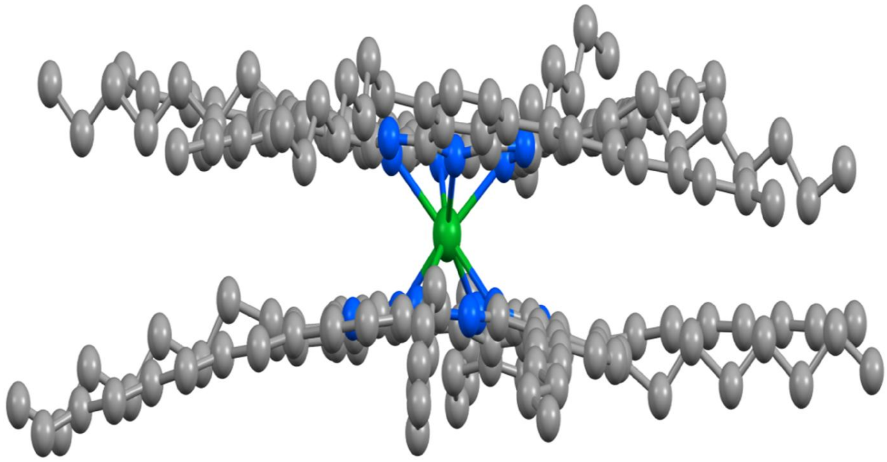

● Metal ion

● Carbon

● Nitrogen

Figure A2.1: **X-Ray crystallographic structure of single molecule as a 'side view' of C_8LuPc_2 and C_8GdPc_2**

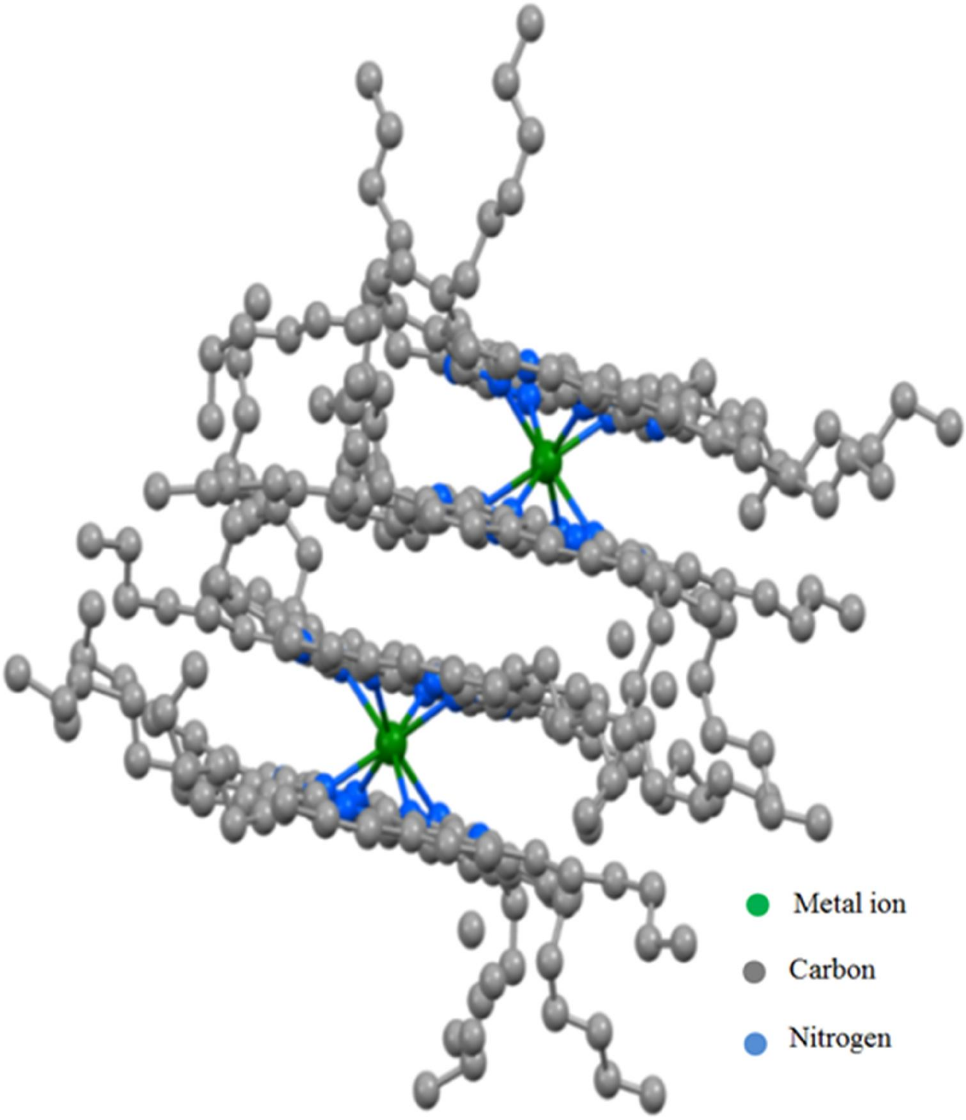

Figure A2. 2: X-Ray crystallographic structure as a 'side view' of a C_6GdPc_2 dimer

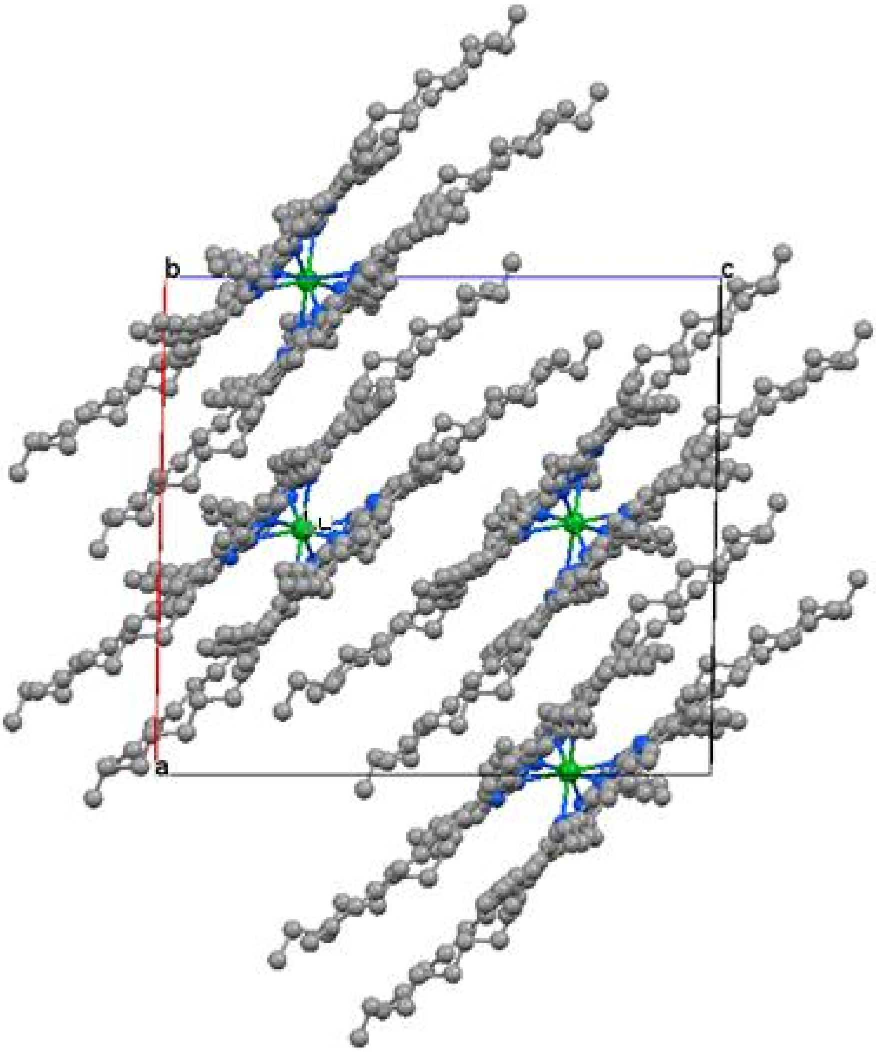

Figure A2. 3: X-Ray crystallographic structure showing the molecular packing of C_8LuPc_2 and C_8GdPc_2 along 'b' axis

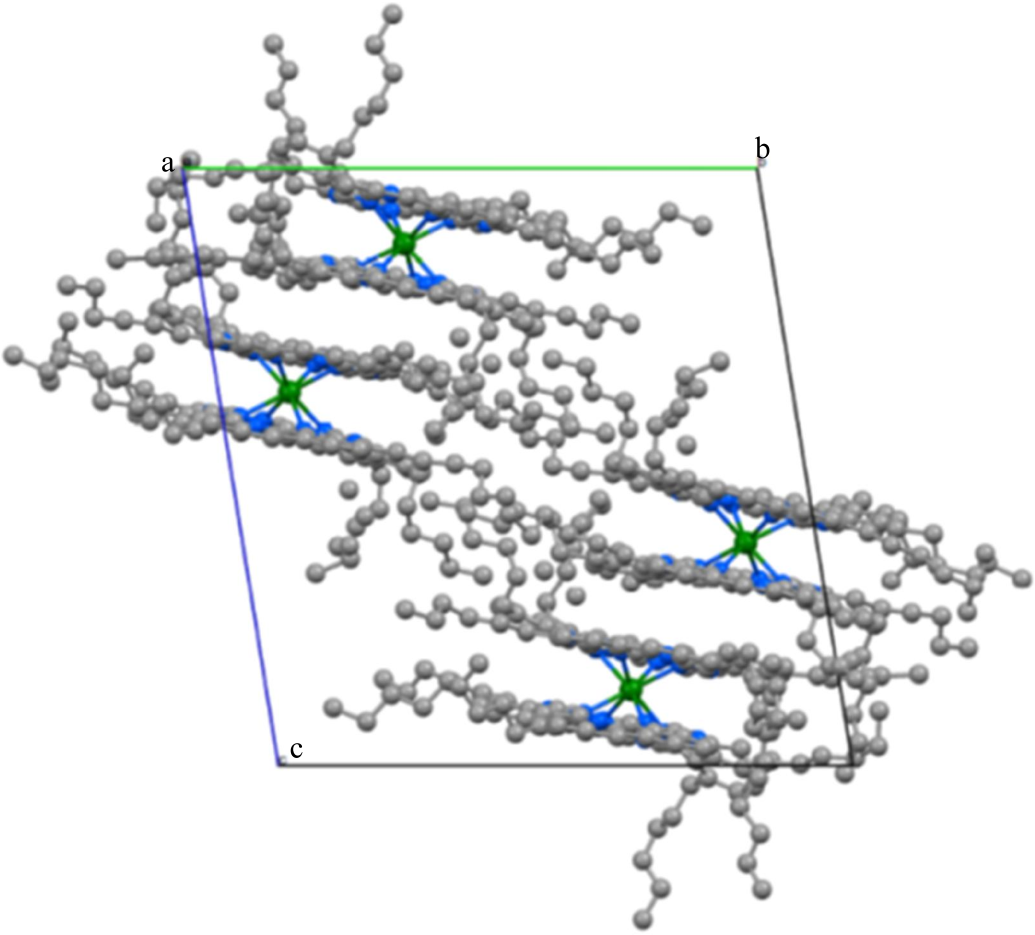

Figure A2.4: **X-Ray crystallographic structure showing the molecular packing of C_6GdPc_2 along 'a' axis**

Table A2.1: X-Ray Structure determination of the bisphthalocyanines – crystallographic data

Formula	C_8LuPc_2	C_8GdPc_2	C_6GdPc_2
Oxidation state of metal ion	+3	+3	+3
Electronic configuration of the metal ion	[Xe] $4f^{14}$	[Xe] $4f^7$	[Xe] $4f^7$
Ionic radius of the metal ion (Å)	0.86	0.94	0.94
Space group	D_4	D_4	D_4
a (Å)	21.51	21.59	21.94
b (Å)	32.45	32.47	26.73
c (Å)	24.16	24.098	27.463
V (Å^3)	16859.81	16897.50	13673.40
Mean M-N(Pc) distances(Å)	2.39	2.45	2.45
Mean M…N_4 (Pc)plane distance (Å)	1.35	1.46	1.42
Mean Pc ring-ring distances(Å)	2.39	2.92	2.83
Mean angles of twist of Pc ligands from eclipsing(degree)	39.10	38.30	39.70

Appendix 3 - Analysis of the XRD data after curve fitting in TOPAS software

A3.1 Analysis of the XRD data of PbS quantum dots after curve fitting in TOPAS software (Courtesy of Dr. George Fern, Brunel University).

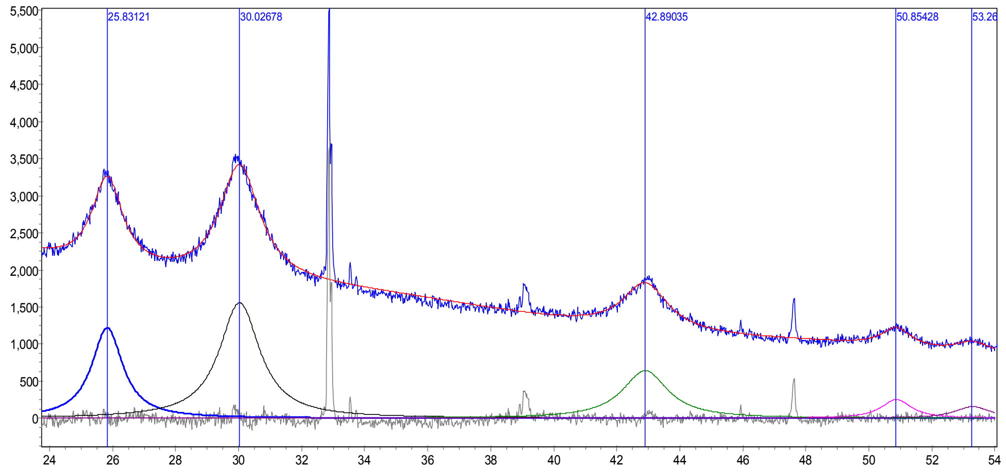

Figure A3.1: Curve fitting of PbS quantum dots XRD peaks

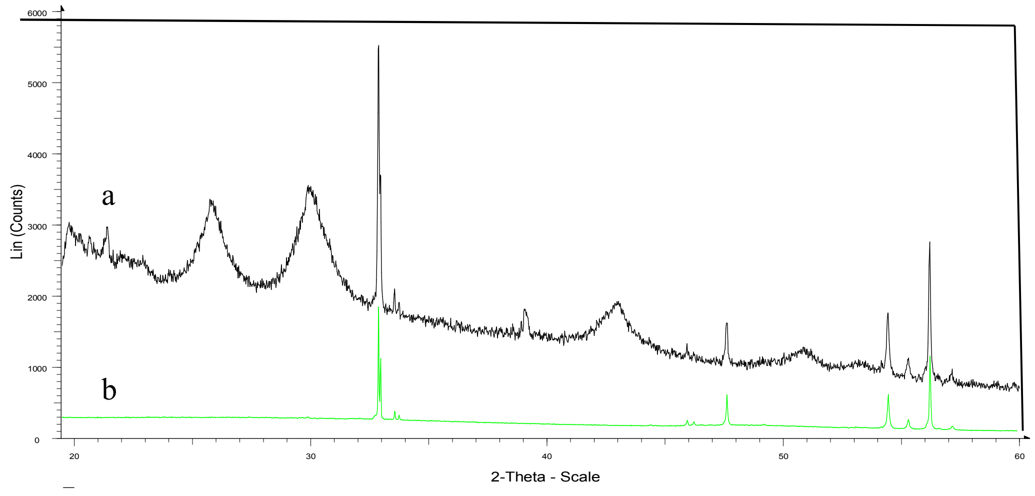

Figure A3. 2: (a) XRD peaks of Si substrate for the nanocomposite material (b) Si peaks from TOPAS database

Analysis Report

Data Files

```
    Data file 1 : C:\Diffplus\Diffdata\Chandana\7th jan pbs2.raw
    Data file 2 : C:\Diffplus\Diffdata\Chandana\Si-reference.raw
```

Global R-Values

```
Rexp : 2.34    Rwp : 7.24     Rp  : 3.40   GOF : 3.09
Rexp`: 11.80   Rwp`: 36.50    Rp` : 23.47  DW  : 0.27
```

File 1 : "C:\Diffplus\Diffdata\Chandana\7th jan pbs2.raw"

```
Range Number :  1
```

R-Values

```
Rexp : 2.34    Rwp : 7.24     Rp  : 3.40   GOF : 3.09
Rexp`: 11.80   Rwp`: 36.50    Rp` : 23.47  DW  : 0.27
```

Quantitative Analysis - Rietveld

Background

```
   Chebychev polynomial, Coefficient  0      1607.358
                                      1      -883.2488
                                      2      157.3903
                                      3      -66.36605
                                      4      71.07543
                                      5      -53.0118
                                      6      -6.097661
                                      7      24.4949
```

Instrument

```
   Primary radius (mm)                       217.5
   Secondary radius (mm)                     217.5
   Receiving slit width (mm)                 0.1703957
   Divergence angle (°)                      0.3
   Full Axial Convolution
      Filament Length (mm)                   12
      Sample Length (mm)                     15
      Receiving Slit Length (mm)             12
      Primary Sollers (°)                    2.3
      Secondary Sollers (°)                  2.5
   Tube_Tails
      Source Width (mm)                      0.02922497
      Z1 (mm)                                -0.8287595
      Z2 (mm)                                1.225314
      Fraction                               0.0007853681
```

Corrections

```
   Zero Error                                -0.1257669
   Specimen displacement                     -0.2191128
   LP Factor                                 0
```

Miscellaneous

Convolution Steps	5
Start X	20
Finish X	54

Peaks Phase 1

Phase name	Peak Phase:0

Type	Position	I		
FP	25.83121	61.29013	Cry Size Lor(nm)	7.8
FP	30.02678	140.912	Cry Size Lor(nm)	6.0
FP	42.89035	143.3264	Cry Size Lor(nm)	5.5
FP	50.85428	54.23249	Cry Size Lor(nm)	8.8
FP	53.26939	44.54512	Cry Size Lor(nm)	7.4

A3.2 Analysis of the XRD data of bulk galena by curve fitting in TOPAS software.

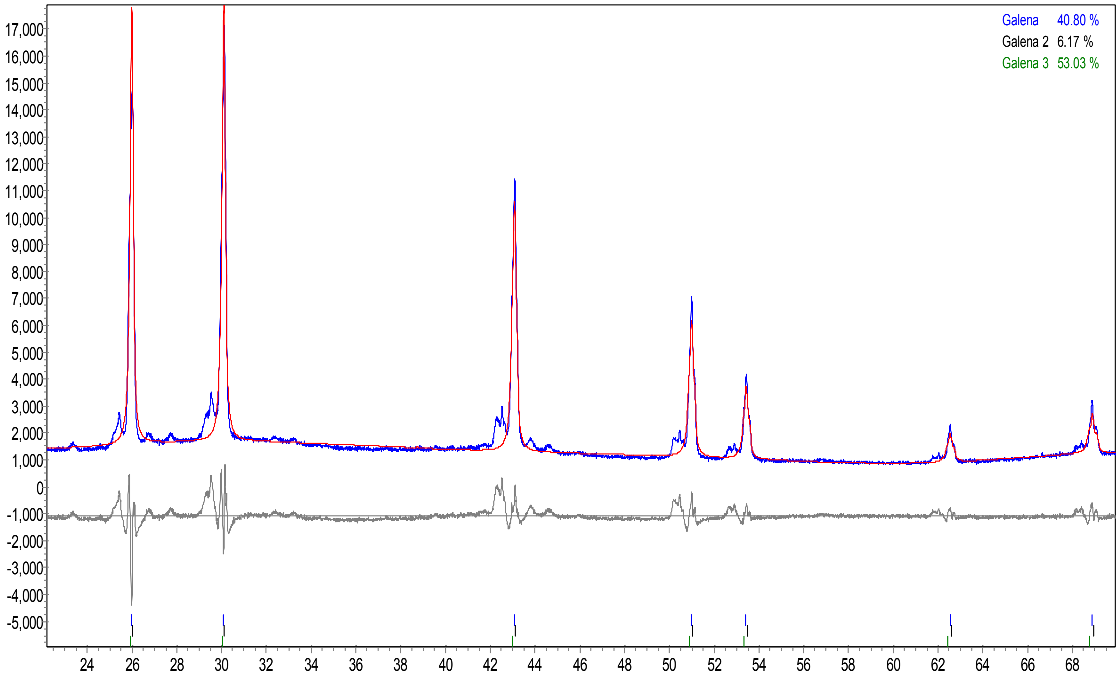

Figure A3.3: XRD peaks of bulk galena (PbS) after curve fitting using TOPAS software

Analysis Report

Data Files

```
    Data file 1 : C:\Diffplus\Diffdata\Chandana\pbs bulk.raw
```

Global R-Values

```
Rexp : 2.49    Rwp : 10.99    Rp  : 7.69   GOF : 4.40
Rexp`: 6.77    Rwp`: 29.79    Rp` : 33.83  DW  : 0.12
```

File 1 : "C:\Diffplus\Diffdata\Chandana\pbs bulk.raw"

```
Range Number :  1
```

R-Values

```
Rexp : 2.49    Rwp : 10.99    Rp  : 7.69   GOF : 4.40
Rexp`: 6.77    Rwp`: 29.79    Rp` : 33.83  DW  : 0.12
```

Quantitative Analysis - Rietveld

```
   Phase 1  : Galena                       40.798 %
   Phase 2  : "Galena 2"                   6.173 %
   Phase 3  : "Galena 3"                   53.029 %
```

Background

```
   Chebychev polynomial, Coefficient  0      1303.163
                                      1      -266.0085
                                      2      45.89796
                                      3      199.209
                                      4      23.23772
                                      5      -26.75148
                                      6      20.0481
                                      7      -59.5816
```

Instrument

```
   Primary radius (mm)                       217.5
   Secondary radius (mm)                     217.5
   Receiving slit width (mm)                 0.1703957
   Divergence angle (°)                      0.3
   Full Axial Convolution
      Filament Length (mm)                   12
      Sample Length (mm)                     15
      Receiving Slit Length (mm)             12
      Primary Sollers (°)                    2.3
      Secondary Sollers (°)                  2.5
   Tube_Tails
      Source Width (mm)                      0.02922497
      Z1 (mm)                                -0.8287595
      Z2 (mm)                                1.225314
      Fraction                               0.0007853681
```

Corrections

```
   Zero Error                                -0.1257669
```

```
   Specimen displacement                    -0.2670942
   LP Factor                                0
```

Miscellaneous

```
   Convolution Steps                        5
   Start X                                  20
```

Structure 1

```
   Phase name                               Galena
   R-Bragg                                  4.116
   Spacegroup                               225
   Scale                                    0.000108108389
   Cell Mass                                957.070
   Cell Volume (Å^3)                        209.16984
   Wt% - Rietveld                           40.798
   Crystallite Size
      Cry Size Lorentzian (nm)              129.1
k:  1  LVol-IB (nm)                   82.170
k:  0.89  LVol-FWHM (nm)              114.875
Crystal Linear Absorption Coeff. (1/cm)   1584.631
   Crystal Density (g/cm^3)                 7.598
   Preferred Orientation (Dir 1 : 1 0 0)    1
   Lattice parameters
a (Å)                                 5.9360792

Site  Np    x          y          z         Atom Occ       Beq
s1    4   0.00000    0.00000    0.00000     PB   1         1.29
s2    4   0.50000    0.50000    0.50000     S    1         1.23
```

Structure 2

```
   Phase name                               Galena 2
   R-Bragg                                  4.010
   Spacegroup                               225
   Scale                                    1.64067631e-005
   Cell Mass                                957.070
   Cell Volume (Å^3)                        208.52803
   Wt% - Rietveld                           6.173
   Crystallite Size
      Cry Size Lorentzian (nm)              810.3
Crystal Linear Absorption Coeff. (1/cm)   1589.509
   Crystal Density (g/cm^3)                 7.621
   Preferred Orientation (Dir 1 : 1 0 0)    1
   Lattice parameters
a (Å)                                 5.9300016

Site  Np    x          y          z         Atom Occ       Beq
s1    4   0.00000    0.00000    0.00000     PB   1         1.29
s2    4   0.50000    0.50000    0.50000     S    1         1.23
```

Structure 3

```
   Phase name                                Galena 3
   R-Bragg                                   3.002
   Spacegroup                                225
   Scale                                     0.000139788913
   Cell Mass                                 957.070
   Cell Volume (Å^3)                         210.26400
   Wt% - Rietveld                            53.029
   Crystallite Size
      Cry Size Lorentzian (nm)               57.9
Crystal Linear Absorption Coeff. (1/cm)   1576.385
   Crystal Density (g/cm^3)                  7.558
   Preferred Orientation (Dir 1 : 1 0 0)     1
   Lattice parameters
a (Å)                                  5.9464117

Site  Np    x           y           z         Atom Occ       Beq
s1    4   0.00000     0.00000     0.00000     PB   1         1.29
s2    4   0.50000     0.50000     0.50000     S    1         1.23
```

Appendix 4- List of Publications

1. Pal, C., Cammidge, A. N., Cook, M. J., Sosa-Sanchez, J. L., Sharma, A. K. and Ray, A. K. (2012) 'In situ chemichromic studies of interactions between a lutetium bis-octaalkyl-substituted phthalocyanine and selected biological cofactors', *Journal of the Royal Society Interface*, 9 (66), pp. 183-189, DOI: 10.1098/rsif.2010.0726.
2. Pal, C., Sharma, A. K., Cammidge, A. N., Cook, M. J. and Ray, A. K., (2013) 'Octaoctyl substituted lutetium bisphthalocyanine for NADH biosensing', *Journal of Physical Chemistry B*, 117 (48), pp 15033–15040, DOI: 10.1021/jp4078568.
3. Cruz Blanco C. F., Pal, C., Ojeda, J. J., Ray, A.K. and Sharma, A.K. (2012) 'Morphological and elemental studies on titania thin films electrodeposited at different bath temperatures', *Journal of the Electrochemical Society*, 159 (2), pp 30-36, DOI:10.1149/2.016202jes.
4. Feizi, E., Scott, K., Baxendale, M., Pal, C., Ray, A.K., Wang, W., Pang, Y. and Hodgson, S. N. B. (2012) 'Synthesis and characterisation of nickel nanorods for cold cathode fluorescent lamps', *Materials Chemistry and Physics*, 135 (s2-3), pp 832 - 836, DOI:10.1016/j.matchemphys.2012.05.066.
5. Chaure, N. B., Pal, C., Barard, S., Kreouzis, T., Ray, A. K., Cammidge, A. N., Chambrier, I., Cook, M. J., Murphy, C. E. and Cain, M. G. (2012) 'A liquid crystalline copper phthalocyanine derivative for high performance organic thin film transistors', *Journal of Materials Chemistry*, 22(36), pp 19179-19189, DOI:10.1039/c2jm33301e.
6. Paul, S., Harris, P., Pal, C., Sharma, A. K. and Ray, A. K. (2014) 'Low cost zinc oxide for memristors with high on-off ratios', *Materials Letters,* 130(1), pp. 40-42, DOI: 10.1016/j.matlet.2014.05.071.

References

A

- Adachi, K., Chayama, K. and Watarai, H. (2006) 'Control of optically active structure of thioether-phthalocyanine aggregates by chiral Pd(II)-BINAP complexes in toluene and at the toluene/water interface,' C*hirality,* 18(8), pp. 599-608, DOI: 10.1002/chir.20293.
- Adhikamsetty, R. K. and Jonnalagadda, S. B. (2009) 'Kinetics of reaction between 1,10-phenanthroline, ferric and ferrocyanide ions in the presence of acid', *Oxidation Communications,* 32(4), pp. 844-857.
- Alberts, B., Bray, D., Lewis, J., Raff, H., Roberts, K. and Watson, J.D. (1994) 'Energy conversion: mitochondria and chloroplasts in molecular biology of the cell', 3rd edn. New York: Garland Publishing.
- Alibart, F., Pleutin, S., Bichler, O., Gamrat, C., Serrano-Gotarredona, T ., Linares-Barranco, B. and Vuillaume, D. (2012) 'A memristive nanoparticle/organic hybrid synapstor for neuroinspired computing', *Advanced Functional Materials*, 22(3), pp. 609-616, DOI**:** 10.1002/adfm.201101935.
- Anthopoulos, T. D. and Shafai, T. S. (2003) 'Alternating current conduction properties of thermally evaporated α-nickel phthalocyanine thin films: Effects of oxygen doping and thermal annealing',*Journal of Applied Physics,* 94(4), pp. 2426-2433, DOI: 10.1063/1.1592626.
- Arellano, I. H. J., Mangadlao, J., Ramiro, I. B. and Suazo, K. F. (2011) '3-component low temperature solvothermal synthesis of colloidal cadmium sulphide quantum dots', *Materials Letters*, 64, pp. 785-788, DOI: 10.1016/j.matlet.2010.01.021.

- Asunskis, D.J. and Hanley, L. (2007) 'Valence band and core level X-ray photoelectron spectroscopy of lead sulfide nanoparticle-polymer composites', *Surface Science,* 601(19), pp. 4648-4656, DOI: 10.1016/j.susc.2007.08.002.
- Asunskis, D. J., Bolotin, I.L., Wroble, A. T., Zachary, A. M. and Hanley, L. (2008) 'Lead sulfide nanocrystal-polymer composites for optoelectronic applications', *Macromolecular Symposia,* 268, pp. 33-37, DOI: 10.1002/masy.200850807.
- Aroca, R., Bolourchi, H., Battisti, D. and Najafi, K. (1993) 'Gas adsorption and electrical properties of Langmuir-Blodgett layers of cerium bisphthalocyanine', *Langmuir,* 9, pp. 3138-3141.
- Atilla, D., Kilinc, N., Yuksel, F., Gürek, A.G., Öztürk, Z. Z. and Ahsena, V. (2009) 'Synthesis, characterization, mesomorphic and electrical properties of tetrakis(alkylthio)-substituted lutetium(III) bisphthalocyanines,' *Synthetic Metals* 159(1-2), pp. 13-21.
- Atilla, D., Gürek, A.G., Basova, T.V., Kiselev, V.G., Hassane, A., Sheludyakovab, L. A. and Ahsena, V. (2011) 'The synthesis and characterization of novel mesomorphic octa- and tetra-alkylthio-substituted lead phthalocyanines and their films', *Dyes and Pigments,* 88(3), pp. 280-289.
- Azim-Araghi, M. E. and Sahebi, R. (2014) 'Effect of temperature and post-deposition annealing on Schottky barrier characterization of bromoindium phthalocyanine/aluminum interfaces', *Physica B-Condensed Matter,* 433, pp. 144-148, DOI: 10.1010/j.physb.2013.10.033.
- Azimirad, R., Khademi, A., Akhavan, O. and Moshfegh, A. Z. (2009) 'Growth of NaO.3WO3 nanorods for the field emission application' *Journal of Physics D-Applied Physics,* 42(20), pp. 2054051-2054056, DOI: 10.1088/0022-3727/42/20/205405.

B

- Ban, K. Z., Nishizawa, K., Ohta, K. and Shirai, H. (2000) ‘Discotic liquid crystals of transition metal complexes 27: supramolecular structure of liquid crystalline octakis-alkylthiophthalocyanines and their copper complexes’, *Journal of Materials Chemistry,* 10(5), pp. 1083-1090, DOI: 10.1039/b000134l.
- Ban, K., Nishizawa, K., Ohta, K., DeCraats, A. M. V., Warman, J. M., Yamamoto, I. and Shirai, H. (2001) ‘Discotic liquid crystals of transition metal complexes 29: mesomorphism and charge transport properties of alkylthio-substituted phthalocyanine rare-earth metal sandwich complexes’, *Journal of Materials Chemistry,* 11(2), pp. 321-331, DOI: 10.1039/b003984p.
- Bai, J., Lu, B. P., Bo, X. J. and Guo, L. P. (2010) ‘Electrochemical property and electroanalytical application of large mesoporous carbons’, *Electrochemistry Communications*, 12(11), pp. 1563-1567, DOI: 10.1016/j.elecom.2010.08.034.
- Bao, M., Wang, R. M., Rintoul, L., Liu, Q. Y., Arnold, D. P., Ma, C. Q. and Jiang, J.Z. (2006) ‘Vibrational spectroscopy of phthalocyanine and naphthalocyanine in sandwich-type (Na)phthalocyaninato and porphyrinato rare earth complexes - part 12 - part 13. The raman characteristics of phthalocyanine in unsubstituted and peripherally octa(octyloxy) -substituted homoleptic bis(phthalocyaninato) rare earth complexes’, *Polyhedron,* 25, pp. 1195-1203.
- Baran, J. D. and Larsson, J.A. (2010) ‘Inversion of the shuttlecock shaped metal phthalocyanines Mpc (M = Ge, Sn, Pb) - a density functional study’, *Physical Chemistry Chemical Physics,* 12, pp. 6179-6186, DOI: 10.1039/B924421B.
- Barr, T. L., Seal, S., Chen, L. M. and Kao, C. C. (1994) ‘A new interpretation of the binding-energies in X-ray photoelectron studies of oxides’, *Thin solid films*, 253(1-2), pp. 277-284, DOI: 10.1016/0040-6090(94)90334-4.
- Basova, T., Jushina, I., Gurek, A.G., Ahsen, V. and Ray, A. K. (2008) ‘Use of The Electrochromic Behaviour of Lanthanide Phthalocyanine Films for Nicotinamide

Adenine Dinucleotide Detection', *Journal of Royal Society of Interface,* 5, pp. 801-806.

- Basova, T. V., Ayse, G. G., Devrim, A., Aseel, K. H. and Vefa, A. (2007) 'Synthesis and characterisation of new mesomorphic octakis(alkylthio)-substituted lead phthalocyanines and their films,' *Polyhedron,* 26 (17), pp. 5045-5052.
- Basova, T.V., Kol'tsov, E., Hassan, A. K., Ray, A. K., Gürek, A.G. and Ahsen, V. (2006) 'Effects of structural reorganization in phthalocyanine films on their electrical properties,' *Materials Chemistry and Physics,* 96(1), pp. 129-135 DOI:10.1016/J.Matchemphys.2005.06.055.
- Basova, T.V., Jushina, I., Gürek, A. G., Ahsen, V. and Ray, A. K. (2008) 'Use of the electrochromic behaviour of lanthanide phthalocyanine films for nicotinamide adenine dinucleotide detection', *Journal of Royal Society Interface,* 5, pp. 801–806, DOI:10.1098/rsif.2007.1241)10.1098/rsif.2007.1241.
- Basova, T.V., Durmus, M., Gürek, A.G., Ahsen, V. and Hassan, A. (2009) 'Effect of interface on the orientation of the liquid crystalline nickel phthalocyanine films', *Journal of Physical Chemistry C,* 113(44), pp. 19251-19257, DOI: 10.1021/jp905907n.
- Basova, T. V. and Kolesov, B. A. (1998) 'Raman polarization studies of the orientation of molecular thin films', *Thin solid films,* 325(1-2), pp.140-144, DOI: 10.1016/S0040-6090(98)00485-4.
- Basova, T. V., Kurochkina, N. M., Tsivadze, A.Y. and Ray, A. K.(2010) 'Formation of hybrid inorganic/organic nanocomposites', *Journal of Electronic Materials,* 39(2), pp. 145-148, DOI: 10.1007/s11664-009-1024-8.
- Basova, T. V., Kolesov, B.A., Gurek, A.G. and Ahsen, V. (2001) 'Raman polarization study of the film orientation of liquid crystalline NiPc', Th*in solid films* 385(1-2), pp. 246-251, DOI:10.1016/S0040-6090(01)00779-9.
- Basova, T., Tsargorodskaya, A., Nabok, A., Hassan, A.K., Gurek, A.G., Gumus, G. and Ahsen, V. (2009) 'Investigation of gas-sensing properties of copper

phthalocyanine films', *Materials Science & Engineering C-Biomimetic And Supramolecular Systems,* 29(3), pp. 814-818, DOI: 10.1016/j.msec.2008.07.020.

- Bilgin, A., Ertem, B. and Gok, Y. (2007) 'Highly organosoluble metal-free phthalocyanines and metallophthalocyanines: Synthesis and characterization', *European Journal Of Inorganic Chemistry*, 12, pp. 1703-1712, DOI: 10.1002/ejic.200600943.
- Brédas, J. L., Calbert, J. P., da Silva Filho D. A. and Cornil J. (2002) 'Organic semiconductors: A theoretical characterization of the basic parameters governing charge transport', *Proceedings of the National Academy of Sciences,* 99(9), 5804–5809, DOI: 10.1073/pnas.092143399.
- Braun D. (2003) 'Electronic Injection and Conduction Processes for Polymer Devices', *Journal of Polymer Science Part B-Polymer Physics,* 41(21), pp. 2622-2629, DOI**:** 10.1002/polb.10654.
- Buchler, J. W. and Ng, D. K. P. (2000) 'Metal tetrapyrrole double- and triple-deckers with special emphasis on porphyrin systems.In The Porphyrin Handbook Volume 3 (eds. Kadish, K. M., Smith, K. M. and Guilard, R.) Academic Press, pp. 245-294.

C

- Cammidge, A. N., Tseng, C. H., Chambrier, I., Hughes, D. L. and Cook M. J. (2009) 'Phthalocyanines bearing bulky cycloalkylmethyl substituents on non-peripheral sites,' *Tetrahedron Letters*, 50 (37), pp. 5254-5256.
- Castellan, G. W. (2010) Physical chemistry. Massachusetts: Addison-Wesley Publishing Co., Inc.
- Chakraborty, I. and Moulik, S. P. (2005) 'On PbS nanoparticles formed in the compartments of water/AOT/n-heptane microemulsion', *Journal of Nanoparticle Research*, 7, pp. 237-247, DOI: 10.1007/s11051-005-3472-2.

- Chamberlain, G.A. (1983) 'Organic solar-cells - a review', *Solar Cells,* 8 (1), pp: 47-83. DOI: 10.1016/0379-6787(83)90039-x.
- Chwang, A. B and Frisbie, C.D. (2001) ‘Temperature and gate voltage dependent transport across a single organic semiconductor grain boundary,’ *Journal of Applied Physics,* 90(3), pp.1342-1349, DOI: 10.1063/1.1376404.
- Chaure N. B., Sosa-Sanchez J. L., Cammidge A. N., Cook M. J. and Ray A.K. (2010) ‘Solution processible lutetium phthalocyanine organic field-effect transistors,’ *Organic Electronics,* 11(3), pp. 434-438.
- Chaure N.B., Basova, T., Ray A.K., Gürek, A. G. and Ahsen, V. (2009) ‘Memory effects in thin film organic transistor characteristics,’ *Journal of Physics D: Applied Physics,* 42(12), pp. 1251031-1251035, DOI:10.1088/0022-3727/42/12/125103.
- Chaure, N. B., Sosa-Sanchez, J. L., Cammidge, A. N., Cook, M. J. and Ray, A. K. (2010) ‘Solution processable lutetium phthalocyanine organic field-effect transistors’ *Organic Electronics*, 11(3), pp 434-438, DOI:10.1016/j.orgel.2009.11.023.
- Chaure, N.B., Pal, C., Barard, S., Kreouzis, T., Ray, A. K., Cammidge, A. N., Chambrier, I., Cook, M. J., Murphy, C. E. and Cain, M. G. (2012) ‘A liquid crystalline copper phthalocyanine derivative for high performance organic thin film transistors,’ *Journal of Materials Chemistry,* 22(36), pp. 19179-19189, DOI:10.1039/C2jm33301e.
- Chemat Technology Inc. available at: http://www.trade2cn.com/companyShop/26266807/supply/ (Accessed: 2 April 2014).
- Chen, H. J., Wu, H. T., Hung, K. T., Fu, S. W. and Shih, C. F. (2013) ‘Sodium doping in copper-phthalocyanine/C-60 heterojunction for organic photovoltaic applications’, *Thin solid films*, 544, pp. 249-253, DOI: 10.1016/j.tsf.2013.03.110.
- Chen, Y. L., Zhao, S. Y., Li, X. Y. and Jiang, J. Z. (2005) ‘Tuning the arrangement of mono-crown ether-substituted phthalocyanines in Langmuir-Blodgett films by the length of alkyl chains and the cation in subphase’, *Journal of Colloid and Interface Science*, 289(1), pp. 200-205, DOI: 10.1016/J.Jcis.2005.03.051.

- Choi K.H., Maria M., Khalid R., Bum K. J. and Yang H. D. (2012) ‘Cost-effective fabrication of memristive devices with ZnO thin film using printed electronics technologies’, *Applied Physics A,* 106, pp. 165-170, DOI 10.1007/s00339-011-6670-z.
- Claessens, C. G., Hahn, U. and Torres, T. (2008) ‘Phthalocyanines: from outstanding electronic properties to emerging applications’, *The Chemical Record*, 8(2), pp. 75-97, DOI:10.1002/Tcr.20139.
- Clavijo, R. E., Battisti, D., Aroca, R., Kovacs, G. J. and Jennings, C. A. (1992) ‘Surface-enhanced Raman-spectra and gas chemisorption of langmuir-blodgett layers of lutetium and ytterbium diphthalocyanines’*, Langmuir,* 8(13), pp.113-117, DOI:10.1021/la00037a022.
- Cook, M. J. (1994) ‘1,4,8,11,15,18,22,25-octasubstituted phthalocyanines - the contrasting effects of alkyl and alkoxy substituents on molecular self-assembly,’ *Journal of Materials Science-Materials in Electronics,* 5(2), pp. 117-128.
- Cook, M. J., Chambrier, I., White, G. F., Fourie. E. and Swarts. J. C. (2009) ‘Electrochemical and EPR studies of two substituted bis-cadmium tris-phthalocyanine complexes: elucidation of unexpectedly different free-radical character,’ *Dalton transactions,* 7, pp. 1136-1144, DOI:10.1039/b811451j.
- Cook, M.J. (2002) ‘Properties of some alkyl substituted phthalocyanines and related macrocycles’, *Chemical Record, 2* (4), pp. 225-236, DOI: 10.1002/Tcr.10028.
- Cui, L. L., Lv, G. J., Dou, Z. Y. and He, X.Q. (2013) ‘Fabrication of iron phthalocyanine/graphene micro/nanocomposite by solvothermally assisted pi-pi assembling method and its application for oxygen reduction reaction’, *Electrochimica Acta*, 106, pp. 272-278, DOI:10.1016/J.Electacta.2013.05.077.
- Cullity, B.D. and Stock, S.R. (2001) Elements of X-ray diffraction, 3rd edition Prentice Hall.

D

- Daira, R., Boudjema, B., Mordjaoui, M. and Meziri, M. (2011) 'Electrical properties of metallophthalocyanine thin films', Optoelectronics and Advanced Materials-Rapid Communications, 5(1-2), pp. 167-171.
- Dayal, S., Yongbing, L., Samia, A. C. S., Berlin, J. C., Kenney, M. E. and B.Clemens (2006) 'Observation of non-fo1rster-type energy-transfer behavior in quantum dot-phthalocyanine conjugates,' *Journal of the American Chemical Society,* 128 (43), pp. 13974-13975, DOI:10.1021/ja063415e.
- Dean, J. A. (1967) Lange's handbook of Chemistry, 15th edn., New York St.: Mcgraw-hill, inc.
- Deng, B., Zhong, S. L., Wang, D. H., Wang, S. S., Zhang, T. K., Qua, W. G. and Xu, A. W. (2010) 'High yield synthesis of matchstick-like PbS nanocrystals using mesoporous organosilica as template', *Nanoscale,* 3(6), pp. 1014-1021, DOI: 10.1039/c0nr00741b.
- De Saja, J. A. and Rodriguez-Mendez, M.L. (2005) 'Sensors based on double-decker rare earth phthalocyanine', *Advance Colloid Interface Science,* 116(1-3), pp 1-11.
- Deore, B. A. and Freund, M. S. (2005) 'Reactivity of poly (anilineboronic acid) with NAD(+) and NADH', *Chemical Materials,* 17(11), pp 2918-2923, DOI: 10.1021/cm050647o.
- Discotic liquid crystals (2010). Available at: http://translatorchineseenglish-.blogspot.co.uk/ (Accessed: 4 April 2014)
- Djurovich, P. I., Mayo, E. I., Forrest, S. R. and Thompson, M. E. (2009) 'Measurement of the lowest unoccupied molecular orbital energies of molecular organic semiconductors', *Organic Electronics*, 10(3), pp. 515-520, DOI: 10.1016/j.orgel.2008.12.011.
- Donald, A. M., Windle, A. H. and Hanna, S. (2006) 'Liquid Crystalline Polymers', 2nd edn., Cambridge University Press.

- Donley, C .L., Zangmeister, R., Xia, W., Minch, B., Drager, A., Cherian, S. K., LaRussa, L., Kippelen, B., Domercq, B., Mathine, D.L., O'Brien, D. F. and Armstrong, N. R.(2004) ‘Anisotropies in the electrical properties of rod-like aggregates of liquid crystalline phthalocyanines: Direct current conductivities and field-effect mobilities’, *Journal of Materials Research,* 19(7), pp. 2087-2099, DOI: 10.1557/JMR.2004.0278.
- Dvorak, M., Wei, S. andWu, Z. (2013) 'Origin of the variation of exciton binding energy in semiconductors', *Physical Review Letters*, 110(1), pp. 0164021-0164025.

E

- EDN Network available at: http://www.edn.com/design/led/4396478/2/White-LEDs-Printed-on-Paper-A-Doctoral-Thesis-Part-V (Accessed: 5 April, 2014).
- Eichhorn, H. (1998) ‘Mesomorphic phthalocyanines, tetraazaporphyrins, porphyrins and triphenylenes as charge-transporting materials*’, Journal of porphyrins and phthalocyanines,* 4(8), pp. 88-103, DOI: 10.1002/(SICI)10991409(200001/02)-4:1<88::AID-JPP208>3.0.CO;2-6 .
- El-Nahass, M. M., Atta, A. A. and El-Zaidia, E. F. M. (2011) ‘Fourier-transform infrared and electrical properties of magnesium phthalocyanine thin films’, *European Physical Journal-Applied Physics* , 54(1), 147-164, DOI: 10.1051/epjap/ 2011100355.
- El-Nahass, M. M., Abd-El-Rahman, K. F., Farag, A. A. M. and Darwish, A. A. A. (2006) ‘Structural and transport properties of thermally evaporated nickel phthalocyanine thin films’, *Physica Scripta*, 73(1), pp. 40-47, DOI: 10.1088/0031-8949/73/1/006.
- Erk, P. and Hengelsberg, M. (2003) ‘Phthalocyanine Dyes and Pigments. In The Porphyrin Handbook: Applications of phthalocyanines’, Vol. 19’ (eds. Kadish, K.M., Smith, K.M., and Guilard, R.) San Diego : Academic Press.

F

- Fan, F. and Faulkner, L. (1978) ‘Photo-voltaic effects of metal-free and zinc phthalocyanines .2. Properties of illuminated thin-film cells’, *Journal of Chemical Physics,* 69(7), pp. 3341-3349, DOI: 10.1063/1.436988.
- Ferraro, J. R., Nakamoto, K. and Brown C. W. (2003) ‘Introductory Raman Spectroscopy’, 2nd Edn. San Diego, California: Academic Press.
- Feyman, R. (1960) ‘There's plenty of the room at bottom-Engineering and science’ California: California Institute Of Technology.
- Freyer, W. F., Neacsu, C. C. and Raschke, M. B. (2008) ‘Absorption, luminescence, and Raman spectroscopic properties of thin films of benzo-annelated metal-free porphyrazines’, *Journal of Luminescence*, 128(4), pp. 661-672, DOI: 10.1016/j.jlumin.2007.11.070.
- Fu, X.Q., Pan, Y., Wang, X. and Lombardi, J. R. (2011) ‘Quantum confinement effects on charge-transfer between PbS quantum dots and 4-mercaptopyridine’, *Journal of Chemical Physics*, 134(2), pp. 0247071-0247075.

G

- Gabbay, K. H., Bohren, K. M., Morello, R., Bertin, T., Liu, J., and Vogel, P. (2010) ‘Ascorbate synthesis pathway, dual role of ascorbate in bone homeostasis,’ *The Journal of Biological Chemistry,* 285(25), pp. 19510-19520, DOI:10.1074/Jbc. M110.110247.
- Garcia-Sanchez, M. A. and Campero, A. (2000) ‘Aggregation properties of metallic tetrasulfophthalocyanines embedded in sol-gel silica’, Polyhedron, 19(22-23), pp. 2383-2386, DOI: 10.1016/S0277-5387(00)00575-1.
- Ghosh, D., Levault, K. R., Barnett, A. J. and Brewer, G. J. (2012) ‘A reversible early oxidized redox state that precedes macromolecular ROS damage in aging

nontransgenic and 3xtg-ad mouse neurons,' *Journal of Neuroscence*, 32, pp. 5821-5832.

- Godovsky, D. Y. (2000) 'Device applications of polymer-nanocomposites', *Biopolymers/PVA hydrogels/anionic polymerisation nanocomposites*, 153, pp. 163-205.
- Gonidec, M., Luis, F., Vilchez, A., Esquena, J., Amabilino, D. and Veciana, J. (2010) 'A liquid-crystalline single-molecule magnet with variable magnetic properties', *Angewandte Chemie International Edition*, 49(9), pp. 1623-1626, DOI: 10.1002/anie.200905007.
- Gorsuch R.L. and Lehmann C.S. (2010) 'Correlation Coefficients: Mean Bias and Confidence Interval Distortions', Journal of Methods and Measurement in the Social Science, 1(2), pp. 52-65.
- Gould, R. D. and Safai, T. S. (2000) 'Conduction in lead phthalocyanine films with aluminium electrodes', *Proceedings of the 11th International Conference on Thin Films,* 373(1-2), pp. 89-93, DOI: 2048/10.1016/S0040-6090(00)01097-X.
- Gregory, P. (2000) 'Industrial applications of phthalocyanines', *Journal of Porphyrins and Phthalocyanines,'* 4(4), pp. 432-437, DOI: 10.1002/(SICI)1099-1409(200006/07)4:4<432::AID-JPP254>3.0.CO;2-N.
- Guchhait, A., Das, S., Ray, S. K. and Pal, A. J. (2013) 'Photoinduced Hole-Transfer in Nanoparticle-Dye Hybrid Composites: A Route for Exciton Dissociation Leading to Photovoltaic Devices', *Nanoscience and nanotechnology letters,* 5(1), pp. 13-18, DOI: 10.1166/nnl.2013.1415.
- Guillaud, G., Simon, J. and Germain, J. P. (1998) 'Metallophthalocyanines - Gas sensors, resistors and field effect transistors', *Coordination Chemistry Reviews,* 178(2), DOI: 10.1016/S0010-8545(98)00177-5.
- Guo, M., Yan, X. Z., Kwon, Y., Hayakawa, T., Kakimoto, M. A.and Goodson, T.(2006) 'High frequency dielectric response in a branched phthalocyanine,' J*ournal*

of the American Chemical Society, 128(46), pp. 14820-14821, DOI: 10.1021/ja063796w.

- Gupta, S. K., Singh J. and Akhtar, J. (2012) ‘Materials and Processing of Gate Dielectric on Silicon Carbide (SiC) Surface’, Physics and Technology of Silicon Carbide Devices, Croatia: InTech publisher.
- Gürek, A. G., Basova, T., Luneau, D., Lebrun, C., Kol'tsov, E., Hassan, A. and Ahsen, V. (2006) ‘Synthesis, structure, and spectroscopic and magnetic properties of mesomorphicoctakis(hexylthio)-substituted phthalocyanine rare-earth metal sandwich complexes’, *Inorganic Chemistry,* 45(4), pp. 1667-1676, DOI:10.1021/Ic051754n.

H

- H and J aggregates, DST Unit of Nanoscience. Available at; http://www.dstuns.-iitm.ac.in/teaching-and-presentations (Accessed 17 April, 2014).
- Hadzsiev, K., Maasz, A., Kisfali, P., Kalman, E. Gomori, E., Pal, E., Berenyi, E., Komlosi, K. and Melegh, B. (2010) ‘Mitochondrial DNA 11777C > a mutation associated leigh syndrome: case report with a review of the previously described pedigrees’, *NeuroMolecular Medicine,* 12(3), pp. 277-284, DOI 10.1007/S12017-010-8115-9.
- Hanack, M. and Dini, D. (2003) ‘Stacked polymeric phthalocyanines: synthesis and structure-related properties’, In the Porphyrin Handbook, Vol. 18, (Eds: Kadish, K.M., Smith, K.M., Guilard R.), Academic Press.
- Hatsusaka, K., Ohta, K., Yamamoto, I. and Shirai, H. (2001) ‘Discotic liquid crystals of transition metal complexes, Part 30: spontaneous uniform homeotropic alignment of octakis(dialkoxyphenoxy)phthalocyaninatocopper(II) complexes’, *Journal of Materials Chemistry,* 11(2), pp. 423–433, DOI: 10.1039/b004406g.
- Hattori, K., Kajimura, M., Hishiki, T., Nakanishi, T., Kubo, A., Nagahata, Y., Ohmura, M., Yachie-Kinoshita, A., Matsuura, T., Morikawa, T., Nakamura, T.,

Setou, M. and Suematsu, M. (2010) 'Paradoxical ATP elevation in ischemic penumbra revealed by quantitative imaging mass spectrometry', *Antioxid Redox Signaling,* 13(8), pp.1157-1167, DOI: 10.1089=Ars.2010.3290.

- Hiemenz, P. C. and Lodge T. P. (1984) 'Polymer Chemistry'. 2nd edn. New York: Marcel Dekker, Inc. Press.
- Huang, T., Hao, Z., Gong, H., Liu, Z. J., Mao, S., Li, S. Y., Zhai, Y. Y., You, S. Z., Wang, Q. Q. and Qin, J. G. (2008) 'Third-order nonlinear optical properties of a new copper coordination compound: a promising candidate for all-optical switching,' *Chemical Physics Letters,* 451(4-6), pp. 213-217, DOI: 10.1016/J.Cplett.2007.12.001.
- Hunter, C. A. and Sanders, J. K. M. (1990) 'The nature of pi-pi interactions,' *journal of the American Chemical Society,* 112(14), pp. 5525-5534, DOI: 10.1021/ja00170a016.
- Hurd, C.M. (1985) 'Quantum tunneling and the temperature-dependent dc conduction in low-conductivity semiconductors,' *Journal of Physics C-Solid State Physics,*18(35), pp. 6487-6499, DOI: 10.1088/0022- 3719/18/35/014.
- Hussein, N. A. (1990) 'Semiconducting properties of some μ-bridged phthalocyanines', Ph.D thesis, University of Nottingham, United Kingdom.

I

- Ishikawa, N. (2001) 'Electronic structures and spectral properties of double- and triple-decker phthalocyanine complexes in a localized molecular orbital view', *Journal of Porphyrins and Phthalocyanines,* 5(1), pp. 87-101, DOI: 10.1002/1099-1409(200101)5:1<87:AID-JPP304>3.3.CO;2-H.
- Ishikawa, N., Ohno, O., Kaizu, Y. and Kobayashi, H. (1992) 'Localized orbital study on the electronic-structure of phthalocyaninedimers', *Journal of physical chemistry,* 96(22), pp. 8882-8839, DOI: 10.1021/j100201a028.

- Iwatsu F., Kobayashi T. and Uyeda N. (1980) ‘Solvent effects on crystal growth and transformation of zinc phthalocyanine’, *Journal of Physical Chemistry*, 84(24), pp. 3223-3230, DOI: 10.1021/j100461a018.

J

- Jafari, M., Azim-Araghi, E. and Gholami M. (2012) ‘Chemiresistive electrical properties of chloroaluminumphthalocyanine nanostructured thin films’, *Optoelectronics and Advanced Materials Rapid Communications,* 6(9-10), pp. 868-874.
- Jiang, J.Z., Bao, M., Rintoul, L. and Arnold, D. P. (2006) ‘Vibrational spectroscopy of phthalocyanine and naphthalocyanine in sandwich-type (na)phthalocyaninato and porphyrinato rare earth complexes’, *Coordination Chemistry Reviews,* 250 (3-4), pp. 424-448, DOI: 10.1016/j.ccr.2005.09.009.
- Jiang, J., Rintoul, L. and Arnold, D. P. (2000) ‘Raman spectroscopic characteristics of phthalocyanine andnaphthalocyanine in sandwich-type (na)phthalocyaninato andporphyrinato rare earth complexes’, *Polyhedron*, 19(11), pp. 1381-1394, DOI: 10.1016/S0277-5387(00)00426-5.
- Jones, R., Krier, A. and Davidson, K. (1997) ‘Structure, electrical conductivity and electrochromism in thin films of substituted and unsubstituted lanthanide bisphthalocyanines’, *Thin solid films,* 298(1-2), pp. 228-236, DOI: 10.1016/S0040-6090(96)09302-9.

K

- Kane, A. J. and Evans, D. J. (1996) ‘An instruction systolic array architecture for neural networks,’ *International Journal of Computer Mathematics*, 61(1-2), pp. 63-89, DOI: 10.1080/00207169608804500.

- Kadish K. M., Nakanishi, T., Gürek, A., Ahsen, V. and Yilmaz, I. (2001) 'Electrochemistry of a double-decker lutetium (III) phthalocyanine in aqueous media. The first evidence for five reductions', *Journal of Physical Chemistry B,* 105 (40), pp. 9817-9821, DOI: 10.1021/jp012636y.

- Kasha, M., Rawls, H. R. and El-Bayoumi, M. A. (1965) 'The exciton model in molecular spectroscopy,' *Pure and Applied Chemistry,* 11(3-4), pp. 371-392, DOI:org/10.1351/pac196511030371.

- Ke, M.R., Yeung, S.L., Fong, W.P., Ng, D.K. P. and Lo, P.C. (2012) 'A phthalocyanine-peptide conjugate with high in vitro photodynamic activity and enhanced in vivo tumor-retention property',*Chemistry-A European Journal,* 18 (14), pp. 4225-4233, DOI:10.1002/Chem.201103516.

- Keeley, G. P., O'Neill, A., McEvoy, N., Peltekis, N., Coleman, J. N. and Duesberg, G.S. (2010) 'Electrochemical ascorbic acid sensor based on DMF-exfoliated grapheme,' *Journal of Materials Chemistry,* 20(36), pp. 7864-7869, DOI: 10.1039/C0jm01527j.

- Khan, M. A. M ., Zulfequar, M., Kumar, A. and Husain, M. (2004) 'Conduction mechanism in amorphous $Se_{75}In_{25}$-xPb_x films', *Materials Chemistry and Physics,* 87 (1), pp. 179-183, DOI: 10.1016/j.matchemphys.2004.05.033.

- Khan, Z. H., Malik, M. M., Zulfequar, M. and Husain, M. (1995) 'Electrical-conduction mechanism in a-Se-80-xTe_xGa_{20} films (0-less-than-or-equal-to-x-less-than-or-equal-to-20)', *Journal of Physics-Condensed Matter,* 7 (47), pp. 1979-8991, DOI:10.1088/0953-8984/7/47/017.

- Khozaee, Z. (2012) 'Studies on organic/inorganic nanocomposites of lead sulphide quantum dots in solution processed phythalocyanine films', Queen Mary, University of London.

- Kılınç, N., Öztürk, S., Atilla, D., Gürek, A., Ahsen, V. and Öztürk, Z. Z. (2012) 'Electrical and NO2 sensing properties of liquid crystalline phthalocyanine thin films' *Sensors and Actuators B Chemical,* 173, pp. 203- 210, DOI:10.1016/j.snb.2012.06.072.

- Kim, Y.D., Jae, P. K., Kwon, O. S. and Chob, I. H. (2009) ‘The synthesis and application of thermally stable dyes for ink-jet printed LCD color filters’, *Dyes and Pigments,* 81(1), pp. 45-52.
- Kim, D., Kim, D. H., Lee, J. H. and Grossman, J. C. (2013) ‘Impact of stoichiometry on the Electronic Structure of PbS Quantum Dots’, *Physical review letters*, 110(19), DOI: 10.1103/PhysRevLett.110.196802.
- Koca, A., Dincer, H.A., Kocak, M. B. and Gul, A., (2006) ‘Electrochemical Characterization of Co(II) and Pd(II) Phthalocyanines Carrying Diethoxymalonyl and Carboxymethyl Substituents,’ R*ussian Journal of Electrochemistry,* 42(1), pp. 31-37, DOI: 10.1134/S102319350601006X.
- Kudrik, E.V., Smirnova, A.L., Maizlish, V.E., Tararykina, T.V., Shaposhnikov, G.P. and Usol'tseva, N.V. (2006) ‘Copper 2,9(10),16(17),23(24)- and 1,8(11),15(18),22(25)-tetra-(4-carboxyphenoxy)phthalocyanines and their esters: the synthesis and liquid -crystalline properties’, *Russian Chemical Bulletin,* 55(6), pp. 1028-1037, DOI: 10.1007/S11172-006-0372-2.
- Kumar, S. (2010) ‘Recent developments in the chemistry of triphenylene-based discotic liquid crystals’, *Liquid Crystals,* 31(8), pp. 1037-1058, DOI: 10.1080/02678290410001724746.
- Kuila, T., Bose, S., Khanra, P., Mishra, A. K., Kim, N. H. and Lee, J.H. (2011) ‘Recent advances in graphene-based biosensors’, *Biosensors and Bioelectronics,* 26 (12), pp. 4637-4648, DOI: 10.1016/j.bios.2011.05.039.
- Kullerud, G. (1969) ‘The lead-sulfur system’, *American Journal of Science*, 267-A, pp. 233-256.
- Kwong, C. Y., Djurisic, A. B., Chui, P. C., Lam, L. S. M. and Chan, W. K. (2003) ‘Improvement of the efficiency of phthalocyanine organic Schottky solar cells with ITO electrode treatment,’ *Applied Physics A-Materials Science &Processing,* 77(3-4), pp. 555-560, DOI: 10.1007/s00339-002-1493-6.

L

- Lampert M. **A.** (1965) 'Volume-controlled current injection in insulators',*Reports on Progress in Physics,* 27, pp. 329-367, DOI:10.1088/0034-4885/27/1/307.
- Lawton, E. A. (1958) 'The thermal stability of copper phthalocyanine,' *The Journal of Physical Chemistry,* 62 (3), pp. 384-384, DOI: 10.1021/J150561a051.
- Lee, K. S., Won, M. S., Noh, H. B. and Shim, Y. B. (2010) 'Triggering the redox reaction of cytochrome C on a biomimetic layer and elimination of interferences for NADH detection', *Biomaterials,* 31(30), pp. 7827-7835, DOI:10.1016/J.Bio materials.2010.06.052.
- Lee, W., Yuk, S. B., Choi, J., Jung, D. H., Choi, S. H., Park, J. and Kim, J. P. (2012) 'Synthesis and characterization of solubility enhanced metal-free phthalocyanines for liquid crystal display black matrix of low dielectric constant', *Dyes and Pigments*, 92(3), pp. 942-948, DOI: 10.1016/j.dyepig.2011.08.001.
- Lehninger, A.L. (1975) 'Vitamins and coenzymes' *Biochemistry, 2nd Edition, The John Hopkins University School Of Medicine*, New York: Worth Publishers Inc., pp. 337 – 342.
- Li, L., Tang, Q., Li, H., Yang, X., Hu, W., Song, Y., Shuai, Z., Xu, W., Liu, Y. and Zhu, D. (2007) 'An ultra-closely pi-stacked organic semiconductor for high performance field-effect transistors,' *Advanced Materials,*19(18), pp. 2613-2617, DOI: 10.1002/Adma.200700682.
- Li L. Q., Tang Q. X., Li H. X., Hu W., Yang X. O., Shuai Z., Liu Q. and Zhu D., (2008) 'Organic thin-film transistors of phthalocyanines', *Pure and applied chemistry,* 80(11), 2231-2240, DOI: 10.1351/pac200880112231.
- Li, Q. and Zhou, X. (2006) 'Light-harvesting discotic liquid crystalline porphyrins and metal complexes,' *Patent Number: US 7291727 B1, DE112006003607T5, US20070152189, WO2007081490A1*, Patent Assignee: Kent State University.

- Li, X. F., Zhang, S. X. and Sun, C. Q. (2003) ‘Fabrication of a covalently attached multilayer film electrode containing cobalt phthalocyanine and its electrocatalytic oxidation of hydrazine’, *Journal of Electroanalytical Chemistry,* 553, pp. 139-145, DOI:10.1016/S0022-0728(03)00307-3.
- Liao, M. and Scheiner, S. (2001) ‘Electronic structure and bonding in metal phthalocyanines metal = Fe,Co,Ni,Cu,Zn,Mg’, *Journal of Chemical Physics,* 114(22), pp. 9780-9791, DOI:10.1063/1.1367374.
- Lide, D. R. (2007) ‘CRC Handbook of Chemistry and Physics’, 88th Edn., CRC press.
- Lin, S.J. and Guarente, L. (2003) ‘Nicotinamide adenine dinucleotide, a metabolic regulator of transcription, longevity and disease’, *Current Opinion in Cell Biology,* 15(2), pp. 241-246, DOI: 10.1016/S0955-0674(03)00006-1.
- Linstead, R.P. (1934) ‘Phthalocyanines - Part I - a new type of synthetic colouring matters’, *Journal of the Chemical Society*, pp. 1016-17.
- Liu, J. C., Yu, H. Z., Wu, Z. L., Wang, W. L., Peng, J. B. and Cao, Y. (2008) ‘Size-tunable near-infrared PbS nanoparticles synthesized from lead carboxylate and sulfur with oleylamine as stabilizer’, *Nanotechnology,* 19(34), pp. 3456021-3456026, DOI: 10.1088/0957-4484/19/34/345602.
- Liu, T., Brown, D. A.and O'Rourke, B. (2010) ‘Role of mitochondrial dysfunction in cardiac glycoside toxicity’, *Journal of Molecular and Cellular Cardiology,* 49(5) pp. 728-736, DOI:10.1016/j.yjmcc.2010.06.012.
- Lu, F.L., Bao, M., Ma, C. Q., Zhang, X. X., Arnold, D. P. and Jiang, H. Z. (2003) ‘Infrared spectra of phthalocyanine and naphthalocyanine in sandwich-type (na)phthalocyaninato and porphyrinato rare earth complexes. Part 3. The effects of substituents and molecular symmetry on the infrared characteristics of phthalocyanine in bis(phthalocyaninato) rare earth complexes’, *Spectrochimica Acta Part A-Molecular and Biomolecular Spectroscopy,* 59(14), pp. 3273-3286, DOI: 10.1016/S1386-1425(03)00158-6.

M

- Machol, J. L., Wise, F. W., Patel, R. C. and Tanner, D. B. (1993) ‘Vibronic quantum beats in pbS microcrystallites’, P*hysical Review* B, 48(4), pp. 2819-2822, DOI: 0.1103/PhysRevB.48.2819

- Manjunatha, K. B., Dileep, R., Umesh, G. and Bhat, B. R. (2013) ‘Nonlinear optical and all-optical switching studies of palladium (II) complex’, *Materials Letters*, 105, pp. 173-176, DOI:10.1016/j.matlet.2013.03.076.

- Majumdar. H., Bandyopadhyay. A. and Pal, A. J. (2003) ‘Data-storage devices based on layer-by-layer self-assembled films of a phthalocyanine derivative’, *Organic Electronics,* 4 (1), pp. 39–44, DOI: org/10.1016/S1566-1199(03)00007-7.

- Martin, M.G., de Saja, J. A., Munoz, R. and Rodriguez-Mendez, M. L. (2012) ‘Multisensor system based on bisphthalocyanine nanowires for the detection of antioxidants’, *Electrochimia Acta,* 68, pp. 88-94, DOI:10.1016/J.Electacta.-2012.02.042.

- Mekprasart, W., Jarernboon, W. and Pecharapa, W. (2010) ‘TiO2/CuPc hybrid nanocomposites prepared by low-energy ball milling for dye-sensitized solar cell application,’ M*aterials Science and Engineering B-Advanced Functional Solid-State Materials,* 172(3), pp. 231-236.

- McDonald, S.A., Konstantatos, G., Zhang, S. G., Cyr, P.W., Klem, E. J. D., Levina, L. and Sargent, E.H. (2005) 'Solution-processed PbS quantum dot infrared photodetectors and photovoltaics’, *Nature Materials*, 4(2), pp. 138-U14.

- Mendonca, C.R., Gaffo, L., Misoguti, L., Moreira, W. C., Oliveira, O. N. and Zilio, S. C. (2000) ‘Characterization of dynamic optical nonlinearities in ytterbium bis-phthalocyanine solution’, *Chemical Physics Letters,* 323(3-4), pp. 300-304, DOI:10.1016/S0009-2614(00)00509-1.

- Moeno, S. and Nyokong, T. (2009) ‘Opposing responses elicited by positively charged phthalocyanines in the presence of CdTe quantum dots’, *Journal of*

Photochemistry and Photobiology A: Chemistry, 201(2-3), pp. 228-236, DOI:10.1016/j.jphotochem.2008.10.027.

- Molecular Fluorescence Spectroscopy. Available at: http://www.chemistry.-adelaide.edu.au/external/soc-rel/content/mol-fluo.htm. (Accessed: 2 April 2014).
- Moreels, I., Lambert, K., Smeets, D., Muynck, D., Nollet, T., Martins, J.C., Vanhaecke, F., Vantomme, A., Delerue, C., Allan, G. and Hens, Z. (2009) 'Size-dependent optical properties of colloidal pbS quantum dots', *ACS Nano,* 3 (10), pp. 3023-30.
- Mott, N. F. and Davis, E. A. (1971) Electronic Processes in Non-Crystalline Materials. Oxford: Clarendon press.
- Msayib, K., Makhseed, S. and Mckeown, N. (2001) 'Synthetic strategies towards macrodiscotic materials. Can a new dimension be added to liquid crystal polymers', *Journal of Materials Chemistry,* 11 (11), pp. 2784-2789.
- Mukherjee, B., Ray, A. K., Sharma, A. K., Cook, M. J. and Chambrier, I. (2008) 'A simply constructed lead phthalocyanine memory diode', *Journal of applied physics*, 103(7), DOI: 10.1063/1.2903061.
- Murray, C., Dozova, N., McCaffrey, J. G., FitzGerald, S., Shafizadeh, N. and Crepin, C. (2009) 'Infra-red and Raman spectroscopy of free-base and zinc phthalocyanines isolated in matrices' *Physical Chemistry Chemical Physics*, 12(35), pp. 10406-10442, DOI: 10.1039/c0cp00055h.

N

- Nabok A. V., Ray, A. K. Cook, M. J., Burnham, P. M., Iwantono, Y. H., Simmonds, M. and Basova, T.V. (2004) 'Lead sulphide/phthalocyanine nanocomposite spun films' *IEEE Transactions on Nanotechnology*, 3(3), pp. 388-394, DOI: 10.1109/-TNANO.2004.834155.
- Nair, P.S., Radhakrishnan, T., Revaprasadu, N., Kolawole, G.A., Luyt, A.S. and Djoković, V. (2005) 'Structure and properties of PbS-polyacrylamide

nanocomposites', *Applied Physics A,* 81(4), pp. 835-838, DOI: 10.1007/s00339-005-3283-4.

- Nakanishi, T., Yilmaz, I., Nakashima, N. and Kadish, K. M. (2003) 'Thermodynamic study of ion-pairing effects between reduced double-decker lutetium(III) phthalocyanines and a cationic matrix,' *Journal of Physical Chemistry B,* 107(46), pp. 12789-12796, DOI: 10.1021/jp035497o.
- Nalwa H.S. and Miyata S. (1997), 'Nonlinear optics of organic molecules and polymers', Ed., Boca Raton, FL: CRC Press.
- Nekelson, F., Monobe, H., Shiro, M. and Shimizu, Y. (2007) 'Liquid crystalline and charge transport properties of double-decker cerium phthalocyanine complexes', *Journal of Materials Chemistry*, 17 , pp. 2607-2615, DOI: 10.1039/B616848p.
- Nemykin, V.N. and Lukyanets, E. A. (2010) 'Synthesis of substituted phthalocyanines' Arkivoc, Part 1, pp. 136-201.
- Nensala, N. and Nyokong, T. (1998) 'Photoassisted reduction of thionyl chloride by neodymium, europium, thulium and lutetium diphthalocyanines', *Polyhedron* 17(19) pp. 3467- 3475, DOI: 10.1016/S0277-5387(98)00133-8.
- Neudeck, A., Marken, F. and Compton, R. G. (1999) 'Complex electron transfer kinetic data from convolution analysis of cyclic voltammograms: theory and application to diamond electrodes', *Electroanalysis,* 11(15), pp. 1149-1154, DOI: 10.1002/(SICI)1521-4109(199911)11:15<1149::AID-ELAN1149>3.0.CO;2-L.

O

- Ohta, K., Hatsusaka, K., Sugibayashi, M., Ariyoshi, M., Ban, K., Maeda, F., Naito, R., Nishizawa, K., van de Craats, A. M. and Warman, J. M. (2003) 'Discotic liquid crystalline semiconductors', *Molecular crystals and liquid crystals*, 397(2), pp. 325-345, DOI: 10.1080/15421400390213690.
- Orti, E., Brédas J. L. and Clarisse, C. (1990) 'Electronic-structure of phthalocyanines - theoretical investigation of the optical-properties of phthalocyanine monomers,

dimers, and crystals', *The Journal of Chemical Physics,* 92, pp. 1228-1235, DOI:10.1063/1.458131.

- Ortiz, J, Parejo, C., Paya, F., Fernandez-Lazaro, F., Luer, L. and Sastre-Santos, A. (2013) 'Synthesis and optical properties of phthalocyaninedihydrobenzocyclobut-acenaphthylene Systems', *Journal of Porphyrins and Phthalocyanines*, 17(10), pp. 1008-1015, DOI: 10.1142/S1088424613500879.
- Orwa J. O., Shannon J. M., Gateru R. G. and Silva S. R. P. (2005) 'Effect of ion bombardment and annealing on the electrical properties of hydrogenated amorphous silicon metal–semiconductor–metal structures', *Journal of Applied Physics,* 97, pp. 023519-023525, DOI: 10.1063/1.1834710.
- Özer, L. M., Özer, M., Altindal, A., Özkaya, A. R., Salih, B. and Bekaroğlu, Ö. (2013) 'Synthesis, characterization, OFET and electrochemical properties of novel dimeric metallophthalocyanines', *Dalton Transactions,* 42(18), pp. 6633-6644, DOI: 10.1039/C3dt50212k.

P

- Passard, M., Blanc, J. P. and Maleysson, C. (1995) 'Gaseous oxidation and compensating reduction of lutetium bis-phthalocyanine and lutetium phthalo-nap hthalocyanine films', *Thin Solid Films,* 271(1-2), pp. 8-14, DOI:10.1016/0040-6090(95)06673-X.
- Patel, A., Wu, F., Zhang, J., Martinez, C., Mehra, R., Yang, Y. and Risbud, S. (2000) 'Synthesis, optical spectroscopy and ultrafast electron dynamics of PbS nanoparticles with different surface capping,' *The Journal of Physical Chemistry B,* 104 (49), pp. 11598 -11605, DOI: 10.1021/jp000639p.
- Patel, J.D., Mighri, F., Ajji, A. and Chaudhuri, T. K. (2012) 'Morphology and size control of lead sulphide nanoparticles produced using methanolic lead acetate trihydrate-thiourea complex via different precipitation techniques', *Materials Chemistry and Physics,* 132(2-3), pp. 747-755.

- Patnaik, P. (2003) Handbook of Inorganic Chemical Compounds. New York: McGraw-Hill.
- Paul, S., Paul, D., Basova, T. and Ray, A. K. (2010) 'Characterisation of protein adsorption on different liquid crystal phthalocyaninethin films,' *IET Nanobiotechnology,* 4(1), pp. 1-9, DOI: 10.1049/iet-nbt.2009.0011.
- Peisert, H., Biswas, I., Zhang, L., Knupfer, M., Hanack, M., Dini, D., Cook, M. J., Chambrier, I., Schmidt, T., Batchelor, D. and Chasse, T. (2005) 'Orientation of substituted phthalocyanines on polycrystalline gold: distinguishing between the first layers and thin films', *Chemical Physics Letter,* 403(1-3), pp.1-6, DOI: 10.1016/j.cplett.2004.12.039.
- Perkin-Elmer Hardware Guide.Available at: http://www2.ul.ie/pdf/234493239.pdf. (Accessed: 2 April, 2014).
- Phan B.T., Jung C., Choi T. and Lee J. (2006) 'Trap-controlled space-charge-limited current conduction in the Cr-doped $SrTiO_3$ thin films deposited by using pulsed laser deposition', *Journal of the Korean Physical Society,* 51(2), pp. 664-668.
- Piechocki C., Simon, J., Skoulios, A., Guillon, D. and Weber, P. (1982) 'Discotic mesophases obtained from substituted metallophthalocyanines- Toward liquid crystalline one-dimensional conductors,' *Journal of the American Chemical Society,* 104(19), pp. 5245-5247, DOI: 10.1021/ja00383a050.
- Pope, M. and Swenberg. C. E. (1999) 'Electronic Processes in Organic Crystals and Polymers'. 2nd edn., Oxford: Oxford university press.
- Pu, Z. J., Chen, L., Tong, L. F., Long, Y., Huang, X. and Liu, X. B. (2013) 'Facile synthesis of copper phthalocyanine supported on MWCNTs to improve their dispersibility and compatibility in PEN matrix', *Materials Letters,* 109, pp. 116-119, DOI: 10.1016/j.matlet.2013.07.055.

R

- Radoi, A. and Compagnone, D. (2009) ‘Recent advances in NADH electrochemical sensing design’, *Bioelectrochemistry,* 76(1-2), pp. 126-134.

- Ragoussi, M. E., Ince, M. and Torres, T. (2013) ‘Recent advances in phthalocyanine-based sensitizers for dye-sensitized solar cells’, *European Journal of Organic Chemistry,* 2013(29), pp. 6475-6489, DOI:10.1002/ejoc.201301009.

- Rakshit, P. C. (2001) ‘Physical Chemistry’.7th edn., Kolkata:Sarat Book Distributors.

- Ray, A.K., Nabok, A.V., Hassan, A. K., Omar, O. and Taylor, R. (1999) ‘An interpretation of the structure of Langmuir - Blodgett films of octa-substituted metal-free phthalocyanine molecules from optical spectra’, *Philosophical Magazine Part B*, 78(1), pp. 53-64, DOI:10.1080/13642819808206726.

- Raynaud-Simon, A., Cohen-Bittan, J., Gouronnec, A., Pautas, E., Senet, P., Verny, M. and Boddaert, J. (2010) ‘Scurvy in hospitalized elderly patients’, *The Journal of Nutrition, Health and Aging*, 14(6), pp. 407-410.

- Robertson J. M., (1935) 'An X-ray study of the structure of the pthalocyanines part I - the metal-free, copper, and platinum compounds,' *Journal of Chemical Society*, pp. 615-621, DOI: 10.1039/JR9350000615.

- Rodriguez-Mendez, M. L., Gay, M. and de-Saja, J. A. (2009) ‘New insights into sensors based on radical bisphthalocyanines’, *Journal of Porphyrins and Phthalocyanines,* 13(11), pp. 1159-1167, DOI:10.1142/S1088424609001509.

- Rousseau, R., Aroca, R. and Rodriguez-mendez, M.L. (1995) ‘Extended Hückel molecular orbital model for lanthanide bisphthalocyanine complexes,’ *Journal of Molecular Structure,* 356(1), pp. 49-62, DOI: 10.1016/0022-2860(95)08905-B.

- RoyChoudhury, K., Samoc, M., Patra, A. and Prasad, P. (2004) 'Charge carrier transport in poly(n-vinylcarbazole): CdS quantum dot hybrid nanocomposite', *Journal of Physical Chemistry B,* 108 (5), pp. 1556-1562.

- RoyChoudhury, K., Song, D. W. and So, F. (2010) 'Efficient solution-processed hybrid polymer–nanocrystal near infrared light-emitting devices,' *Organic Electronics*, 11(1), pp. 23-28, DOI: 10.1016/j.orgel.2009.09.017.

S

- Saglam, O. (2013) 'Soft solution synthesis and intense visible photoluminescence of lamellar zinc oxide hybrids', *Scripta Materialia,* 69(6), pp. 441-444, pp. 1-9, DOI: 10.1016/j.scriptamat.2013.05.023.
- Sahu, N., Parija, B. and Panigrahi, S. (2009) Fundamental understanding and modelling of spin coating process: A review', *Indian Journal of Physics*, 83 (4), pp. 493-502.
- Saleh A.M., Hassan, A.K. and Gould, R.D. (2003) 'DC conduction processes and electrical parameters of the organic semiconducting zinc phthalocyanine, ZnPc, thin films', *Journal of Physics and Chemistry of Solids,* 64(8), pp. 1297-1303.
- Salimi, A., Lasghari, S., and Noorbakhash, A. (2010) 'Carbon nanotubes-ionic liquid and chloropromazine modified electrode for determination of NADH and fabrication of ethanol biosensor' *Electroanalysis,* 22(15), pp. 1707-1716, DOI: 10.1002/Elan.201000020.
- Sargent, E.H. (2005) 'Infrared quantum dots', *Advanced Materials,* 17(5), pp. 515-522, DOI: 10.1002/adma.200401552.
- Sarma, S. and Datta, P. (2010) 'Characteristics of poly(vinyl alcohol)/lead sulphide quantum dot device', *Nanoscience and Nanotechnology Letters*, 2(3), pp. 261-265, DOI: 10.1166/nnl.2010.1091.
- Sen, P., Dumludag, F., Salih, B., Ozkaya, A. R. and Bekaroglu, O. (2011) 'Synthesis and electrochemical, electrochromic and electrical properties of novel S-triazine bridged trinuclear Zn(II), Cu(II) and Lu(III) and a tris double-decker Lu(III) phthalocyanines', *Synthetic Metals,* 161(13-14), pp. 1245-1254, DOI: 10.1016/-J.Synthmet.2011.04.012.

- Shao, Y., Wang, J., Wu, H., Liu, J., Aksay, I. A. and Lin, Y. H. (2010) 'Graphene based electrochemical sensors and biosensors: a review', *Electroanalysis*, 22(10), pp. 1027-1036, DOI: 10.1002/elan.200900571.
- Shih C. F., Hung, K. T., Chen, H. J., Hsiao, C. Y. and Huang, K., T. (2011) 'Incorporation of potassium at CuPc/C60 interface for photovoltaic application', *Applied Physics Letter,* 98, pp. 1133071-1133073, DOI: 10.1063/1.3568884.
- Silerova, R., Kalvoda, L., Neher, D., Ferencz, A., Wu, J. and Wegner, G. (1998) 'Electrical conductivity of highly organized Langmuir-Blodgett films of phthalocyaninato-polysiloxane', *Chemistry of Materials,* 10(8), pp. 2284-2292, DOI: 10.1021/cm980251v.
- Simmons, J. G. (1971) 'Conduction in thin dielectric films', *Journal of Physics D-Applied Physics,* 4(5), pp. 613-657, DOI: 10.1088/0022-3727/4/5/202.
- Sosa-Vargas, L., Chambrier, I., MacDonald, C. J., Tizzard, G. J., Cammidge, A. N. and Cook, M. J. (2013) 'Synthesis and characterization of some octaalkyl substituted lead phthalocyanines and unexpected variations in lead lability arising from the position of substituents and their chain length', *Journal of Porphyrins and Phthalocyanines*, 17(6-7), pp. 511-521, DOI: 10.1142/S108842461350020X.
- Streetman, B.G. (2000) 'Solid state electronic devices.' 2nd edn: United Kingdom: Prentice Hall.
- Strukov D.G., Snider, G.S., Stewart, D.R. and Williams, S.R. (2008) 'The missing memristor found', *Nature*, 453 (7191), pp. 80-83.
- Sun, R., Wu, X., Hao, Z. and Zhang, X. (2012) 'Crystal structure and self-assembly property of sandwich-type mixed (phthalocyaninato)(porphyrinato) rare earth double-decker complexes', *Inorganica Chimica Acta,* 384(1), pp. 204-209.
- Sun, J., Zhu, M., Fu, K., Lewinski, N. and Drezek, R. A. (2007) 'Lead sulfide near-infrared quantum dot bioconjugates for targeted molecular imaging', *International Journal of Nanomedicine,* 2(2), pp. 235-240.

- Sun, X., Ma, C. Q. and Jiang, J.Z. (2003) 'Luminescence and photophysics of sandwich-type bis(phthalocyaninato) europium compound', *Synthetic Metals,* 139(2), pp. 497-500, DOI: 10.1016/s0379-6779(03)00206-6.
- Swarts, J. C., Langner, E. H. G., Krokeide-Hove, N. and Cook, M. J. (2001) ‘Synthesis and electrochemical characterisation of some long chain 1,4,8,11,15,18,22,25-octa-alkylated metal-free and zinc phthalocyanines possessing discotic liquid crystalline properties’, *Journal of Material Chemistry,* 11(2), pp. 434-443, DOI: 10.1039/B006123I.
- Sykora, M., Petruska, M.A., Alstrum-Acevedo, J., Bezel, I., Meyer, T. J. and Klimov, V. I. (2006) ‘Photoinduced charge transfer between CdSe nanocrystal quantum dots and Ru-polypyridine complexes’, *Journal of the American Chemical Society,* 128(31), pp. 9984 -9985, DOI: 10.1021/Ja061556a.
- Szybowicz, M., Runka, T., Drozdowski, M., Bala, W., Wojdyla, M., Grodzicki, A., Piszczek, P. and Bratkowski, A. (2007) ‘Temperature Study of Raman, FT-IR and photoluminescence spectra of ZnPc thin layers on Si substrate’, *Journal of Molecular Structure*, 830(1-3), pp. 14-30, DOI: 10.1016/j.molstruc.2006.06.026.

T

- Tackley, D. R., Dent, G. and Smith, W. E. (2001) ‘Phthalocyanines: structure and vibrations’, *Physical Chemistry Chemical Physics,* 3(8), pp. 1419-1426, DOI: 10.1039/b007763l.
- Takamatsu, S. and Ishikawa, N. A. (2007) ‘Theoretical study of a drastic structural change of bis(phthalocyaninato)lanthanide by ligand oxidation: towards control of ligand field strength and magnetism of single-lanthanide-ionic single molecule magnet’, *Polyhedron*, 26 (9-11), pp. 1859−1862, DOI: 10.1016/j.poly.2006.09.020.
- Tao, M. (2008) ‘Inorganic photovoltaic solar cells: Silicon and beyond’, *Electrochemical Society Interface*, 17, pp. 30-35.

- Tans, S. J., Miedema, R. G., Geerligs, L.J., Dekker, C., Wu, J., Neher, D. and Wegner, G. (2003) ‘Electronic transport in monolayers of phthalocyanine polymers’, *Nanotechnology,* 14(9), pp. 1043-1050, DOI: 10.1088/0957-4484/14/9/320.
- Tauc, J. and Menth, A. (1972) ‘States in the gap’, *Journal of Non-Crystalline Solids*, 8(10), pp. 569-588.
- Tkachenko, N.V. (2006) ‘*Optical spectroscopy, methods and instrumentation*’, Amsterdam: Elsevier.
- Tran-Thi, T.H., Mattioli, T. A., Chabach, D., De Cian, A. and Weiss, R. (1994) ‘Hole localization or delocalization - an optical, Raman, and redox study of lanthanide porphyrin-phthalocyanine sandwich-type heterocomplexes’, *The Journal of Physical Chemistry*, 98(34), pp. 8279-8288, DOI:10.1021/j100085a004.
- Tripathi, A. M. and Mitra, S. (2014) ‘Tin sulfide (SnS) nanorods: structural, optical and lithium storage property study’, *Rsc Advances,* 4(20), pp. 10358-10366, DOI: 10.1039/c3ra46308g.
- Trogler, W., Bohrer, F. and Kummel, A.C. (2012) ‘Peroxide chemical sensor and sensing method’ *Patent no. US 008178357B2,* Patent Assignee: University of California.
- Turek, P., Petit, P., Andre, J.J., Simon, J., Even, R., Boudjema, B., Guillaud, G. and Maitrot, M. (1987) ‘A new series of molecular semiconductors - phthalocyanine radicals’, *Journal of the American Chemical Society*, 109(17), pp. 5119-5122, DOI: 10.1021/Ja00251a012.

U

- University of Chembridge. Available at: http://www.doitpoms.ac.uk-/tlplib/raman/raman_microspectroscopy.php (Accessed 4 April 2014).
- Upadhyaya, K. S., Yadav, M. and Upadhyaya, G. K. (2002) ‘Lattice dynamics of IV-VI ionic semiconductors: An application to lead chalcogenides’, *Physica Status*

Solidi B-Basic Research, 229(23), pp.1129-1138, DOI:10.1002/15213951-(200202)229:3<1129::AID-PSSB1129>3.0.CO;2-6.

W

- Wagner, C. D., Gale, L. H., and Raymond, R.H. (1979) 'Two dimensional chemical state plots: a standardized data set for use in identifying chemical states by X-ray photoelectron spectroscopy the oxide-water interface', *Journal of Colloid Interface Science,* 51 (4), pp. 466-482.
- Walter, M. G., Rudine, A. B. and Wamser, C.C. (2010) 'Porphyrins and phthalocyanines in solar photovoltaic cells', *Journal of Porphyrins and Phthalocyanines,* 14(9), pp. 759-792, DOI: 10.1142/S1088424610002689.
- Wang, Y. and Herron, N. (1987) 'Optical properties of cadmium sulfide and lead(II) sulfide clusters encapsulated in zeolites', *The Journal of Physical Chemistry,* 91(2), pp. 257-260, DOI: 10.1021/J100286a004.
- Wang, Y., Suna, A., Mahler, W., Kasowski, R. (1987) 'PbS in polymers: From molecules to bulk solids', *Journal of Chemical Physics*, **87**(12), pp. 7315-7322.
- Wang, W., Liu, Y., Zhan, Y., Zheng, C., Wang, G. (2001) 'A novel and simple one-step solid-state reaction for the synthesis of PbS nanoparticles in the presence of a suitable surfactant', *Materials Research Bulletin,* 36(11), pp. 1977-1984, DOI: 10.1016/S0025-5408(01)00678-X.
- Warner J.H. and Watt, A.A. R. (2006) 'Monodisperse PbS nanocrystals synthesized in a conducting polymer', *Materials Letters*, 60(19), pp. 2375-2378.
- Wells, J. W., Cabailh, G., Evans, D. A., Evans, S., Bushell, A. andVearey-Roberts, A. R. (2004) 'An XPS study of the interaction between tin (II) phthalocyanine and polycrystalline iron', *Journal of Electronic Spectroscopic Related Phenomenon*, 141(1), pp. 67-72, DOI : 10.1016/j.elspec.2004.07.002.
- Wöhrle, D., Schnurpfeil, G., Makarov, S. G., Kazarin, A. and Suvorova, O. N., (2012) 'Practical applications of phthalocyanines - from dyes and pigments to

materials for optical, electronic and photo-electronic devices', *Macroheterocycles,* 5(3), pp. 191-202, DOI: 10.6060/mhc2012.120990w.

X

- Xue, J., Uchida, S., Rand, B. P. and Forrest, S. R. (2004) '4.2% efficient organic photovoltaic cells with low series resistances,' *Applied Physics Letter*, 84 (16), 3013-3015, DOI: 2048/10.1063/1.1713036.

Y

- Yofee, A. D. (2001) 'Semiconductor quantum dots and related systems: electronic, optical, luminescence and related properties of low dimensional systems', *Advances In Physics,* 50(1), pp. 1-208, DOI: 10.1080/00018730010006608.
- Yoshino, K., Lee, S.B., Sonoda, T., Kawagishi, H., Hidayat, R., Nakayama, K., Ozaki, M., Ban, K., Nishizawa, K., Ohta, K. and Shirai, H. (2000) 'Optical properties of substituted phthalocyanine rare-earth metal complexes', *Journal of Applied Physics* 88(12), pp. 7137-7143, DOI:10.1063/1.1316050.

Z

- Zhang, Y. X., Zhang, X. X., Liu, Z. Q., Xu, H. and Jiang, J. Z. (2010) 'Comparative density functional theory study of the structures and properties of metallophthalocyanines of group IVB', *Vibrational Spectroscopy,* 40(2), pp. 289-298, DOI:10.1016/j.vibspec.2005.11.004.
- Zhang, L., Hao, W. W., Wang, H. B., Zhang, L. F., Feng, X. M., Zhang, Y. B., Chen, W. X., Pang, H. and Zheng, H. H. (2013) 'Porous graphene frame supported silicon@graphitic carbon via in situ solid-state synthesis for high-performance lithium-ion anodes', J*ournal of Materials Chemistry*, 1(26), pp. 7601-761, DOI: 10.1039/c3ta11034f.

- Zhang, Q., Chen, H. B., Liu, Y. G. and Huang, D. Y. (2004) ‘Study on the transformation of metal-free phthalocyanine polymorph crystals by organic solvent treatment’, *Dyes and Pigments*, 63(1), pp. 11-16, DOI: 10.1016/j.dyepig.2003.12.012.
- Zhang, X. X., Zhang, Y. X. and Jiang, J. Z. (2003) ‘Isotope effect in the infrared spectra of free-base phthalocyanine and its N,N-dideuterio-derivative: Density functional calculations’, *Vibrational Spectroscopy*, 33(1-2), pp. 153-161, DOI: 10.1016/j.vibspec.2003.08.001.
- Zharnikova, N., Usol'tseva, N., Kudrik, E. and Thelakkat, M. (2009) ‘Synthesis, mesomorphism and electrochemical properties of tetrasubstituted zinc and copper phthalocyanines’, *Journal of Materials Chemistry,* 19(20), pp. 3161-3167, DOI: 10.1039/B821306b.
- Zhong A., Zhang, Y. and Bian, Y. (2010) ‘Structures and spectroscopic properties of nonperipherally and peripherally substituted metal-free phthalocyanines: a substitution effect study based on density functional theory calculations’, *Journal of Molecular Graphics and Modelling,* 29(3), pp. 470-480.
- Zhu, P. H., Lu, F. L., Pan, N., Arnold, D. P., Zhang, S. Y. and Jiang, J. Z. (2004) ‘Comparative electrochemical study of unsubstituted and substituted bis(phthalocyaninato) rare earth(III) complexes’, *European Journal of Inorganic Chemistry,* 3, pp. 510-517, DOI: 10.1002/ejic.200300509.